Semi-Annual Progress Report No. 9

to the

NATIONAL AERONAUTICS AND SPACE ADMINISTRATION

in connection with

NASA Grant NGR 47-004-006

FACILITY FORM 602

N70-72382
(ACCESSION NUMBER)

(PAGES)

CR-109034
(NASA CR OR TMX OR AD NUMBER)

(THRU)
None
(CODE)

(CATEGORY)

Virginia Polytechnic Institute

Blacksburg, Virginia

September, 1969

Semi-Annual Progress Report No. 9

to the

NATIONAL AERONAUTICS AND SPACE ADMINISTRATION

in connection with

NASA Grant NGR 47-004-006

Part 1 of 8 parts

ADMINISTRATIVE AND FINANCIAL INFORMATION

Virginia Polytechnic Institute

Blacksburg, Virginia

September, 1969

Fred W. Bull, Chairman
NASA Grant Committee

Coyt T. Wilson, Acting Dean
Research Division

OTHER PARTS ARE NOT IN AND CAN NOT BE LOCATED

Inquiries relating to this report should be addressed to the Dean, Graduate School, Virginia Polytechnic Institute, Blacksburg, Virginia 24061, Telephone (703) 552-6691.

Semi-Annual Progress Report No. 9
NASA Grant NGR 47-004-006
Virginia Polytechnic Institute
September, 1969

Introduction

This report is a compilation of technical reports in which an effort is made to present status of projects funded by the grant. Considering the relatively short duration of the grant, these reports may be regarded as the continuation of an output which will be sustained even beyond the time when NASA funds are no longer involved. Although almost all of this report is represented by technical reports, a brief summary of administrative and financial information is included so as to present some perspective of the scope of the current program. Only brief comments are made in reference to projects not reporting here in depth, most of which will be reported in detail in subsequent progress reports.

Administrative Information

The grant management remains as described in the previous progress reports. Responsibility for policy and project selection is vested in a special committee headed by Dr. Fred Bull, Dean of the Graduate School. General administration of the grant and the individual projects funded from the grant is the responsibility of the Research Division under the direction of Dr. Coyt Wilson.

The current membership of the NASA Multidisciplinary Grant Committee is as follows:

Dr. Fred W. Bull, Chairman, Dean of the Graduate School

Dr. James A. Jacobs, Head, Department of Physics

Dr. Daniel Frederick, Professor, Department of Engineering Mechanics

Dr. Paul B. Siegel, Professor, Department of Poultry Science

Dr. Leslie F. Malpass, Vice President for Academic Affairs, ex-officio member (Dr. Malpass recently succeeded Dr. Warren W. Brandt)

Dr. Coyt Wilson, Acting Dean, Research Division, ex-officio member.

Each principal investigator desiring support from the NASA Multidisciplinary Grant is asked to submit a brief proposal to this committee for review and evaluation. The committee, or a special ad hoc committee formed for this purpose, makes the selection and recommends funding. The Research Division notifies the principal investigator, his department head and dean, and sets up an auditable account for purposes of keeping the fiscal records of the project.

Financial Information

The basic grant and supplements received to date are as follows:

Identification		Period	Amount	Purpose
NGR 47-004-006	March 1, 1965	3 yrs.	$200,000	The Basic Grant-General
Suppl. No. 1	Sept. 1, 1965	30 mo.	100,000	Physics
Suppl. No. 2	Sept. 1, 1965	30 mo.	50,000	Physics
Suppl. No. 3	March 1, 1966	40 mo.	175,000	$25,000 Physics, $150,000 General
Suppl. No. 4	Sept. 1, 1966	3 yrs.	50,000	Physics
Suppl. No. 5	Sept. 1, 1967	3 yrs.	36,000	Physics
Suppl. No. 6	Sept. 1, 1967	3 yrs.	80,000	General
		Total	$691,000	

The funds appropriated as shown above were for two specific and separate space-related purposes: (1) general science and engineering research projects and (2) research specifically in the area of intermediate-energy physics. At the outset, it appeared to be an administrative conven-

ience to combine these programs under one grant. This proved not to be the case, however, and effective September 1, 1967, the support of intermediate-energy physics research was discontinued under this grant number and superseded by NGR 47-004-033. A recapitulation of the grant and supplements, divided according to purpose, is shown below:

General Space-Related Research

March 1, 1965 - February 29, 1966	$100,000
March 1, 1966 - August 31, 1967	150,000
September 1, 1967 - August 31, 1968	70,000
September 1, 1968 - August 31, 1969	65,000
September 1, 1969 - August 31, 1970	45,000
Subtotal	$430,000
Intermediate-Energy Physics	261,000
Total	$691,000

Table I shows the breakdown of the manner in which various space-related research projects have been supported with NASA funds up to the date of this progress report.

Technical Reports

This Administrative and Financial Information report is identified as Part 1 of Progress Report No. 9. The major technical reports covering progress on several individual projects are provided as separate parts of this Progress Report No. 9 as follows:

Part 2 - "Determination of Selective Stimulus Control by Part of a Compound $S^{\Delta 1}$," Final Report, by D.F. Johnson, B.N. Kinder and G.N. Scarboro.

TABLE I

SUMMARY OF SPACE-RELATED RESEARCH PROJECTS
FUNDED BY NASA NGR 47-004-006

Principal Investigator(s)	Project Number	Title	Encumbrances to September 1, 1969	NASA Funds Budgeted	Current Balance	Status
D. H. Pletta	313141	Hydrogen Embrittlement	36,611	36,611	0	Terminated
R. T. Davis	31775	Hypersonic Blunt Body Flow	35,873	35,873	0	Terminated
T.E. Gilmer	313176	Infrared Absorption	71,317	71,317	0	Terminated
D. Frederick	313142	Vibration of Plates and Shells	23,208	24,700	1,492	Continuing
F.J. Maher	31778	Stress Analysis of Shells	10,332	10,332	0	Terminated
J.P. Wightman	313103	Chemistry of Atomic Species	16,433	16,433	0	Terminated
Y. Kashiwagi	31652	Optimization of Rendezvous Maneuver	11,838	11,838	0	Terminated
R.H. Bond & E.M. Walsh	313135	Direct Energy Conversion	15,230	15,230	0	Terminated
D.F. Johnson	313180	Effect of Exposure on Performance	14,750	14,638	-112	Continuing*
J. Germana	313181	Psychophysiological Correlates	13,377	13,428	51	Continuing
F.B. Gessner & M. Crawford	313157	Transient Behavior of Composites	12,668	12,668	0	Terminated
C.H. Long	313159	Burning Rate of Mg and Al Wires	13,784	20,980	7,196#	Terminated
S.J. Ritchey	313151	Protein Metabolism	13,401	13,930	529	Continuing
W.E.C. Moore	31685	Anaerobic Flora of Man	11,590	11,590	0	Terminated
F.R. DeJarnette	313099	Simplified Method for Calculating Convective Heat Transfer	6,672	6,672	0	Terminated
R. H. Bond	313138	Direct Energy Conversion	11,650	13,565	1,915	Continuing*

Principal Investigator(s)	Project Number	Title	Encumbrances to September 1, 1969	NASA Funds Budgeted	Current Balance	Status
R. Chicurel	313144	Suppression of Bending in Shells	6,007	6,007	0	Terminated
J. L. Lytton	313169	Two-Phase Metallic Composites	9,580	9,580	0	Terminated
J.R. Long	313178	Transport Phenomena in Metals	14,149	16,245	2,096	Continuing
J.G. Mason	313113	Oxidation of Organic Fuel Materials	7,350	8,490	1,140	Continuing
W.E.C. Moore	313188	Anaerobes in Man's Environment	1,047	1,047	0	Terminated
W.E.C. Moore & L. V. Holdeman	313245	Anaerobic Flora of Man	5,280	6,800	1,520	Continuing
R.R. Schmidt	313244	Effect of Weightlessness on Metabolism	6,324	7,500	1,176	Continuing
L. T. Taylor	313243	Organo-Cobalt Complexes	1,233	6,560	5,327	Continuing
F. H. Lutze, Jr.	313242	Rotational Motion of a Satellite	7,613	8,080	467	Continuing
J. J. Brown	313241	Glass-Ceramic Composites	6,219	8,000	1,781	Continuing
R. J. Adler & J. M. Alvarez	313240	Low-Mass Meteoroid Cut-Off	985	1,505	520	Continuing
K.L. Reifsnider	313239	Continuum Theory of Material Defects	2,125	2,240	115	Continuing*
R.J. Onega	313246	Proton Interaction with Titanium	2,867	3,160	293	Continuing
W. P. Goss	313247	Spacecraft Powerplant Condensers	3,196	5,490	2,294	Continuing
H. VanLandingham	313248	Variable Parameter Network Design	1,875	5,400	3,525	Continuing
F. R. DeJarnette	313249	Flow Field over Aerodynamic Decelerators	1,183	5,470	4,287	Continuing
TOTAL			395,767	431,379	35,612	

Funds being redistributed.
* Final reports submitted herewith; formal termination to follow.

Part 3 - "Time-Resolved X-ray Diffraction Microscopy: Development of a New Technique," Final Report, by K. Reifsnider.

Part 4 - "High Vacuum System and Instrumentation for Measuring the Derivative of the Current-Voltage Characteristics of a Langmuir Probe," Final Report by R.H. Bond and F.E. Baker, Jr.

Part 5 - "A Fully Bakeable D.C. Glow Discharge Tube for Measurement of Directed Electron Velocity Distributions with a Langmuir Probe," Final Report by R.H. Bond and K.E. Skrivseth.

Part 6 - "A Comparison of Theoretical and Experimental Directed Electron Velocity Distribution in Rare Gas Discharges," Final Report by R.H. Bond and M.G. Funk, Jr.

Also attached as Part 7 of this Progress Report No. 9 is a Science Information Exchange form which provides an abstract for one project for which such a form has not previously been submitted.

In addition to the major reports which comprise the following parts of Progress Report No. 9, brief reports of progress on several other projects are included in this Part 1. In some instances investigators supplied additional more extensive progress reports and these are included as Part 8 of this Progress Report No. 9. The brief progress reports are as follows:

1. "Interaction of ^{50}Ti with Protons and Neutrons," by R.J. Onega.
2. "Effect of Weightlessness on Cellular and Subcellular Metabolism in Human Cells," by R.R. Schmidt.
3. "Organo-Cobalt Oxygen-Carrying Complexes," by L.T. Taylor.
4. "Rotational Motions of a Satellite," by F.H. Lutze, Jr.

5. "The Effects of Restricted Movement on Protein Metabolism and Body Composition," by S.J. Ritchey.
6. "Electrocatalysis of the Oxidation of Organic Fuel Materials Using an Oxidation-Reduction Couple as Catalyst," by J.G. Mason.
7. Variable Parameter Network Design," by H.F. VanLandingham.
8. "Method for Calculating the Flow Field Over Aerodynamic Decelerators," by F.R. DeJarnette.
9. "Preparation of Glass-Ceramic Composites by Controlled Crystallization Techniques," by J.J. Brown.
10. "Effect of Water Vapor on the Burning Rate of Aluminum and Magnesium Wire," by C.H. Long.
11. "A Theoretical Investigation of Low Mass Meteroid Cut-off," by R.J. Adler.
12. "The Psychophysiological Correlates of Learning," by J. Germana.
13. "Harmonic Vibrations of Viscoelastic Layered Media," by D. Frederick.
14. "Characterization of Anerobes from the Normal Human Flora," by J.J. Johnson (for W.E.C. Moore).
15. "A Study of Spacecraft Powerplant Condensors," by W.P. Goss.
16. "Transport Phenomena in Metals," by J. Long.

Report No. 1 - "Interaction of ^{50}Ti with Protons and Neutrons"

Principal Investigator: R.J. Onega
Department of Physics

The interaction of protons and neutrons on titanium is an important consideration for space travel due to the biological damage that may result

from cosmic rays impinging on the space craft material. The purpose of this work was to investigate the gamma rays emitted from the (P,γ), $(P,P'\gamma)$ reactions and the gamma rays following the beta decay of ^{50}Ti produced by the $^{50}Ti(n,\gamma)^{51}Ti$ reaction.

There were three gamma rays emitted following the beta decay of ^{51}Ti. Their energies were 0.319, 0.613 and 0.934 MeV with relative intensities of 100, 3.75 $\pm$ 0.4 and 8.8 $\pm$ 0.8 respectively. The half life for the decay of ^{51}Ti was 5.80 min. The ^{51}Ti sample was made by pneumatically firing a sample of ^{50}Ti into the VPI 100 keV reactor whose flux was 10^{12} n/cm^2-sec and irradiating for about 1 minute. The sample was then withdrawn from the reactor and counted.

The VPI Van de Graaf accelerator was used to study the $^{50}Ti(P,\gamma)^{51}V$ and $^{50}Ti(P,P'\gamma)^{50}Ti$ reactions. Only the gamma rays were observed after the reaction so that no differentiation of the gamma rays arising from the (P,γ) and $(P,P'\gamma)$ reactions was made. The experiments were carried out at 1.5 MeV, 2.25 MeV and 3.0 MeV incoming proton beam energy. The ^{50}Ti was deposited on a bismuth backing and inserted into the proton beam. The gamma rays were observed with a NaI(Tl) detector and the end point energy was about 10 MeV for the 3 MeV incoming proton beam and about 8.5 MeV for the 1.5 incoming proton beam.

The proton interaction gamma rays could produce a radiation hazard for the men in the space vehicle. The cosmic rays themselves would produce neutrons by interactions with space vehicle, the neutrons in turn would constitute a hazard to the personnel. The neutrons could also give rise to a gamma ray environment due to the (n,γ) reactions as well as the fact that radioactive nuclei would be produced and emit radiation after the beta decay of nucleus.

Report No. 2 - "Effect of Weightlessness on Cellular and Subcellular Metabolism in Human Cells"

Principal Investigator: R.R. Schmidt
Department of Biochemistry and Nutrition

One major goal of the first phase of this research project was to elucidate the biochemical mechanisms regulating the synthesis of enzymes located within subcellular organelles and the cytoplasm of eukaryotic cells during their cell cycle. Excellent progress has been made in this area in the last 6 months.

1. Carboxydismutase, an enzyme solely located in the chloroplast, is synthesized during the early part of the cell cycle when neither the chloroplast nor nuclear DNA is replicating, thus eliminating the proposal that gene transcription (read-out of the genetic code) is obligately coupled to gene replication. Comparison of rates of synthesis of the enzyme in daughter cells, having received a prior dark treatment, to those selected from continuously lighted cultures with Ficoll gradients indicates that the rate of synthesis of this enzyme is controlled primarily by end-product repression. The structural gene for this enzyme appears to be fully derepressed following a 6 hour dark period.

2. In contrast to carboxydismutase, the cytoplasmic form of the enzyme aspartate transcarbamylase, appears to be synthesized in direct parallel with the replication of nuclear DNA, suggesting that the synthesis of this enzyme is coupled to the replication of DNA or that the structural gene of this enzyme is fully repressed at all times. That the latter possibility is correct comes from the finding that uracil added to the culture does not further repress the synthesis of this enzyme. In these studies, uracil was shown to enter the cell and to be used for RNA synthesis.

3. Two forms of glutamic dehydrogenase have been discovered in Chlorella,

one requiring DPNH and the other TPNH as a coenzyme. The synthesis of these two isoenzyme appears to be independently controlled during the cell cycle. The intracellular location of these enzymes is currently being investigated.

4. New procedures for the extraction and quantitation of total cellular DNA were developed.

5. Studies on estimating the purity of chloroplasts and mitochondria isolated on discontinous and continuous density gradients of sucrose were also performed.

Report No. 3 - "Organo-Cobalt Oxygen-Carrying Complexes"

Principal Investigator: L. T. Taylor
Department of Chemistry

The primary goals of this research are (1) to synthesize structurally related but electronically different cobalt (II) complexes which reversibly add oxygen and determine their stability to repeated cyclizations and (2) to completely describe the interaction or bonding between the oxygen molecule and cobalt complex by application of as many of the modern structural techniques as possible. The oxygen adducts of such compounds would probably have the following postulated structure where X may be a variety of donor atoms of differing ligand field strengths.

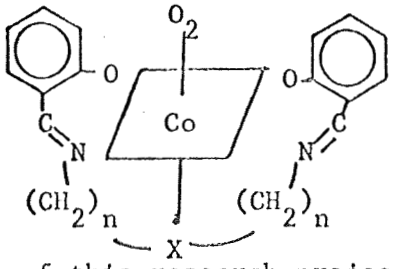

Since commencement of this research project (January 1, 1969) efforts have been channelled toward (1) synthesizing the pentadentate ligands which are required for complexation with cobalt (II), (2) gaining a better

understanding of the non-oxygenated complexes of cobalt (II), nickel (II) and copper (II) with several of these pentadentate ligands and (3) the construction of a magnetic susceptibility balance.

At the outset of this work only one of the desired pentadentate ligands was known, SALDPT (n=3, X=N-H). The following ligands have now synthesized and characterized: SALDIEN (n=2, X=N-H), SALDAES (n=2, X=S), SALDAPE (n=3, X=0) and SALDAPS (n=3, X=S). These ligands have been prepared by the interaction of salicylaldehyde with the corresponding polyamine, which in several cases had not been synthesized previously, in a Schiff base reaction.

It was felt that an adequate knowledge of the precursors was necessary for any results concerning the oxygen adducts to be meaningful. Therefore the physical, chemical and sterochemical properties of the non-oxygenated complexes of cobalt (II) as well as nickel (II) and copper (II) were investigated. The latter two metal ions were included in hopes that the results gained from these metal ion systems would aid in unraveling the factors responsible for reversible oxygenation with certain cobalt systems. (i.e. Chemical and structural theories are considerably advanced in relation to cobalt complexes and nickel and copper systems are less susceptible to attack by oxygen.)

Complexes of the previously mentioned metal ions have been prepared with SALDIEN and SALDAES. Complexes of general formula M(SALDIEN), M(SALDAES) and M(SALDAES) (H_2O) have been isolated. Magnetic and spectrophotometric studies have shown the stereochemistry of these complexes to be four coordinate square planar, high spin five coordinate and pseudo octahedral six coordinate respectively. The results with M(SALDIEN) have proven interesting in that only four of the potentially five donor atoms of SALDIEN appear to be coordinated to the metal ion whereas all five donor atoms of

SALDAES are believed to be coordinated. Studies with nickel and copper were especially useful in this regard). These findings may be rationalized on the basis of the relative sizes of the unique donor atom in each ligand. A study of stereomodels of complexes with these two ligands reveals that with n=2 the ligand must undergo quite severe strain in order for the X donor atom to reach a fifth coordination position on the metal. Sulfur being a larger atom than nitrogen as evidenced by its greater van der Waal's radius is more able to reach this coordination position on the metal. Sulfur being a larger atom than nitrogen as evidenced by its greater van der Waal's radius is more able to reach this coordination position than is nitrogen. This interpretation is supported by independent findings concerning complexes of SALDPT (n=3, X=N-H) that show the secondary nitrogen coordinated. In other words, the methylene carbon chain has been increased by two carbons which allows the nitrogen atom to more easily approach the fifth coordination position of the metal.

Presently, reactivity of the cobalt complexes of SALDIEN and SALDAES toward oxygen is suspected but no conclusive evidence is available. The reactivity of these materials in solution and in the solid state with oxygen under a variety of conditions is planned. Reactions of cobalt (II) with other appropriately designed ligands is also anticipated in the near future. Experiments dealing with the kinetics of oxygenation of known cobalt systems via an electron spin resonance technique are also planned in conjunction with Professor R.E. Dessy of this department.

Along with this experimental work, some effort has been directed toward the construction of both Gouy and Faraday magnetic susceptibility balances. It is believed that the spin state of the metal atom plays a major role in determining whether reversible oxygenation will take place. Construction of this facility will enable information of this type to be obtained more readily.

Report No. 4 - "Rotational Motions of a Satellite"

Principal Investigator: F. H. Lutze, Jr.
Department of Aerospace Engineering

In this investigation, the in-plane rotational motion of an arbitrary shaped satellite is studied for the possibility of "locked-in" motion at rotational rates higher than one rotation per orbit revolution (1/1). The motion of the planet Mercury relative to the Sun (3/2) suggests that higher rotational locks are possible.

The principal parameters involved in such "lock-in" motion are the shape of the elliptical orbit, determined by the orbit eccentricity, e, ($0 \leq e < 1$) and the shape of the satellite determined by the satellite parameter, a, where a = 0 corresponds to a spherical satellite and a = 1, a dumbell shaped satellite. Consequently the investigation is broken down into studying the motion for two situations: (1) small a, arbitrary e; and (2) arbitrary a and e.

Small a case

For a = 0, the satellite experiences no gravitational torque and consequently continues to rotate at its original rate regardless of the eccentricity of the orbit. Such a solution serves as a generating solution for the case of small a. The averaging technique of Kryloff and Bugoliuboff as applied by Chernous'ko (1963) was used to investigate this case and the main results are outlined here. (see figure)

(1) Locked-in motion is possible for locks given as n/2, where n is an integer.

(2) The eccentricity for which a given lock reaches its strongest locked-in motion increases with rotational lock.

(3) In most cases, the axis of least moment of inertia must be nearly aligned with the radius vector at periapse for a stable rotational lock.

Arbitrary a and e case

The in-plane rotational equation of motion for a satellite has been shown to have odd 2π periodic solutions. These solutions have been shown to extend to the case where the satellite is in an n/2 rotational lock. The "initial" conditions at periapse for such periodic solutions were determined for various values of the parameters a and e. Small disturbances about the periodic solutions were considered and the resulting linear equations were investigated by numerical integrations. Floquet theory was applied to determine stability of the periodic solutions. Second order terms in the small disturbances are now being investigated in order to find the range of validity for the stability results.

Non-periodic solutions are being investigated for their stability by a stroboscopic analysis in the phase plane using the results of numerical integration. It is intended to correlate the results of this investigation in a manner which will enable lock strength, satellite parameter and orbit eccentricity to be related as in the small a case.

REFERENCES

Beletskii, V. V.: 1966, Motion of an Artificial Satellite About Its Center of Mass, NASA TTF-429, pp 257-261.

Brereton, R. C. and Modi, V. J.: 1966, "On the Stability of Planer Librations of a Dumbell Satellite in an Elliptic Orbit," Royal Aeronautical Society 70, 1098-1102.

Chernous'ko, F. L.: 1963, "Resonance Phenomena in the Motion of a Satellite Relative to Its Mass Center," U.S.S.R. Computational Mathematics and Mathematical Phys. 3, 699-713.

Zlatoustov, V. A., et al: 1964, "A Study of the Oscillations of a Satellite in the Plane of an Eliptic Orbit," Cosmic Research 2, 569-576.

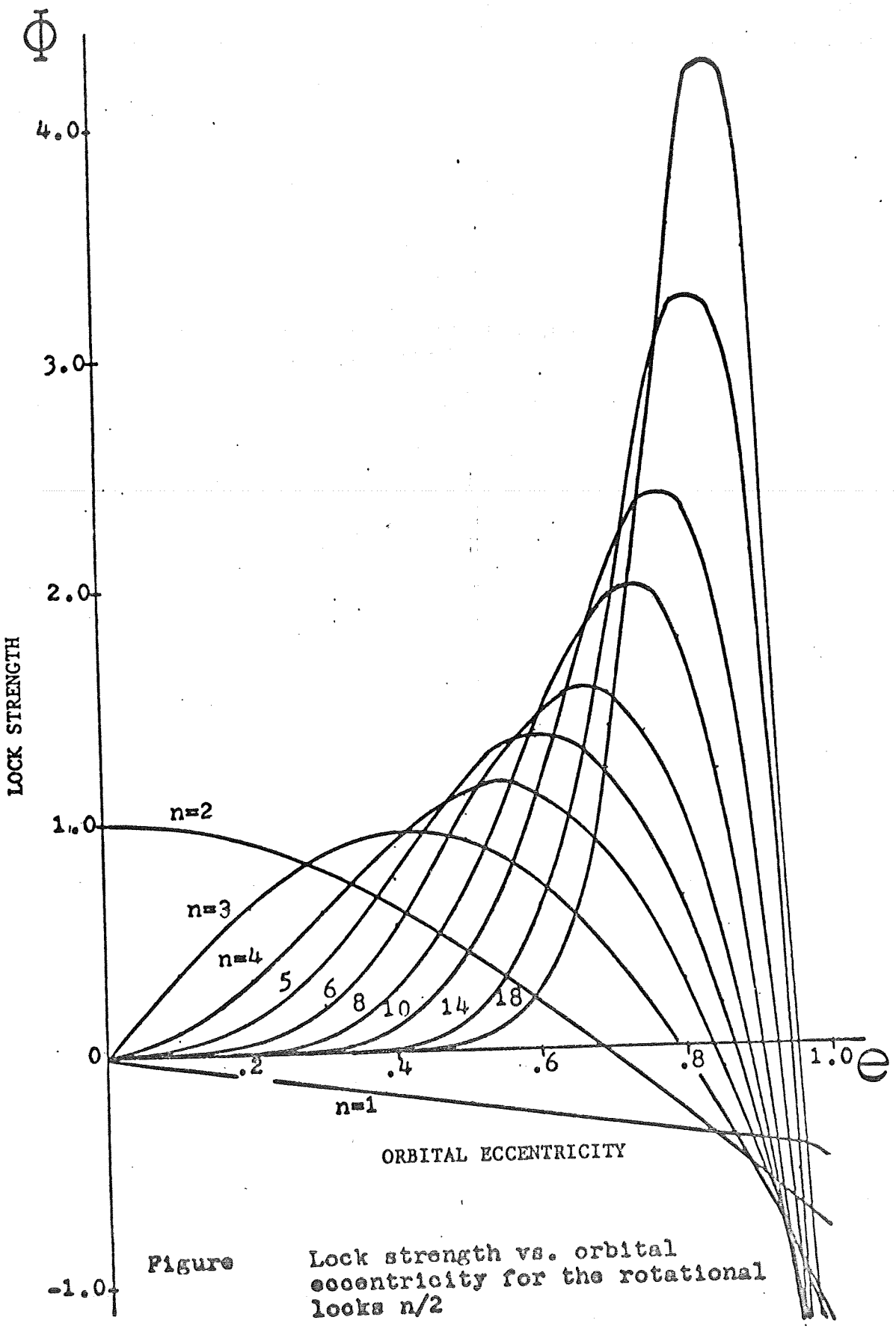

Figure Lock strength vs. orbital eccentricity for the rotational locks n/2

Report No. 5 - "The Effects of Restricted Movement on Protein Metabolism and Body Composition"

Principal Investigator: S. J. Ritchey
Department of Human Nutrition and Foods

The effects of certain conditions imposed upon man in space ventures on body composition and protein metabolism are continuing under this project. An experiment designed to test the effects of severe weight loss as a result of restricted movement upon recovery of weight and length of life is presently in progress. Preliminary data from this experiment are reported herein.

Adult rats were assigned to weight groups and then to one of three treatments:

1. Restricted movement - housed in small restriction units so that there was a minimum of movement. Given access to food and water one hour daily.
2. Pair-fed controls - each restricted animal (Group 1) had a pair mate in this group. The pair mate was not restricted in movement, but was given the same amount of food as the restricted mate.
3. Ad Libitum Control - allowed free movement and both feed and water were accessible at all times.

During the restricted period, both the restricted animals and the pair-fed controls lost considerable weight (Table 1). The amount of weight loss was greater in the restricted animals, thus suggesting that restriction per se may be a major determinant. Statistical analyses have not been accomplished at the time of this report, but in seven of the nine pairs the restricted animal lost more weight.

Table 1. Changes in weight during 7-day period of restricted movement[1]

Treatment	Av. Initial Wt. (g)	Av. Final Wt. (g)	Change in Wt. (%)
Restricted Movement	208.1	159.2	-23.5
Pair-Fed Control	208.2	170.3	-18.2
Ad Libitum Control	208.7	230.7	+10.5

After a 7-day restriction period, all animals were allowed feed and water ad libitum. Both the restricted and the pair-fed controls regained weight quite rapidly (Table 2), although neither group weighed as much as the ad libitum controls after 56 days of free movement. Data will be collected to determine the effect of severe restriction and loss in weight upon length of life.

Table 2. Changes in weight during recovery period following restricted movement[1]

Treatment	Initial Wt. (g)	Wt. at End of Restriction (g)	Weights Following Period of Restriction		
			Day 7	Day 28	Day 56
Restricted Movement	208.1	159.2	204.0	318.9	378.5
Pair-Fed Control	208.2	170.3	215.6	313.3	368.3
Ad Libitum Control	208.7	230.7	253.8	330.0	394.0

Another experiment designed to determine changes in individual tissue components during restriction and weight loss is being planned.

---

[1]Data are average of 9 animals per group.

Report No. 6 - "Electrocatalysis of the Oxidation of Organic Fuel Materials Using an Oxidation-Reduction Couple as Catalyst"

Principal Investigator: J. G. Mason
Department of Chemistry

As reported previously, the current investigation has been divided into two parts:

(1) the investigation of the oxidation of aliphatic alcohols with electrogenerated halogens, and

(2) platinum catalysis of redox processes.

For part (1), the results of the Cl_2 oxidation of isopropanol are being prepared for publication. The results previously reported for the Br_2 oxidation have been confirmed in detail using spectrophotometric measurement. The rates appear to be markedly sensitive to acidity and to indicate considerably more mechanistic complexity than the Cl_2 oxidation. The results of this study indicate that Cl_2 is the simple halogen of choice to date. Oxidations of other alcohols have been accomplished, however, the products are rapidly chlorinated destroying the catalytic efficiency. Investigations into mixed halogens as oxidants are being initiated.

Part (2) has been concerned with the reported catalysis of the Tl(III) - Fe(II) reaction by sheet platinum. Current work has confirmed the reported data on the thermal rate and demonstrated that the catalysis is a function of the nature of the platinum surface. Platinum electrodes which have been preoxidized exhibit virtually no catalytic effect. Pre-reduced electrodes show catalysis. Electrode potentials have been measured as a function of the reaction time for both the thermal and catalyzed rates. It appears that these potentials are not adequately described by considering equilibrium processes at the platinum survaces. The previous work of others (Gilks and Waind, Disc. Faraday Soc. 29, 135 (1960)) reported that the effect of platinum was due

not to catalysis of the primary reaction but to the elimination of the back reaction of equation (1).

$$Tl^{3+} + Fe^{2+} \underset{k_2}{\overset{k_1}{\rightleftharpoons}} Tl^{2+} + Fe^{3+} \qquad (1)$$

$$Fe^{2+} + Fe^{2+} \xrightarrow{k_3} Tl^{+} + Fe^{3+} \qquad (2)$$

The catalytic effect arises from acceleration of reaction (2). Results obtained in this laboratory indicate that both preconditioning of the electrode and electrode size are vital factors in determining the measured rates. While simple kinetics are obtained in the presence of Pt, the magnitude of k_1 is significantly larger than that measured for the thermal rate. Presently, the investigation of the relation between the potential of the electrode surface and the catalytic effect using controlled potential electrolysis techniques is in progress.

Report No. 7 - "Variable Parameter Network Design"

Principal Investigator: H. F. VanLandingham
Department of Electrical Engineering

The project has been delayed in order to develop an appropriate background in a research assistant. Up to this time, primary effort has been directed toward equipment acquisition - circuit components and test equipment have been obtained.

Report No. 8 - "Method for Calculating the Flow Field Over Aerodynamic Decelerators"

Principal Investigator: F. R. DeJarnette
Department of Aerospace Engineering

The purpose of this research is to develop a method for calculating the flow field over aerodynamic decelerators which are deployed in the wake

of a vehicle traveling at supersonic speeds. For the decelerator, the wake produces a nonuniform free stream which has been found to cause the decelerator flow-field to deviate significantly from that of a uniform free stream. Previous research at VPI has also shown that boundary layer separation can occur, even on such simple shapes as pointed cones. The net result is a large change in the aerodynamic performance of decelerators, e.g. drag and stability coefficients, when compared with the performance for a uniform free stream.

The current approach is to formulate a method to calculate the inviscid flow field and then use the surface solution from this method to calculate the boundary layer properties up to the separation point. Beyond the point of boundary layer separation, the inviscid solution will be continued using a free streamline instead of the body surface as the inner boundary.

The inviscid flow-field method is being developed from a modified form of a combined inverse method - method of characteristics, which was developed by Inoyue, Rakich, and Lomax in NASA TN D-2970. In particular the shock wave conditions must account for the nonuniform free stream, and the inner boundary beyond the separation point must be a free streamline. Laminar boundary layer computations, up to the separation point, will be performed by the method of Davis and Flugge-Lotz (J. Fluid Mechanics, 1964).

Presently, the inviscid flow-field method is being programmed for pointed and blunted cones at zero angle of attack. Experimental wake profiles (determined by Campbell and Grow, NASA TN D-5365) will be used as the non-uniform free stream in the flow-field computations.

Report No. 9 - "Preparation of Glass-Ceramic Composites by Controlled Crystallization Techniques"

Principal Investigator: J. J. Brown
Department of Metals and Ceramic Engineering

Strengthening of glass by introducing a second immiscible phase was investigated using a portion of the ternary system SiO_2, Li_2O, and TiO_2. The major portion of the work was confined to compositions taken along the 70 weight percent SiO_2 isopleth. Modulus of rupture (bending) and elasticity data indicate that strengthening increases as the TiO_2 content is increased beginning with composition "C" (a miscible glass), which yielded an average modulus of rupture strength of 20,900 psi. A marked increase was recorded as compositions were formed inside the immiscibility region and continued until a maximum of 34,600 psi was attained with a TiO_2 content of approximately 15 weight percent. At this point, nucleation could no longer be controlled and crystallization became predominant when 20 weight percent TiO_2 was used. The modulus of rupture (bending) of this crystallized composition decreased rapidly, yielding an average strength of 26,800 psi.

Report No. 10 - "Effect of Water Vapor on the Burning Rate of Aluminum and Magnesium Wire"

Principal Investigator: C. H. Long
Department of Mechanical Engineering

Work has been done on the burning of wires oriented horizontally in environments at high pressures when heating them to rupture point by passing a current through them. The burning rate, along with other phenomena, was measured as the flame moved along the two parts of the wire or ribbon.

It was proposed in 1966 that an investigation should be conducted on vertical wires ignited at one end. These tests should be conducted at elevated pressures and temperatures, the burning phenomena observed, and the burning rate determined for various amounts of moisture and oxygen composing the environment in the chamber. This was done in dry oxygen at room

temperature and pressures up to forty atmospheres and reported in September, 1967 as Phase I of this project.

In 1968 the project was extended (Phase II) by mixing given quantities of moisture with the oxygen at pressures up to twenty atmospheres.

It was found that heating of the oxygen and the chamber wall to 280°F approximately, in order to allow all the moisture admitted to evaporate into steam, had a very definite effect of increasing the burning rate of aluminum and magnesium wires up to approximately fifteen atmospheres while the addition of the moisture increased the burning rate of aluminum up to approximately six atmospheres but had no beneficial effect on the burning rate of magnesium.

A final report will appear in the V.P.I. semi-annual report, April, 1970.

Report No. 11 - "A Theoretical Investigation of Low Mass Meteoroid Cut-off"

Principal Investigator: R. J. Adler
Department of Physics

Work on this project is nearly complete, and we believe that the most relevant mechanisms have been investigated. The hypothesis of a low mass cut-off is consistent with particle penetration data from the Explorer, Pegasus, and Ariel II probes.

The Poynting Robertson effect, predicted by special relativity, involves a tangential drag on a particle in solar orbit. Such a drag causes the particle to eventually spiral into the sun, or be blown out of the system by radiation pressure. This effect has been investigated; as a numerical example of our findings we find that a particle of size 5×10^{-2} cm, density 3.5 gm/cc, in a circular orbit of 3 AU, will fall into the sun in $\sim 10^{7}$ years if it is not blown out by radiation pressure. This is short compared to the age of the solar system.

The second mechanism investigated is that of particle-particle collisions, usually referred to as comminution processes. Two situations are dominant for high velocity collisions: one particle is destroyed, or both are catastrophically fragmented. The size of particles, due to such comminution processes, decreases to the point where solar radiation pressure ejects them from the system.

It remains to investigate the effects of the sun's electromagnetic field, including "normal" fields and the complex solar mind.

Our tentative conclusion is that the comminution processes dominate, and reduce particle size to a point where solar radiation pressure ejects them from the solar system. The significance of the work for manned space-flight (especially crossings of the asteroid belt) is obvious; other implications of the work have appeared and will be discussed in the final work.

Report No. 12 - "The Psycholophysiological Correlates of Learning"

Principal Investigator: J. Germana
Department of Psychology

The purpose of this research was to investigate the nature of the autonomic, activational responses (e.g., galvanic skin responses, cardiac responses) which accompany learning or conditioning. Briefly, the present investigator has shown that as subjects are learning, as they are acquiring the "correct" responses, activational responses to the conditioned stimuli demonstrate systematic, trial-by-trial increments. These increments in activation typically occur on those trials immediately preceding the attainment of criterion performance, i.e., while the subjects are making their final errors. Subsequent to response acquisition, activational responses decrease in magnitude.

The present investigator has suggested that activational responses constitute preparations to respond overtly, that they support and facilitate behavior, and that they may be anticipated correlates of situations in which: (a) subjects are required to go from a period of inactivity to one of behavioral responding; (b) subjects are undergoing a transition to a more complex or sustained behavior sequence; and, (c) subjects are required to learn a behavioral response to a stimulus and, in the early stages of acquisition, cannot initiate a specific preparation to respond. This interpretation of activational responses, then equates the autonomic and somatic activity, described as activational, with intensive and extensive preparations to respond behaviorally.

The research which has been carried out under this project has consistently supported this general view of activational responses and the specific interpretation which has been offered as an explanation of the

psychophysiological correlates of learning. A detailed description of these experiments will be presented in the terminal report.

Report No. 13 - "Harmonic Vibrations of Viscoelastic Layered Media"

Principal Investigator: D. Frederick
Department of Engineering Mechanics

For steady state vibrations, the stresses, strains, and displacements in the three-dimensional theory of harmonic vibrations of linearly viscoelastic bodies of arbitrary shape are taken in the form

$$\sigma_{jk} = \mathrm{Re}\ (\bar{\sigma}_{jk} e^{i\omega t}) \tag{1a}$$

$$\epsilon_{jk} = \mathrm{Re}\ (\bar{\epsilon}_{jk} e^{i\omega t}) \tag{1b}$$

$$u_j = \mathrm{Re}\ (\bar{u}_j e^{i\omega t}) \tag{1c}$$

where σ_{jk}, ϵ_{jk}, and u_j are the desired stresses, strains, and displacements, respectively, the corresponding quantities with a bar are complex functions of position, ω is the frequency, t is the time, j and k take on the values 1, 2, 3, and Re means to select the real part.

Based upon the above forms, the solution for forced torsional oscillations of a circular cylindrical bar is

$$u_\theta = \mathrm{Re}\ \left[Ar(e^{ikx} - e^{-ikx}) e^{i\omega t} \right] \tag{2}$$

where u_θ is the displacement, r is the radius, x is the axial coordinate, $k = k' - ik''$, k' is the propagation constant, and k'' is the attenuation constant. The factor Re $(Ar\ e^{+ikx\ +i\omega t})$ is a minus x traveling wave of torsion, and Re $(Ar\ e^{-ikx\ +i\omega t})$ is an identical wave traveling in the plus x direction. Thus the solution is expressed by the difference of two interacting spacially-damped waves. This observation led to the conclusion that for free vibration, the commonly accepted method of selecting the time dependence as $e^{i\omega t - \delta t}$ is only an approximation of what is actually occurring in the freely vibrating

body.

The problem being investigated at present is forced torsional oscillations of a circular cylindrical sandwich shell. This shell is composed of a viscoelastic core between two elastic layers. All layers are symmetrically arranged. The reason for choosing torsional oscillations is to avoid the appearance of the bulk modulus in the equations. Very little experimental data exists for the bulk modulus of a viscoelastic material since such materials are usually nearly incompressible resulting in difficulties in measurement. However, a large amount of experimental data exists for the shear modulus for many viscoelastic materials, and one of these materials will be chosen for the core of the shell. The displacement, principal shear stress, and an approximation of the small delamination shear stress tending to cause separation of the layers will be computed for a shell made of the selected materials.

An analysis of the vibrating Timoshenko beam was performed in which the normal to the middle surface was divided into three equal segments each of which remains straight but rotates independently of the other segments during deformation. A comparison with the published literature showed that this procedure results in an improvement of the governing equations. This analysis is currently being applied to the sandwich shell mentioned above. The normal to the middle surface is divided into three equal segments in the core plus a segment in each of the two thin outer layers. Again, each segment remains straight during deformation but rotates independently of the other segments. These rotations approximate the warpage of the cross-sectional surfaces due to transverse shear.

Report No. 14 - "Characterization of Anerobes from the Normal Human Flora"

Principal Investigator: J. L. Johnson (for W.E.C. Moore)
Department of Veterinary Science

The project was established January 1, 1969 and provides salary for one technician. The technician assists in the preparation and analysis of samples of deoxyribonucleic acid (DNA) from anaerobic bacteria. Among the organisms under investigation are representative strains from the genus Corynebacterium (anaerobic strains), Propionibacterium, and Clostridium.

The anaerobic bacteria on earth are indigenous to most environments including the intestinal tract and the skin of animals and man, the soil and the sea. The bulk of these anaerobic bacteria, however, have not been studied or have been studied only to a limited extent. A large percent of all isolates cannot now be recognized. With improved isolation methods now available, one may detect many that apparently have not been seen before. The purpose of this project is to determine, at the level of the genetic material (DNA), relationships within and between various groups of anaerobic bacteria. These relationships are determined by measuring the ratios of purine and pyrimidine bases in the DNA and by comparing the arrangement of the bases in the DNA from the various organisms. These analysis will allow the determination of the types of bacteria within the groups and to determine phenotypic characteristics that accurately differentiate the different types. This information will be of interest to the manned space flight program and to the evolution of interplanetary quarantine control.

DNA preparations from 45 strains of clostridia and from 95 strains of anaerobic corynebacteria and propionibacteria have been analyzed. In some

instances the results show distinct types of anaerobes in groups of superficially similar organisms and in other cases show a high degree of similarity among organisms that were thought to be distinct.

Report No. 15 - "A Study of Space Craft Powerplant Condensors"

Principal Investigator: W. P. Goss
Department of Mechanical Engineering

The four phase program has been proceding in accordance with the program of study. The first two phases have been completed and work is progressing into the third phase.

The completed work includes the programming of thermodynamic and transport properties of Freon - 113 and potassium into digital computer subroutines and the development of improved empirical correlations. The specific correlations studied were the wall shear stress and the interfacial shear stress for turbulent, condensing liquid films. These correlations were obtained through the application of momentum integral techniques. This consists of writing the momentum equation of the liquid film in integral form, and assuming velocity and eddy viscosity distributions in the film. The distributions assumed were different from the classical forms assumed for single phase systems since the mechanics of turbulent two-phase flows are not the same as in single phase flows. The unknown constants in these distributions were obtained from experimental data found in the literature. The initial results indicate that the correlations compare quite well with a wide range of experimental conditions.

The above correlations and property data have been incorporated into the theoretical model for the condenser tube. Several computer runs have been made for steam condensers and the analytical results compare quite

well with the experimental data. The Freon-113 and potassium condenser computer runs are presently being set up and will be run in the near future.

Report No. 16 - "Transport Phenomena in Metals"

Principal Investigator: J. Long
Department of Physics

The object of this project was to develop a laboratory and perform measurements which would elucidate some details of electrical and thermal transport phenomena in complex metals. An emphasis was placed on an understanding of processes which are fundamental to thermoelectric phenomena. It was argued that certain aspects of these phenomena might be well suited for application to a magnetothermoelectric energy conversion device in a spacecraft. Magnetothermoelectric energy conversion devices are usually of limited value due to lack of sufficiently large magnetic fields and a suitable low temperature reservoir. If, however, a cryogenic magnet should be employed in the spacecraft for any reason such as charged cosmic ray shielding, the arguments in favor of including a magnetothermoelectric energy conversion device became obvious.

Under joint support of this project grant and funds of the Commonwealth of Virginia a program for the study of magnetotransport phenomena in complex metals was initiated. Commonwealth funds were used primarily for the purpose of purchasing a 50 kOe superconducting magnet and current source. NASA funds were used to build or purchase the cryogenic apparatus necessary to operate the magnet, electronic instruments necessary to measure the transport effects, and metallic single crystal specimens.

The process of selection or design and construction of suitable

apparatus for the work consumed most of the funds and manpower expended on this project under NASA support. The development of an experimental capability has been the primary consequence of this project to date. Experiments are now possible which utilize d.c. and phase sensitive detection of sub-microvolt potentials in metals which experience an environment of temperatures down to 1 Kelvin and magnetic fields in excess of 50 kOe.

Concurrently with the program of apparatus development, preliminary measurements of the electrical resistivity of the conducting refractory compounds TiN and TiC were performed. Although these compounds have many interesting and promising properties, further work on them is in doubt due to problems of sample preparation.

Also concurrently with the development of apparatus, the Summer research time which was made possible by this grant was utilized for the completion of a similar project begun under previous support by ARPA. A large amount of raw data on the magneto-transport effects in tungsten was reduced, analyzed and interpreted. This effort resulted in the preparation of three publications on transport phenomena in tungsten which will be submitted to the Physical Review. Support for these publications is credited jointly to NASA and ARPA. The papers are titled:

I. The Behavior of the Thermal and Electrical Transport Coefficients of Tungsten at High Magnetic Fields and Low Temperatures by Jerome R. Long.

II. The Relation of Transport Coefficients to Fermi Surface Details in Tungsten by Jerome R. Long.

III. Lattice Conduction, Lorentz Numbers and Apparent Drag Effects in Tungsten by Jerome R. Long.

Semi-Annual Progress Report No. 9

to the

NATIONAL AERONAUTICS AND SPACE ADMINISTRATION

in connection with

NASA Grant NGR 47-004-006

Part 2 of 8 Parts

Final Report

V.P.I. Project 313180

DETERMINATION OF SELECTIVE STIMULUS CONTROL BY PART OF A COMPOUND $S^{\Delta 1}$

by

Daniel F. Johnson
Bill N. Kinder
Glenn N. Scarboro

Virginia Polytechnic Institute
Blacksburg, Virginia

September, 1969

Determination of selective stimulus control by part of a compound S^{Δ}[1]

DANIEL F. JOHNSON, BILL N. KINDER, and GLENN N. SCARBORO, Virginia Polytechnic Institute, Blacksburg, Va. 24061

Eight White King pigeons were trained to peck at each of four stimuli presented alone: white vertical line, white horizontal line, red background, green background. Then each pigeon was given 10 sessions of single stimulus discrimination training and 5 sessions of compound stimulus discrimination training with these stimuli; four pigeons received single stimulus training first and four received compound stimulus training first. Vertical line and green background were always S^{D} components, and horizontal line and red background were always S^{Δ} components. In generalization tests, when all four stimuli were again presented alone, nonresponding was selectively controlled by the single stimulus discrimination training, S^{Δ}, regardless of training sequence.

Selective stimulus control of responding by a single component of a compound stimulus correlated with reinforcement has often been demonstrated, e.g., Lashley (1938), Reynolds (1961). Reynolds trained two pigeons to discriminate a white triangle on a red background from a white circle on a green background. When these four stimuli, including the two S^{Δ} components, were presented alone in an extinction test, one S responded only to the red background and the second S responded only to the white triangle. Johnson & Cumming (1968) recently demonstrated control of selection among components of a compound stimulus by training a discrimination between single components separate from their appearance in a compound stimulus discrimination.

In these experiments, selection occurred with respect to components of positive compound training stimuli. Since responding to S^{Δ} components was essentially zero, it would appear that nonresponding was nonselectively controlled by components of the negative compound training stimuli. However, without prior measure of response strength to each stimulus component, it is impossible, as Eckerman (1967) pointed out, "... to determine whether this non-selective control reflects a *reduction* of response strength in both components or the mere *absence* of response strength to these two stimuli [p. 299]."

Eckerman (1967) trained three pigeons to peck at each of four stimuli alone before repeating the essential conditions of the Reynolds experiment. Compound stimulus discrimination training employed a white vertical line on a green background as S^{D} and a white horizontal line on a red background as S^{Δ}. When these four components were again presented alone in an extinction test, nonresponding by at least one S during the test was selectively controlled by the red background.

The present experiment obtained prior response measures to four stimulus components, then trained a single stimulus discrimination either before or after a component stimulus discrimination using the four stimuli.

SUBJECTS

Eight 5- to 6-year-old White Carneau and White King cock pigeons were maintained at 80% free-feeding body weights and were experimentally naive at the outset.

APPARATUS

A standard pigeon operant chamber (LVE 1519) had a single pecking key which could be transilluminated from behind by an IEE display unit. The automatic feeder presented grain (50% Kaffir, 40% vetch, 10% hempseed) for 4-sec periods. White noise (86-dB SPL) through the chamber speaker masked extraneous laboratory sounds and a houselight provided general illumination.

PROCEDURE

Key-pecking for each S was established to a white, fully lighted key, and maintained on a random-interval schedule of reinforcement having a mean interreinforcement interval of 1 min (RI 1; Farmer, 1963) for three daily 1-h sessions. In 20-25 subsequent, daily 1-h sessions, each of four stimuli-green background (G), red background (R), white vertical line (V), and white horizontal line (H), appeared alone, equally often, in mixed orders for 1-min periods. Colored backgrounds filled the key area and white lines were diameters .18 in. wide. Responses to each stimulus were reinforced on the RI 1 schedule. This initial training phase was terminated when, for any S, responses per session to each stimulus did not change more than 5% over five successive sessions.

All Ss were then given 10 1-h sessions of single stimulus discrimination training (SSDT) and 5 1-h sessions of compound stimulus discrimination training (CSDT). Four Ss, S13, S16, S18, and S15, received SSDT before CSDT, and four Ss, S79, S78, S77, and S76, received the reversed sequence. For SSDT, each S from each sequence was assigned one of the four possible combinations keeping vertical line and green background positive, and horizontal line and red background negative. SSDT discriminative stimuli were assigned as S^{D} and S^{Δ}, respectively, among Ss as follows: S13 and S79–vertical line, horizontal line; S16 and S78–green background, horizontal line; S18 and S77–vertical line, red background; and S15 and S76–green background, red background. During CSDT, the missing components were added to form component

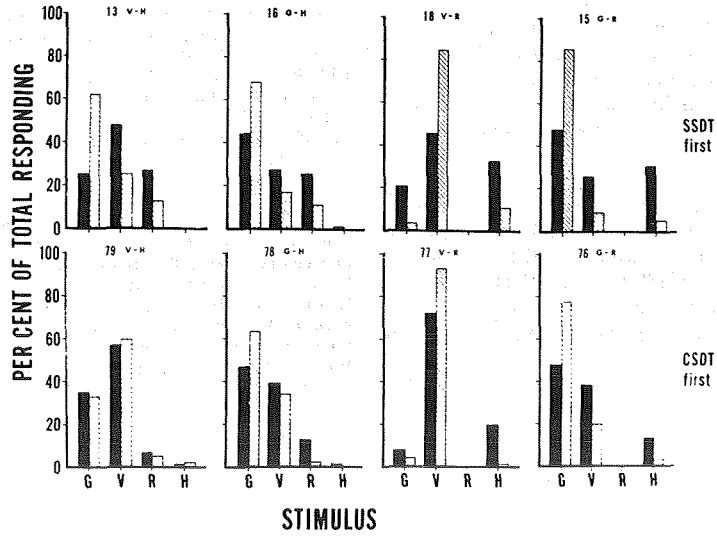

Fig. 1. Per cent of total responding in the two test sessions to each of the four stimuli for each S. Solid and striped bars indicate values from the first and second test sessions, respectively.

discriminative stimuli of S^D—vertical line on green background—and S^Δ—horizontal line on red background. In discrimination training, responses to S^D were reinforced on the RI 1 schedule, and responses to S^Δ were never reinforced.

Following training, all four stimuli were again presented alone in mixed orders for two 1-h test sessions. Responses were recorded but never reinforced.

Any stimulus period in all phases lasted for 1 min, and a 5-sec "time-out" period intervened between stimulus periods. In "time-out," the houselight remained on, but stimulus lights were off and responses were never reinforced.

RESULTS

Initial Training

During the 20-25 initial training sessions, "preferences" (portions of total-session responding greater than 25%) and "avoidances" (portions of total-session responding less than 25%) occasionally appeared but in no consistent pattern for any S throughout the initial training phase. In the final five sessions, when response distributions stabilized within 5% of mean rates, approximately 25% of total session responding occurred to each stimulus, ranging from 19% to 32% for any stimulus in any session.

Discrimination Training

All but three Ss acquired both discriminations to precisions of less than 2% S^Δ responses within 5 h of exposure. S15 required 9 h on G-R SSDT to reach this level. S78 on G-H SSDT and S79 on V-H SSDT exhibited extremely high response rates (about 90 responses/min compared to a mean of about 40 responses/min for other Ss) and displayed minima of 12% and 25% S^Δ responding, respectively, during initial CSDT and 5% and 10% S^Δ responding respectively, during subsequent SSDT.

In general, the discriminations were acquired with steady increments in precision of performance. Performances were about equally disrupted when the second discrimination training phase, whether SSDT or CSDT, was introduced, but performances returned to equal or greater precisions within 5 h exposure.

Test for Stimulus Control

Proportions of total responding in the two test sessions to the four stimuli for each S are presented in Fig. 1. Solid and striped bars indicate values from first and second test sessions, respectively. For Ss initially exposed to SSDT, the total number of responses ranged from 1035 to 1759 in the first test session. The greatest portion of responding, from 45% to 48%, occurred in the presence of the component, which was S^D in SSDT. Of principal interest, the least amount of responding, as much as 1% for only one S, occurred to the single S^Δ of SSDT. Portions of test session responding to stimulus components added in CSDT were about equal. Portions ranged from 21% to 28% to the added S^D component and from 21% to 33% to the added S^Δ components.

For Ss initially exposed to CSDT, total responses in the first test session ranged from 1438 to 2938. Again, the greatest proportion, from 47% to 72%, of test responding occurred to the SSDT S^D, and, again, the least responding, as much as 1.8% for two Ss, occurred to the SSDT S^Δ. Portions of test responding to the removed CSDT S^D component ranged from 8% to 39% and portions of test responding to the removed CSDT S^Δ component ranged from 7% to 14%.

In general, responding during the second test session showed sharpening of the stimulus control observed in the first test session. Except for S13, for which the S^D component exercising primary control reversed, the SSDT S^D controlled even greater portions of responding in the second test session. And, except for S79, no other S responded to the SSDT S^Δ in the second test session. All other components for all other Ss controlled smaller portions of test responding.

Extinction records from each stimulus component for each S were generally smooth, negatively accelerated functions.

DISCUSSION

Initial training established approximately equal response strength to each of the four stimulus components. However, subsequent single stimulus training and compound stimulus training considerably altered the distribution of responses to stimuli. In particular, single stimulus training, regardless of whether it preceded or followed compound stimulus training, determined that stimulus control of responding was exercised primarily by the single stimulus training S^D and stimulus control of nonresponding was primarily exercised by single stimulus training S^Δ.

Nonresponding was exclusively controlled by the SSDT S^Δ for Ss initially exposed to SSDT. While virtually no responding occurred to SSDT S^Δ in the cases that SSDT followed CSDT, the other component of the compound S^Δ nevertheless retained some control of nonresponding. In three of the four Ss, response strength to the removed S^Δ component was less than to the removed S^D component. Thus, while the stimulus exercising primary control was determined by separate, single stimulus training, the effects of sequence were not precisely equivalent for the present conditions. Johnson and Cumming (1968) obtained similar results with respect to determining control by parts of a compound S^Δ.

Response strengths to the nonselected component of the S^D compound were generally as high as strengths established in the initial training phase. This finding suggests that studies producing selective stimulus control by pretraining a single stimulus discrimination (cf. Johnson & Cumming, 1968) operate to prevent the acquisition of control by subsequently added stimulus dimensions.

These findings are accountable with a theory which counts reinforcements and extinction time in stimulus components (Spence, 1936), but this type of theory is not generally satisfactory for findings of selective stimulus control (cf. Mackintosh, 1965). Rather, an additional, active mechanism is presumed to occur. The present results suggest that an active stimulus selection mechanism should be applied to negative, as well as positive, compound training stimuli.

REFERENCES

ECKERMAN, D. A. Stimulus control by part of a complex S^Δ. Psychonomic Science, 1967, 7, 299-300.

FARMER, J. Properties of behavior under random interval reinforcement schedules. Journal of the Experimental Analysis of Behavior, 1963, 6, 607-616.

JOHNSON, D. F., & CUMMING, W. W. Some determiners of attention. Journal of the Experimental Analysis of Behavior, 1968, 11, 157-166.

LASHLEY, K. S. The mechanism of vision: XV. Preliminary studies of the rat's capacity for detail vision. Journal of General Psychology, 1938, 18, 123-193.

MACKINTOSH, N. J. Selective attention in animal discrimination learning. Psychological Bulletin, 1965, 64, 124-150.

REYNOLDS, G. S. Attention in the pigeon. Journal of the Experimental Analysis of Behavior, 1961, 4, 203-208.

SPENCE, K. W. The nature of discrimination learning in animals. Psychological Review, 1936, 43, 427-449.

NOTE

1. Portions of these results were presented to the Eastern Psychological Association, Philadelphia, 1969. This research was supported by Grant MH-13383 from the National Institute of Mental Health and by NASA Grant NGR-47-004-006.

Address reprint requests to Daniel F. Johnson, Departme.'t of Psychology, Virginia Polytechnic Institute, Blacksburg, Va. 24061.

Semi-Annual Progress Report No. 9

to the

NATIONAL AERONAUTICS AND SPACE ADMINISTRATION

in connection with

NASA Grant NGR 47-004-006

Part 3 of 8 Parts

Final Report

V.P.I. Project 313239

Time-Resolved X-ray Diffraction Microscopy: Development of a New Technique

by

Kenneth Reifsnider

Virginia Polytechnic Institute
Blacksburg, Virginia

September, 1969

Time-Resolved X-ray Diffraction Microscopy: Development of a New Technique

Introduction:

With advancing technology, the possibility of monitoring in real time the continuous changes in an x-ray diffraction pattern produced by dynamic events has drawn the interest of more and more investigators. In contrast to the rapid development of time-resolved radiographic methods, progress has been much slower in the area of x-ray diffraction, largely because of strict limitations on available intensity and required resolution. Also, in the case of diffraction, not only the apparatus but the technique of application to research must be developed in order to make the equipment compatable with rather specific scientific interests.

In 1968, Reifsnider and Green[1,2,3] reported the development and application of the first apparatus to record the changes in an x-ray diffraction pattern caused by tensile deformation on 16 mm cine film. Their system had a time resolution of $1/300^{th}$ of a second and a geometric resolution of about 2 lp/mm. That system has found application in the investigation of lattice rotations, grain boundary motion, inhomogeneous deformation and strain rate studies.

More recently, several investigators have attempted to extend the work in this area to achieve greater geometric resolution[5,6,7,8]. It was, of course, realized that the most desirable extension would be to

the level of resolution commonly used in x-ray microscopy (sometimes called topography studies). However, little can be done with such techniques without a geometric resolution of detail whose characteristic spacing is considerably less than 100 μm. Also, the diffracted beams are quite low in intensity because of the collimation necessary to obtain the parallel-ray x-ray beam needed for high resolution. Before discussing the successful development which will be presented in detail below, several alternative approaches to this problem will be briefly evaluated.

From the standpoint of simplicity, an x-ray sensitive vidicon represents on excellent possibility for instantaneous display of x-ray patterns. Such a system has been reported by Chikawa[5]. His camera used a PbO target on the berylium faceplate of a specially built vidicon camera to record Lang Topographs with a scan rate of 15 cm/min. While he did not measure the resolution of his system, the x-ray arrangement which he reported had a resolution of 50 μm, i.e., he was not resolving α_1 and α_2 for example. More important, the PbO vidicon was extremely insensitive, requiring a threshold illumination of about 5×10^5 x-ray photons $sec^{-1} mm^{-2}$. Such a device could not be used to record any diffraction detail which displayed intensity contrast near to the perfect crystal diffraction intensity (which is several orders of magnitude below the threshold given above). Also, the 8000 watt x-ray source which he used to provide such great intensities is not commonly available.

Alternative to the PbO target, a silicon diode array target indicon has also been used[6,7] to display x-ray patterns directly. Although the theoretical limit on resolution is the electron beam size, i.e. about

30 μm, the resolution was not measured. Also, topography was not attempted. The sensitivity was, again, very low requiring about 30 seconds to record a Laue pattern produced by a standard source. This can be compared to the 1/300 sec. mentioned earlier.

A considerable gain in sensitivity can be achieved by adding one step to the imaging process. The X-ray image is converted into a light image which is intensified and then recorded. In this case, then, the usual recording film is replaced by a fluorescent screen which converts the X-rays to optical light. The low light level image (about 10^{-5} ft. cd.) is then intensified and finally recorded. One rather successful way of viewing the screen has been reported by Meieran et. al.[8] They used a secondary electron conduction (SEC) vidicon system with a resolution of about 30 μm and a sensitivity sufficient for scanning Si wafers at 15mm/min. The threshold sensitivity and resolution limit were not measured, however, and no individual atomic defects were recorded. Also, the cost of such a system is presently between $40,000 and $60,000.

For the present system, it was decided to view a fluorescent screen with a high gain, low noise optical image intensifier which was, in turn, to be viewed by a closed circuit vidicon television system. Such an arrangement is similar to the original system used by Reifsnider and Green.

PROGRAM DESCRIPTION:

The Lang method of transmission X-ray topography is a widely used standard technique and has been described elsewhere.[3,4] The geometric resolution limit of such an arrangement is about 1 μm and the thickness of specimens commonly examined (chosen so that $\mu t \tilde{>} 1$ for optimum contrast) is of the order of 1 mm. for soft radiation. The particular X-ray system used for the present investigation consisted of a Phillips fine focus X-ray tube, collimator-slit arrangement, and Lang topograph camera. Commonly, a 3° takeoff angle was used to obtain a projected spot size of 400 by 400 μm from a Mo or Ag target whose dimensions were 8 mm by 400 μm. A source-to-specimen distance of 40 cm was maintained and the specimen to recording surface distance ranged from 1 to 2 cm so that the geometric resolution limit was between 10 and 20 μm. In all cases the width of the incident beam was restricted so that the α_1 and α_2 reflections were clearly resolved. The fine-focus X-ray tube was operated at a maximum of 800 watts. Dental X-ray film was used to obtain quick section and projection topographs for reference and alignment, and nuclear emulsion plates were used for permanent recording of comparison topographs in the usual manner.

While the Lang topographic system was completely standard, the equipment for continuous monitoring of the X-ray diffraction patterns had to be developed. After some correspondence, the EMI corporation of England agreed to provide on loan a 4-stage 9694 magnetically focused cascaded image intensifying tube for use in the development reported below. The tube had a bi-alkali photocathode and an on-axis luminous flux gain of about 10^5. The image tube was lens coupled

in front to a fluorescent screen which replaced the film in the Lang camera. The rear phosphor of the image tube was viewed by an EMI type 9A vidicon camera which displayed the output on a T.V. monitor.

During the course of our development, several different fluorescent screens and coupling lens systems were tested. Seven different screens were used in the system and compared for intensity and resolution. Subjective estimates of relative intensities of these screens in a direct beam of 40 kv filtered by a 2 mm thickness of silicon are shown in Table I. The approximate resolution of the two screens used for most of our program is also shown. For AgK_{α} radiation, the thickness of the ScI (Tℓ) screen was increased to 300 μm.

The fluorescent screens were made to order according to specifications determined in the following way. Three factors control the desirability of a fluorescent screen, absorption, conversion efficiency and resolution. For the polycrystal screens the conversion efficiency is fixed by choice of type of material to be used and, in fact, that consideration is the major factor in the choice of type. The resolution is determined by grain size and screen thickness, both of which need to be as small as possible for best resolution. The absorption for a given naterial, then, is determined by the screen thickness. Polycrystalline screens are commonly classified by weight per square centimeter of deposit so that the thickness is defined by the density, i.e.:

$$\text{thickness} = \frac{\text{weight/unit area}}{\text{density}} \qquad (1)$$

The determination of optimum thickness will be demonstrated by an example. For AgK_{α_1} radiation we wish to determine the thickness of a Zn S(Ag) screen for 75% absorption. The mass absorption coefficients for the phosphor elements are:

$$(\mu/\rho)_{Zn} = 28.8 \qquad (\mu/\rho)_{S} = 4.84$$

Screen Material	CsI(Na)	CsI(Tl) (6mm thick)	CsI deformed (300μm thick)	CsI(Tl) (200μm thick) with Al reflector	GNSF ZnS (Ag) (150μm thick)	GNSF ZnS(Ag) 350μm thick	NaI(Tl) with Al reflector
Relative Brightness	1	4	8	12	16	32	1
Resolution (1p/mm)				10		5	

TABLE 1

Fluorescent Phosphors

and the respective molecular weights are 65.4 and 32. The molecular weight of ZnS is then 97.4 and the mass absorption coefficient of the compound is:

$$(\mu/\rho)_{ZnS} = \frac{(65.4)(28.8) + (32 \times 4.84)}{97.4} = 20.9$$

Now the density of ZnS is 4.1 so that the absolute absorption coefficient is 85. Now if I_o is the incident X-ray intensity, the intensity at a depth "t" is given by:

$$I = I_o e^{-\mu t} \qquad (2)$$

so that the fraction of incident intensity absorbed by a thickness "t" is given by:

$$\frac{I_o - I}{I_o} = 1 - e^{-\mu t} \qquad (3)$$

Thus, 75% absorption corresponds to $\mu t \gtrsim 1$ or a thickness of 120μm of ZnS. In standard terms, then, a 48 mg / cm^2 screen deposit would be required.

Due to light dispersion and the finite dimensions of the fluorescing region for a given X-ray detail element, the resolution of the fluorescent screens is inversely proportional to their thickness, Therefore, one has to make a compromise choice between required resolution and available intensity using a chart of values such as those shown in Table II. The manor in which the screens are incorporated into the system will determine the exact relationship between screen thickness and the resultant resolution.

The GNSF screens are polycrystalline but the others were single crystals. The particle size of the GNSF phosphors was 8 μm. The resolution values were determined by interposing wire mesh screens in a direct or diffracted X-ray beam just before it strikes the fluorescent screen of the complete image system so that the resolution quoted is really the resolution of the system with a particular screen in place and not the resolution of a single component. Also, the resolution is a measured value.

	RADIATION	thickness for		
		50% absorption	77% absorption	90% absorption
Zn S(Ag) $\rho = 4.1$ (polycrystal)	AgK α_1	81.5 µm (33.4 mg/cm^2)	129 µm (53.0 mg/cm^2)	270 µm (111 mg/cm^2)
	MoK α_1	42.2 µm (17.3 mg/cm^2)	67.0 µm (27.4 mg/cm^2)	140 µm (57.5 mg/cm^2)
CsI (Tℓ) $\rho = 4.5$ (single crystal)	AgK α_1	80.8 µm	128 µm	268 µm
	Mo K α_1	39.4 µm	62.0 µm	130 µm

TABLE II

Representative absorption values for fluorescent screen materials used.

During the course of our development, two basic modes of operation seemed to be particularly useful. The first of these was developed in an effort to observe Moire fringe patterns caused by simultaneous diffraction by two superposed crystal lattices. Such patterns have recently been used as a powerful tool in the analysis and quantitative characterization of atomic defects.[9] The diffraction arrangement for such fringe production is shown in Figure 1. Since the fringes are being produced by periodic structures with atomic spacing, the usual fringe spacing formulae become:

$$D = \frac{d}{\varepsilon} \tag{4}$$

and

$$D = \frac{d_1 d_2}{d_1 - d_2} \tag{5}$$

for rotation and dilatation respectively where "d" is the atomic spacing, ε is the angle between active diffracting reciprocal lattice vectors, d_1 and d_2 are slightly different lattice spacings, and D is the Moire spacing. If there are "n" lattice dislocation outcroppings in the second crystal, the number of half-lines crossed in a circuit around the corresponding discontinuity in the Moire pattern will be equal to:

$$\sum_{j=1}^{n} \underset{\sim}{g} \cdot \underset{\sim}{b}_j \tag{6}$$

where $\underset{\sim}{g}$ is the active reciprocal lattice vector and b_j are the Burgers vectors of the dislocations in the region. For atomic disorder the spacing of the Moire fringes ranges between 25 μm and 1 mm (providing, of course, the reciprocal vectors $\underset{\sim}{g}_1$, and $\underset{\sim}{g}_2$ are sufficiently well aligned). For such investigations, then, resolution should not be a serious problem. For this work we found the system shown in Figure 2 to be most desirable. The phosphor was polycrystalline ZnS (Ag), either 150 μm or 300 μm thick.

The lens pair in front of the image tube was an Old Delft 1:1, f:0.75, 104 mm system. Hence the image size on the photocathode was the same as that on the fluorescent screen and there was no loss of brightness due to magnification. With this system quantum fluctuations in the X-ray (diffracted) beam were not a major limitation on resolution. However, dispersion in the thick polycrystalline screen combined with those fluctuations to limit our resolution to about 5 lp/mm.

With this arrangement we were, in fact, able to resolve "crossover," the high intensity region which is crosshatched in Figure 1, which occurs when $\mathcal{g}_1$ and $\mathcal{g}_2$ are very closely aligned (to within about 10^{-10} steradian). However, we were unable to maintain sufficient stability in our alignment apparatus to record a rapid Moire pattern (or a change in one). It is believed, however, that the imaging equipment was sufficiently sensitive and had sufficient resolution to do so.

The second arrangement that proved useful is shown in Figure 3. The thin single crystal fluorescent screen (CsI (Tl)) provided somewhat better absolute resolution with about 20% less conversion efficiency than the former polycrystal GNSF. The front coupling lens pair provided a magnification of about 2.3 so that the image tube did not limit the resolution of the system. The rear lens provided some demagnification (about 2X) so that the image filled about half of the output screen on the vidicon. Hence the vidicon may have limited our resolution somewhat. With test patterns this system easily resolved 12 lp/mm (no finer grid was available).

An arrangement was constructed whereby the image tube, fluorescent screen, specimen, and vidicon camera could be scanned through the X-ray beam synchronously. The traveling image produced on the television monitor then produced a section topograph by the usual Lang method. The primary

limitation on resolution for this case was the quantum fluctuation in the X-ray image, i.e., we were "brightness limited" in the absolute sense in this case. However, the overall resolution was superior to the first arragnement, especially if some time integration was used during recording.

RESULTS:

Using the system shown in Figure 3, section topographs of several materials were recorded in 10-12 seconds. We were able to scan at the rate of 30 mm/min. which represented about 1/2 second time integration per unit image area. An example of our results is shown in Figure 4a and b. Both topographs are the 220 reflection from a diamond specimen with rough dimensions of 5 mm square. Both topographs were recorded with MoK_{α}, radiation. The topograph shown in Figure 4b was recorded in 12 seconds by scanning the fluorescent screen and imaging components synchronously with the specimen through the incident X-ray beam. A standard Polaroid camera was used to make a 12 second time exposure of the moving (and changing) pattern on the T.V. monitor. In actuality, a slotted black curtain was moved along with the traveling image on the T.V. monitor to reduce the integrated intensity of the background produced by the monitor roster and dark current of the image tube being repoduced by the T.V. system.

It can be seen by comparing Figure 4a and 4b that the "instant topograph" displays most of the major features shown by the high resolution topograph recorded in the usual manner (requiring an 11 hour exposure time). The central nucleation defect, the surrounding burst of radiating dislocations, and the surface damage at the edges are all clearly shown. Also, the very faint line extending more or less horizontally from the central point to the right has been identified as a single dislocation with $\underset{\sim}{g} \cdot \underset{\sim}{b} = 2$. While the geometric resolution of the "instant topograph" is good, the most encouraging aspect is the sensitivity which it indicates. The perfect crystal diffracted intensity is recorded and, therefore, the diffraction detail which is only slightly more intense is also resolved. Without this sensitivity a great deal of the low contrast diffraction detail is lost regardless of the geometric resolution capabilities of

the system. The threshold sensitivity of our system using the ZnS(Ag) screen was 10 incident X-ray photons $sec^{-1}mm^{-2}$ at the fluorescent phosphor compared to about 10^5 photons $sec^{-1}mm^{-2}$ required for direct vidicon viewing.

Figure 5a and b show another comparison of a standard topograph and a 12 second "instant topograph". The material used was natural quartz. As in the previous example the major detail shown by the standard topograph is displayed by the "instant" version also. Most interesting, in this case, are the growth horizons which are (barely) resolved. They are, again, very low contrast detail that would be lost if the system was significantly less sensitive. There are a number of twins also shown in both topographs. (Although no examples are shown, we also produced "instant topographs" of Amethyst quartz which showed, among other things, regularly spaced optical twins.)

In addition to actual recording of topographs, the time-resolved system also seemed to be very useful for the purpose of general alignment such as finding the α_1, α_2 and β reflections, and expecially for the alignment of crystals to produce Moire fringes. Also, it was possible to scan a specimen with a given reflection quickly to ascertain the desirability of making a high resolution topograph (requiring several hours). Hence, the apparatus functions quite well as a significant time and labor saving device during preparations for otherwise static investigations.

CONCLUSIONS AND REMARKS:

The system developed during the course of this research has the following advantages.

1. The high-gain low-noise characteristics of the image intensifier allows one to:
   a) take useful topographs with scan speeds of 30 mm/min. with
   b) a standard low-wattage fine-focus X-ray source (800 watts) with
   c) X-ray geometrical resolution of 10-15 μm and
   d) separation of the α_1 and α_2 components for all but the lowest 2θ relections.
2. The image intensifier with independent optical input and output systems allows:
   a) a choice of fluorescent screen to optimize balance between resolution and intensity
   b) variation of magnification to minimize resolution limitations caused by individual components
   c) use of direct viewing, cine-recording, T.V. display, etc. for data retrieval.

Use of the present system for study of dynamic diffraction events is being initiated. Possible areas of work include: 1) study of motion of magnetic domains, 2) observation of moving dislocations under stress, 3) examination of crack nucleation during cycled loading, 4) rapid recording of relative intensities of diffraction spots for the analysis of the structure of metastable protein molecules, 5) study of precipitation and defect decoration, 6) investigation of grain nucleation, growth, and general recrystallization kinetics, 7) analysis of inhomogeneous development of strain including deformation dislocation arrays, and 8) continuous study of abrasion damage. The present technique certainly is not the last word in development. An obvious improvement would be the use of fiber optic coupling rather than the standard lenses. Other improvements will be made as technology permits.

The author wishes to thank Dr. A. R. Lang for his contribution to the present work, especially in the realm of topographic methods. The present research was carried out at the H. H. Wills Physics Laboratory, University of Bristol in Bristol, England. The author was supported in part by NASA contract NGR 47-004-006.

BIBLIOGRAPHY

1. Reifsnider, K. and Green, R. E., Jr.; Rev. Sci. Instr. 39, #11, (1968), 1651

2. Reifsnider, K. and Green, R. E., Jr.; Trans. AIME 245, (1969), 1615

3. Lang, A. R.; Acta Metallurgica 5, (1957), 358

4. Lang, A. R.; Acta Cryst. 12, (1959), 249

5. Chikawa, J. I. and Fujimoto, I.; Appl. Phys. Letters 13, (1968), 387

6. Chester, A. N., Loomis, T. C. and Weiss, M. M.; Bell System Tech. J. 48, (1969), 345

7. Chester, A. N. and Koch, F. B.; Advan. X-Ray Anal. 12 (1969)

8. Meieran, E. S., Landre, J. K. and O'Hara, S.; Appl. Physics Letters 14 No. 12, (1969), 368

9. Lang, A. R.; Nature, 220 No. 5168, (1968), 652

10. Reifsnider, K. and Green, R. E. J.; J. Metals, 20, (1968), 83A

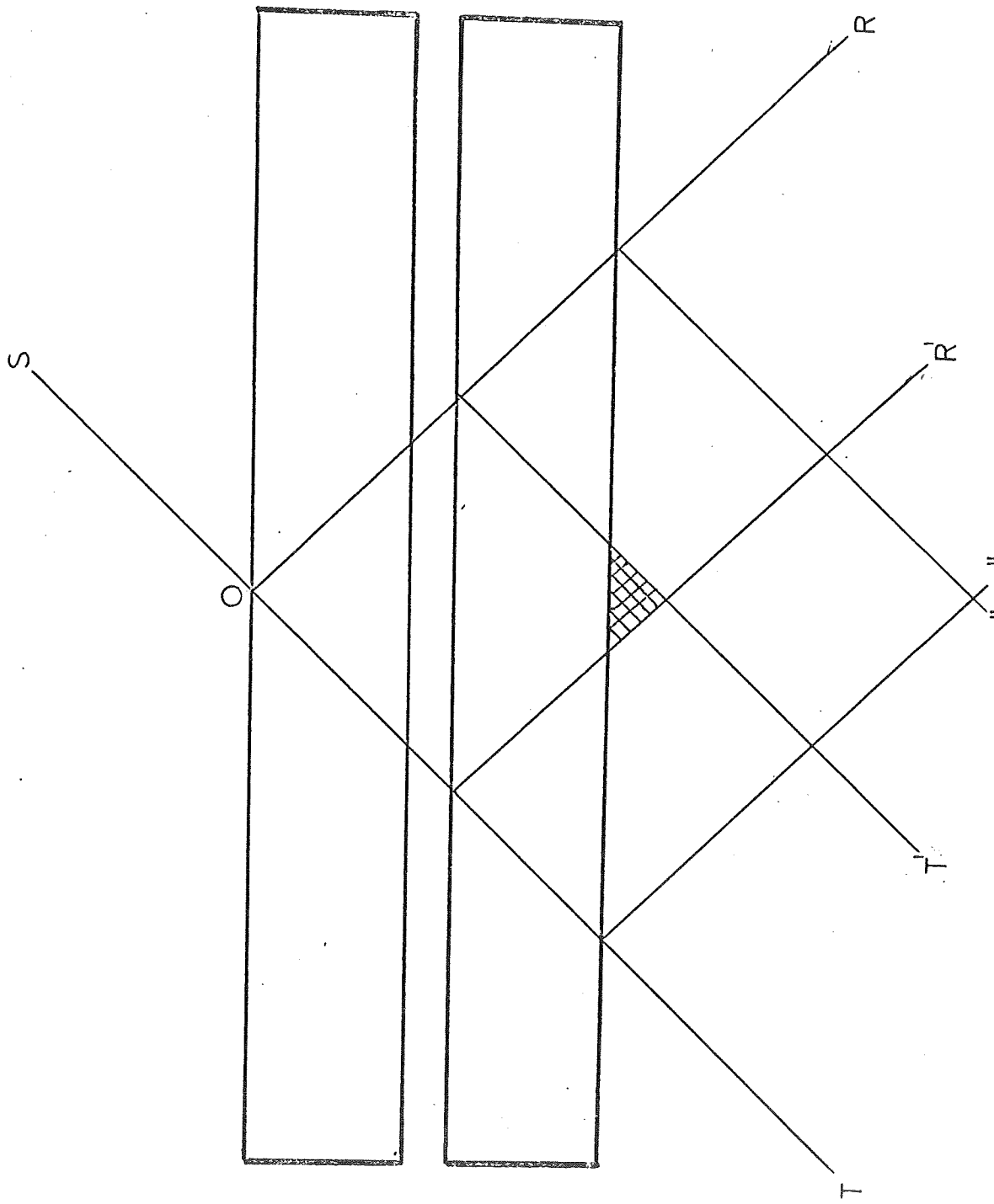

Fig. 1
Diffraction geometry for the production of Moire fringes

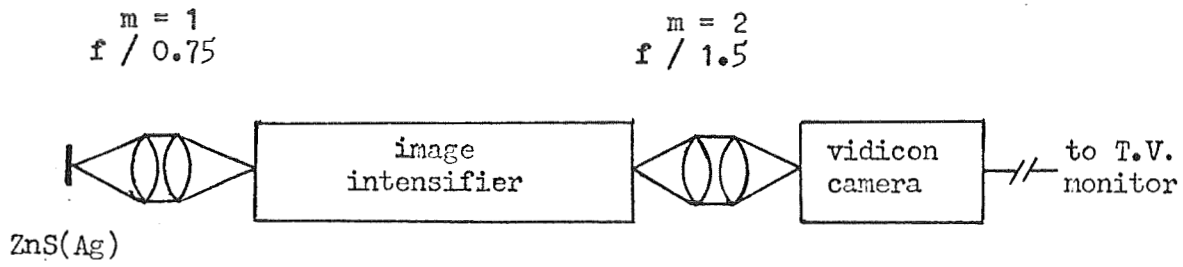

Fig.2
Imaging system for greatest brightness

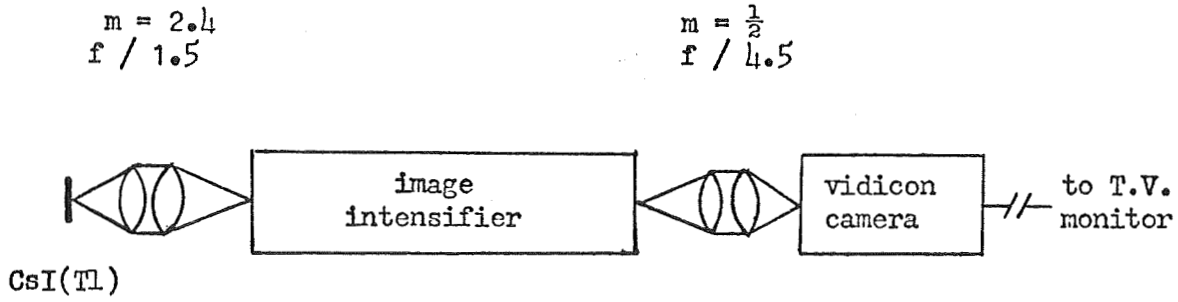

Fig.3
Imaging system for greatest resolution

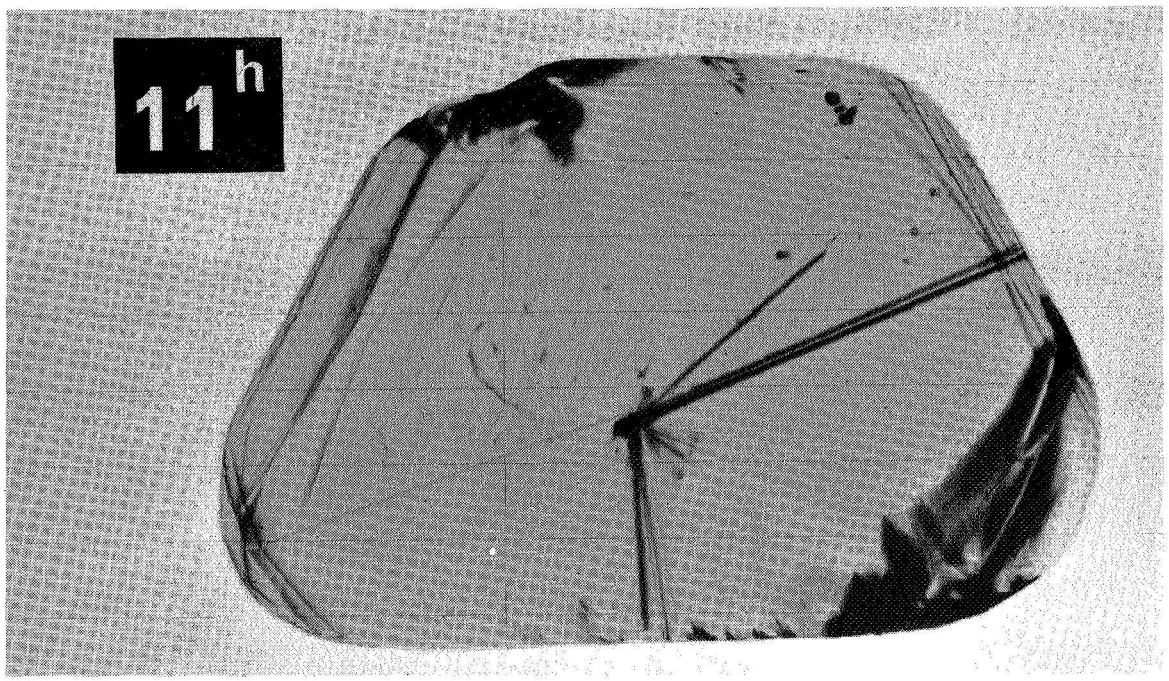

a) Recorded on 50 μm thick Ilford L4 nuclear emulsion, 150 watts X-ray source, 11 hours exposure.

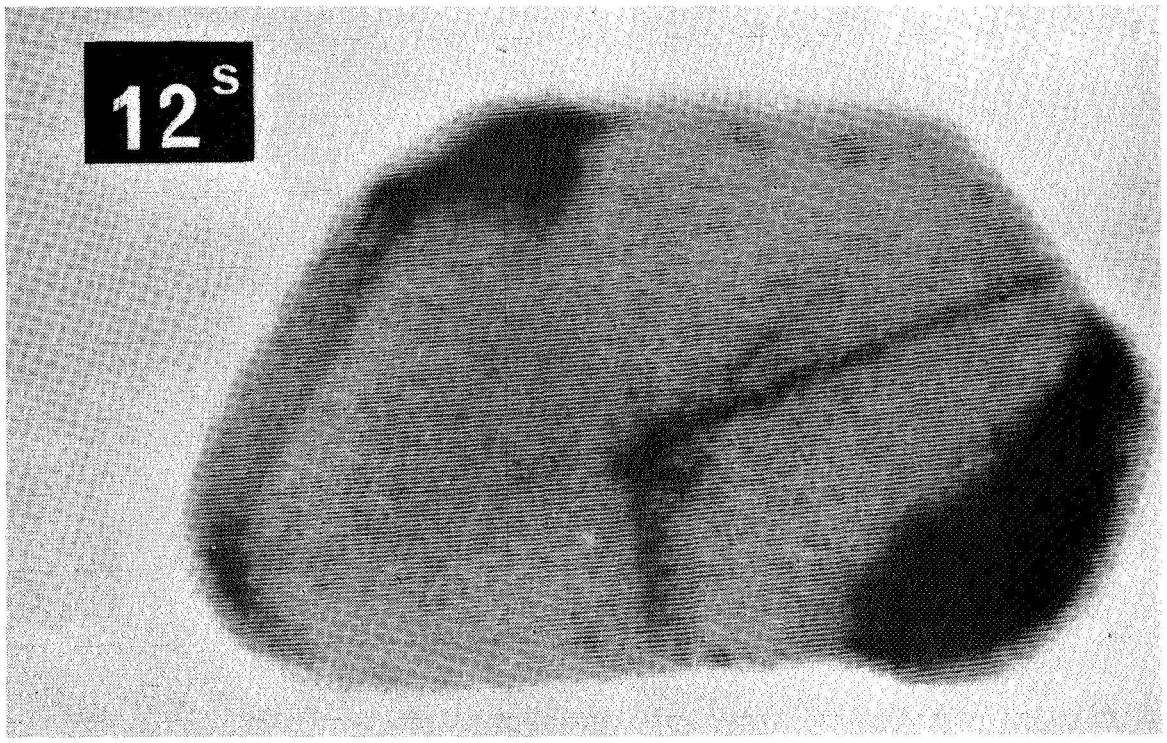

b) Polaroid photograph of television screen displaying image intensifier output, 800 watts X-ray source, specimen traverse duration 12 seconds, photographic processing 10 seconds.

Fig. 4

Projection topographs of natural diamond 5.2 mm wide, (220) reflection, $MoK\alpha_1$ radiation. Extra diffracted intensity appears as extra blackness.

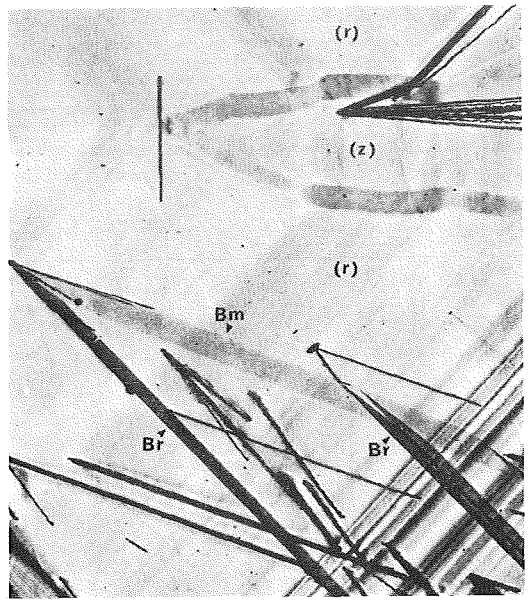

a) Standard Topograph requiring 9 hours exposure time.

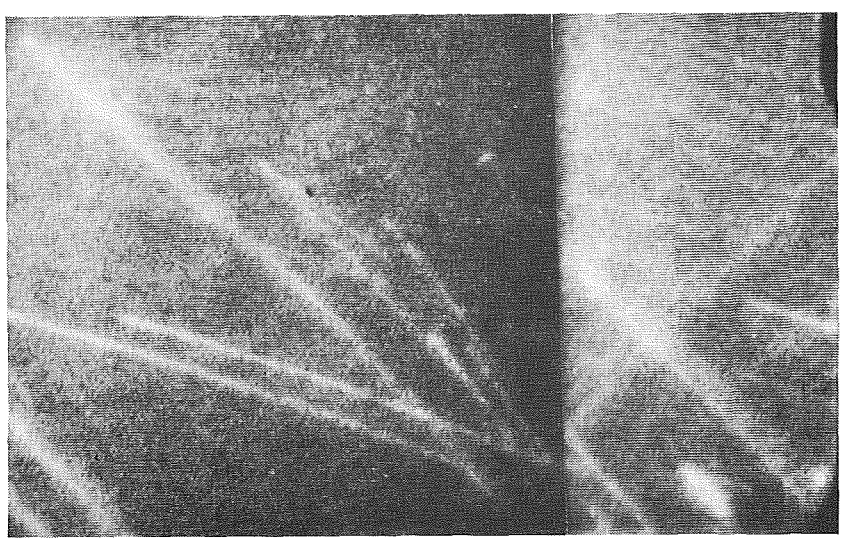

b) Polaroid photograph of television screen recorded as described in Fig. 4b.

Fig. 5

Topograph of natural quartz plate inclined 11° to major rhombohedron $(10\bar{1}1)$. Thickness 1 mm, $(10\bar{1}1)$ reflection, AgKα radiation. Field area 1 x 1.3mm. Plate is viewed along a direction tilted 40° away from the c-axis towards the normal to (1011). Projection of diffraction vector is horizontal, direction [12$\bar{1}$0] is vertical on the topograph.

Semi-Annual Progress Report No. 9

to the

NATIONAL AERONAUTICS AND SPACE ADMINISTRATION

in connection with

NASA Grant NGR 47-004-006

Part 4 of 8 Parts

Final Report

Part A

V.P.I. Project 313138

High Vacuum System and Instrumentation for Measuring the Derivative of the Current-Voltage Characteristic of a Langmuir Probe

by

Francis E. Baker, Jr.

Robert H. Bond

Virginia Polytechnic Institute
Blacksburg, Virginia

September, 1969

TABLE OF CONTENTS

		PAGE
	ACKNOWLEDGMENT	iv
	INDEX OF FIGURES	v
	INDEX OF SYMBOLS	vii
	INDEX OF TABLES	ix
I.	INTRODUCTION	1
	1.1 Background Information	1
	1.2 Object of This Experiment	3
II.	HIGH VACUUM SYSTEMS	4
	2.1 The Initial Vacuum Station	5
	2.2 All Glass Sorption Trap	10
	2.3 The Gas Manifold	11
	2.4 Gauges for Measurement of Pressure	16
	2.5 Experimental Tube	20
	2.6 Circuit and Equipment used to Fire the Discharge	21
III.	THEORY AND INSTRUMENTATION	29
	3.1 Operational Amplifier Method	29
	3.2 Lock-In Amplifier Method	33
IV.	EXPERIMENTAL PROCEDURE	38
	4.1 Operational Amplifier Method	38
	4.2 Lock-In Amplifier Method	42

PAGE

V. DISCUSSION OF RESULTS AND CONCLUSION 49

5.1 Results 49

5.2 Conclusion 50

VI. BIBLIOGRAPHY 51

INDEX OF FIGURES

FIGURE		PAGE
2.1	View of the Initial Vacuum System	6
2.2	View of the Initial Vacuum System	7
2.3	Diagram of the Initial Vacuum System	8
2.4	Work Done by Edward Price	9
2.5	Glass Sorption Trap	12
2.6	Diagram of Gas Manifold	13
2.7	View of the Gas Manifold	14
2.8	View of the Gas Manifold	15
2.9	Diagram and Placement of Ionization Gauge Tubes	17
2.10	Ionization Gauge Controller and Pirani Vacuum Gauge Controller	19
2.11	Circuit to Fire Discharge	22
2.12	Discharge Tube with a Cold Cathode Discharge	24
2.13	View of the Vacuum System	26
2.14	View of the Vacuum System	27
2.15	View of the Vacuum System	28
3.1	I-V Characteristic	29
3.2	Operational Amplifier Set-Up	30
3.3	Lock-in Amplifier Set-Up	34
3.4	Block Diagram of Lock-in Amplifier	37
4.1	View of Experimental Set-Up	39

FIGURE PAGE

4.2 Test Set-Up Using Operational Amplifier Differentiator 40

4.3 Triangular Voltage Waveform 43

4.4 Output Voltage of the Differentiator 44

4.5 Test Set-Up Using Lock-in Amplifier 46

INDEX OF SYMBOLS

A	collecting area of the probe
B	gain of operational amplifier
C	series input capacitor of the operational amplifier
D	gain of differentiator
E	peak amplitude of small a-c voltage
e	magnitude of the charge of an electron
$f(v)$	speed distribution of the electrons
I_p	instantaneous probe current
K_n	constant, where n = 1, 2, 3, . . .
m	mass of an electron
R	feedback resistance of the differentiator
R_1	variable resistor
R_2	fixed resistor
R_3	fixed resistor
R_4	variable resistor
R_s	sensing resistor
R_F	fixed resistor
T	period of the triangular voltage
t	time
V_s	instantaneous voltage across sensing resistor
V_o	output of the differentiator
V_{TRI}	instantaneous voltage of the triangular wave

V_p	probe voltage with respect to the anode
V_{DC}	d-c bias voltage
V	sum of the triangular voltage and d-c bias
V'_s	output voltage of the operational amplifier
V_L	output voltage of the lock-in amplifier

INDEX OF TABLES

TABLE		PAGE
I	Data and Results of Differentiator Test	45
II	Data and Results of Lock-in Amplifier Test	48

I. INTRODUCTION

1.1 Background Information

In 1923 two experimenters, Irving Langmuir and H. Mott-Smith, were investigating some of the phenomena of gas discharges using planar, cylindrical, and spherical collectors, or probes. The probes used by Langmuir and Mott-Smith were biased at some voltage with respect to the anode and the resulting current was measured. The current-voltage characteristic obtained from such a "Langmuir Probe" can be used to determine the electron velocity distribution and the plasma potential with respect to the anode.

Druyvesteyn showed in 1930 that the electron speed-distribution-function could be obtained from the probe I-V characteristic as follows:

$$f(v) = \frac{4}{Ae^2}\frac{m}{}\frac{V_p}{}\frac{d^2 I_p}{d V_p^2}$$

where

$$\frac{1}{2} mv^2 = eV_p$$

A is the collecting area of the probe, m and e are the mass and charge of the electrons, and I_p and V_p are the current and voltage of the probe. Some successful applicatons of the Druyvesteyn Theory to determine the electron speed-distribution-function depend on applying a small a-c potential to the probe. Experimenters have shown that the probe current, including that due to the small a-c potential, could be expanded into an infinite series and that some particular term

of the series was proportional to the second derivative of the I-V characteristic. Various techniques were then used to detect the harmonic term of interest and obtain the speed distribution function.

In 1965 Dr. Robert H. Bond, using planar probe theory, showed that the anistropy of the electron velocity distribution could be obtained using the concept that the directed electron velocity distribution is proportional to the first derivative of the probe current-voltage characteristic. He showed, using a technique that did not require the use of a small a-c potential superimposed on the probe voltage, that the electron velocity distribution in a hot cathode discharge containing either neon or helium was nearly Druyvesteyn.

There has been some controversy over whether the a-c signal superimposed on the probe voltage produces oscillations that prevent the true distribution function from being obtained. Because the experiment performed by Dr. Bond did not involve an a-c signal superimposed on the probe voltage, it would be advantageous to compare results obtained using his methods to those obtained using a small a-c signal.

When a small a-c signal is superimposed on the probe voltage, it can be shown that the rms value of the fundamental frequency component of the probe current is proportional to the first derivative of the I-V characteristic, if the cube of the amplitude of the a-c signal is small compared with the amplitude of the a-c signal. Thus, if it were possible to detect the fundamental component of the probe current and also obtain the distribution function from the first derivative of the

I-V characteristic, one could compare these results with those obtained using Dr. Bond's method and determine if the a-c signal does alter the electron speed-distribution-function.

1.2 Object of This Experiment

In order to perform the experiment described above, it is essential to have a high vacuum system. The construction of such a vacuum system is discussed in this work. Some things considered are gauges, valves, cold traps, sorption traps, vacuum pumps, and the experimental tube. The vacuum system, except for the experimental tube, can be baked at a temperature of 350° C for several days. Pressures in the range of 10^{-7} to 10^{-8} Torr can be obtained with this system.

This thesis also presents two methods for obtaining the derivative of the probe I-V characteristic. The instrumentation of both methods and tests to determine if the instrumentation operates correctly are described. In the first method an operational amplifier is used to differentiate the I-V curve, and in the second method a lock-in amplifier is used to obtain the desired derivative.

II. CONSTRUCTION OF A HIGH VACUUM SYSTEM

Low pressures or high vacuums can be obtained when the following equation is satisfied:

$$\text{Rate of Removal of Gas} \geq \text{Rate of Inflow of Gas}$$

Some of the factors affecting the rate of removal of gas are the vacuum pumps, the diameter of tubing, and the type of cold trap used. Pressures of 10^{-4} mm of mercury can be obtained using a forepump or mechanical pump, but to achieve higher vacuums it is necessary to use a diffusion pump. When using a diffusion pump, which must be exhausted into a mechanical pump to be efficient, pressures of 10^{-11} Torr (1 Torr = 1 mm Hg) can be obtained. The pumping fluid for the forepump is oil and that for a diffusion pump is oil or mercury. The larger the pumps the greater the rate of removal of gas. The diameter of tubing is important in determining the flow of gas out of a system. If the mean free path of a gas molecule is small compared with the diameter of a tube, the flow is described as viscous, but if the mean free path is large compared with the diameter of a tube, the molecules collide with the walls and proceed in a chaotic manner. The flow is then described as molecular flow. Thus, it is important not to use tubing with a very small inner diameter. The mean free path at atmospheric pressure is of the order of 7×10^{-6} cm and it is about 5×10^{3} cm at 10^{-6} Torr. Several types of traps can be used on a vacuum system to

collect vapors. A liquid-nitrogen cold trap is frequently used on vacuum systems, but sometimes it is possible to use an all glass sorption trap in place of the liquid nitrogen cold trap.

Two factors that affect the rate of inflow of gas are leaks and outgassing. There are various methods for detecting leaks and these will not be discussed here. Outgassing is the flow of materials (such as oil and water vapor) out of a surface such as stainless steel or rubber. One way to combat outgassing of a metal or glass system is to bake the entire vacuum system, excluding pumps, at a high temperature for several days.

2.1 The Initial Vacuum System

The initial vacuum station was a Granville-Phillips series 225 ultra-high vacuum pumping station. This system consisted of a forepump, oil diffusion pump, cold trap, and control panel. Figures 2.1, 2.2, and 2.3 show the initial vacuum system. The forepump is a two-stage 21-liter-per-minute electric motor driven rotary pump, and the diffusion pump is a three-stage fractionating pump with a two-inch diameter pumping port. Because of its low vapor pressure and its high resistance to oxidation, Dow Corning type DC 705 oil was used in the diffusion pump. Added to the initial vacuum station by a former graduate student, Edward Price, were three valves, a table with a marinite top to support the experiment, and gauge B as shown in Figure 2.4. Valve A is used as the main gate valve which allows the system pressure to be raised to atmospheric pressure while the pumps are still operating.

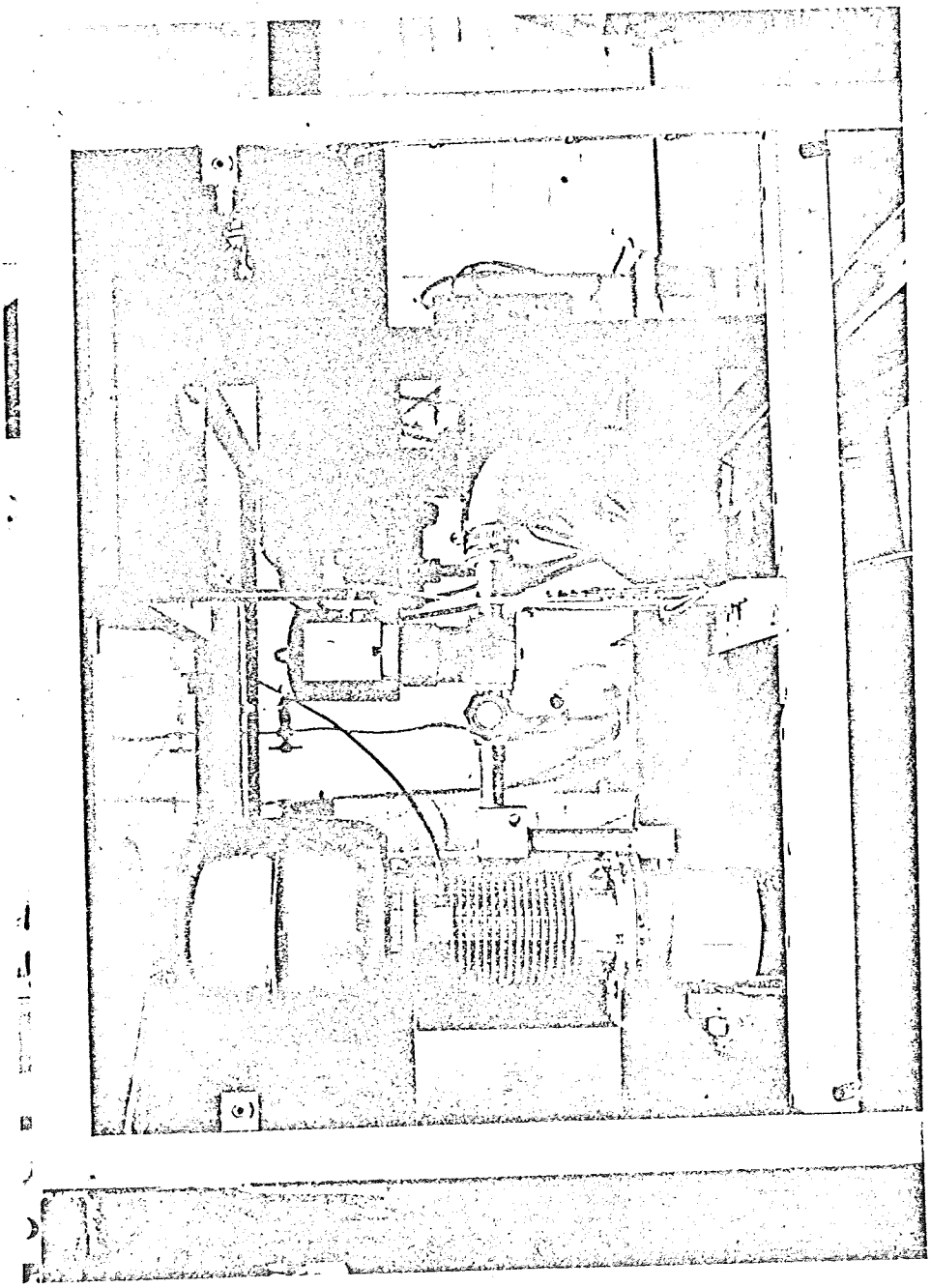

FIGURE 2.1
VIEW OF THE INITIAL VACUUM SYSTEM

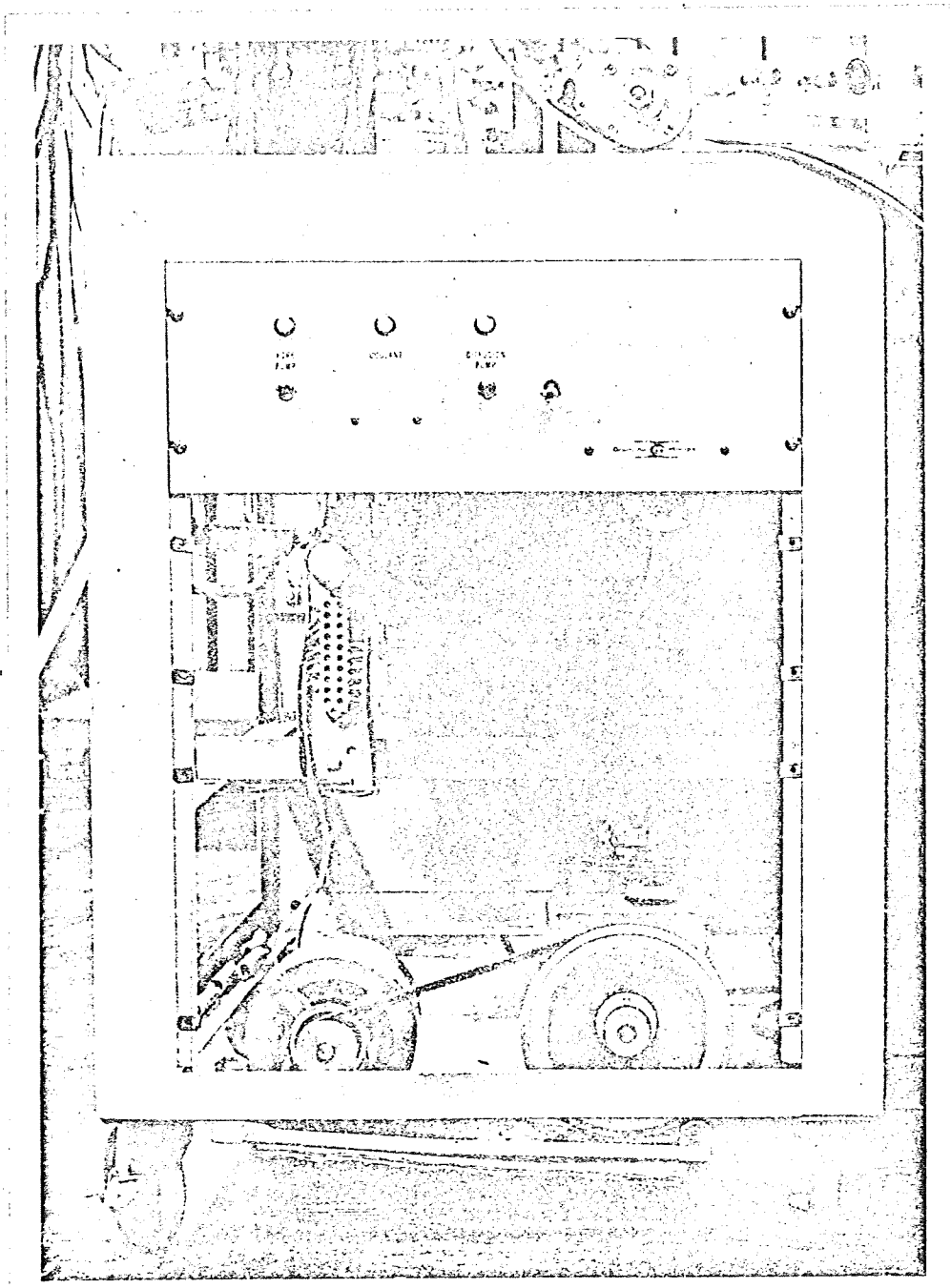

FIGURE 2.2
VIEW OF
THE INITIAL VACUUM SYSTEM

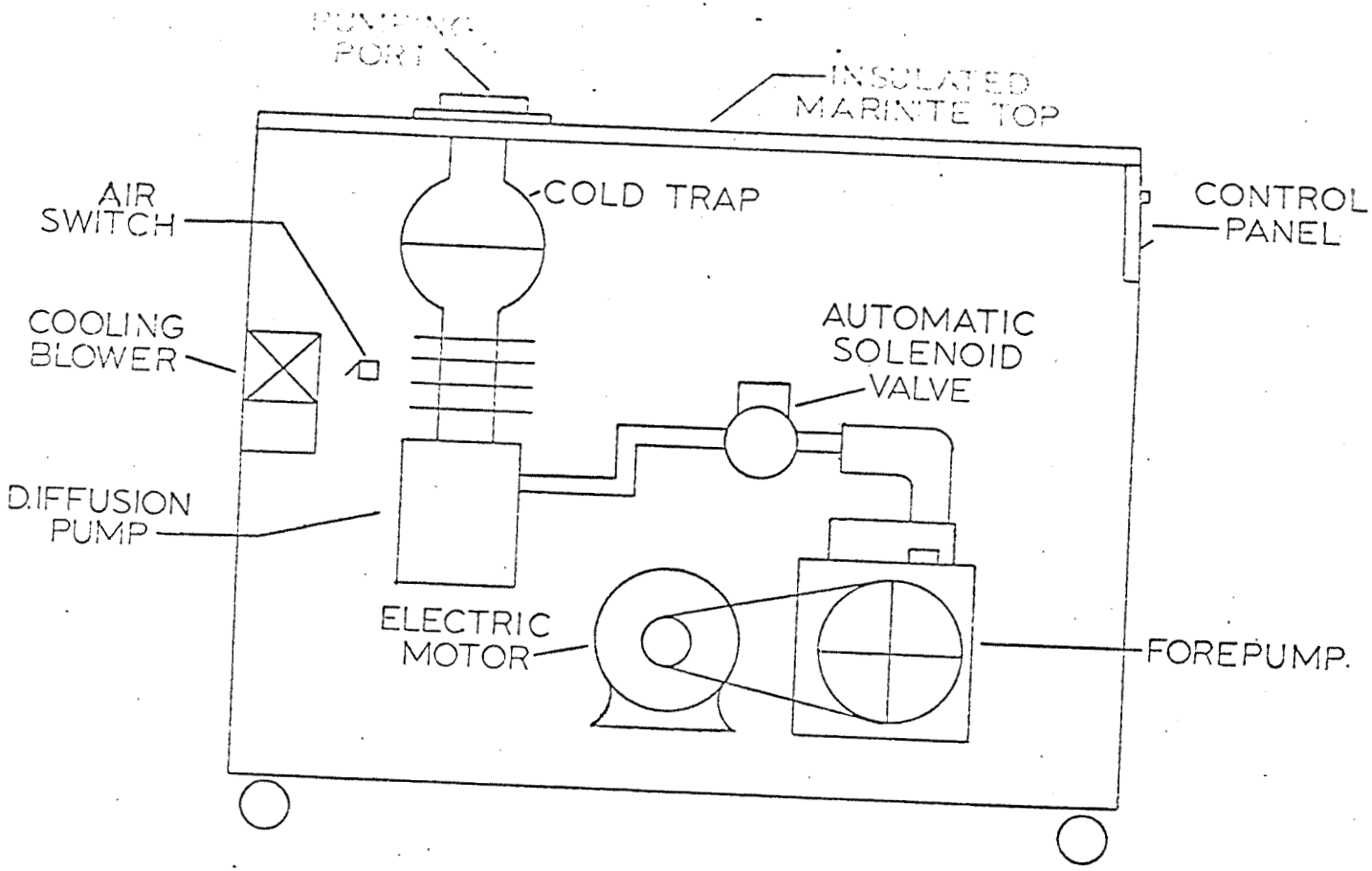

FIGURE 2.3
DIAGRAM OF INITIAL VACUUM SYSTEM

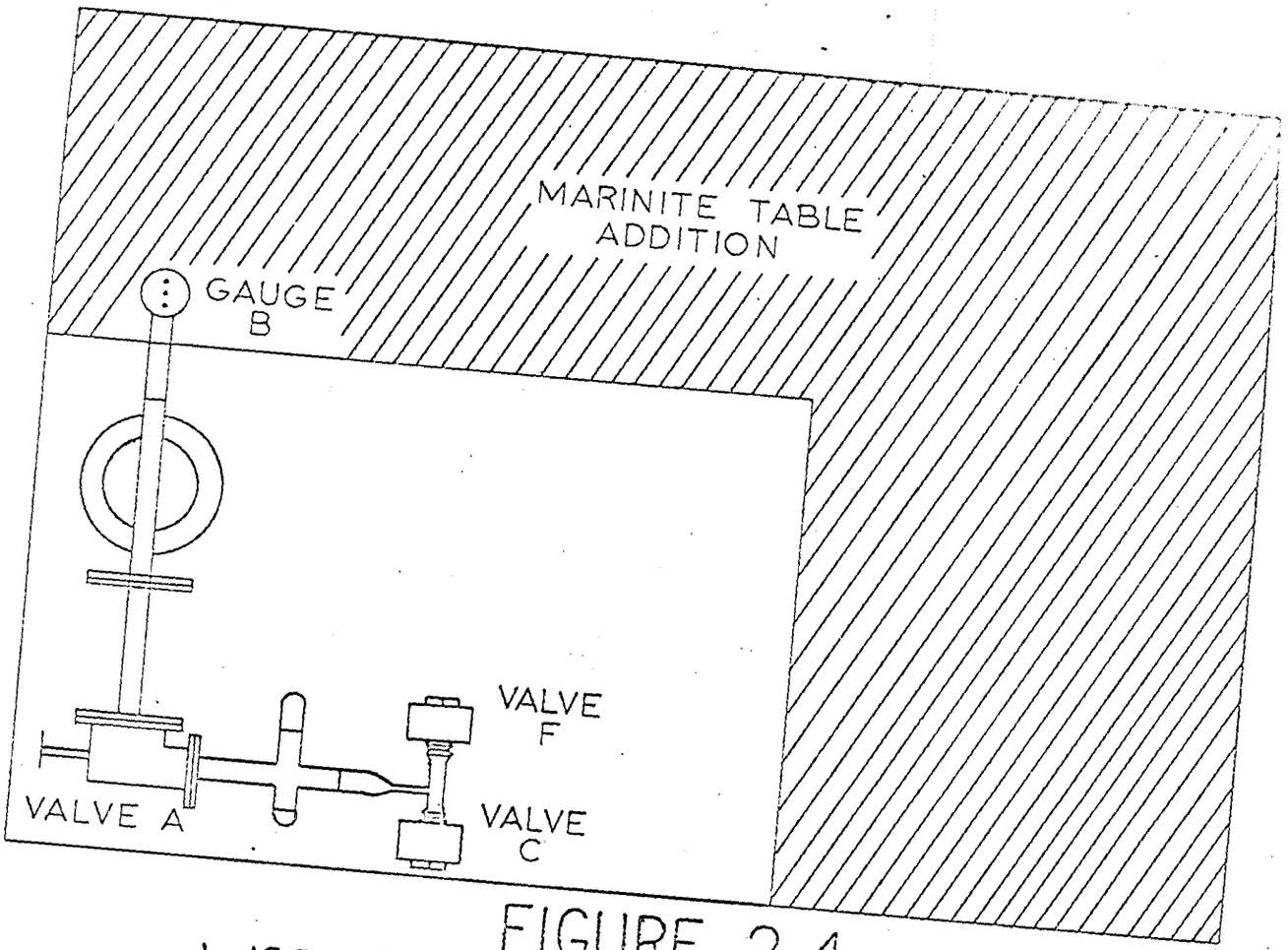

FIGURE 2.4
WORK DONE BY EDWARD PRICE

Valve A is a one-inch Granville-Phillips type L ultra-high vacuum valve. Valve F is used to allow the system to be rough pumped before opening valve A. Valve F is a Granville-Phillips type C ultra-high vacuum valve series 202. Valve C is used to let the gas into the system from the gas manifold. Valve C is the same type as valve F. Gauge B is a Bayard-Alpert ionization gauge, capable of measuring pressures from 10^{-4} to 10^{-9} Torr. The gauge is a Veeco type RG75P.

2.2 All Glass Sorption Trap

The type of trap that was used, to catch the oil that diffuses out of the vacuum pump and the vapors drawn off the system is an all glass sorption trap. A Cryosorb Cold Trap came with the initial vacuum station. This trap uses liquid nitrogen as a coolant. The trap requires refilling every 15 hours; if the trap is allowed to become empty, collected vapors will diffuse back into the system. To circumvent the possibility of having the vacuum system become contaminated in the event the cold trap becomes empty, and to alleviate the problem of obtaining liquid nitrogen and of filling the trap every 15 hours, a new vacuum trap made entirely of glass was built and used. This glass sorption trap, as it is called, was designed by F. B. Haller at the National Bureau of Standards in Boulder, Colorado, in 1964. The trapping agent is Vycor Brand thirsty glass (Corning code 7930). The thirsty glass is a very porous glass which exhibits very good adsorbing properties. This glass is mechanically hard and strong, nondusting, nonflaking, and chemically inert. The glass provides

approximately 250 square meters of internal surface area per gram. The sorption trap is shown in Figure 2.5. The sorption trap was made from five 3 mm thick disks, which are 5 cm in diameter. The body used to support the disks was made of Corning type 7052 glass. The body was paddled around the disks as a means of support. Each disk had a V-shaped slot cut into it so that the pumping speed would not be reduced. The disks were then stacked and the slots were staggered to provide an optically dense baffle through the trap. The trap was connected to metal flanges by means of glass to metal seals, and it was then bolted into the system. After an initial bakeout at 350° C for two days, pressures of 10^{-9} Torr were measured on the system side of the sorption trap with a Bayard Alpert ionization gauge. With the gas manifold and experimental tube on the system, a pressure of 10^{-7} Torr has been maintained on the system side of the sorption trap for several months. This glass sorption trap is easily adapted to a glass or metal system, and it can be mounted in any position that is desired.

2.3 The Gas Manifold

The problem of filling the vacuum system with a gas that will be used during an experiment is considered next. The gas manifold was constructed as shown in Figures 2.6, 2.7, and 2.8. The gas bottles, containing one liter of neon and helium at one atmosphere, were supported on a cardboard subframe and a plywood mainframe. The bottles are sealed and a little tit, as shown in Figure 2.6, must be broken

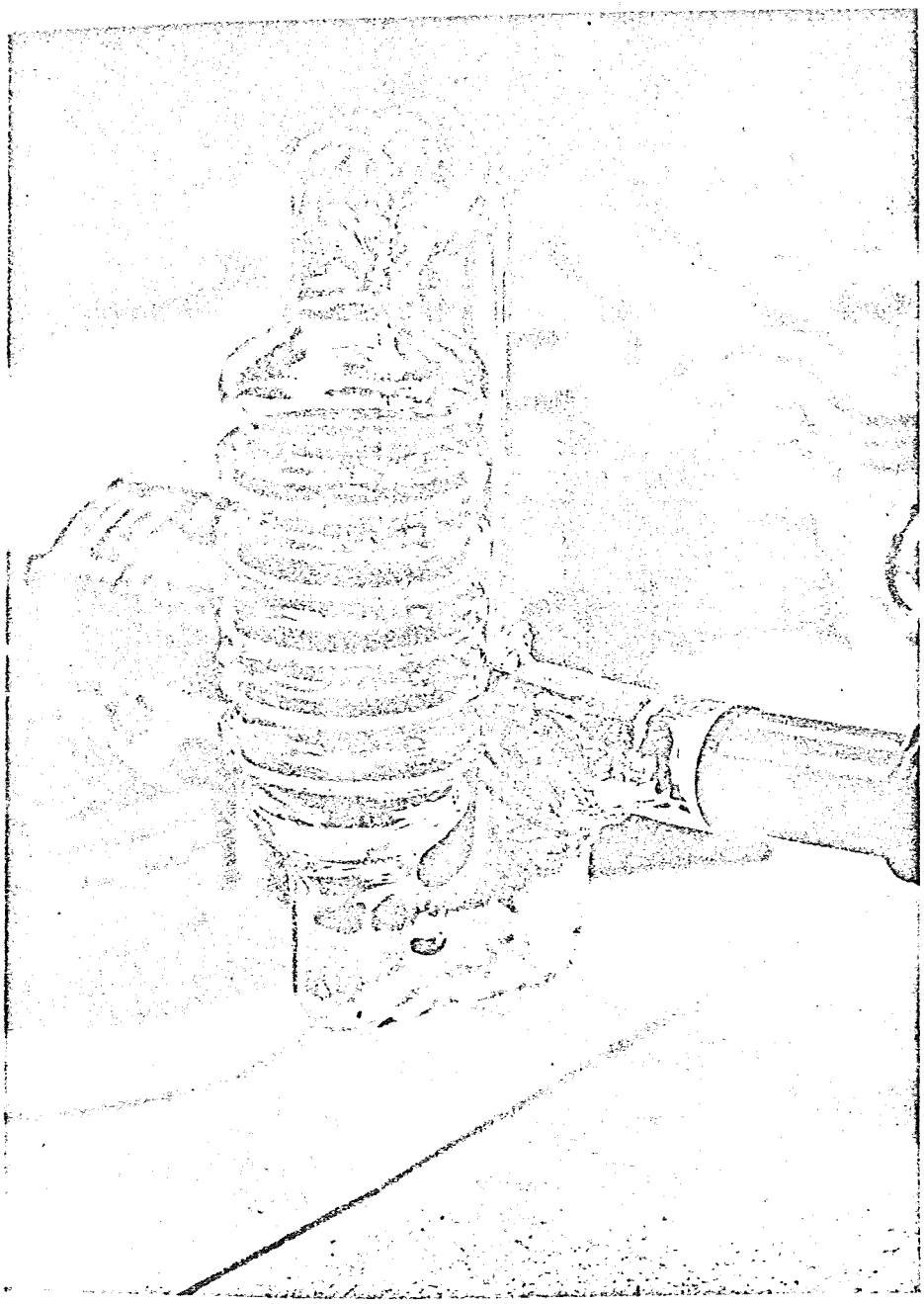

FIGURE 2.5
GLASS SORPTION TRAP

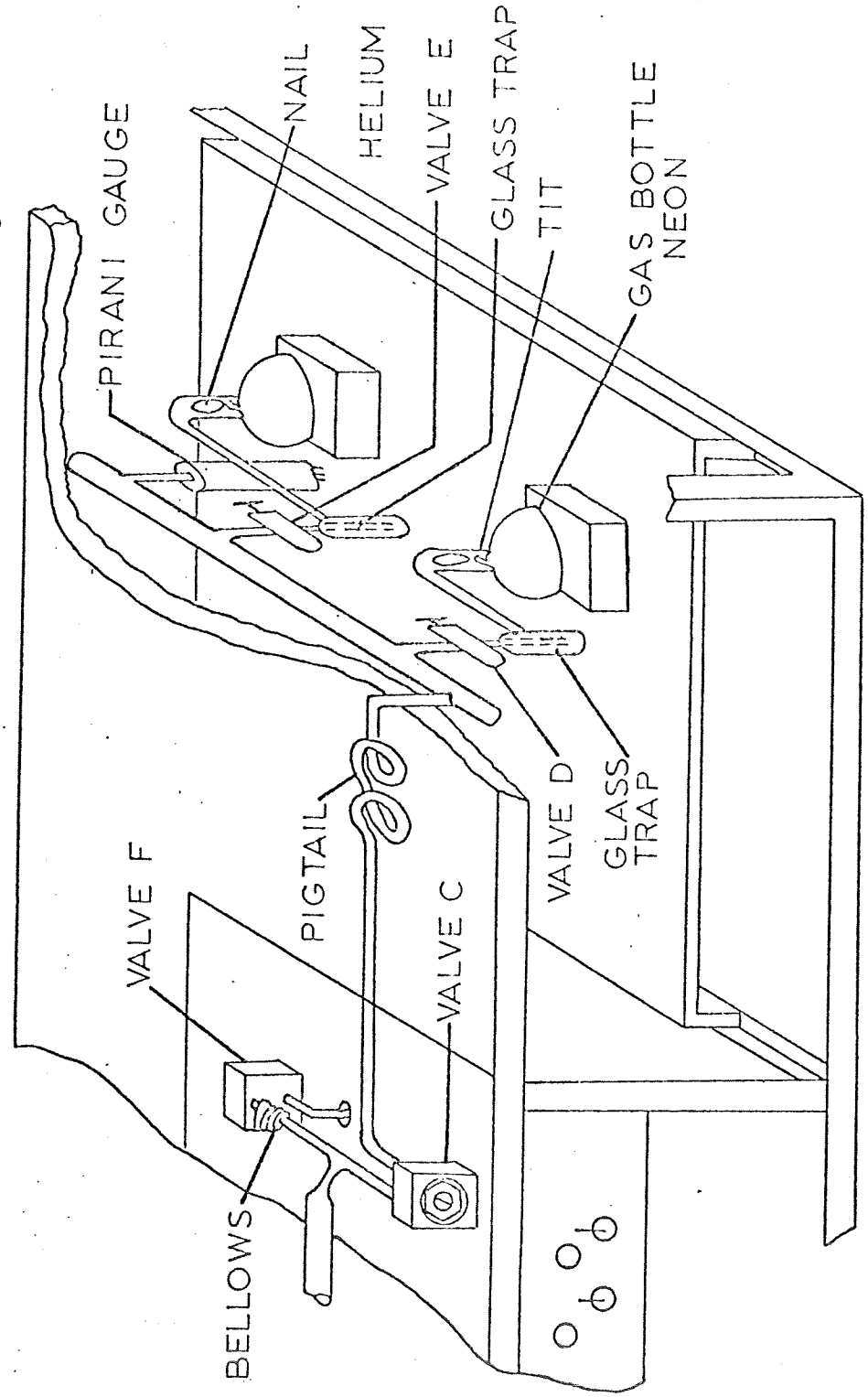

FIGURE 2.6
DIAGRAM OF GAS MANIFOLD

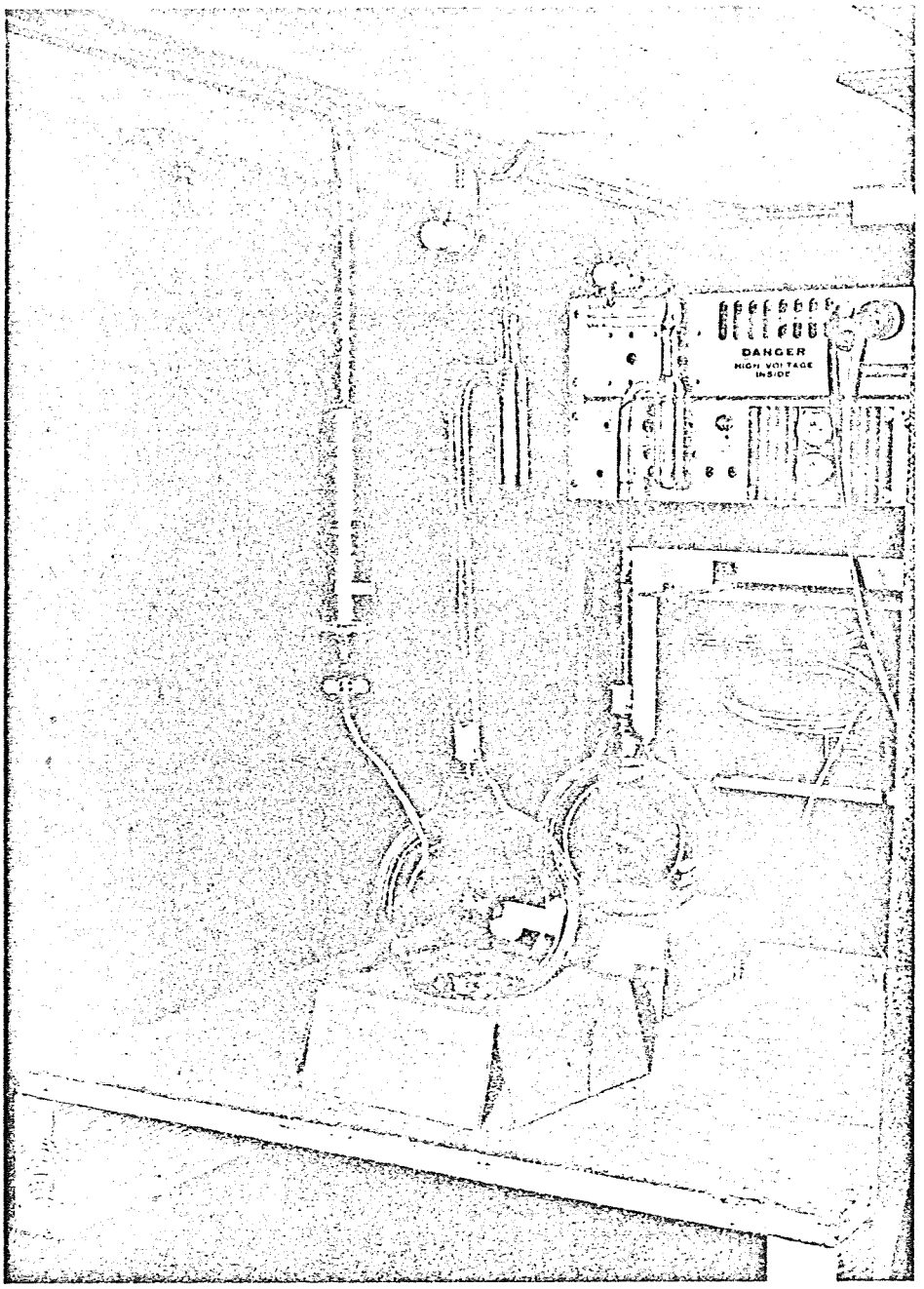

FIGURE 2.7
VIEW OF THE GAS MANIFOLD

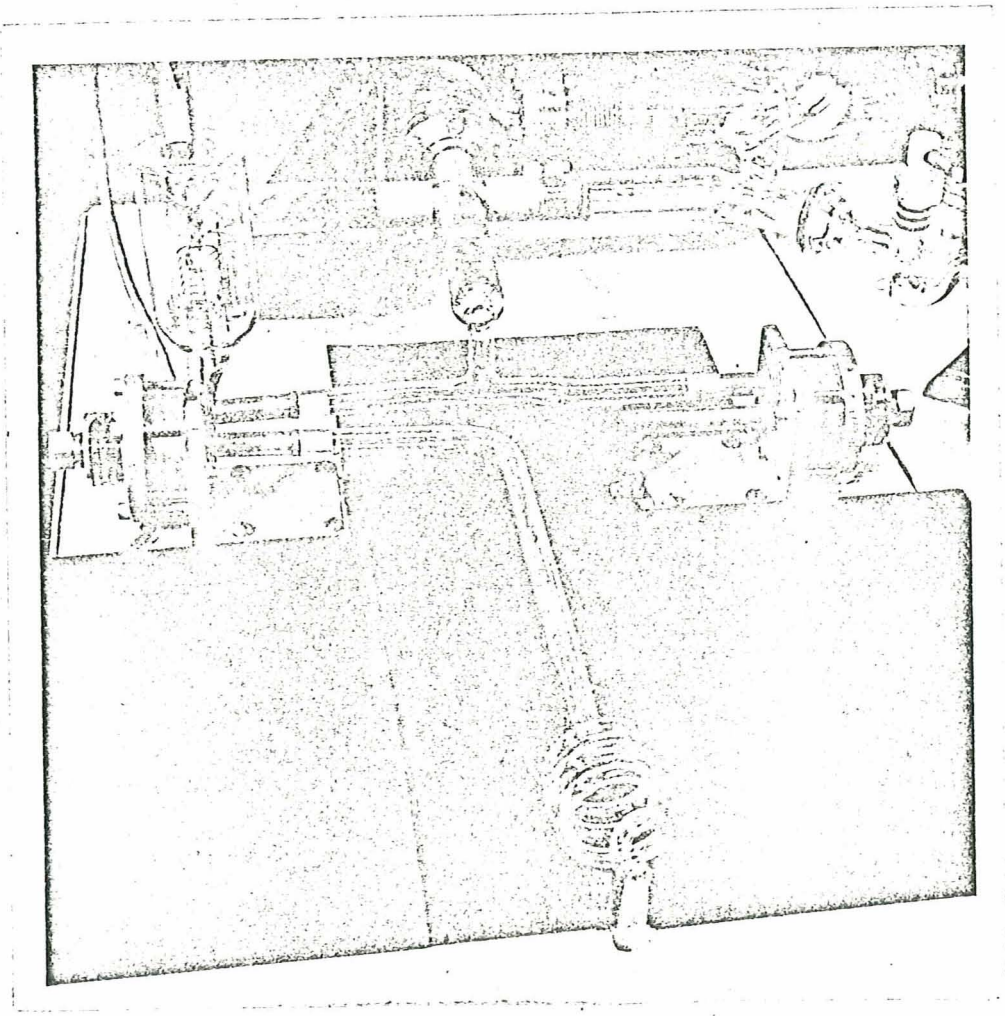

FIGURE 2.8
VIEW OF THE GAS MANIFOLD

to release the gas. A glass enclosed nail, which can be lifted with a magnet, was used to break the seals. Before the tit is broken the gas manifold must be evacuated with valves D and E opened. Then a heat tape was wrapped around the tubing and glass traps, and the temperature was increased to 300° C to help eliminate outgassing. The glass was baked for several days. The valves C, D, and E were closed and the seals broken. Glass traps were placed between the valve and the bottle to catch any glass fragments that would be sucked into the system from the broken seal. These fragments could damage valve seats and prevent them from sealing. The pigtail, shown in Figures 2.6 and 2.8, was used to allow for expansion of glass during the bakeout and for contraction of the bellows on valves C and F when under vacuum. With the gas manifold as shown, the system may be filled to a pressure of 1000 microns several hundred times.

2.4 Gauges for Measurement of Pressure

The range of pressures (10^{-7} to 2 Torr) is so great that one gauge cannot be used to measure the entire range of pressure. A Bayard-Alpert ionization gauge was used to measure the pressure in the range of 10^{-4} to 10^{-10} Torr. This triode tube shown in Figure 2.9 operates as follows. The tube is placed on the vacuum system, and the filament is heated so that the emission is temperature limited; the grid is at a positive potential with respect to the cathode, and the collector is at a slight negative potential with respect to the cathode. When the tube is operating, the grid will pull a stream of electrons

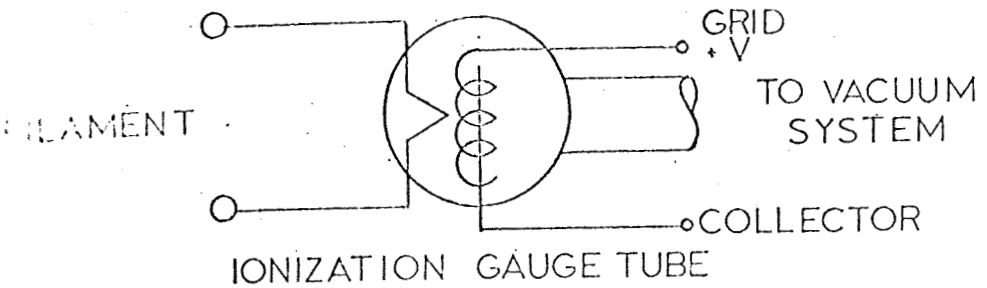

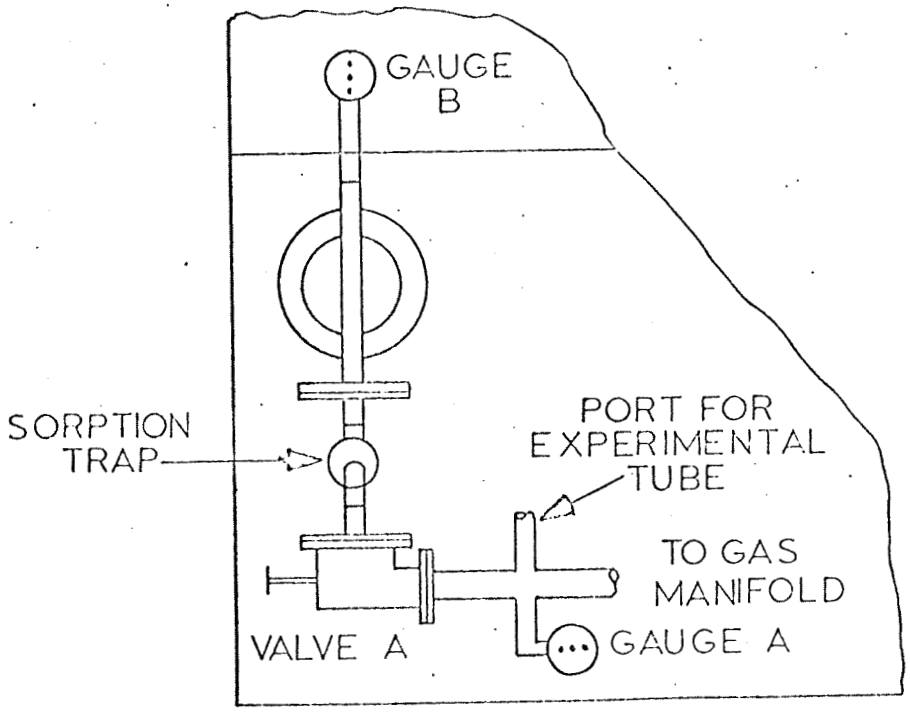

FIGURE 2.9
DIAGRAM AND PLACEMENT OF
IONIZATION GAUGE TUBES

from the filament. Most of these electrons will pass through the grid, and since the collector is at a negative potential, it will repel the electrons, sending them back toward the filament. Some of the electrons will make many oscillations past the grid before being attracted to it. As the electrons travel between the grid and collector, some will ionize gas molecules that might be present, and the positive ions will be collected by the collector, which is negative with respect to the grid. A measure of the ion current is a measure of the pressure. Figure 2.9 shows the location of the Bayard-Alpert gauges. Gauges A and B are the same type ionization gauge. Gauge A enables the experimenter to measure the pressure on the system side of valve A, and gauge B allows for measurement of the pressure on the pump side of valve A. The ionization gauge controller is shown in the top of Figure 2.10. It is a Granville-Phillips Series 236 model 02 controller, and it is capable of indicating pressures from atmosphere to 10^{-11} Torr.

A Pirani vacuum gauge can be used to measure the pressure in the range of 2 Torr to 10^{-4} Torr. The Pirani gauge is a resistance element that is temperature sensitive. A small amount of power, which is maintained constant, is applied to the resistance element, and as gas molecules hit the element and absorb energy, the temperature will change and cause the resistance to change. The change in resistance can be related to a change in pressure. One Pirani gauge was used on this vacuum system. It was located on the main line of the gas manifold as shown in Figure 2.6. On this vacuum system the Pirani gauge was used

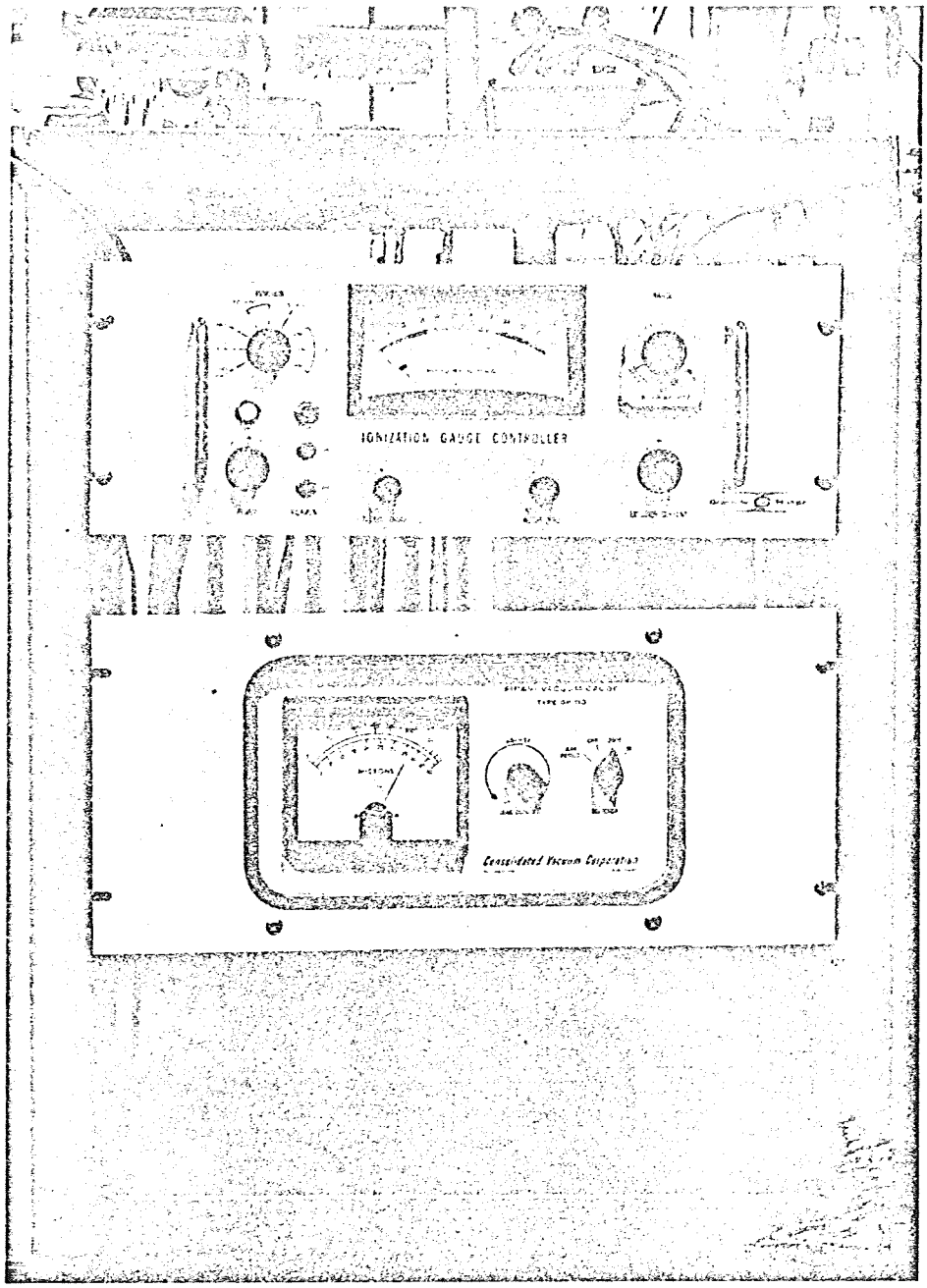

FIGURE 2.10
IONIZATION GAUGE CONTROLLER AND
PIRANI VACUUM GAUGE CONTROLLER

to measure pressures from 100 microns to 1500 microns. The Pirani gauge controller with its indicating meter is shown in the bottom of Figure 2.10. The Pirani gauge is used to monitor the pressure in the vacuum system during actual experiments.

2.5 The Experimental Tube

The experimental tube is shown in Figure 2.12 with a cold-cathode discharge in it. The tube is 110 cm long and 5 cm in diameter, and the spacing between the anode and cathode is 80 cm. The tube had previously been used for studying gas discharges. It had a movable cathode assembly which used a viton "O" ring seal. The movable cathode assembly was removed, and a fixed cathode was assembled and mounted on the tube. The cathode was made from tungsten wire, and it was supported by two molybdenum rods. The molybdenum rods were welded to tungsten feedthroughs on a glass press. A heat shield was necessary to prevent the glass around the cathode from becoming hot enough to sag or melt. The heat shield was made of stainless steel and supported by a molybdenum rod. At the anode end of the tube there were several ports which would allow the experimenter to probe the positive column of the gas discharge. The ports not being used by the probe were sealed with glass rods that were etched to fit with hydrofluoric acid. Also an "O" ring sealed valve was located at the anode end of the tube. This valve allowed the experimenter to isolate the experiment from the rest of the system. After complete construction of the tube, it was washed with Alconox, a detergent, and then the tungsten feedthroughs and cathode assembly were

cleaned by electrolytic action using a sodium hydroxide solution as the electrolyte. The tungsten to be cleaned was one electrode, and a piece of stainless steel was the other electrode. The tube was then cleaned with Alconox, and washed with a solution of hydrochloric acid. The hydrochloric acid was used to clean the stainless steel anode and heat shield. The tube was then washed with Alconox and rinsed with distilled water. The tube was allowed to dry while the rest of the vacuum system was being baked. The tube itself could not be baked because of the "0" ring seals, in the probe ports and in the valve on the anode end of the tube. These "0" rings cannot be raised to high temperatures.

The oven used for baking out the system was made from steel rods and zonolite glass fiber insulation covered with aluminum foil. Electric stove elements were used as a source of heat, and a -5 to 400° C thermometer was used to monitor the temperature.

After the system cooled to room temperature the experimental tube was mounted to it by means of a 35/20 ball joint with an "0" ring seal. The entire system was then brought to a low pressure. The experimental tube was wrapped with heat tape and the temperature was raised to 300° C being careful not to let the "0" ring seals get over heated. After several days the tube was allowed to cool to room temperature. The system was then ready to be used.

2.6 Circuit and Equipment Used to Fire the Discharge

The circuit used to fire the discharge is shown in Figure 2.11.

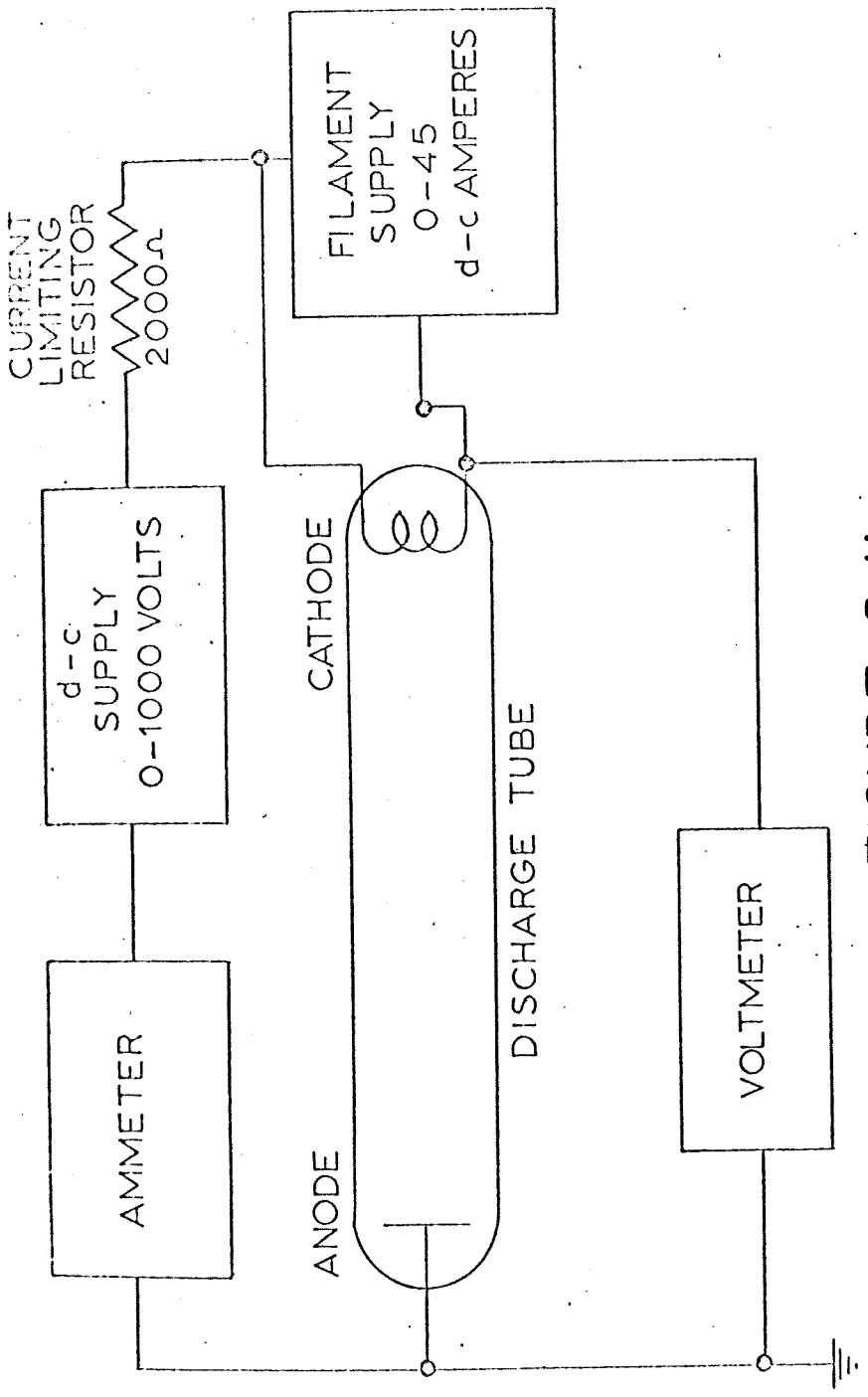

FIGURE 2.11
CIRCUIT TO FIRE DISCHARGE

The filament supply was a Western Electric Flotrol Model U1200B. The filament supply was varied by varying the input a-c voltage. The d-c supply voltage used to fire the discharge was a Kepco model 605 (0-600V) in series with a Heathkit Model PS-4(0-400V). A current limiting resistor was inserted into the circuit to limit the tube current when the discharge initially fires. A Hewlett Packard Model 427A voltmeter measured the tube voltage. A Pyro Micro-Optical Pyrometer, serial number M5341, was used to measure the cathode temperature so that it could be adjusted for correct emission. The cathode temperature was approximately 2143° K which corresponded to a d-c filament current of 43 amperes. A blower kept the glass around the cathode cool.

An existing probe was inserted into a port on the tube, and the output was monitored with an oscilloscope. The oscilloscope determined whether the discharge was oscillating. The discharge tube was filled with neon to a pressure of 1000 microns from the gas manifold. With the filament current at 43 amperes, approximately nine hundred volts were required across the tube to fire the discharge. The voltage was reduced to 350 volts when the gas was ionized. The discharge was initially a purple color, indicating "dirt" in the tube. Some of this contamination is caused by electrons knocking molecules off surfaces inside the tube. After the discharge tube was filled several times and fired, the color became a bright orange as shown in Figure 2.12. The orange color indicated a clean discharge.

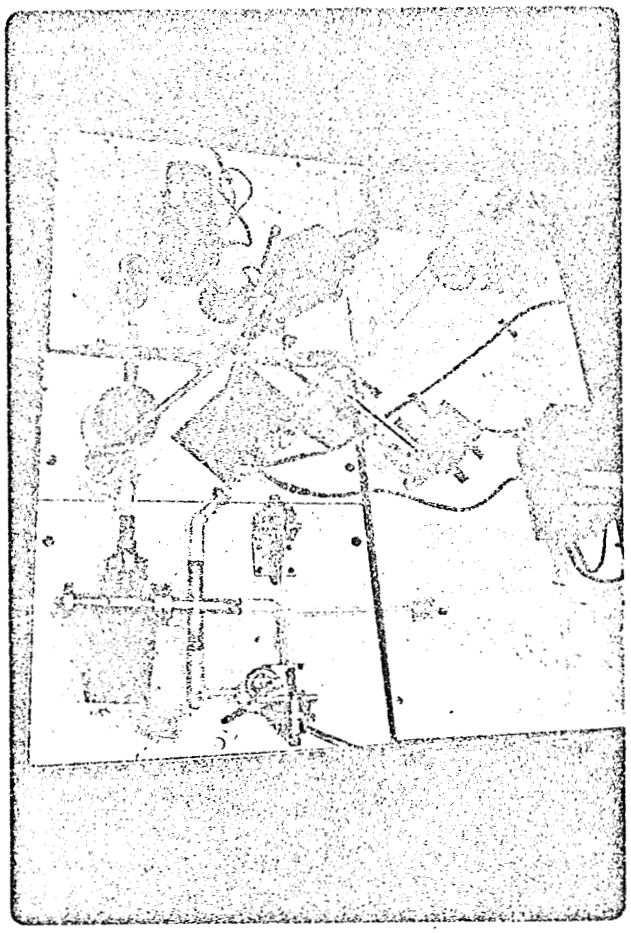

FIGURE 2.12

DISCHARGE TUBE
WITH A COLD CATHODE DISCHARGE

Several parameters were found to affect whether a quiet discharge could be obtained. They were contamination in the tube, filament current, pressure, and tube voltage. A quiet discharge was obtained with a pressure of 250 microns, filament current of 43 amperes, tube voltage of 325 volts, and tube current of 50 milliamperes. Through continued use of the discharge tube, ions sputtered away some of the stainless steel of the heat shield. The stainless steel molecules were collected on the glass tube. This can be seen as the darkened end of the discharge tube in Figure 2.12.

A pressure of 1×10^{-7} Torr was measured after the system was pumped down. The vacuum system has been operating continuously since June, 1968. Figures 2.13, 2.14, and 2.15 show different views of the vacuum system.

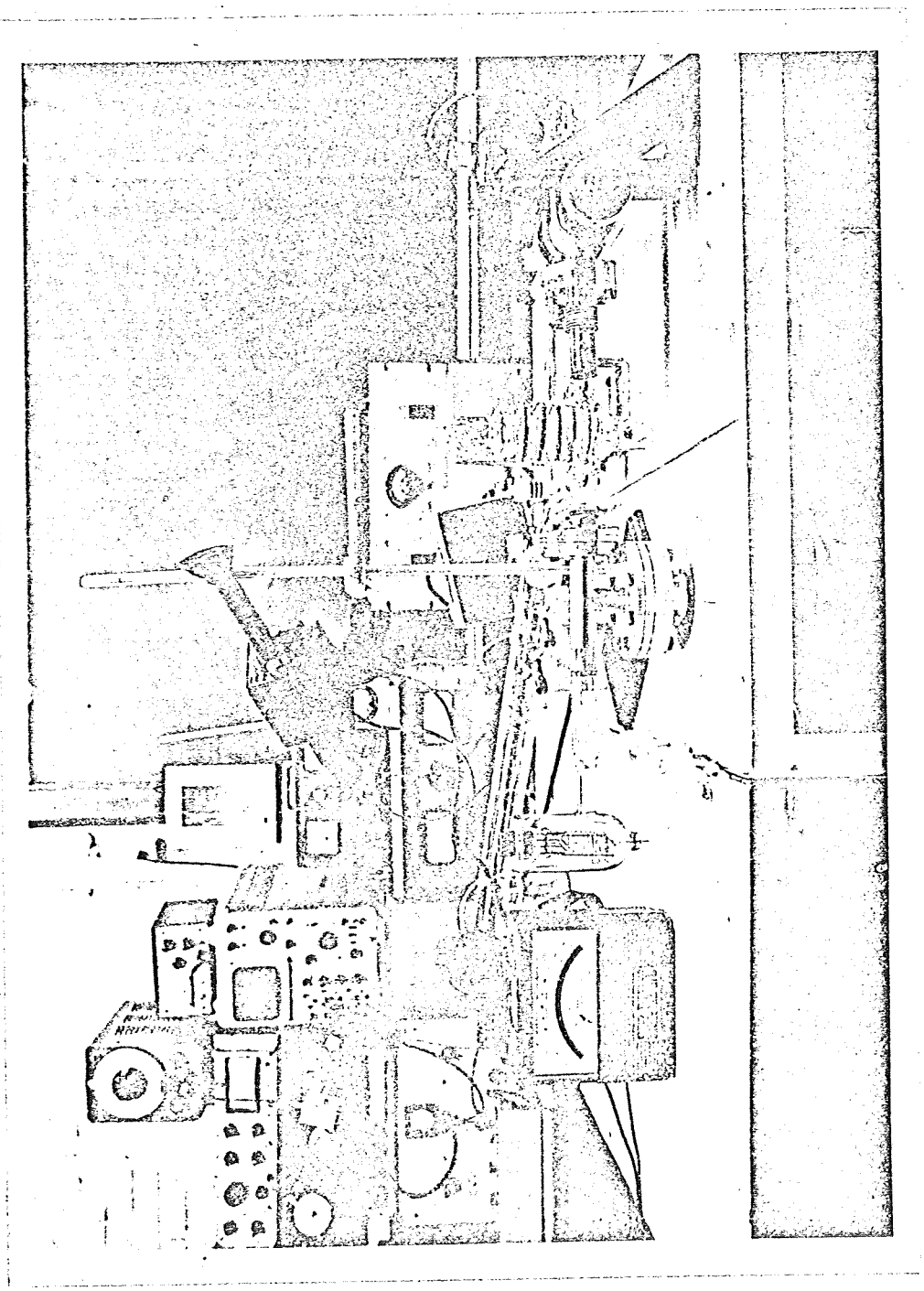

FIGURE 2.13
VIEW OF THE VACUUM SYSTEM

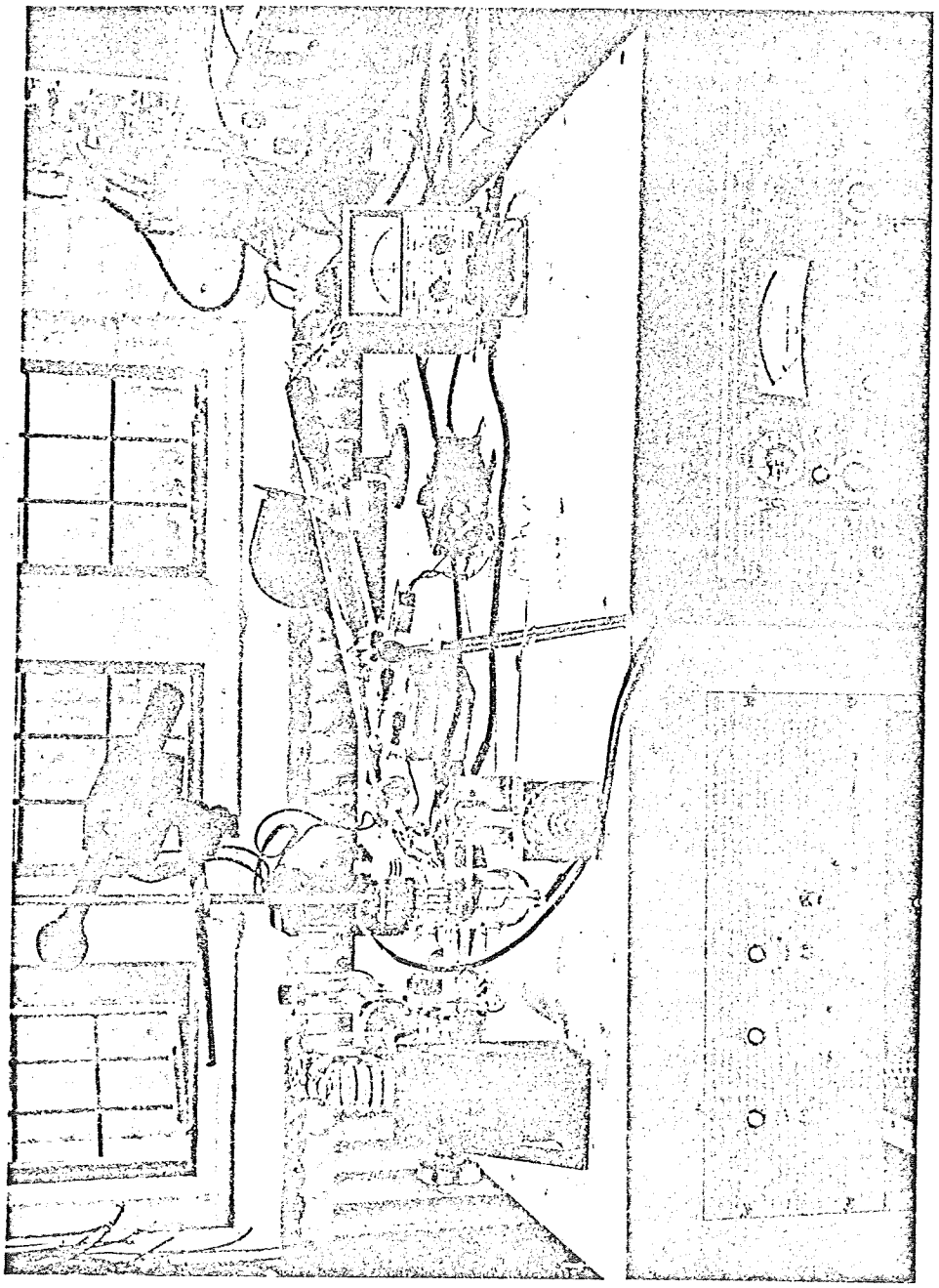

FIGURE 2.14
VIEW OF THE VACUUM SYSTEM

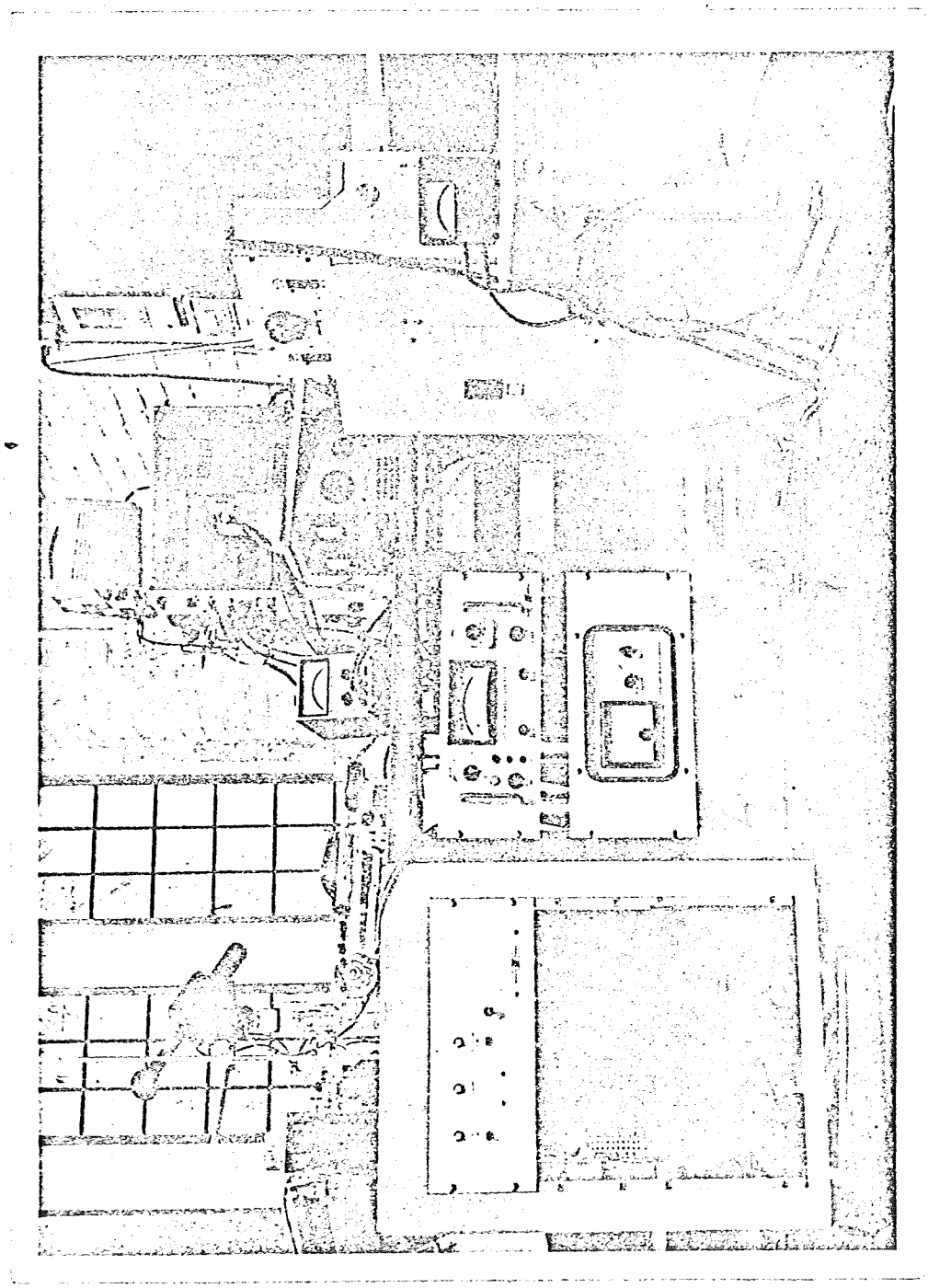

FIGURE 2.15
VIEW OF THE VACUUM SYSTEM

III. THEORY AND INSTRUMENTATION

There are several ways to obtain the first derivative of some function. The two methods that will be discussed here are the use of an operational amplifier as the differentiator and the use of a lock-in amplifier to obtain the derivative of the function. It is known that the signal to be differentiated is the current-voltage characteristic of a Langmuir Probe. The general shape of the I-V characteristic is shown in the Figure 3.1, below.

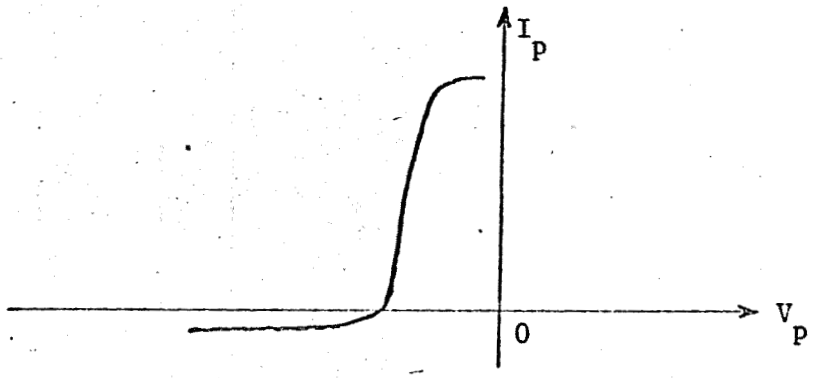

←Probe Voltage Relative to Anode→

Figure 3.1

I-V Characteristic

3.1 The Operational Amplifier Method

A block diagram of a differentiator employing an operational amplifier is shown in Figure 3.2. The Probe is biased at a negative potential and swept linearly in time at a frequency of 0.1 Hz by a triangular-wave generator. The probe current is determined by measuring the voltage across a sensing resistor.

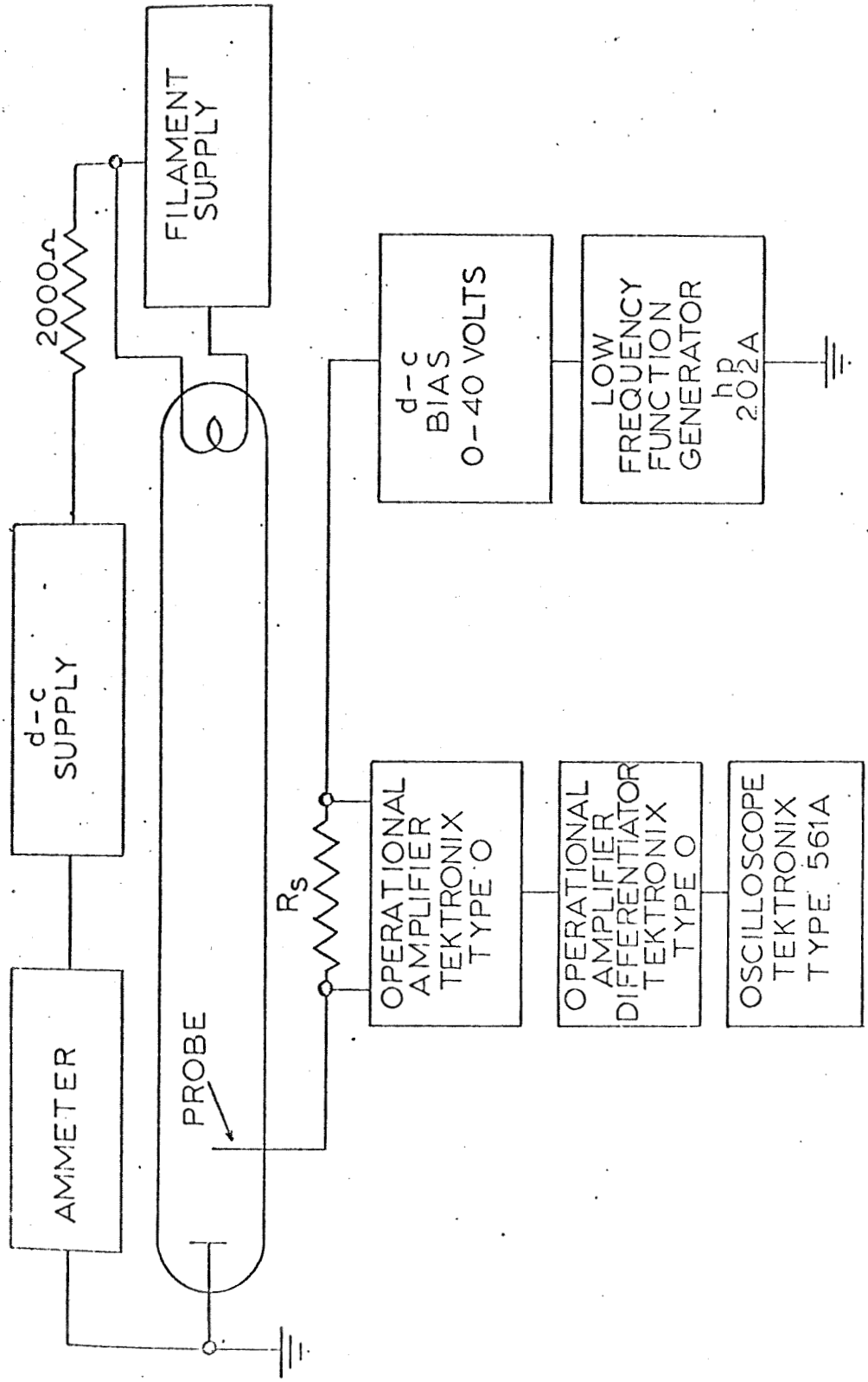

FIGURE 3.2
OPERATIONAL AMPLIFIER SET UP

The amplifier used is an operational amplifier with a gain (-B) equal to the negative of the ratio of the feedback resistance to the resistance in series with the input.

The differentiator has a gain (-D) determined by the negative of the product of the feedback resistance and the capacitance in series with the input.

A low-frequency function generator is used to supply the triangular voltage waveform, and a d-c supply is used for the negative bias potential.

The output of the differentiator can be seen on an oscilloscope or plotted by an X-Y recorder.

Since the output of the differentiator is some constant times the derivative of the probe current with respect to time, it is necessary to show how this is related to the derivative of probe current with respect to probe voltage.

The voltage V_s across the sensing resistor is:

$$V_s = R_s I_p \tag{3.1.1}$$

The voltage out of the differentiator is therefore:

$$V_o = +BD \frac{dV_s}{dt} = +BDR_s \frac{dI_p}{dt} \tag{3.1.2}$$

Now if we consider one quarter of a cycle of the triangular voltage waveform starting at t = 0, we see that the triangular voltage is:

$$V_{TRI} = K_1 t \text{ where:} \tag{3.1.3}$$

$$K_1 = \frac{4(\text{Peak Value of } V_{TR1})}{T} \tag{3.1.4}$$

The probe voltage with respect to the anode is:

$$V_p = V_{TR1} + V_{DC} = K_1 t - K_2 \tag{3.1.5}$$

The derivative of V_p is:

$$\frac{dV_p}{dt} = K_1 \tag{3.1.6}$$

and

$$\frac{dI_p}{dt} = \frac{dI_p}{dV_p}\frac{dV_p}{dt} \tag{3.1.7}$$

On substituting (3.1.6) into (3.1.7), we have:

$$\frac{dI_p}{dt} = K_1 \frac{dI_p}{dV_p} \tag{3.1.8}$$

Substituting (3.1.8) into (3.1.2) gives:

$$V_o = +BDR_s K_1 \frac{dI_p}{dV_p} \tag{3.1.9}$$

Solving for the derivative of I_p with respect to V_p yields:

$$\frac{dI_p}{dV_p} = + \frac{V_o}{BDR_s K_1} \tag{3.1.10}$$

Thus, we see that the output of the differentiator multiplied by a constant is equal to the desired derivative.

3.2 The Lock-In Amplifier Method

A block diagram for measurement of dI_p/dV_p using a lock-in amplifier is shown in Figure 3.3. The d-c bias, low-frequency function generator, and the operational amplifier are the same as discussed in Section 3.1. An audio oscillator is used as the source of the a-c signal.

R_1 and R_2 serve as a voltage divider to adjust the amplitude of the a-c signal. A small a-c signal is needed so that an accurate derivative curve can be obtained. Also, the reference signal to the lock-in amplifier is fed through a one-to-one audio transformer to isolate the audio oscillator and lock-in amplifier. R_3 and R_4 serve as a voltage divider so that the proper reference signal can be obtained. The lock-in amplifier is a type 121 made by Princeton Applied Research Corporation.

As can be seen from Figure 3.3 the probe voltage is the sum of the triangular voltage from the low-frequency function generator, the a-c voltage from the audio oscillator, and a d-c bias voltage. The probe voltage can be written as follows:

$$V_p = V + E \cos \omega t \quad \text{where} \tag{3.2.1}$$

ω = angular frequency of a-c signal

Then the probe current is some function of the probe voltage and may be expressed as:

$$I_p = f(V_p) = f(V + E \cos \omega t) \tag{3.2.2}$$

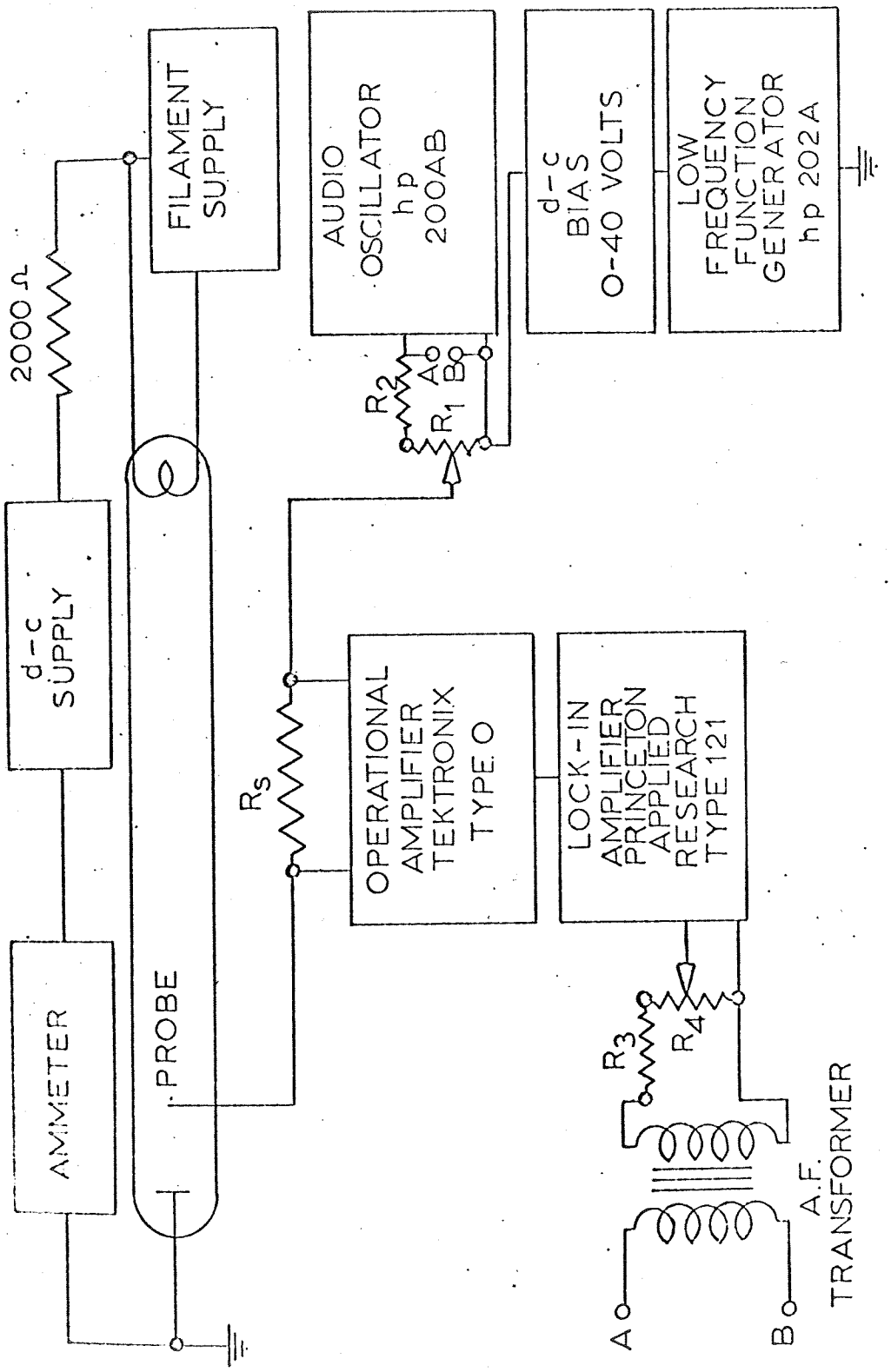

FIGURE 3.3
LOCK-IN AMPLIFIER SET UP

Now if $f(V_p)$ is expanded about V into a Taylor series in powers of E cos ωt, the probe current becomes:

$$I_p = f(V_p) = f(V) + \frac{E \cos \omega t}{1!} f'(V) + \frac{(E \cos \omega t)^2}{2!} f''(V)$$

$$+ \frac{(E \cos \omega t)^3}{3!} f'''(V) + \ldots + \frac{(E \cos \omega t)^n}{n!} f^n(V) \qquad (3.2.3)$$

On expanding and collecting terms we obtain:

$$I_p = (f(V) + \frac{E^2}{4} f''(V) + \frac{E^4}{64} f''''(V) + \ldots) +$$

$$(Ef'(V) + \frac{E^3}{8} f'''(V) + \ldots)\cos \omega t +$$

$$(\frac{E^2}{4} f''(V) + \frac{E^4}{48} f''''(V) + \ldots)\cos 2\omega t$$

$$+ \ldots \qquad (3.2.4)$$

If it is possible to detect only the fundamental-frequency component of I_p and if $E^3/8 << E$, then it can be seen that the first derivative of the probe current with respect to probe voltage is proportional to the magnitude of the fundamental frequency component of I_p.

Referring to Figure 3.3, the voltage developed across the sensing resistor is $I_p R_s$. This signal is fed into an operational amplifier with a gain -B. The output of the amplifier is thus $-BI_p R_s$. The signal is then fed into a lock-in amplifier. The lock-in amplifier is a precision detector. A reference signal at the same frequency as the signal to be detected is fed into the reference channel of the lock-in amplifier.

A simplified block diagram of the lock-in amplifier is shown in Figure 3.4. The signal is coupled to a tuned amplifier that passes a band of frequencies centered about the frequency selected on the front-panel frequency-dial. The actual bandwidth of the amplifier is a function of the selected Q. The output of the tuned amplifier is applied along with the reference signal to the Phase Sensitive Demodulator (Mixer). Here synchronous demodulation is employed to convert the a-c signal to a proportional d-c signal. The a-c fluctuations in the d-c level at the output of the mixer are due to noise and other frequency components. The signal is then amplified. The noise fluctuations are reduced to an insignificant level by passing through a d-c amplifier. The frequency response of the d-c amplifier is determined by the setting of a front-panel Time Constant Switch. The mixer and d-c amplifier combination can be thought of as a correlator performing the function of cross correlation of the input signal and reference signal. The time constant controls the period of integration. If fluctuation appears at the output of the lock-in amplifier the time constant is increased; thus, increasing the integration time and averaging out the frequencies not at the reference frequency. The time constant is set by observing the panel meter and increasing the time constant until a satisfactory compromise between the suppression of noise and the speed of response is reached. Because the lock-in amplifier is detecting the first harmonic of the probe current, its output is equal to a constant times the derivative of I_p with respect to V_p.

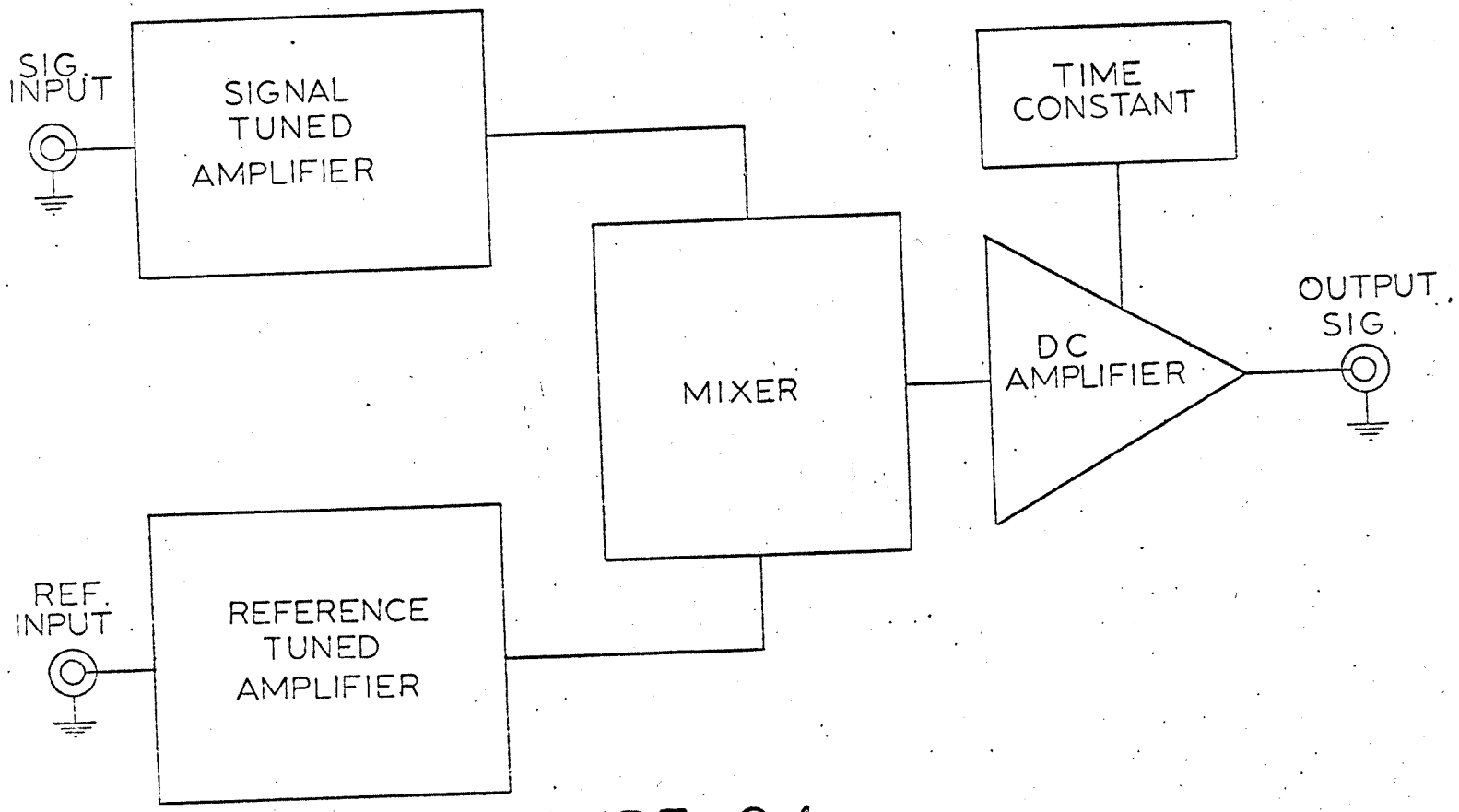

FIGURE 3.4
SIMPLIFIED
BLOCK DIAGRAM OF LOCK-IN AMPLIFIER

IV. EXPERIMENTAL PROCEDURE

Since a plot of the current-voltage characteristic for a Langmuir Probe is desired when making probe studies, one can think of the I-V plot as a measure of the variable resistance of the discharge. Each point along the curve represents some value of resistance. One possible way to check the instrumentation and see that it is operating correctly, is to replace the probe with a fixed resistor and to calculate the value of the sensing resistor from output voltage signals. Resistance calculations can be used to check the instrumentation using either the lock-in amplifier or the operational amplifier as a differentiator. Figure 4.1 shows the equipment used in these tests.

4.1 The Operational Amplifier Method

Figure 4.2 shows the experimental set up used to test the instrumentation for the operational amplifier differentiator method. Because the derivative of the d-c voltage is zero, it is only necessary to consider the triangular voltage across R_s in the calculations. The voltage developed across R_s is:

$$V_s = \frac{R_s V_{TR1}}{R_s + R_F} \tag{4.1.1}$$

If $R_s << R_F$, the approximation can be made that:

$$V_s \approx \frac{R_s V_{TR1}}{R_F} \tag{4.1.2}$$

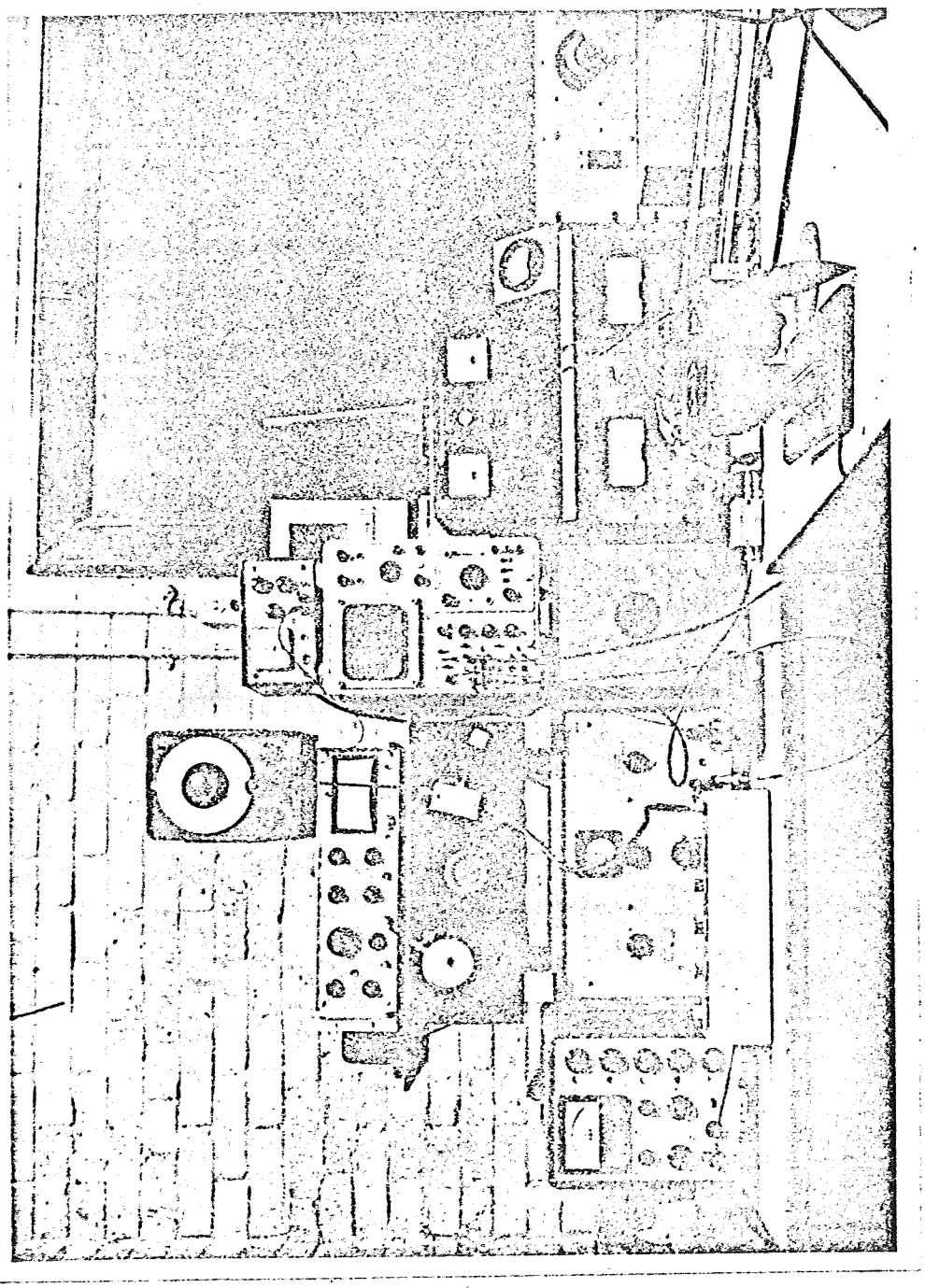

FIGURE 4.1
VIEW OF TEST SET UP

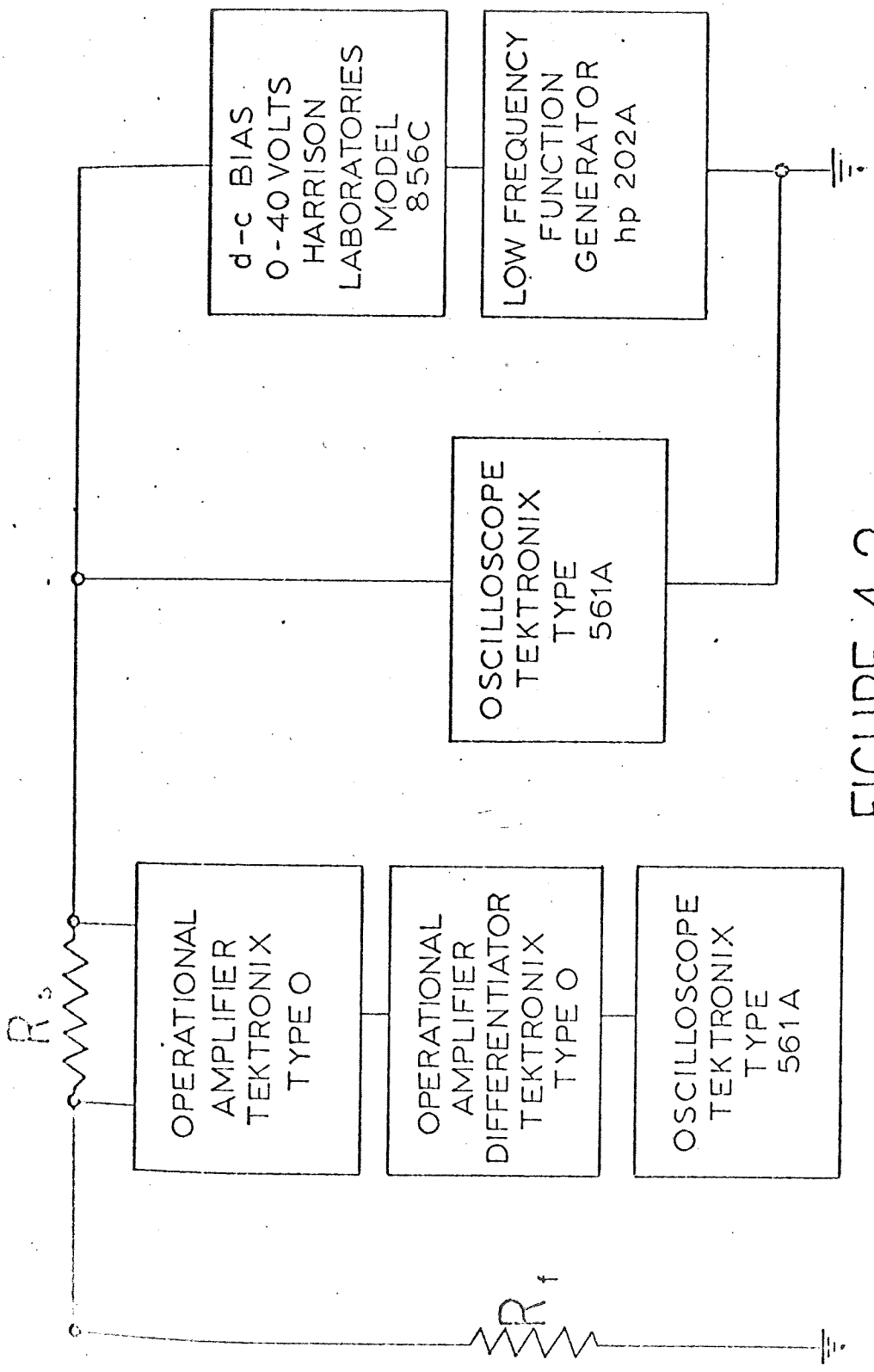

FIGURE 4.2
TEST SETUP USING
OPERATIONAL AMPLIFIER DIFFERENTIATOR

The output of the operational amplifier with a gain of (-B) is:

$$V_s' \approx - \frac{B R_s V_{TR1}}{R_F} \tag{4.1.3}$$

Since the output of the differentiator is (-RC) times the derivative of the input voltage, the differentiator output will be:

$$V_o = \frac{d}{dt} V_s' = \frac{B R_s RC}{R_F} \frac{d}{dt} V_{TR1} \tag{4.1.4}$$

The triangular voltage can be expressed as

$$V_{TR1} = K_1 t \quad o < t < T/4 \tag{4.1.5}$$

K_1 is the slope of the triangular wave form and is equal to:

$$K_1 = \frac{4(\text{Peak Value of } V_{TR1})}{T} \tag{4.1.6}$$

Thus, the derivative of V_{TR1} with respect to time is equal to K_1, and when K_1 is substituted into Equation 4.1.4, we have

$$V_o = \frac{K_1 B R_s RC}{R_F} \tag{4.1.7}$$

Thus, if we assume that B, R, C, and K_1 are known constants, then it is possible to determine R_F or R_s if the other is known, and the output voltage of the differentiator can be measured.

A test was performed using the set up shown in Figure 4.2. The value of R_F was set equal to 15 K Ω and the value of R_s was varied from 20 to 50 Ω. Thus, the approximation that $R_s << R_F$ is valid. The d-c

supply was set at -20 volts and the low-frequency function generator was set approximately to its maximum value of 39 volts. The amplitude of the triangular voltage was measured using a Tektronix oscilloscope type 561A. The frequency of the triangular voltage was set at 0.1 Hz. Figure 4.3 is an oscillogram showing the triangular voltage waveform. The gain of the operational amplifier was set at 100. The value of the feedback resistance was set to 1 M Ω, and the series input capacitance was set to 0.1 μf for the differentiator. The output of the differentiator was monitored using a Tektronix type 561A oscilloscope. Figure 4.4 shows an oscillogram of the differentiator output. The data taken and the calculated results are shown in Table I.

4.2 The Lock-In Amplifier Method

The circuit used to check the instrumentation when using the lock-in amplifier is shown in Figure 4.5. Since the lock-in amplifier will filter out or average out all signals other than those at the same frequency as the a-c source, only the a-c component of the voltage signal needs to be considered when making calculations. The a-c voltage signal developed across the sensing resistor is:

$$V_s = \left(\frac{R_s}{R_s + R_F}\right) E \cos \omega t \qquad (4.2.1)$$

Again if $R_s << R_F$, which is the case, V_s is:

$$V_s \approx \frac{R_s}{R_F} E \cos \omega t \qquad (4.2.2)$$

The amplifier output is then equal to:

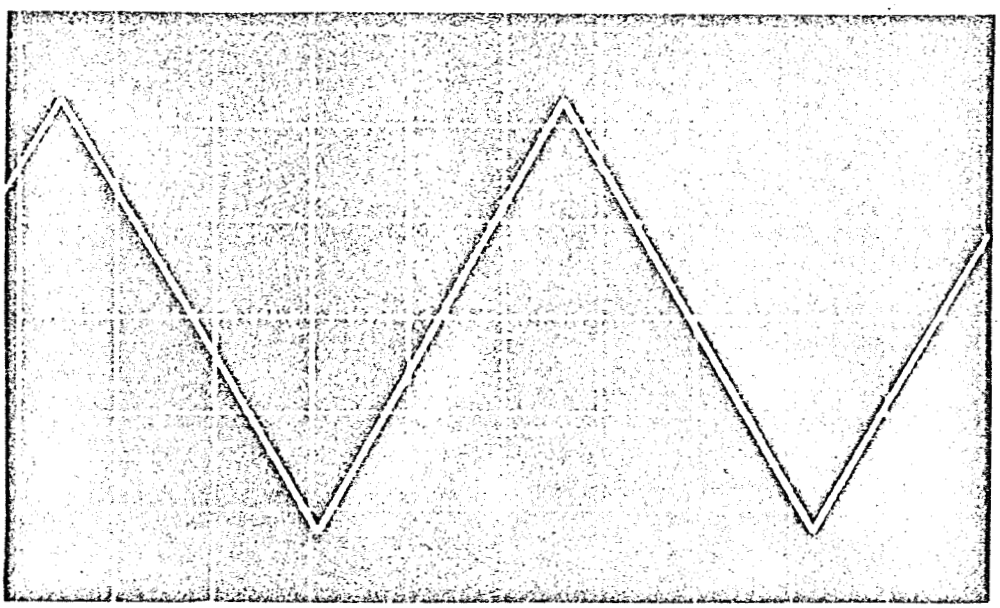

FIGURE 4.3
TRIANGULAR VOLTAGE WAVEFORM

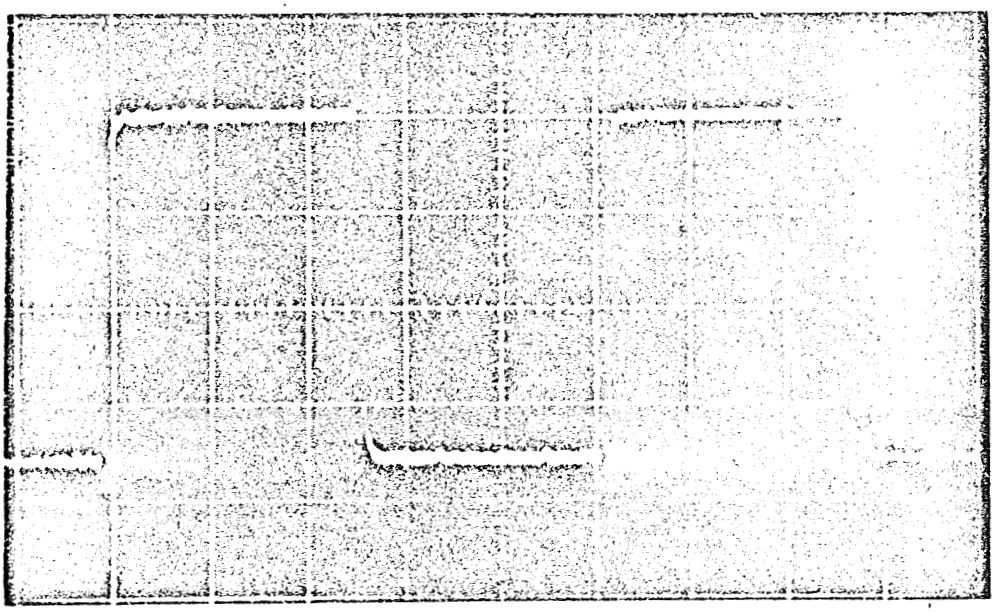

FIGURE 4.4
OUTPUT VOLTAGE
OF THE DIFFERENTIATOR

TABLE I

DATA AND RESULTS OF DIFFERENTIATOR TEST

Value of R_s OHMS	Amplitude of Triangular Wave P-P Volts	Amplitude of Differentiator Output P-P Volts	Calculated Value of R_s OHMS
20	38.5	0.20	19
30	38.5	0.30	29
35	37.5	0.36	35
40	38.5	0.41	39
50	38.5	0.51	49

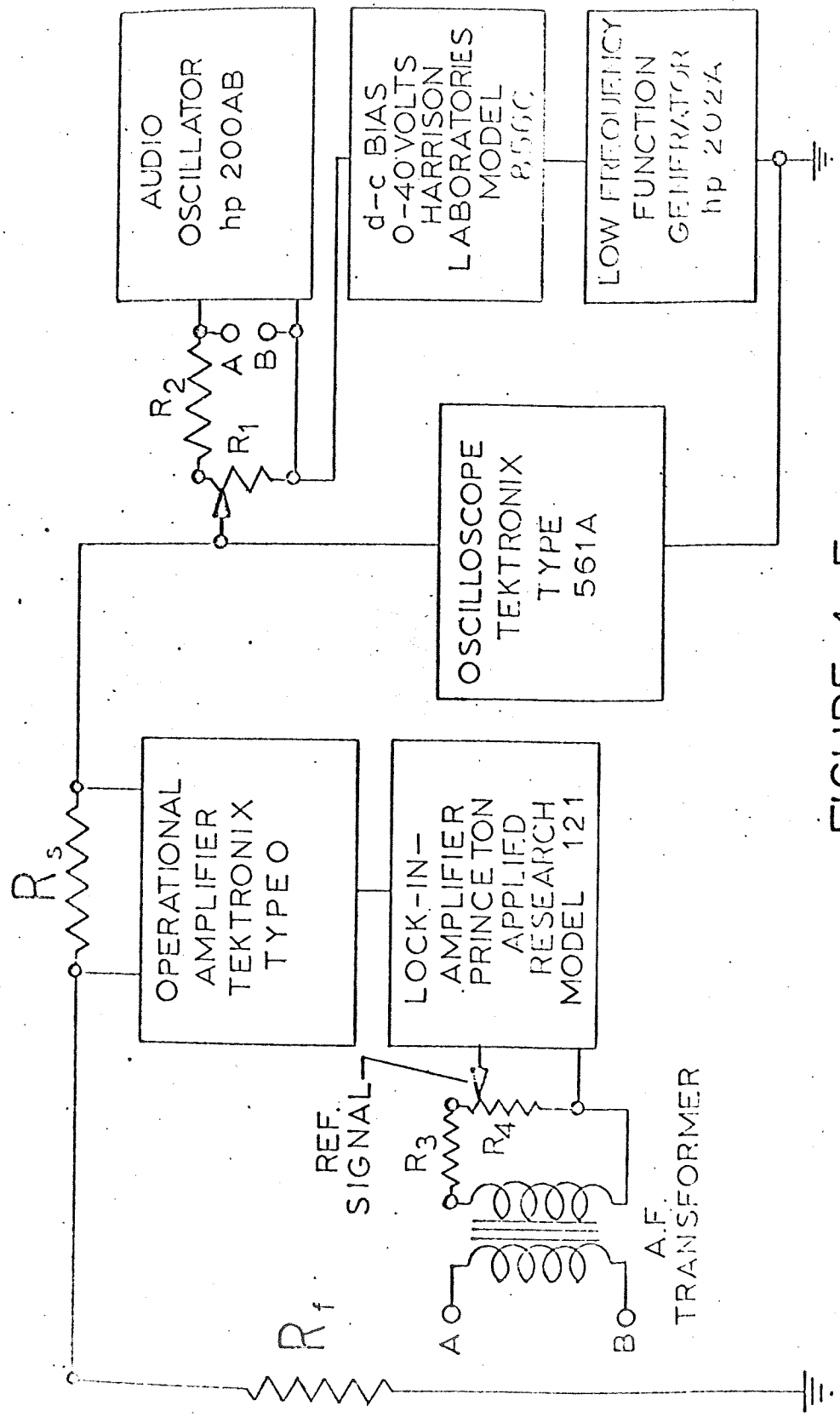

FIGURE 4.5
TEST SET UP USING
LOCK-IN-AMPLIFIER

$$V_s' \lesssim - \frac{B R_s E}{R_F} \cos \omega t \qquad (4.2.3)$$

In this case the lock-in amplifier detects the amplitude of this signal, because it and the reference signal have the same angular frequency. The rms value of this signal can be read on a meter located on the front panel of the instrument. The sensitivity of the meter is adjustable in steps from $\pm$ 10 microvolts to $\pm$ 500 millivolts full scale. The output of the lock-in amplifier would then be

$$V_L = - \frac{B R_s E}{\sqrt{2} R_F} \qquad (4.2.4)$$

Thus, if we assume that B and E are known constants and that V_L can be measured, it is possible to calculate R_s when R_F is known.

A test was performed using the set up shown in Figure 4.5. R_F was a 15-K Ω fixed resistor and the values of R_s were varied from 20 Ω to 50 Ω. The assumption that $R_s << R_F$ is valid. The amplitude of the a-c signal was measured using a 561A Tektronix oscilloscope. The gain of the operational amplifier was set to 100 by choosing a feedback resistor equal to 1 M Ω and a resistor in series with the input of 0.01 M Ω. The d-c voltage was set to -20 volts and the triangular voltage from the low-frequency function generator was set at approximately its maximum value of 39 volts. The audio transformer with a one-to-one turns ratio was used to isolate the lock-in amplifier from the a-c source. Resistors R_1 and R_2 were used as a voltage divider as were R_3 and R_4. These dividers allowed setting of the proper level of voltage signals. The data taken and the calculated results are shown in Table II.

TABLE II

DATA AND RESULTS OF LOCK-IN AMPLIFIER TEST

Value of R_s OHMS	Amplitude of AC Signal P-P Volts	Output of Lock-in Amplifier RMS Millivolts	Calculated Value of R_s OHMS
20	0.82	39	20
30	0.82	58	30
35	0.82	68	35
40	0.83	78	40
50	0.83	98	50

V. DISCUSSION OF RESULTS AND CONCLUSION

5.1 Results

A vacuum system capable of obtaining a pressure of 10^{-8} Torr has been built. It has been possible to sustain the vacuum continuously for several months. The use of an all glass sorption trap eliminated the need for using a cold trap and liquid nitrogen. The experimental part of the vacuum system can be brought up to the pressure needed to fire a discharge while the vacuum pumps are still operating because of placement of valves. It is possible to monitor the pressure in the system continuously over the range of 10^{-9} Torr to atmosphere. An experimental tube was built and a discharge was fired in it. It was found that by varying the tube voltage, filament temperature, and tube pressure, it was possible to obtain a stable discharge.

The two techniques discussed here can be used to obtain the derivative of the I-V characteristic for a Langmuir Probe. The two techniques were instrumented and a method devised to test the instrumentation for proper operation.

The first method, using an operational amplifier differentiator, was tested. The calculated values of the sensing resistor were found to be very close to the actual value used. This indicated that all the instrumentation used in this method was functioning correctly.

The second technique, using a lock-in amplifier, was also tested. The calculated values of R_s were found to be very close to the actual value. The instrumentation used in this method is, therefore, operating correctly.

5.2 Conclusion

The vacuum system operates as desired and the instrumentation works correctly, as verified by the results.

The next step would be to obtain the derivative of the I-V curve for the Langmuir Probe using this instrumentation and to check the derivative curve obtained by one method against the curve obtained by the other method. Then the electron-velocity distribution-function could be plotted for each case and checked to see if they agree. If they do not agree, it would then be advantageous to try to determine why they do not agree. If they do agree, it would be interesting to study the electron-velocity distribution-function in gases other than neon and helium.

VI. BIBLIOGRAPHY

1. Bond, R. H., "Directed Electron Velocity Distribution in Rare Gas Discharges using Guard Ring Probes," California Institute of Technology, Technical Report #25, 1965.

2. Chen, F. F., "Plasma Physics," Summer Institute Princeton University, 1962.

3. Haller, F. B., "All-Glass Sorption Vacuum Trap," The Review of Scientific Instruments, Vol. 35, No. 10, October, 1964.

4. Howatson, A. M., An Introduction to Gas Discharges, Pergamon Press, 1965.

5. Spangenberg, K. R., Fundamentals of Electron Devices, McGraw-Hill Book Company, Inc., 1957.

6. Spangenberg, K. R., Vacuum Tubes, McGraw-Hill Book Company, 1948.

7. Van Atta, C. M., Vacuum Science and Engineering, McGraw-Hill Book Company, 1965.

Semi-Annual Progress Report No. 9

to the

NATIONAL AERONAUTICS AND SPACE ADMINISTRATION

in connection with

NASA Grant NGR 47-004-006

Part 5 of 8 Parts

Final Report

Part B

V.P.I. Project 313138

A Fully Bakeable D. C. Glow Discharge Tube for Measurement of Directed Electron Velocity Distributions with a Langmuir Probe

by

Kenneth A. Skrivseth

R. H. Bond

Virginia Polytechnic Institute
Blacksburg, Virginia

September, 1969

TABLE OF CONTENTS

		Page
1.	INTRODUCTION	1
2.	CONTAMINATION PROBLEMS IN VACUUM SYSTEMS	5
	2.1 Sorption	5
	2.2 Permeation	9
	2.3 Virtual Leaks	10
	2.4 Effect of System Bakeout	10
3.	DESIGN OF A BAKEABLE DISCHARGE TUBE	13
	3.1 General Considerations	13
	3.2 Design and Construction of the Langmuir Probe Region	18
	3.3 Design and Construction of the Cathode Region	29
	3.4 Design and Construction of the Anode Region	36
	3.5 Final Assembly and Testing	40
4.	CONCLUSIONS AND RECOMMENDATIONS	48
	BIBLIOGRAPHY	50

LIST OF FIGURES

		Page
Fig. 1.-1	A Typical Discharge Tube for Langmuir Probe Measurements	2
Fig. 1.-2	The Effect of Moving the Cathode Toward the Anode in a D. C. Glow Discharge Tube	4
Fig. 2.1-1	Energy vs. Distance From Adsorbent for Physical Adsorption	6
Fig. 2.1-2	Exothermic Chemisorption Energy vs. Distance From Adsorbent	8
Fig. 3.1-1	A Portion of the Vacuum System on a Table Top of Marinite	14
Fig. 3.1-2	A Typical Bellows-Sealed Linear Motion Feedthrough	16
Fig. 3.1-3	"Wobble Drive" Bellows-Sealed Rotary Motion Feedthrough	17
Fig. 3.2-1	View of Rotary Motion Feedthrough and Langmuir Probe	20
Fig. 3.2-2	Linear Motion Transfer Device for the Langmuir Probe	22
Fig. 3.2-3	Linear Motion Transfer Device for Langmuir Probe Showing Internal Metal Bellows	23
Fig. 3.2-4	Exploded View of Langmuir Probe Assembly	24
Fig. 3.2-5	Langmuir Probe Centering and Supporting Piece	25
Fig. 3.2-6	Langmuir Probe	26
Fig. 3.2-7	Completed Langmuir Probe Assembly	28
Fig. 3.3-1	Half Section of Press Used for Cathode and Heat Shield Support	30
Fig. 3.3-2	Cathode Motion and Support Assembly	31
Fig. 3.3-3	Detail of Six Inch Spacer Used in Cathode Motion and Support Assembly	33

LIST OF FIGURES (Cont.)

		Page
Fig. 3.3-4	Exploded View of Cathode Motion and Support Assembly	34
Fig. 3.3-5	Head on View of Cathode	35
Fig. 3.3-6	Cathode Region Glasswork in Cross Section	37
Fig. 3.3-7	Completed Glasswork for the Cathode Region	38
Fig. 3.3-8	Partially Assembled Cathode Region	39
Fig. 3.4-1	Isometric View of the Anode Region	41
Fig. 3.4-2	View of Completed Anode Construction, with Probe Assembly in Foreground	42
Fig. 3.5-1	View of Discharge Tube with Approximately 30 Amperes of Cathode Current	45
Fig. 3.5-2	The Discharge Tube with a Discharge Fired	47

SYMBOLS AND ABBREVIATIONS

C.....Centigrade

cm.....centimeters

d.c.....direct current

mm.....millimeters

T.P.I.....threads per inch

UNC.....Unified National Coarse thread

°.....degrees

".....inches or quotes

1. INTRODUCTION

This paper describes the design and construction of a fully bakeable high vacuum d. c. glow discharge tube. The purpose of this glow discharge tube is measurement of directed electron velocity distributions in the positive column of a glow discharge, using a Langmuir probe. The tube itself has a 48 mm inside diameter and a maximum cathode to anode spacing of 80 cm. The Langmuir probe is located 15 cm from the anode. The probe can be rotated through 360 degrees and moved radially from the tube center line to one wall. The cathode can be moved 15 cm in the direction of the stationary anode.

The major objective in the design of this glow discharge tube was to attain a pressure of 10^{-9} torr (mm of Mercury) or lower inside the discharge tube. This required that the tube be bakeable, so it was necessary to eliminate all "O" ring seals. This design should allow more reliable, repeatable, and more predictable measurements to be made with the Langmuir probe.

Langmuir probes have long been used for measurement of electron velocity distributions in glow discharge tubes. Figure 1.-1 shows such a discharge tube, with a planar Langmuir probe inserted into the probe port. To insure accuracy and repeatability of measurements, it is essential that contamination from undesirable gases or vapors be minimized.

To see how the distributions vary with position and direction, it is often desirable to move the Langmuir probe radially in the discharge tube, to rotate it on its own axis, and also to move the probe relative

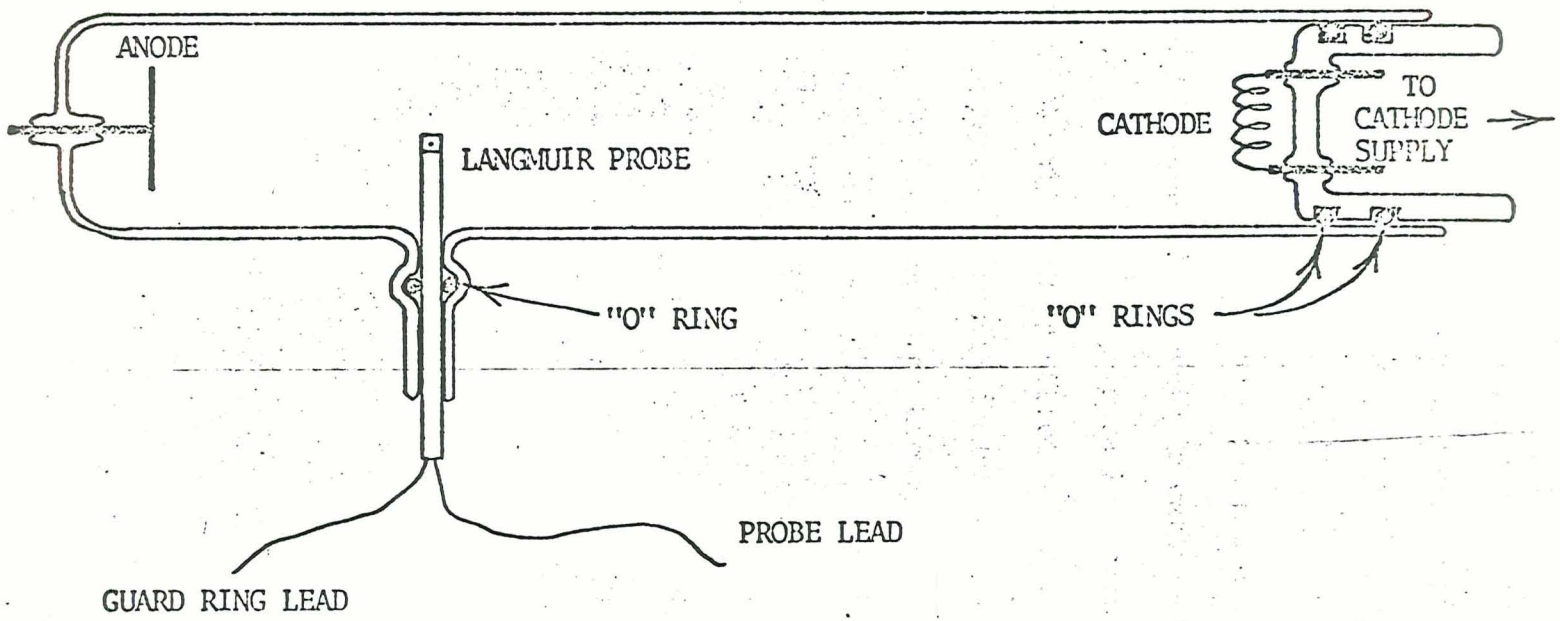

Figure 1.-1 A Typical Discharge Tube for Langmuir Probe Measurements

to the cathode. Normally this last motion is accomplished by cathode movement rather than by actual probe movement, since the probe's motion along its own axis and its rotation make movement of the probe along the axis of the discharge difficult. Besides accomplishing the desired change of cathode-to-probe spacing, cathode movement also involves a change of cathode-to-anode spacing, since the probe and anode have a fixed separation. One might expect this change in cathode-to-anode spacing to alter the discharge radically. Figure 1.-2 shows that this is not the case. Only the length of the positive column of the discharge changes with cathode movement, provided that anode current is held constant. In effect, the probe is moved through the positive column, in the direction of the cathode.

Figure 1.-2 The Effect of Moving the Cathode Toward the Anode in a D. C. Glow Discharge Tube

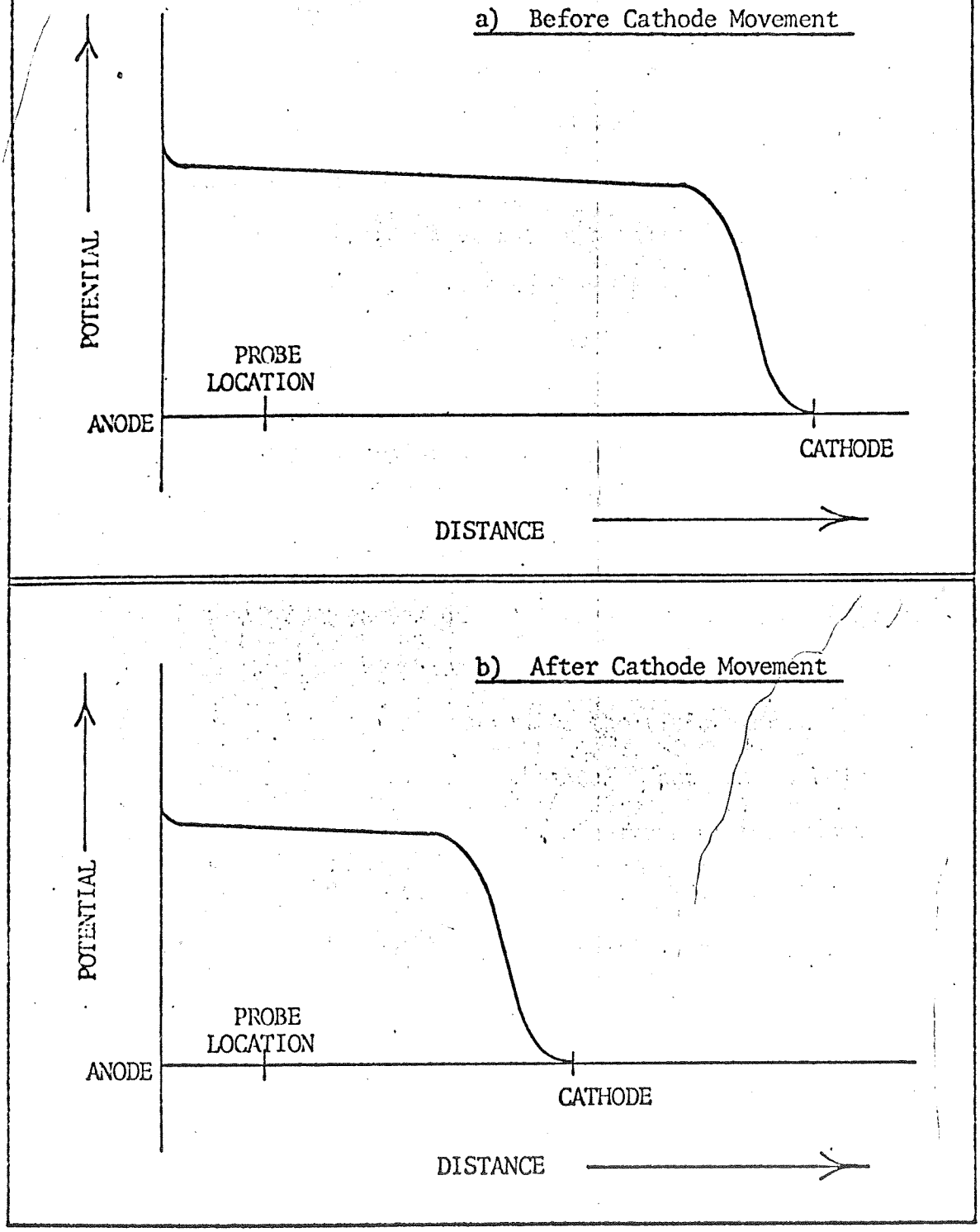

2. CONTAMINATION PROBLEMS IN VACUUM SYSTEMS

2.1 Sorption

Sorption (Refs. 10, 16) is a general term which encompasses any process where, on or within some surface, an excess of a gas or vapor collects as a result of intermolecular and interatomic forces. Sorption includes physical (van der Waals) adsorption, chemisorption, and absorption. Sorption can occur on or within a solid or liquid, but only sorption with respect to solids is considered here. The surface on which sorption occurs is called the sorbent, and the gas or vapor sorbed or collected is called the sorbate. All sorbates must be removed or "outgassed" from the surfaces of a vacuum system before an uncontaminated system is obtained.

Adsorption, as opposed to absorption, is the process in which there is an accumulation of an excess of a gas or vapor exterior to the surface of a solid. Surface roughness increases adsorption, by making the effective area of the adsorbent many times the visible area.

Physical adsorption involves no chemical reactions, and the heat lost by the adsorbate is of the order of magnitude of the heat of liquefaction. Physically adsorbed molecules act in many respects like a two dimensional liquid, shifting on the surface of the solid to maintain equilibrium. Figure 2.1-1 shows a general energy diagram for physical adsorption at the surface of a solid adsorbent. A free molecule in the vicinity of the surface will tend to fall into the low energy well near the surface, giving off a small amount of energy in the form of heat, and will remain there unless disturbed.

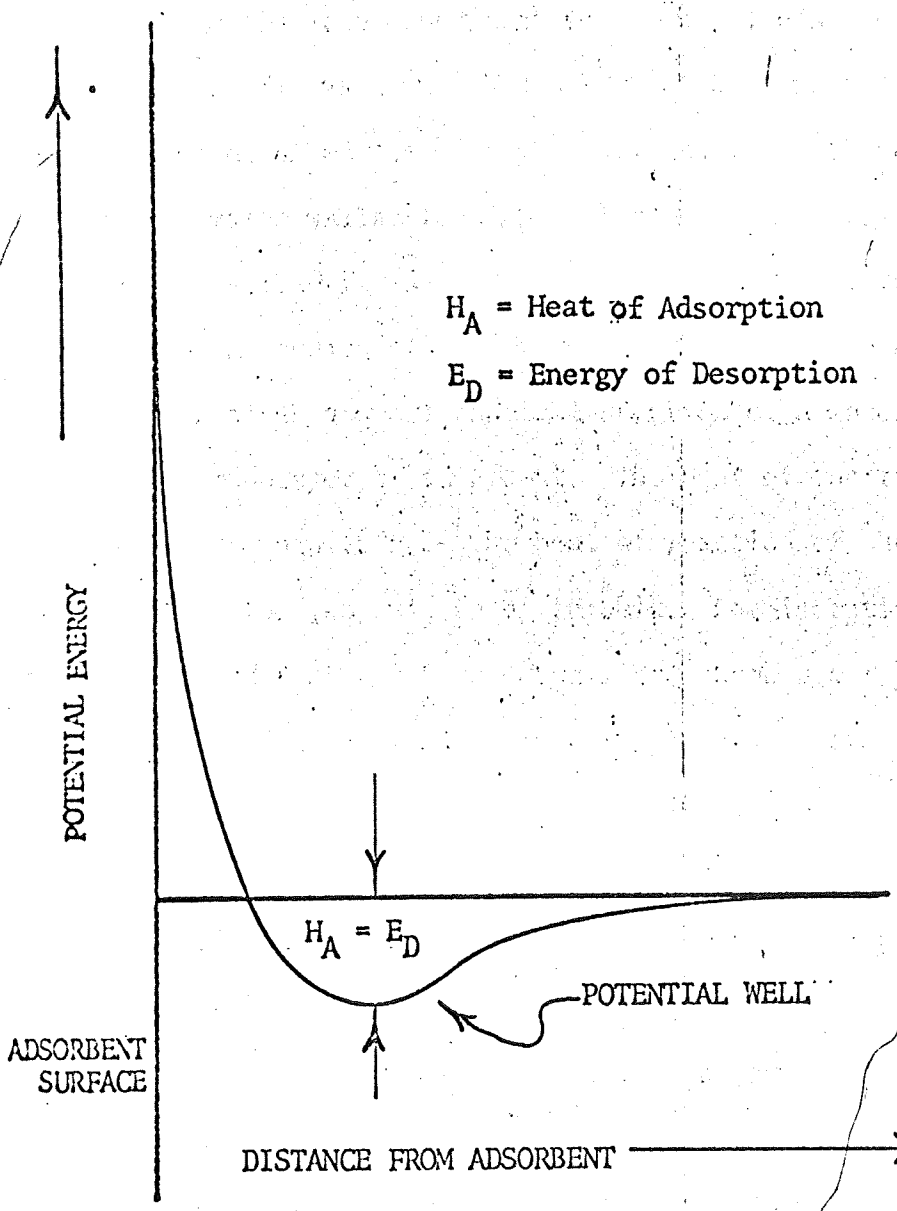

(REF. 10)

Figure 2.1-1 Energy vs. Distance From Adsorbent for Physical Adsorption

While theory indicates only a few layers of adsorbate should occur by physical adsorption, experimental evidence indicates that between 10 and 1000 molecular layers can be formed. Results vary widely for different surfaces and from one experiment to another (Refs. 10, 14). As the pressure of a vacuum system which has been at atmospheric pressure for a time is reduced, an excess of physically adsorbed molecules will remain at the system walls, tending to boil off slowly.

If it is possible for a molecule of a gas or vapor to react chemically with the molecules of an adsorbent, chemisorption may occur. This process involves a quasi-chemical reaction of a monolayer of adsorbate with a monolayer of adsorbent. The heat of the reaction is of the same order of magnitude as the heat of reaction of the chemical reaction between the two substances in bulk. Chemisorption is not quite so simple as a chemical reaction since there are repulsive forces involved between adsorbate ions. This results in a heterogeneous deposition of adsorbate. The energy of a single chemisorption reaction varies with the number of molecules previously chemisorbed. Chemisorption is more prevalent in metals than in glass. Figure 2.1-2 shows the energy diagram for chemisorption involving an exothermic reaction. Frequently chemisorption requires an activation energy, as shown in the figure.

A pumpdown alone will not usually remove many chemisorbed molecules, since chemisorption involves higher energies than physical adsorption. Heat application is usually necessary, but the temperature required is often too high to be practical since it is usually much higher than the melting temperature of standard glass such as Pyrex, which may be in the

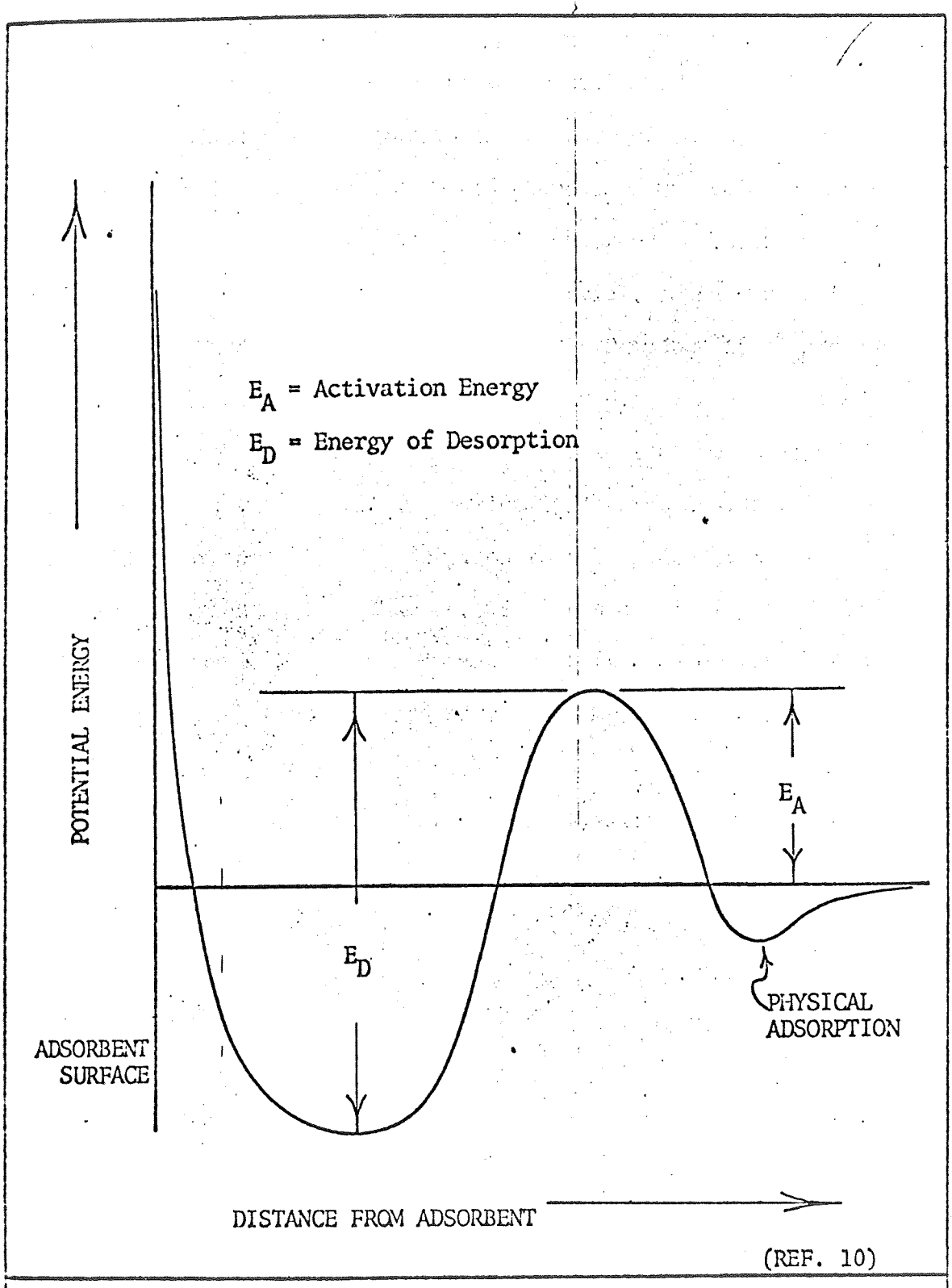

Figure 2.1-2 Energy vs. Distance from Adsorbent for Exothermic Chemisorption

vacuum system. However, the temperature of a cathode may be high enough to remove essentially all of its chemisorbed molecules.

Absorption involves the penetration of the bulk of the absorbent solid by absorbate molecules, by a combined process of molecular attraction and diffusion. During a system pumpdown, absorbed molecules will diffuse back to the surface of the absorbent material, replacing surface sorbate molecules as they are gradually desorbed. Pumpdown times are increased as a result of the diffusion time involved.

The energy diagram for absorption is similar to that for physical adsorption, except the energy well is physically located inside the absorbent solid. For appreciable absorption to take place it is necessary that the absorbent material be porous. Less difficulty from absorption than from physical adsorption will arise from a relatively nonporous material, such as most types of glass. Metals are usually more prone than glass to absorption.

This discussion has been somewhat simplified, since in reality physical adsorption, chemisorption, and absorption may occur simultaneously.

2.2 Permeation

Permeation occurs when gases and vapors in the atmosphere diffuse through a wall in a vacuum system. It is a major contamination problem with "O" ring seals. The effect is very similar to that of the outgassing of sorbates, except that this process continues indefinitely and places a limit on the ultimate vacuum attainable in an otherwise

clean system. Permeation occurs even when the interior of a vacuum system is at atmospheric pressure, as long as the partial pressures of the interior gases and vapors differ from the partial pressures of the gases and vapors in the atmosphere. Vacuum grease on an "O" ring will help to reduce permeation, and leaks around the "O" ring, but it will also add problems of its own in the cleaning of vacuum apparatus.

Permeation through glass and metal does occur, although this effect is usually small. In a baked vacuum system, however, this type of permeation may be essentially the only source of contamination, so it must be recognized.

2.3 Virtual Leaks

A virtual leak can also contaminate a vacuum system. A virtual leak is a source of nearly constant gas or vapor contamination as a result of a trapped volume in the system gradually leaking off through some small, flow-restrictive orifice. An example of a virtual leak might be a trapped volume beneath a screw in a threaded hole. This particular problem can be eliminated by cutting a lengthwise slot in the screw, slightly below the thread depth, to allow the trapped volume to be pumped quickly. Problems from virtual leaks may arise when a vacuum system involves heliarc welds, silver solder joints, and other types of seals and internal connections.

2.4 Effect of System Bakeout

Baking is one of the best methods for eliminating or drastically reducing contamination problems such as described in the previous

sections, and is often the only method for reaching ultra-high vacuum in a reasonable length of time. For Pyrex (7740) glass, a typical bakeout temperature is between 300 and 400 degrees C.

To bake an entire system, it must be first pumped to a high vacuum to reduce oxidations at higher temperatures, and to decrease the read-sorption rate at the system walls. Sometimes an inert gas or dry nitrogen is valved into a system prior to a bakeout, to help flush out active contaminants. A heat-insulated enclosure, containing heating elements, is placed over the entire system exterior. The current in the heating elements is slowly increased, care being taken that the system pressure does not increase over the operating limits of the vacuum pumping system. When the final bakeout temperature has been reached, the state of the system is maintained for the entire baking period, 12 to 24 hours, or longer for a "new" system.

A localized bakeout can be accomplished with heating tape or heat lamps. This method is less effective than a total system bakeout, since any gases desorbed in the baked area may recollect on the walls of some other part of the system, especially if the heating causes a drastic pressure increase.

The heat applied during a bakeout under vacuum conditions increases the energy of the molecules of the walls of the system, and thus the energy of any sorbed molecules is increased. When the energy of one of these sorbed molecules is greater than the energy of its potential well, it will have a good chance of being desorbed. The probability that desorption will take place increases rapidly with temperature, at a constant pressure. The vacuum pump removes most of the gases and vapors

as they are desorbed. Physically adsorbed gases and vapors are generally the most readily removed, and usually form the majority of molecules desorbed during a bakeout. The outgassing rate should of course taper off with time during a bakeout, as most of the sorbed molecules are removed. After a bakeout has been completed, the system is allowed to return to room temperature and the reduced energies of the remaining sorbed molecules should not be sufficient to allow much further desorption. At the reduced temperature, the equilibrium concentration of sorbates on the system walls may well be much higher than the actual concentration, resulting in a gettering action which should substantially reduce the vacuum system pressure (7).

3. DESIGN OF A BAKEABLE DISCHARGE TUBE

3.1 General Considerations

The new discharge tube first had to be compatible with the existing vacuum system which was to be used for pumpdown. This vacuum system is capable of ultrahigh vacuum, pressure less than 10^{-9} torr. The tube was to be connected directly to the vacuum system, separated from the pumping system and trap by a bellows-sealed valve. The Marinite* used for the table top in figure 3.1-1 is bakeable, allowing a removable bakeout oven to be placed over the entire tube and some portions of the vacuum system, using the Marinite itself as the bottom portion of the oven.

The new discharge tube was to be able to support ultrahigh vacuum, which meant "O" ring seals had to be eliminated, since all parts had to be bakeable. Most "O" ring seals decompose at bakeout temperatures. Metal bellows were chosen as the means of providing motion transfer. It still remained to decide on the best way to use the motion transfer capabilities of a metal bellows.

There are two types of metal bellows, the corrugated type, which is one piece, and the washer type. The corrugated type is made by corrugating a piece of flat, thin stainless steel or other metal, bending the corrugations, and then welding a seam, making the bellows circular in cross section. The washer type is made by welding the insides of two washers together, then welding the outside of one end of this

* Trade Mark of Johns Manville Sales Corp.

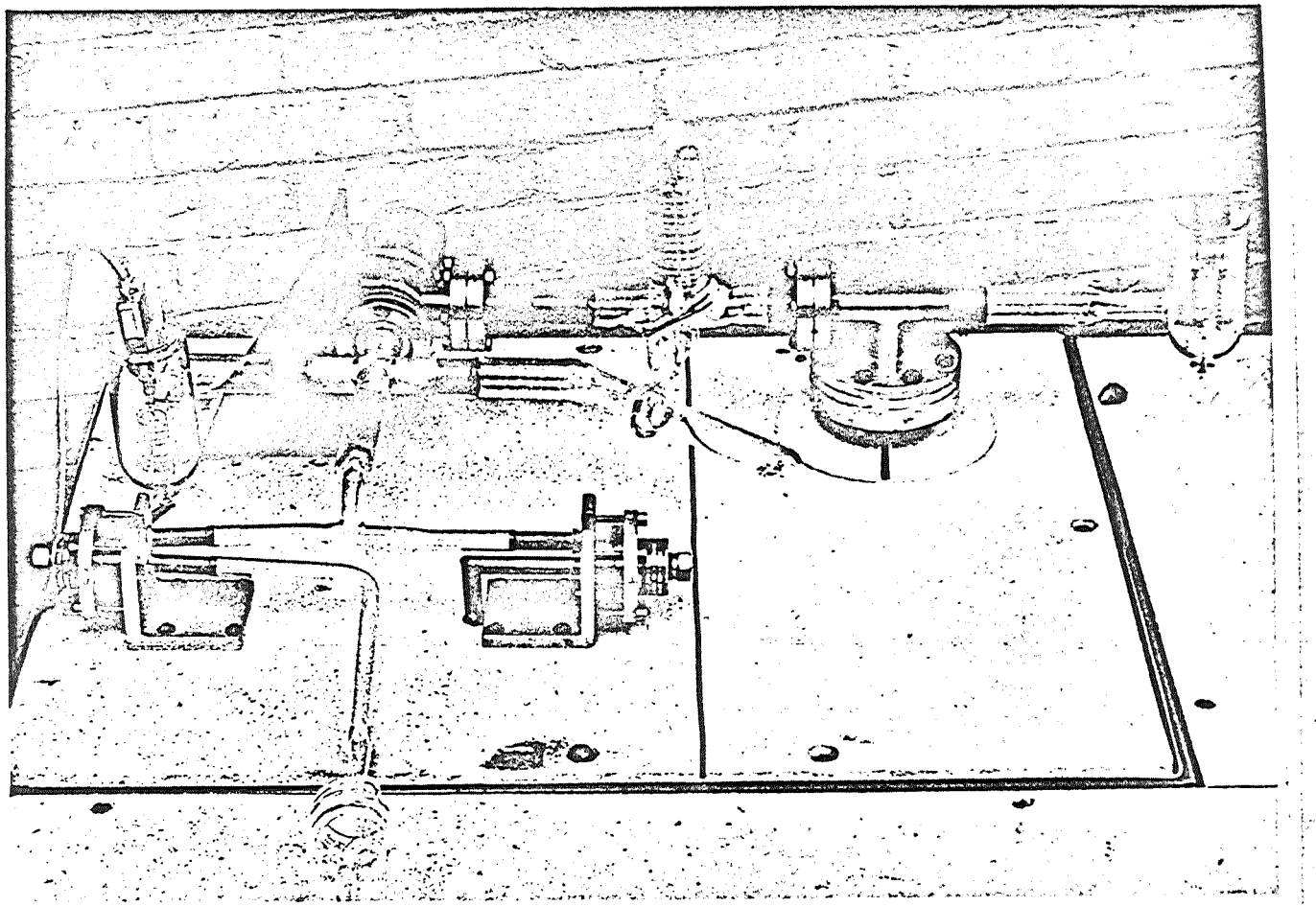

Figure 3.1-1 A Portion of the Vacuum System on a Table Top of Marinite

unit to the outside of another washer, and so on. The two types are shown on page 185 of reference 10. Manufacturer's specifications for maximum flexure and torque limits vary considerably for both types. There are varying opinions on which types of metal bellows are best suited for vacuum applications. The welded type is often more flexible but there is conceivably more chance for leakage with the many welded joints involved.

A simplified model of a commonly used bellows-sealed linear motion feedthrough is shown in figure 3.1-2. This particular model has a direct contact between the vacuum side of the system and the atmosphere side. Some means must be provided to keep the shaft from sliding into the vacuum excessively, and it is thus usually desirable to keep the shaft securely held at some point. The bellows arrangement can be located on either side of the vacuum wall, with the vacuum outside of the bellows or inside.

Figure 3.1-3 is a cross section of a bellows-sealed rotary motion feedthrough. This type of mechanism is known as "wobble drive." Note that there is rotational sliding motion against the extreme right end of the bellows, both in the vacuum and in the atmosphere. This is a potential trouble area for this type of feedthrough, especially when high rotary speeds are involved, and when ultrahigh vacuum is desired, since lubrication on the vacuum side can not be allowed for ultrahigh vacuum work. The portion of this mechanism exposed to atmosphere is sometimes removable from commercially available rotary motion feedthroughs, to allow lubrication of the atmosphere side of the mechanism, using lubricants that would boil off or burn up at bakeout temperatures. When

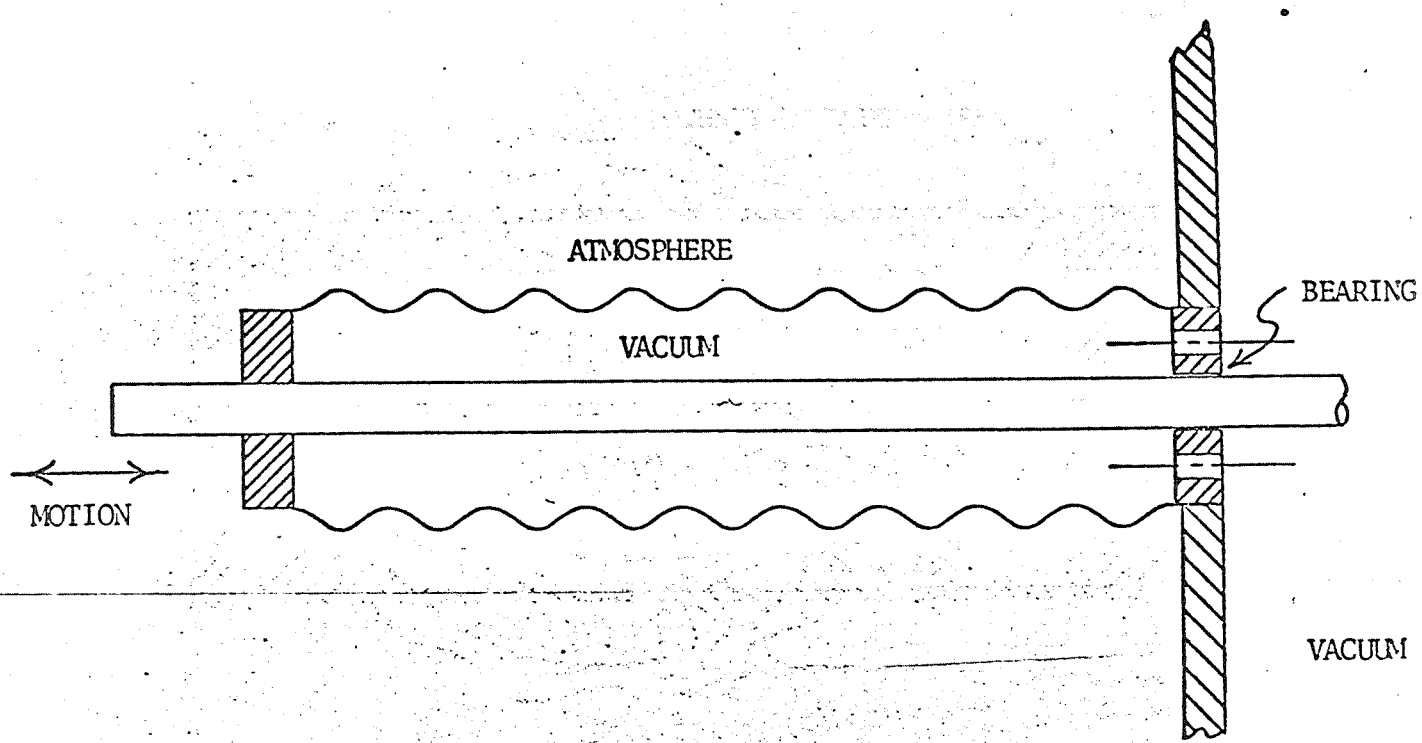

(Ref. 14)

Figure 3.1-2 A Typical Bellows-Sealed Linear Motion Feedthrough

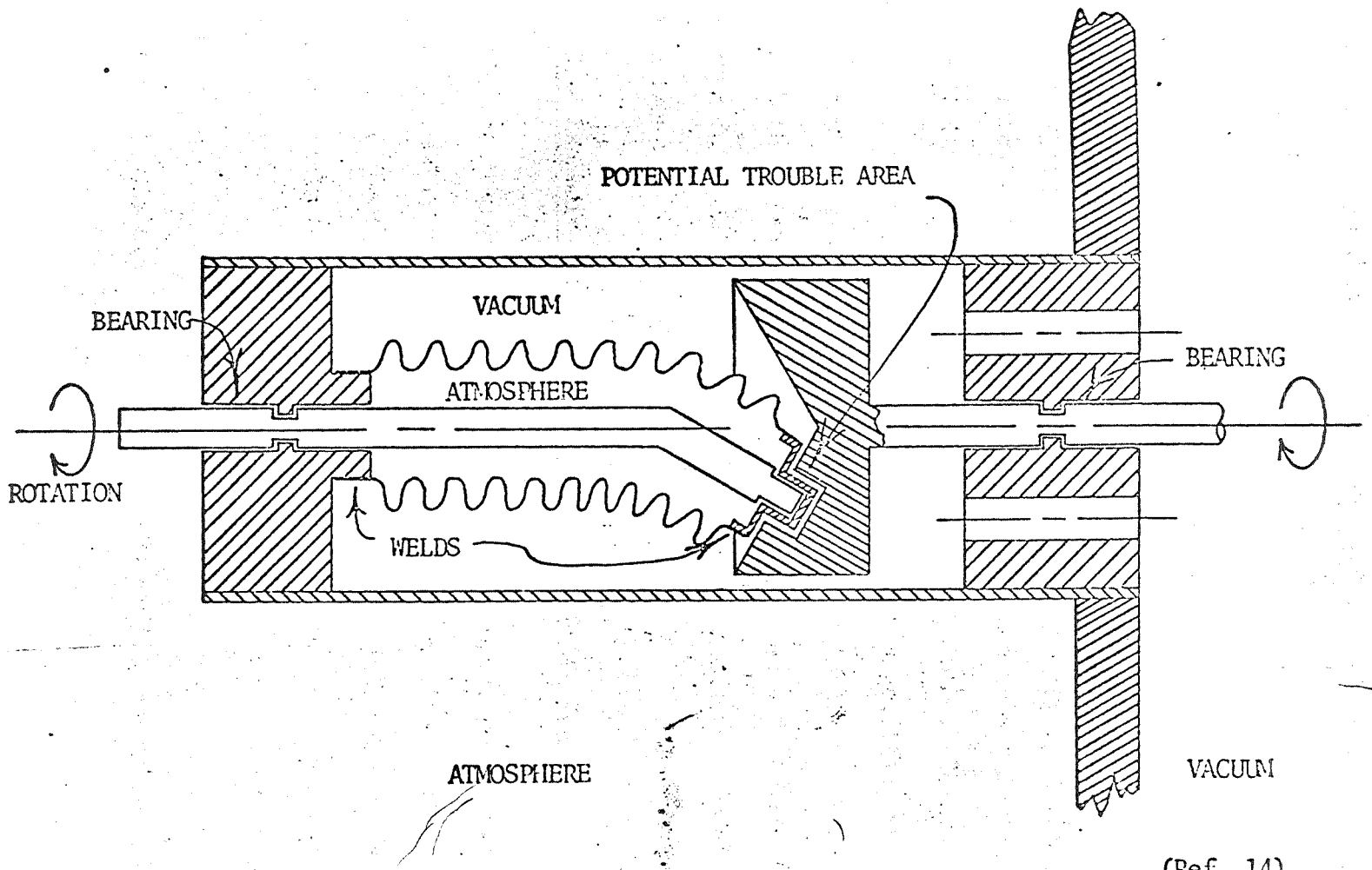

(Ref. 14)

Figure 3.1-3 "Wobble Drive" Bellows Sealed Rotary Motion Feedthrough

only low shaft speeds are desired, no lubrication is usually required. Shaft alignment in this type of feedthrough is critical. The design and construction of such a device would be much more tedious than the design and construction of a bellows-sealed linear motion feedthrough.

Another type of ultrahigh vacuum rotary feedthrough involves the rotation of a magnet in the atmosphere to rotate a magnet in the vacuum. In cases where bakeout is used, the exterior magnet is usually removed, and the interior magnet is made of Alnico, since this material retains most of its magnetic properties at high temperatures. Because any stray magnetic fields could easily upset a glow discharge, this type of feedthrough could not be used in the new discharge tube.

With these general ideas in mind, the design and construction of the Langmuir probe region and the cathode and anode regions of the discharge tube will be described.

3.2 Langmuir Probe Region Design and Construction

The problems encountered in the Langmuir probe region of the glow discharge tube centered around the fact that rotation, linear motion, and electrical output were simultaneously required. The probe itself was to have only two electrical connections, but provision was made for four outputs in case a more intricate Langmuir probe might be required for measurement at a later date.

The only bellows-sealed motion feedthrough known to be on the market which provides rotary and linear motion in one package is made by Varian Associates at a price exceeding the budget of the project. Furthermore, no two motion feedthroughs, one rotary and one linear, are known to be

on the market which together would be compatible in the transfer of linear and rotary motion to a single shaft. Because of extra problems involved in the construction of a rotary motion device, the decision was made to purchase a rotary device and to design a linear motion device which would be compatible with the rotary device.

The rotary motion feedthrough purchased was built by Cooke Vacuum Products of Norwalk, Connecticutt. It was chosen over others available mainly because of reasonable price and excellent specifications. Manufacturer's specifications are as follows.

Maximum Torque	10 Inch Pounds
Maximum Rotary Speed	500 rpm
Operating Pressure	to 1 x 10^{-10} Torr
Bakeout Temperature	to 400 Degrees C.
Weight	2 Pounds

Figure 3.2-1 shows the rotary motion feedthrough in relation to the Langmuir probe.

To transfer linear motion to the Langmuir probe, a linear motion feedthrough was designed. A metal bellows was to be placed around (but not touching) the shaft extending from the rotary motion feedthrough to the probe. To hold the bellows in place, an outer turnbuckle was devised. This arrangement allowed the adjustment and control of the probe position and also provided protection for the inner bellows. A type 316 stainless steel pipe was used which was thickwalled enough to be used for both the male and female portions of the turnbuckle. Following the machining of the turnbuckle portion of the feedthrough, it was welded to the outer portions of two rotatable 2-3/4 inch Conflat* vacuum flanges.

* Trade Mark of Varian Associates

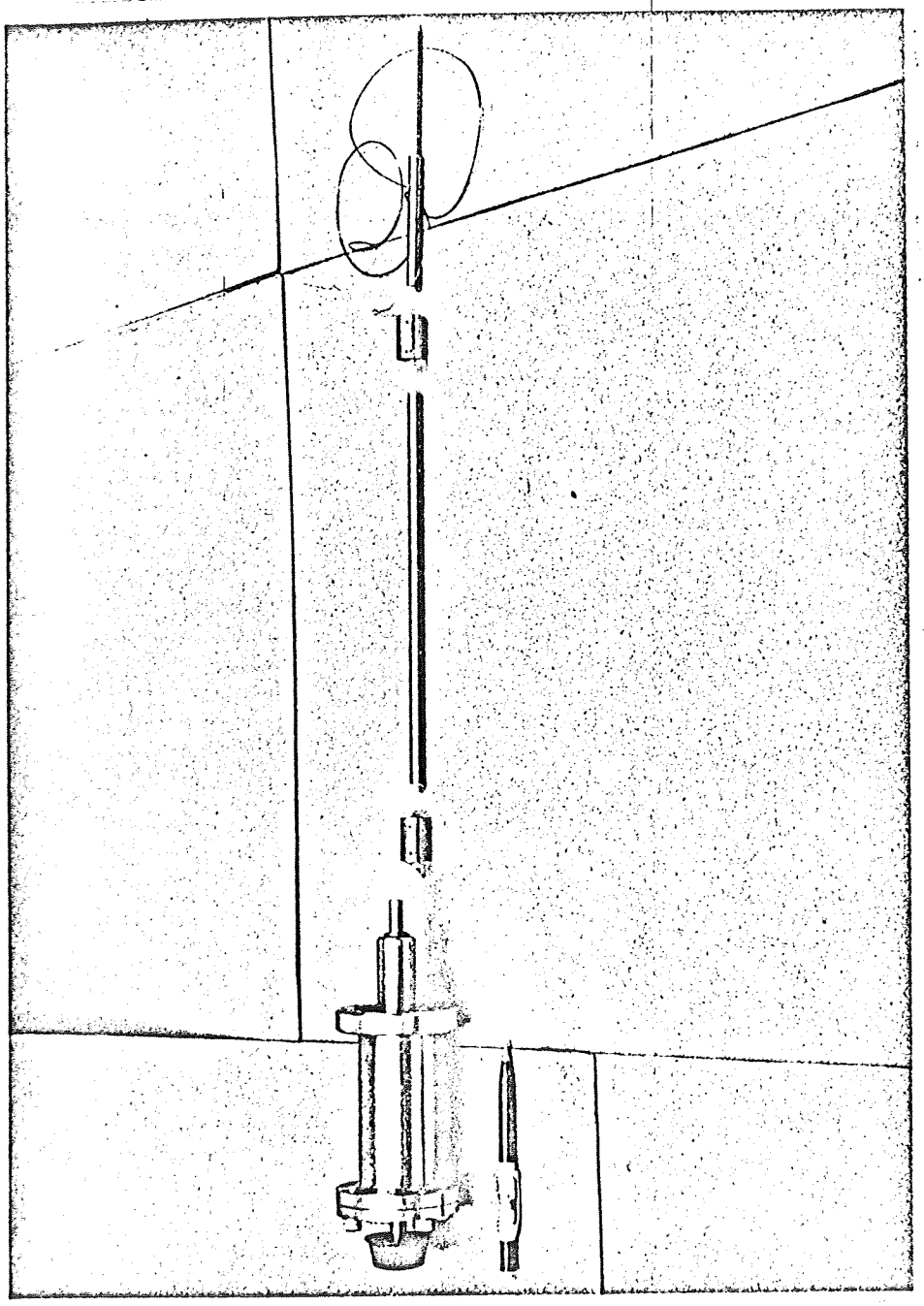

Figure 3.2-1 View of Rotary Motion Feedthrough and Langmuir Probe

To keep the two male ends from rotating with respect to each other, a piece of 1/8 inch flat stock was grooved, shaped, and welded to one of the male ends, and a "follower" was welded to the other male end, as shown in figure 3.2-7. The bellows was silver soldered to the inner or sealing parts of the flanges. A drawing of the completed linear motion motion device is shown in figure 3.2-2, and figure 3.2-3 is a photograph of the device, showing the inner bellows.

Electrical output was provided by four tungsten-to-glass seals made in an "X" arrangement as shown to the right of the linear motion feed-through in figure 3.2-4. Each tungsten-to-glass seal was made at the end of 20 mm Pyrex tubing, and the tubing itself was then attached to 1-1/2 inch diameter Pyrex. These smaller tube extensions reduced the chance of cracking one seal from heat stress while another was being joined by the glassblower.

Directly adjacent to the point where the Langmuir probe enters the discharge is a probe supporting and centering piece which is shown in figure 3.2-5. The piece was made from capillary tubing of proper inside diameter to give the probe a good fit. The ends of the capillary tubing were drawn out to a diameter of just under 1-1/2 inches, and joined to the 1-1/2 inch diameter tubing which already held the electrodes. The extra holes in the ends of the supporting piece allow for pumping. The glasswork was then joined to a glass-to-metal seal, annealed, and sealed to the discharge tube.

The Langmuir probe itself is shown in figure 3.2-6. It was constructed of type 304 3/32 inch diameter stainless steel hollow tubing, 0.010 inch diameter type 304 stainless steel wire, ceramics, and Sauereisen ceramic cement. Electrical insulation of the two stainless

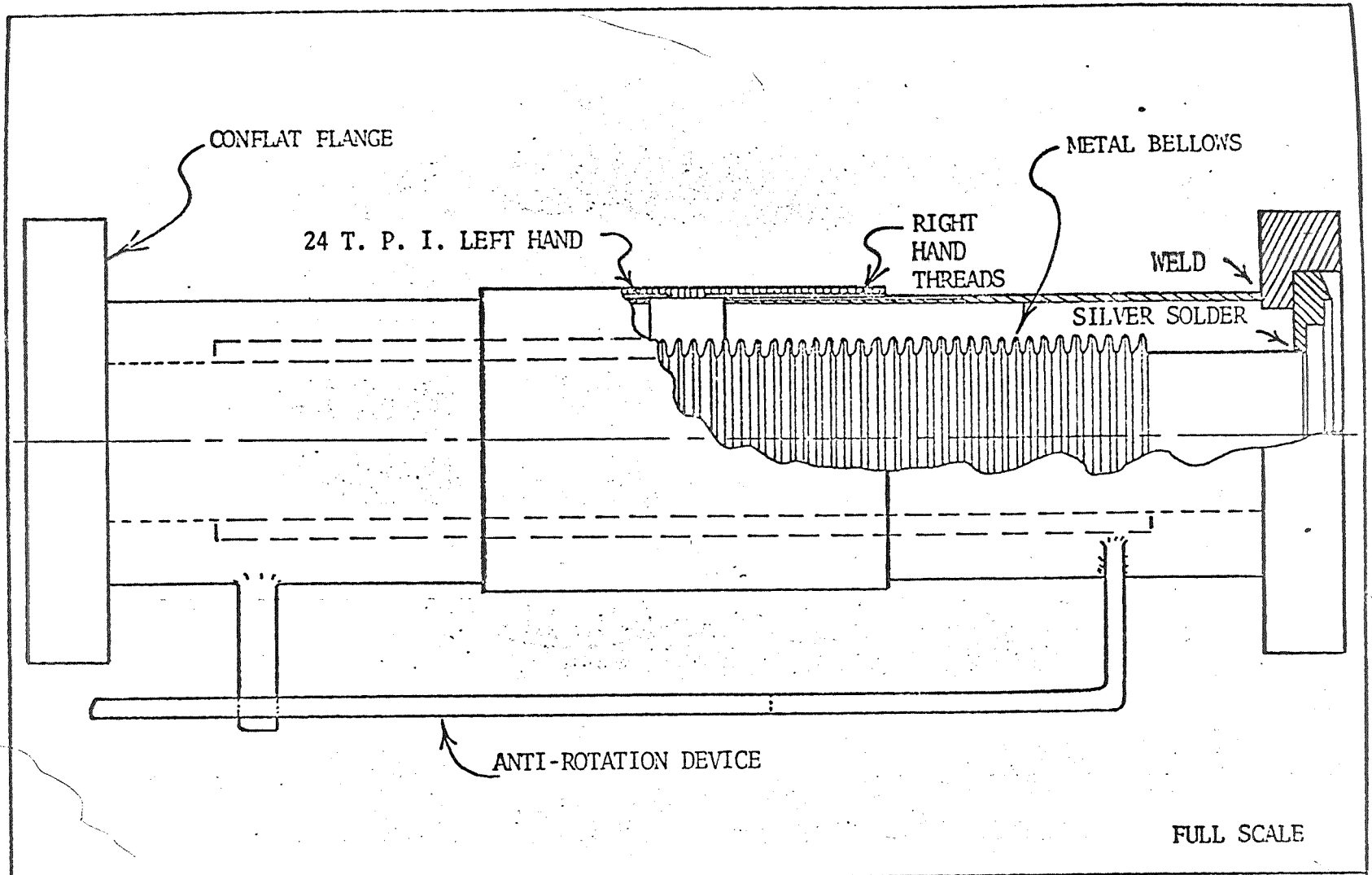

Figure 3.2-2 Linear Motion Transfer Device for the Langmuir Probe

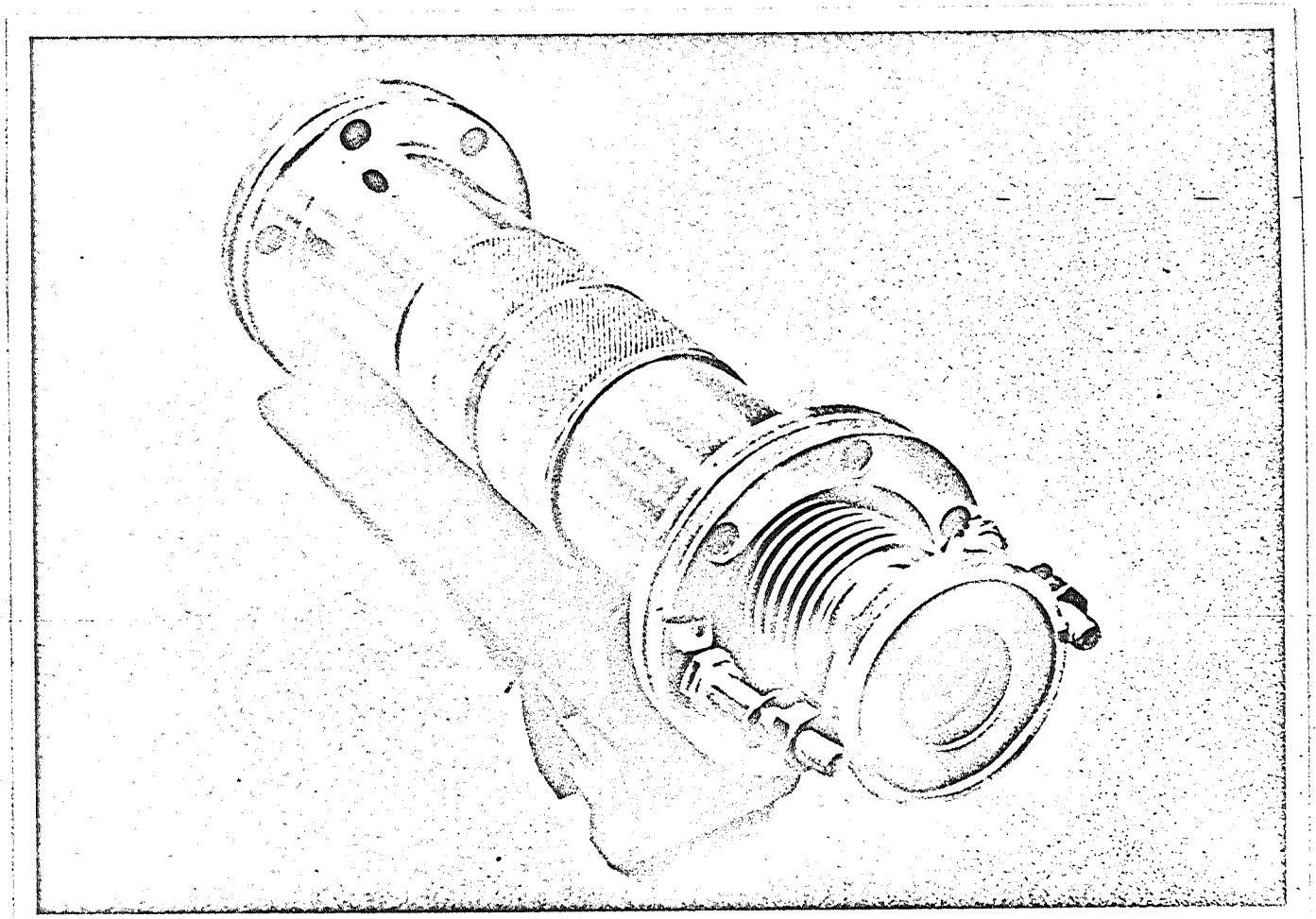

Figure 3.2-3 Linear Motion Transfer Device for Langmuir Probe Showing Internal Metal Bellows

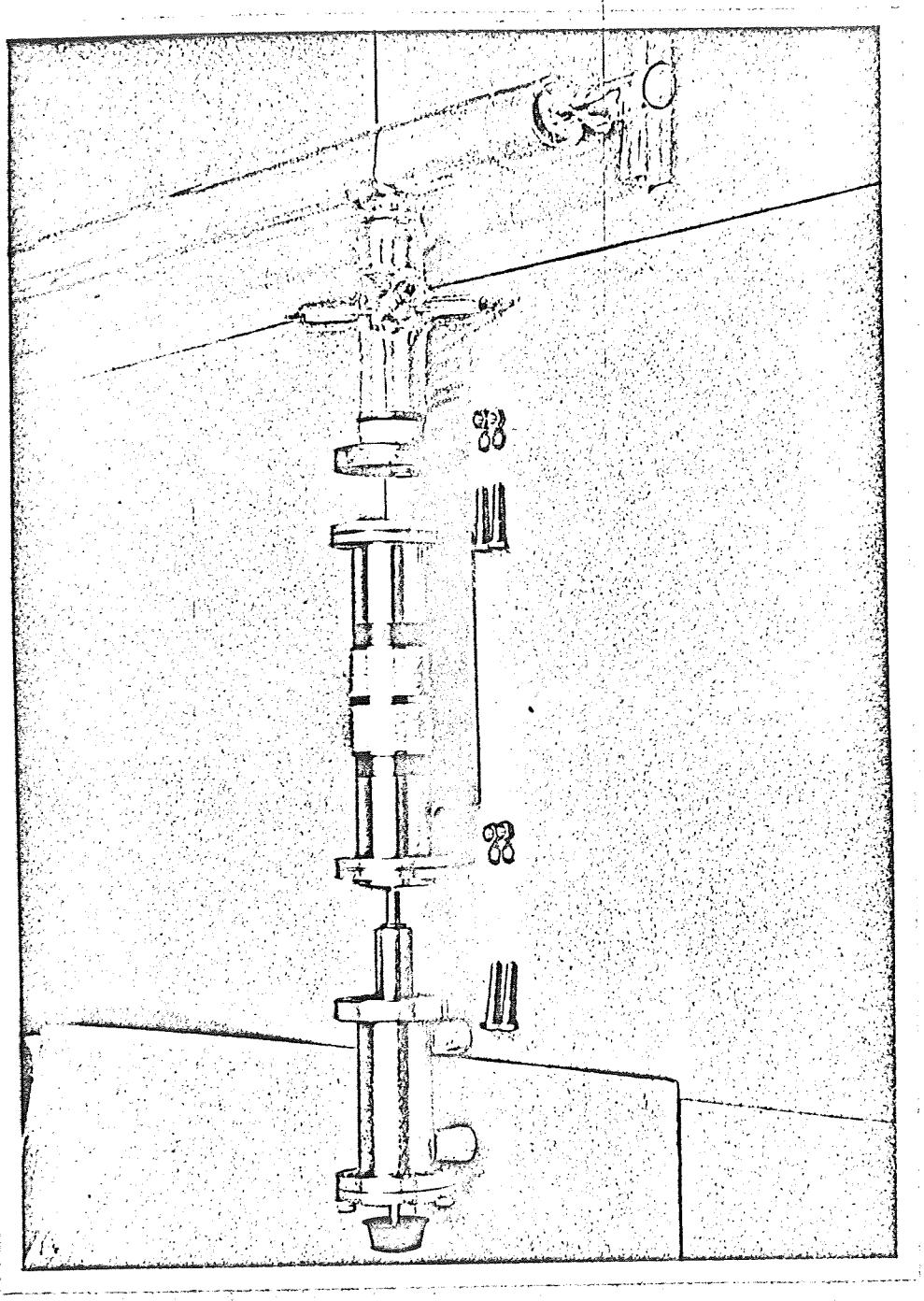

Figure 3.2-4 Exploded View of Langmuir Probe Assembly

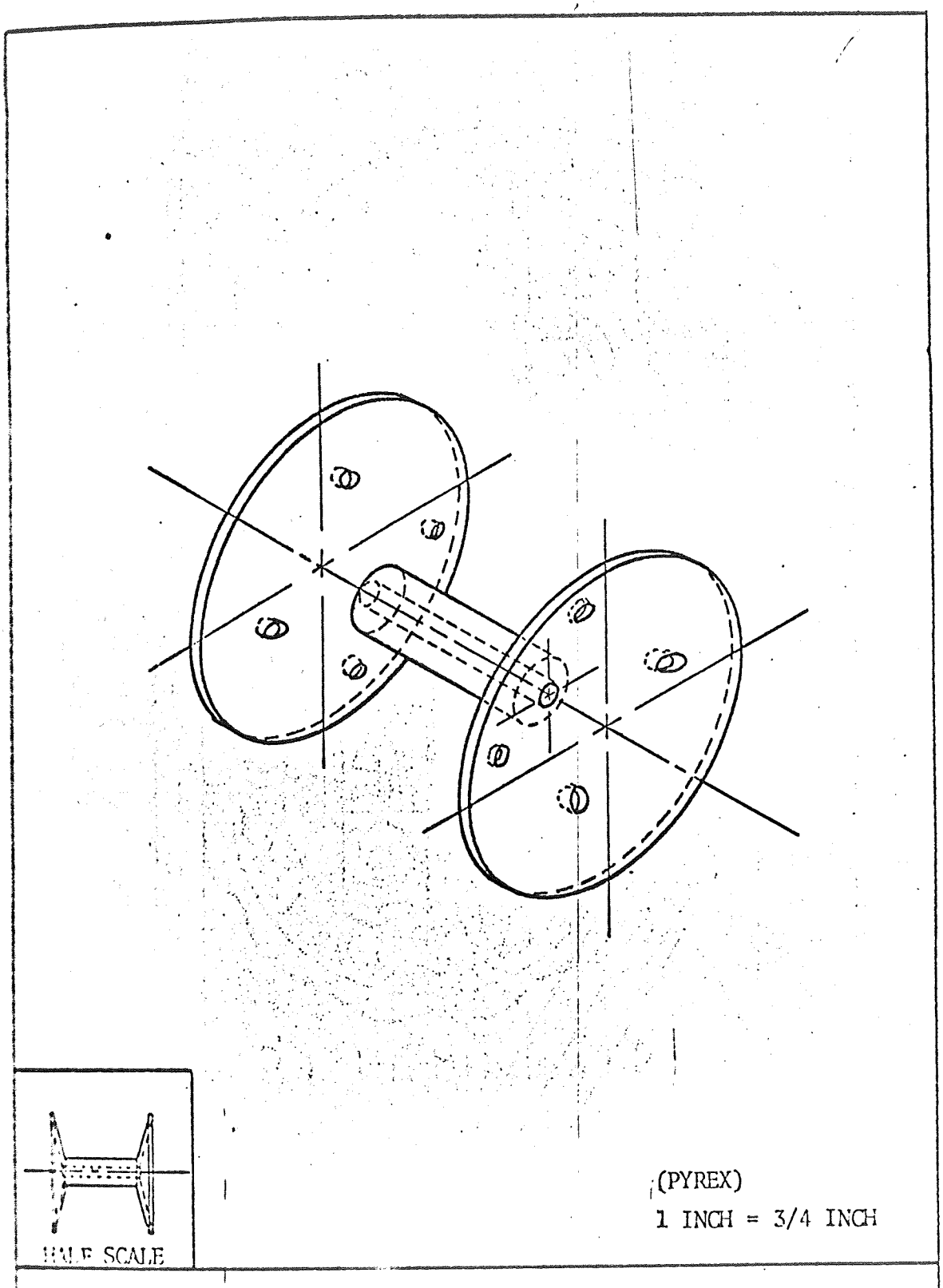

Figure 3.2-5 Langmuir Probe Centering and Supporting Piece

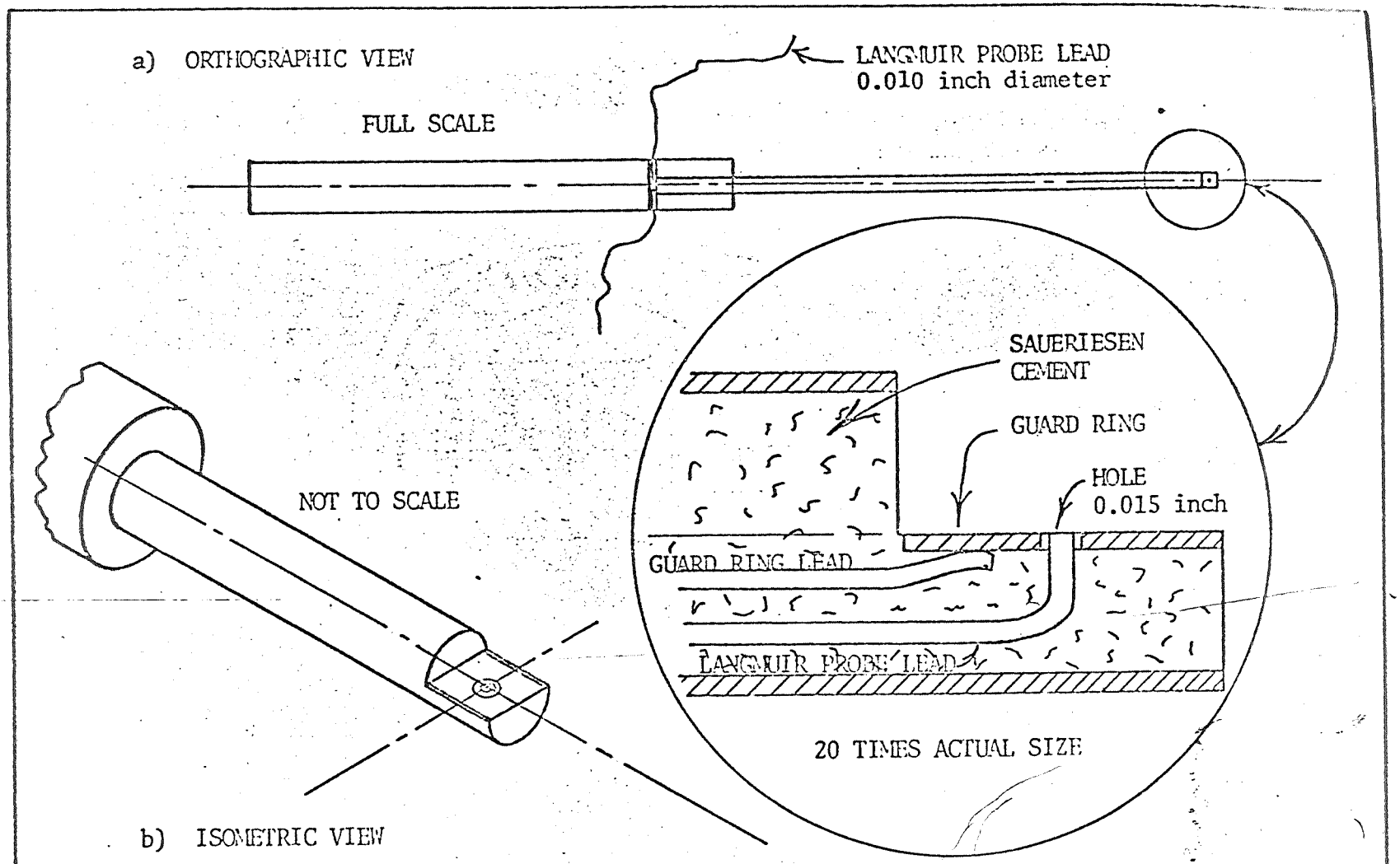

Figure 3.2-6 Langmuir Probe

steel leads from the probe surface and guard ring proved a problem. Most insulation materials will not withstand bakeout temperatures or high vacuum. Several feet of "ML" insulation were provided by PolyScientific of Blacksburg. This insulation is often used at high temperatures in air. As there was no information available on the vacuum capability of the insulation, it was tested by the author. It was given a light bake of just over 100 degrees C., and the pressure in the test vacuum chamber remained at 8×10^{-8} torr. This was approximately the test system's ultimate capability, but still falls short of the ultrahigh vacuum to be reached in the discharge tube. Thus, although no failures of the insulator were noted in these tests, the results were somewhat inconclusive as to the full capability of this material. Nevertheless it was decided to use the ML insulation on the Langmuir probe leads between the probe and the tungsten electrical feedthroughs.

The final step in the Langmuir probe region assembly was the connection of the two probe leads to the tungsten feedthroughs. Two 1/4 inch stainless steel sleeves were used, each of which had a separate hole for a single probe lead and a tungsten rod. The hole for each probe lead was drilled close to the outer surface of a sleeve, so the lead could be inserted into the hole, and the sleeve tapped with a punch for a press fit. The sleeves were manipulated and tightened to the tungsten, not without some difficulty, with a straight Allen wrench in a pin vise. See figure 3.4-2 for a view of the mounted sleeves.

The complete Langmuir probe assembly is shown in figure 3.2-7.

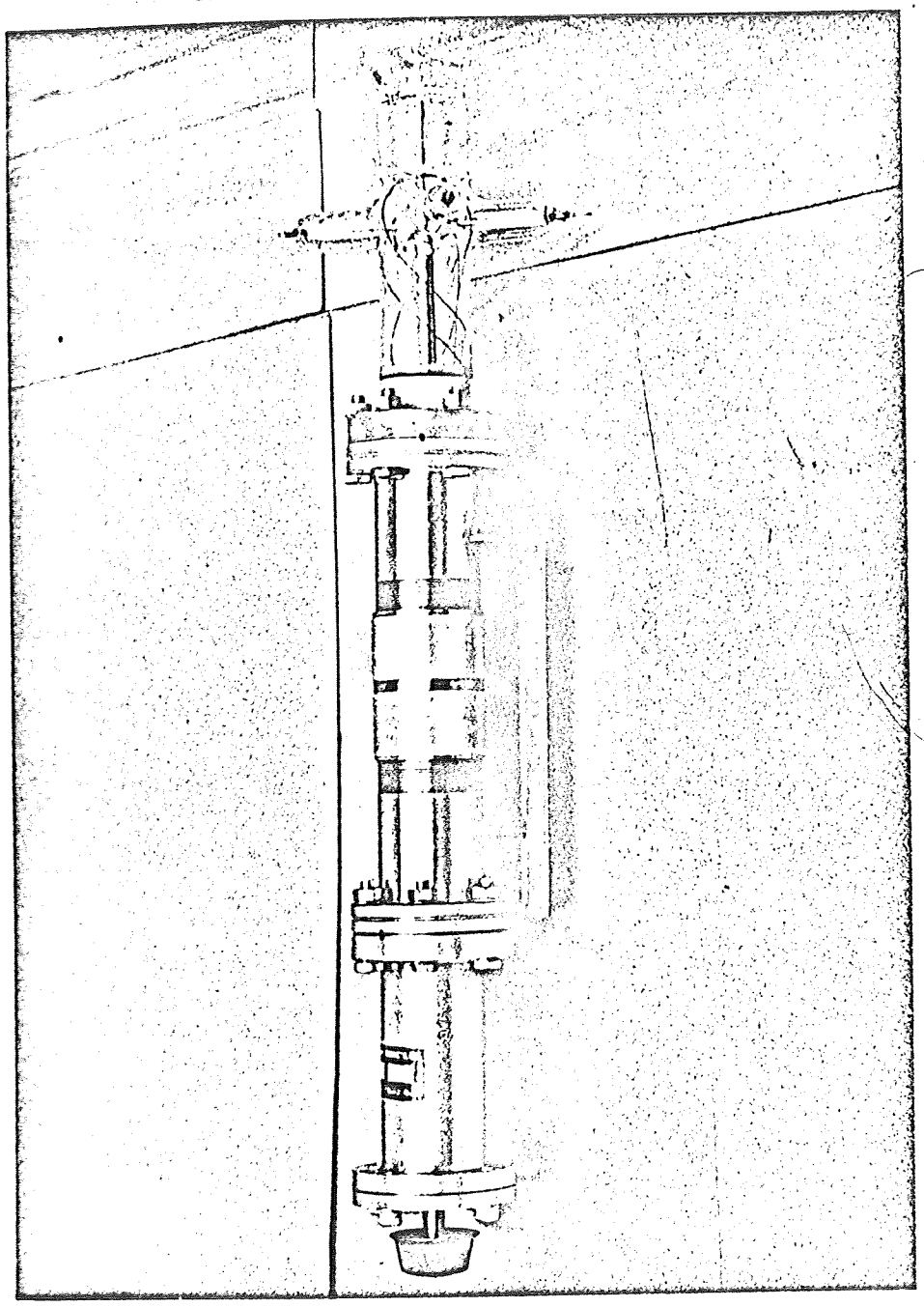

Figure 3.2-7 Completed Langmuir Probe Assembly

3.3 Design and Construction of the Cathode Region

The primary cathode region design problem was the method to be used for imparting 15 cm of linear motion to the cathode. The method chosen involved the transfer of rotary motion to the interior of the discharge tube, where rotary motion would be translated to linear motion. Rotation can be translated to linear motion by rotating a threaded shaft inside a non-rotating, internally threaded sleeve of some sort. With this idea in mind, the problem of support of the cathode remained to be solved.

The cathode itself required a temperature of about 2100 degrees Kelvin for adequate electron emission, since the cathode material was to be pure tungsten. This would require a heating current of roughly 45 amperes in the size of tungsten wire to be used. Some heat shielding of the cathode would obviously be necessary, since the strain point of Pyrex (#7740) is only 485 degrees C., and the stress in the outer glass tubing from the localized heating from the cathode could result in cracking, even if an air blower is used for cooling. A glass press shown in figure 3.3-1 was removed from a type 869B mercury vapor rectifier tube, and it was found that the 1/8 inch diameter tungsten rods in it could handle the required current load without causing the glass press to be heated over 75 degrees C. in air. The press could perform the duties of heat shield support and cathode support, provided that a method could be devised for supporting the press itself.

Finally the cathode support assembly shown in figure 3.3-2 was devised. All parts are stainless steel. The details of the construction

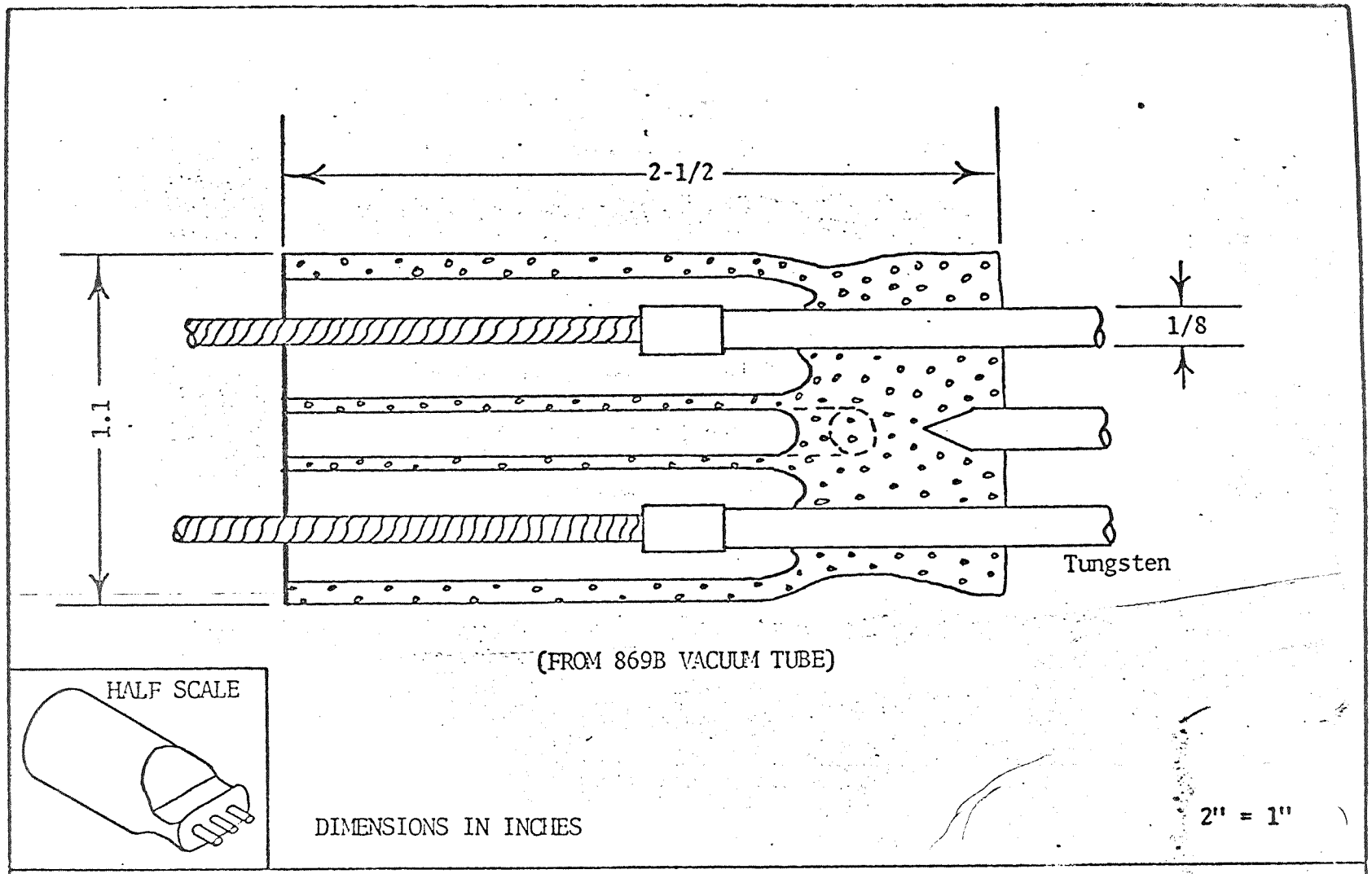

Figure 3.3-1 Half Section of Press Used for Cathode and Heat Shield Support

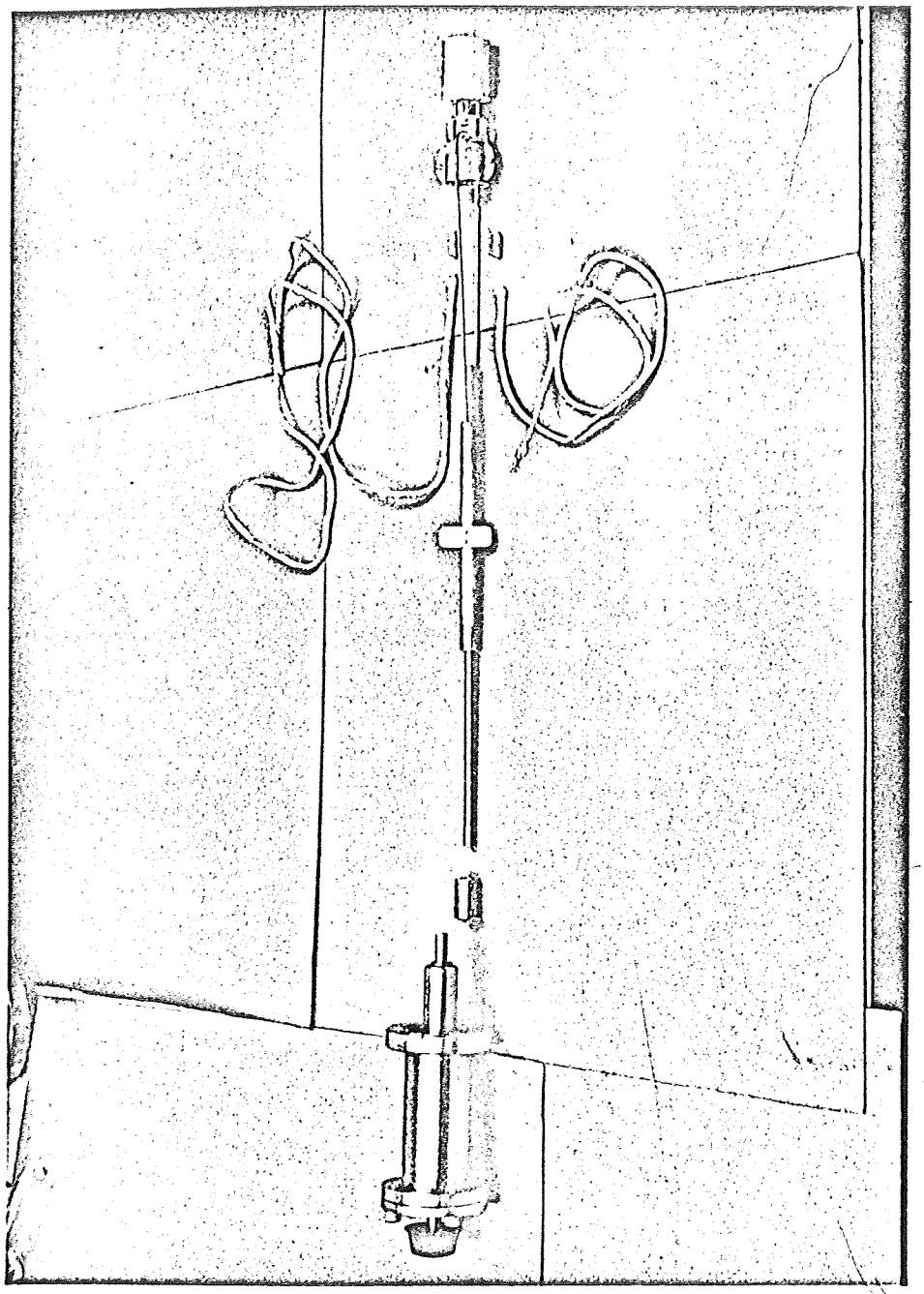

Figure 3.3-2 Cathode Motion and Support Assembly

of the 6 inch threaded spacer are shown in figure 3.3-3. The spacer was designed to be light in weight, and still strong enough to support the cathode assembly. The spacer's 6 inch length serves to maintain alignment between the threaded shaft and the cathode assembly. It has holes drilled in the sides near each end to provide for pumping of the hollow interior. The flat piece on top of the spacer in figure 3.3-2 prevents rotation of the spacer as the inner shaft rotates, by sliding along fixed glass tubing as shown later in this section.

The shaft was threaded for 12 inches of its length to support the threaded spacer and to allow for the 15 cm movement of the spacer and cathode. Figure 3.3-4 is an exploded view of the cathode support assembly. The two 3/32 inch diameter rods connecting the spacer with the clamping device allow the cathode to be retracted without the end of the threaded shaft running into the glass press.

The cathode and heat shield were constructed and mounted on the 869B glass press at International Telephone and Telegraph Company's Electron Tube Division in Roanoke, Virginia. The heat shield was supported by the unused center post of the glass press, and the cathode was connected at each end to the other two 1/8 inch diameter tungsten rods in the press. The cathode is shown in a head on view in figure 3.3-5. The ceramic discs around the cathode leads prevent radiant heat from escaping through the rear of the heat shield.

The lead-in-wires for cathode current would require electrical insulation, to prevent a short circuit to each other or to the cathode supporting mechanism. Glass tubing was deemed the best answer to this problem, and a piece was designed which allowed for insulation of the

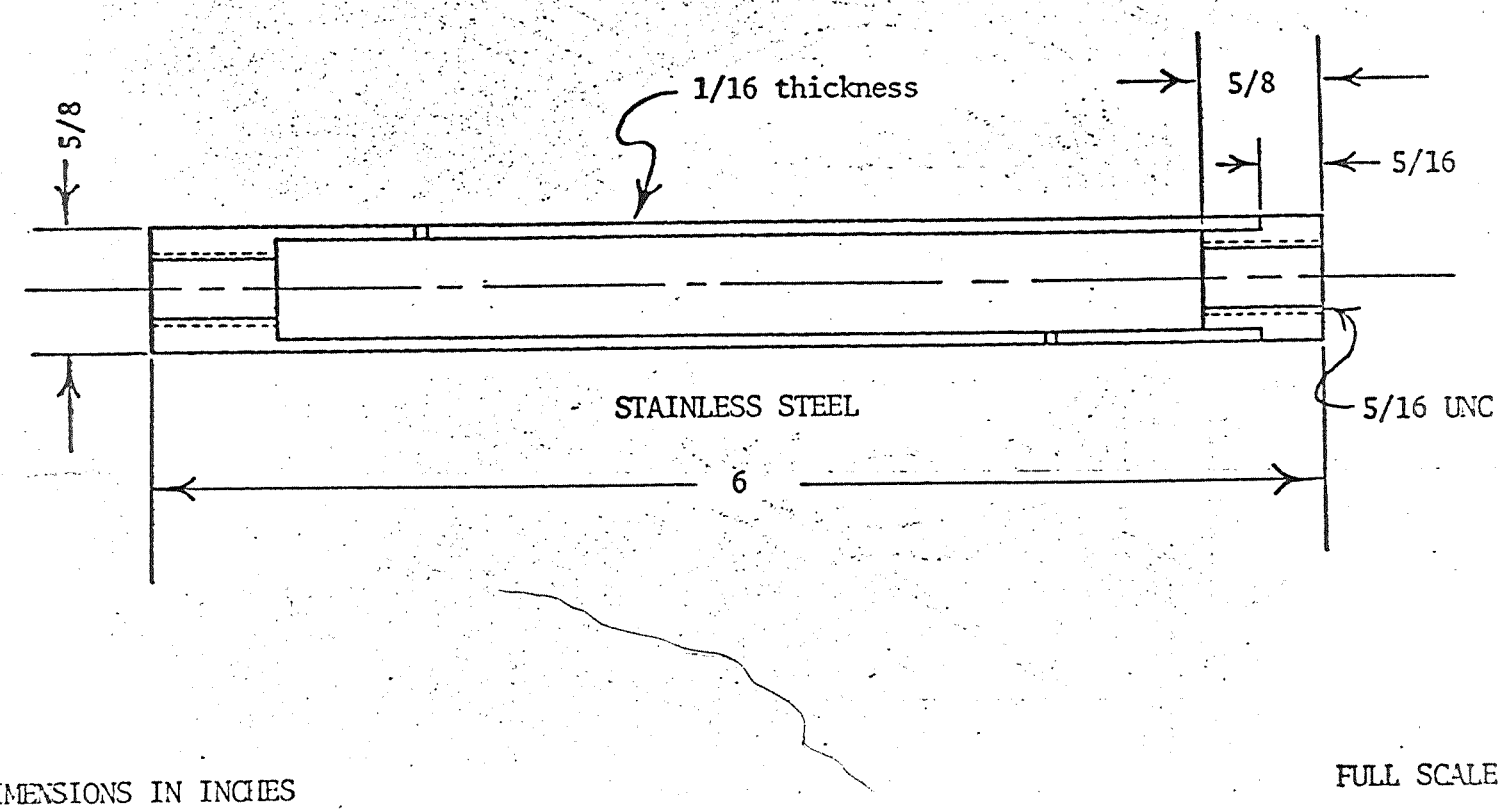

Figure 3.3-3 Detail of Six Inch Spacer Used in Cathode Motion and Support Assembly

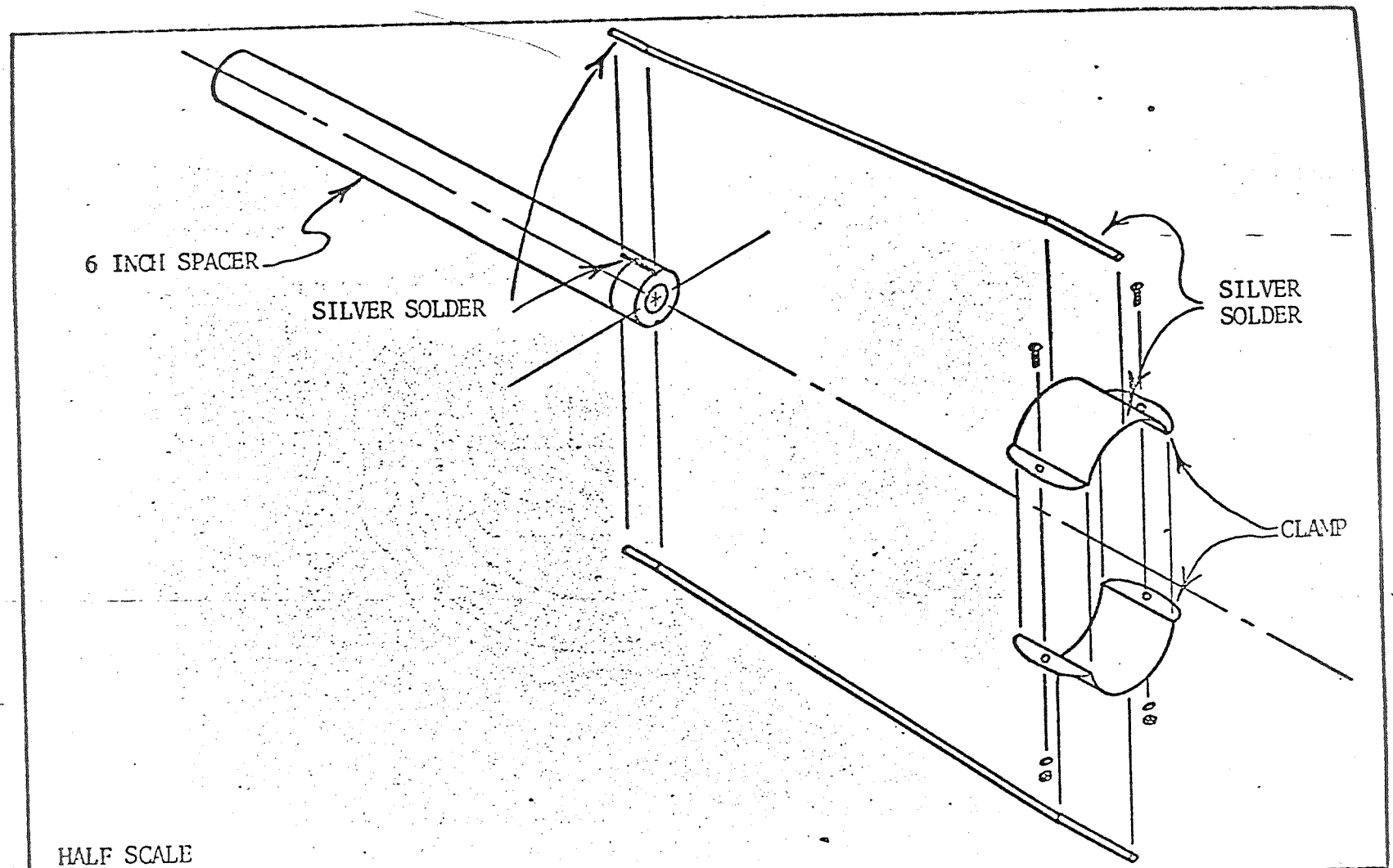

Figure 3.3-4 Exploded View of Cathode Motion and Support Assembly

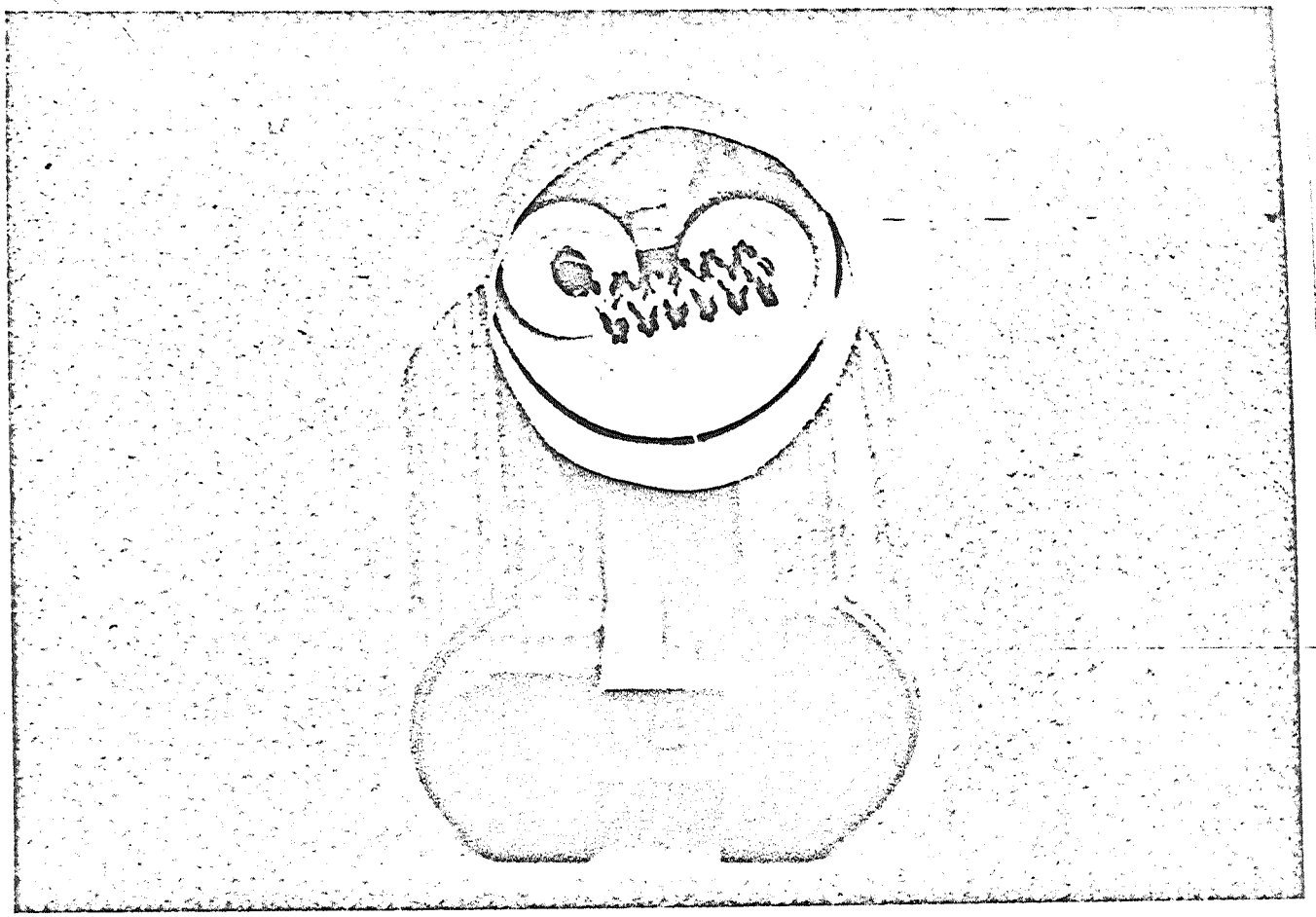

Figure 3.3-5 Head on View of Cathode

lead-in wires for all positions of the cathode. A stationary piece of glass tubing 12 mm in diameter houses a movable piece of 8 mm diameter tubing which, in turn, houses the lead in wire and follows the wire as the cathode is moved. This is illustrated in the cutaway drawing of figure 3.3-6. Figure 3.3-7 is a photograph of the completed glasswork in this area, with a cathode lead in one of the stationary 12 mm diameter tubes. Figure 3.3-8 shows the partially assembled cathode region. The flat stainless steel piece is shown in the figure as it rides on the 12 mm glass tubing, preventing rotation of the cathode assembly. The movable 8 mm tubing is not shown in either photograph.

The cathode leads themselves are finely stranded, silver coated copper wire, clamped to existing wires in the rear of the glass press. A means of retracting the wire when the cathode is moved away from the anode is provided by the glass reservoirs shown in figure 3.3-6. The copper leads, when given a twist, tend to ball up in the reservoir, placing a small tension on the wire in the tubing to prevent it from binding. The final sealing of the cathode leads to two 1/8 inch diameter tungsten feedthroughs was made with stainless steel sleeves 1-3/8 inches long, and 5/16 inch in diameter. The sleeves were long so that the glass-blower's torch would not cause excess oxidation on the copper cathode leads.

3.4 Design and Construction of the Anode Region

The anode itself was removed from a vacuum tube, type 3B25. The anode was first mounted on a glass tripod, and the tripod was mounted in Pyrex tubing, at the point where the glow discharge tube tapers to

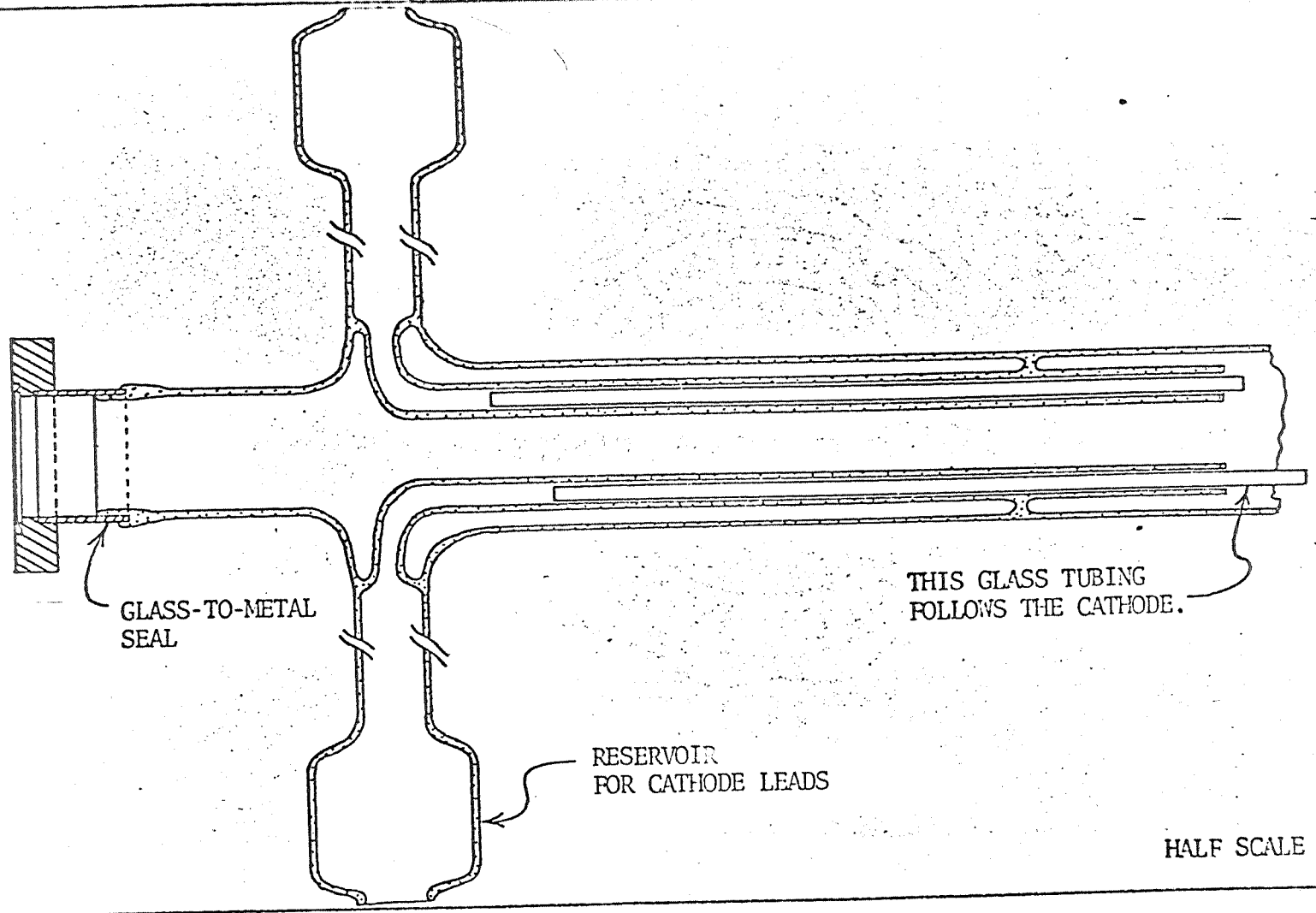

Figure 3.3-6 Cathode Region Glasswork in Cross Section

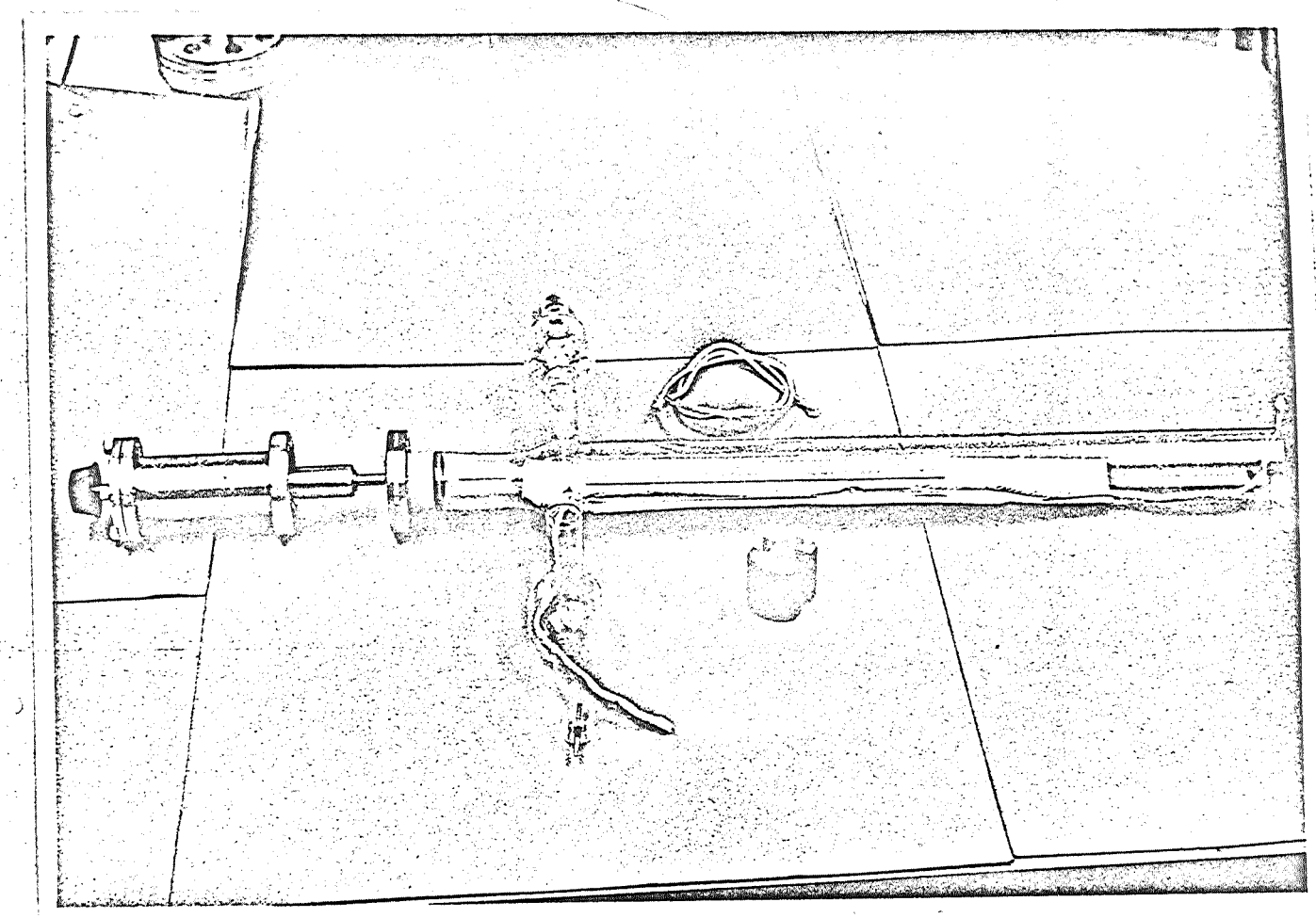

Figure 3.3-7 Completed Glasswork for the Cathode Region

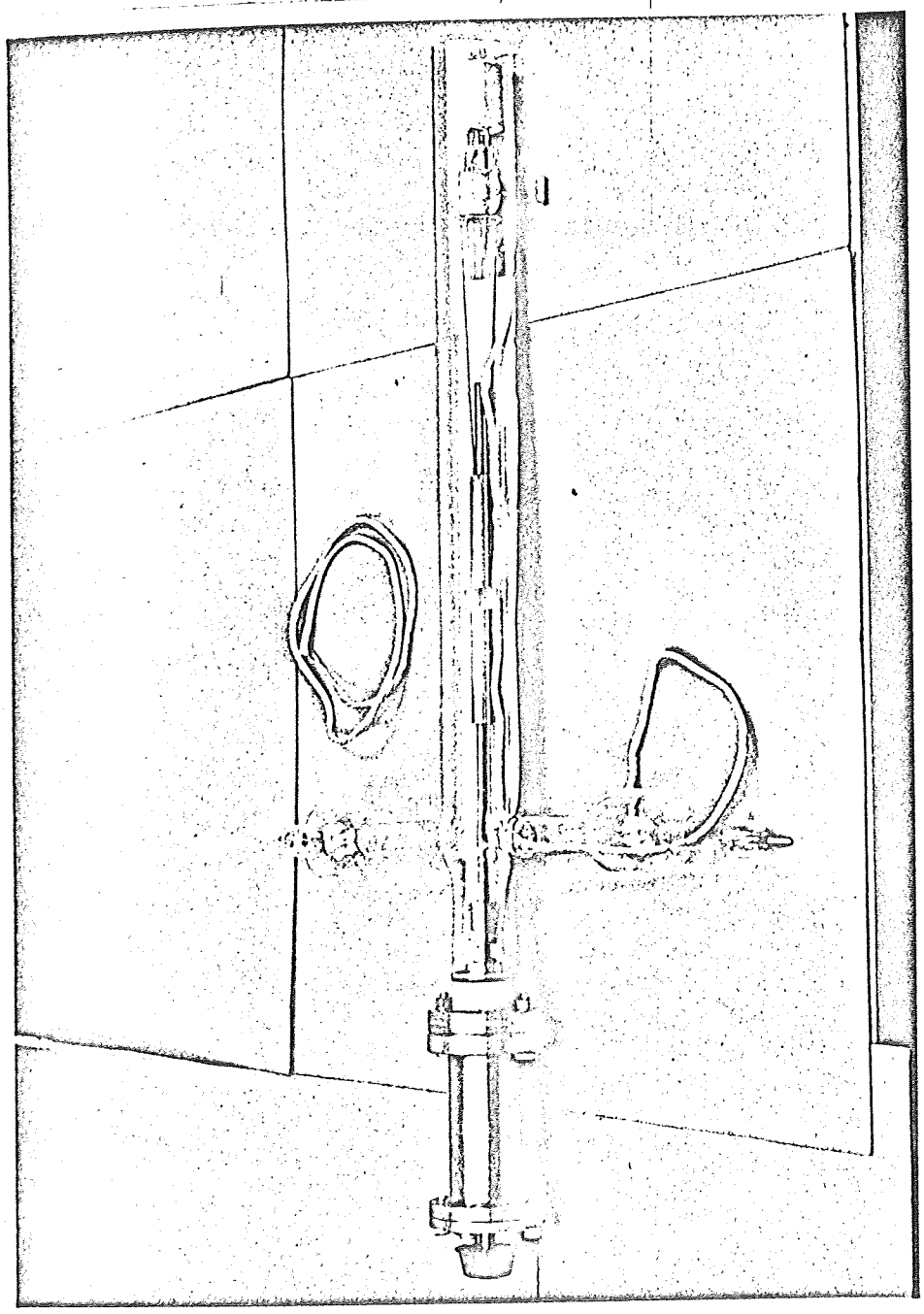

Figure 3.3-8 Partially Assembled Cathode Region

26 mm as shown in figure 3.4-1. This positioning allowed tube symmetry to be maintained and permitted a pumpout port to be located directly behind the anode in the discharge tube. A wire was fastened to the anode with a copper sleeve. The other end of the wire was originally fastened to a tungsten electrical feedthrough by spotwelding, but this proved to be an unreliable connection. This connection was replaced by a stainless steel sleeve which fits over the tungsten rod and the wire. The stainless steel sleeve was manipulated and tightened with an Allen wrench, similar to the manner in which the Langmuir probe leads were attached.

The tungsten-to-glass seal for electrical feedthrough to the anode was originally made practically flush with the 26 mm diameter pumpout port tubing, as shown in figure 3.2-4. During the cleaning process the tungsten electrical feedthrough at the anode was inadvertently over-cleaned, resulting in a possible leak at the seal. Subsequent reheatings by glassblowers, in an attempt to remake the seal, only resulted in the appearance of cracks in the glass. Finally a new tungsten seal was made with a length of 1/8 inch diameter tungsten rod. The seal was first made in 15 mm diameter Pyrex tubing, and the tubing itself was joined to the glass at the pumpout port. Since this type of tungsten to glass seal is a stronger one, there were no further problems encountered at the seal.

Figure 3.4-2 shows the completed anode construction.

3.5 Final Assembly and Testing

The first regions to be joined together in the discharge tube were

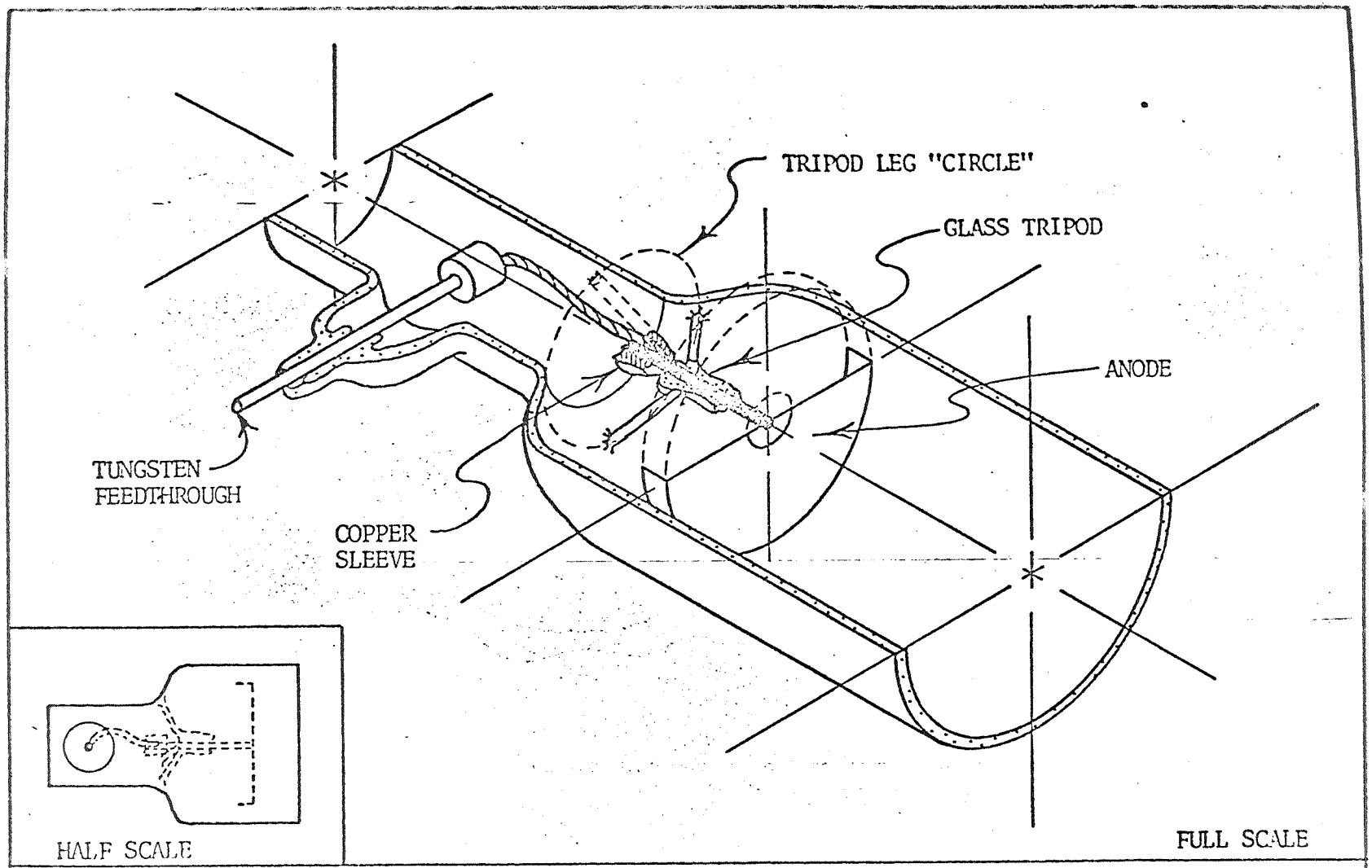

Figure 3.4-1 Isometric View of the Anode Region

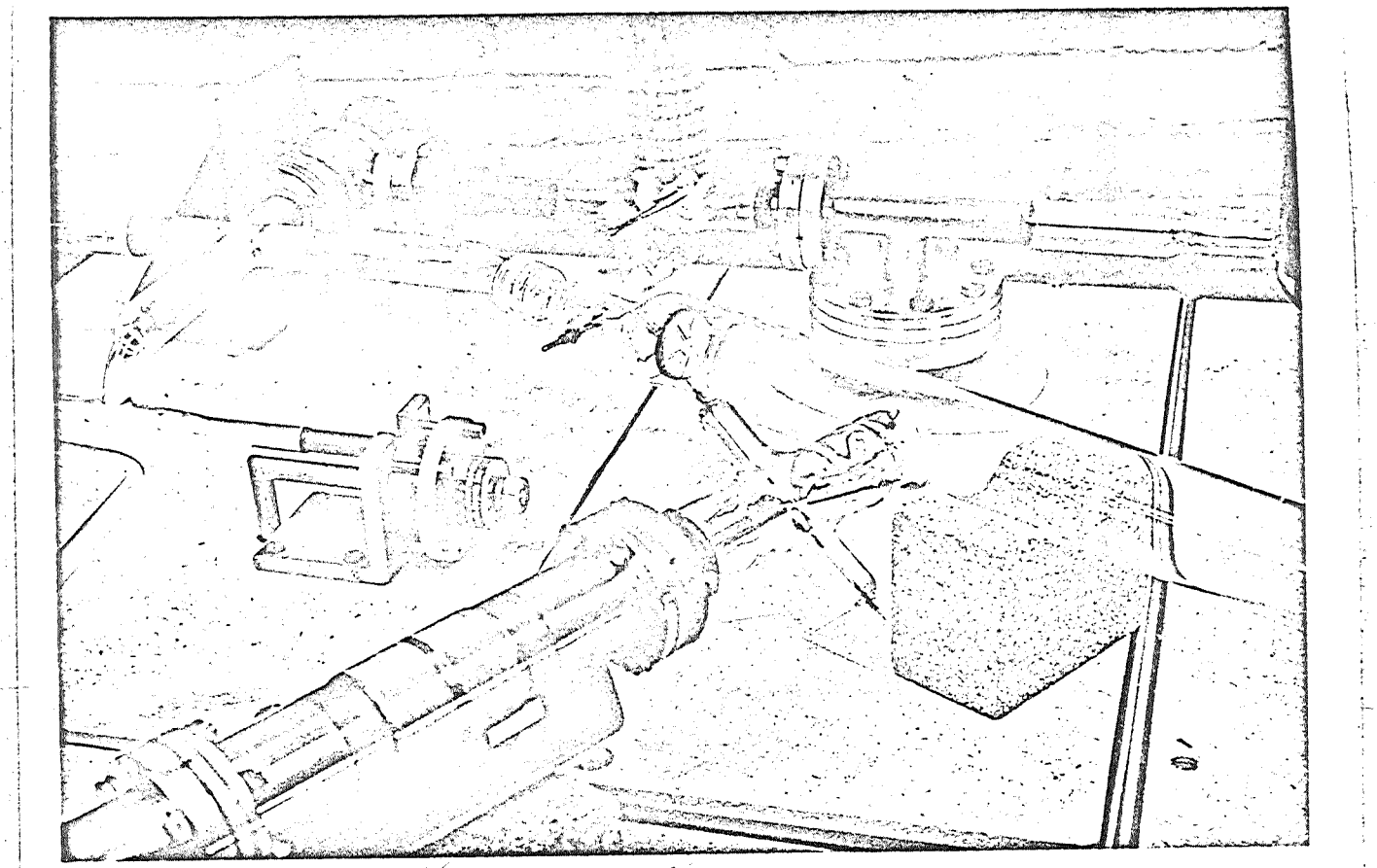

Figure 3.4-2 View of Completed Anode Construction, with Probe Assembly in Foreground

the anode and Langmuir probe assembly. These two areas were finished while the cathode was in the final design stages. When the cathode assembly had been completed, it was sealed to the other section of the discharge tube, after which the entire tube was sealed to the vacuum system near the anode.

After a short pumpdown, it was apparent that a leak existed, since the pressure would not go below 7×10^{-5} torr. Two leaks were discovered and repaired, one due to an improperly tightened Conflat flange seal, and the other at one of the probe's glass-to-tungsten seals. The latter leak was repaired by a glassblower. The pumpdown was reinitiated, and a pressure of 3.5×10^{-6} torr was reached without baking. During this pumpdown, it was noted that the cathode assembly threaded shaft had galled, at first refusing to rotate more than a half turn, then freezing completely. In attempting to free the threads by turning the shaft, two screws holding the flat piece in place on the 6 inch spacer were loosened. (Refer to figure 3.3-2.) This problem was temporarily neglected, and localized baking was begun.

The localized baking involved the wrapping of heat tape around one portion of the tube, followed by the complete covering of the area with aluminum foil, in an attempt to maintain uniform heating. The localized baking was well underway when a crack formed at the discharge tube connection to the vacuum system, near the anode.

The crack was apparently due to the torsion and other stresses applied to the joint, and because the joint had not been annealed. The crack opened the entire system to atmospheric pressure. A glass bellows was blown at the VPI Glassblowing Shop, and placed at the anode pumpout

port. The pumpdown was started again and the localized baking was reinitiated. Current was applied to the cathode for a short time, with a great degree of outgassing the result.

The pressure limit had been reduced to 4.5×10^{-7} torr when a small intermittent leak was discovered in the purchased rotary motion feedthrough located near the Langmuir probe. The leak temporarily sealed itself, and baking continued.

The loose screws in the cathode region were tightened after the system had been opened again to the atmosphere. Before this was done, some neon was bled into the system, in an effort to reduce contamination when the air was let in. To get to the loose screws without completely dismantling the discharge tube, a hole was made in the glass directly above the screws. To keep the screws from loosening again, 0.005 inch diameter stainless steel wire was placed around the screw heads to act as washers, as no stainless steel washers were available. The system was resealed and again the pumping began. The pressure dropped to its former limit in a short time, perhaps attributable to the neon coating of the interior walls.

Cathode heating was begun. So as not to increase the pressure in the discharge tube too drastically, the current was incremented in steps of 1 ampere from 15 to 41 amperes, the system pressure remaining below 5×10^{-6} torr at all times. Figure 3.5-1 shows the cathode with approximately 30 amperes of current. Localized baking with heat tape continued while the cathode was being heated. After all heat had been removed, the pressure was reduced to 1.9×10^{-7} torr. A bakeout oven was then placed over the entire system and heating was begun. The final

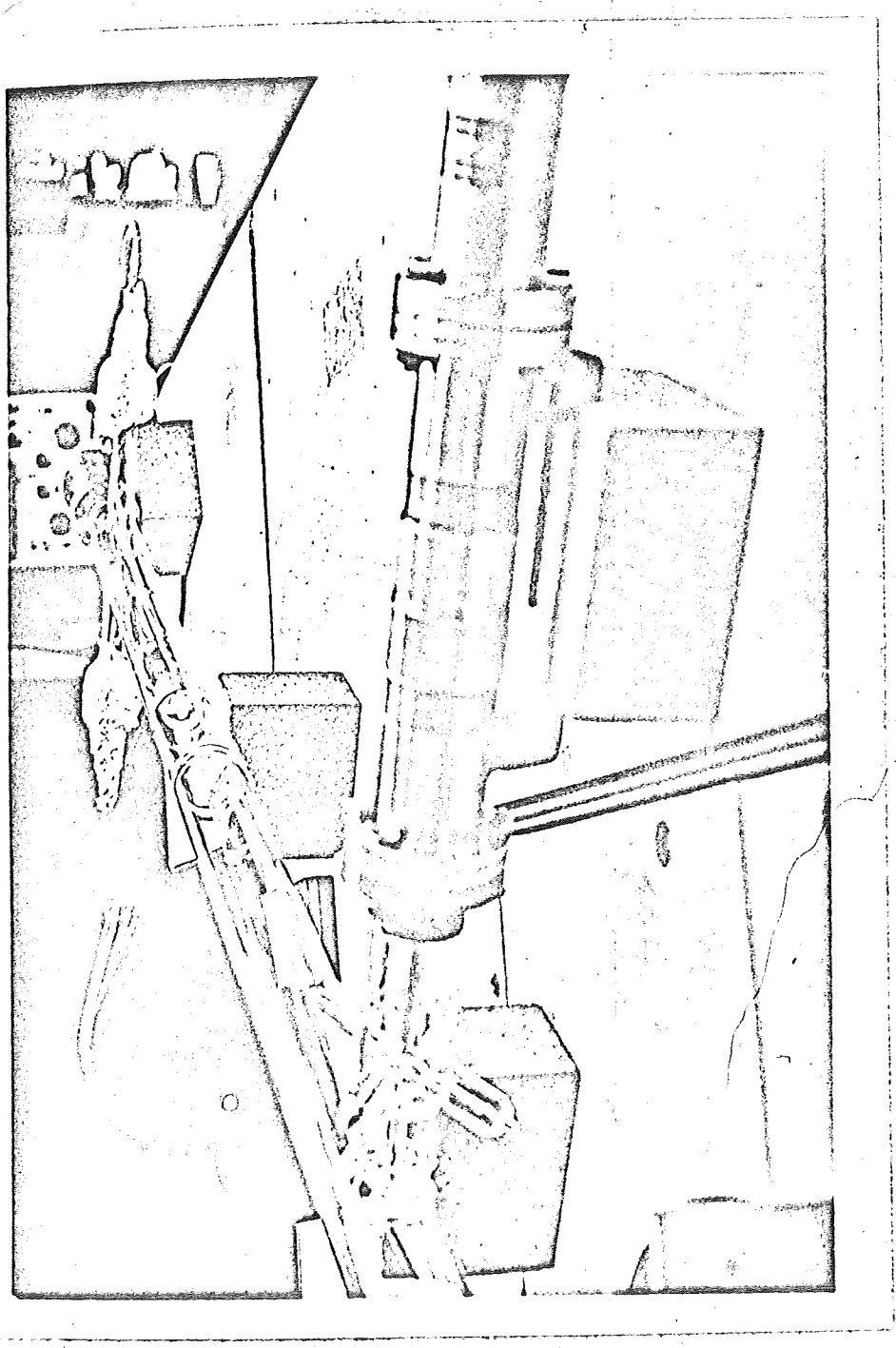

Figure 3.5-1 View of Discharge Tube with Approximately 30 Amperes of Cathode Current

bakeout temperature used in this bake was 200 degrees C. Following the bakeout, which lasted 48 hours at maximum temperature, the pressure reached was still 1.9×10^{-7} torr.

A leak check was made, and two leaks were located which had not been discovered previously. One was in the cathode region rotary motion feedthrough, and the other in the glasswork which connected bottles of inert gas to the discharge tube. Spraying methanol on the leaking regions at least temporarily sealed the leaks in the rotary motion devices, and the pressure was reduced almost immediately to 5×10^{-8} torr. The leak in the glass under the vacuum system table continued. By closing a bellows-sealed valve leading to the gas bottles, it was found that the system pressure was reduced quickly to 3×10^{-8} torr.

Figure 3.5-2 shows the discharge tube with a gas discharge fired.

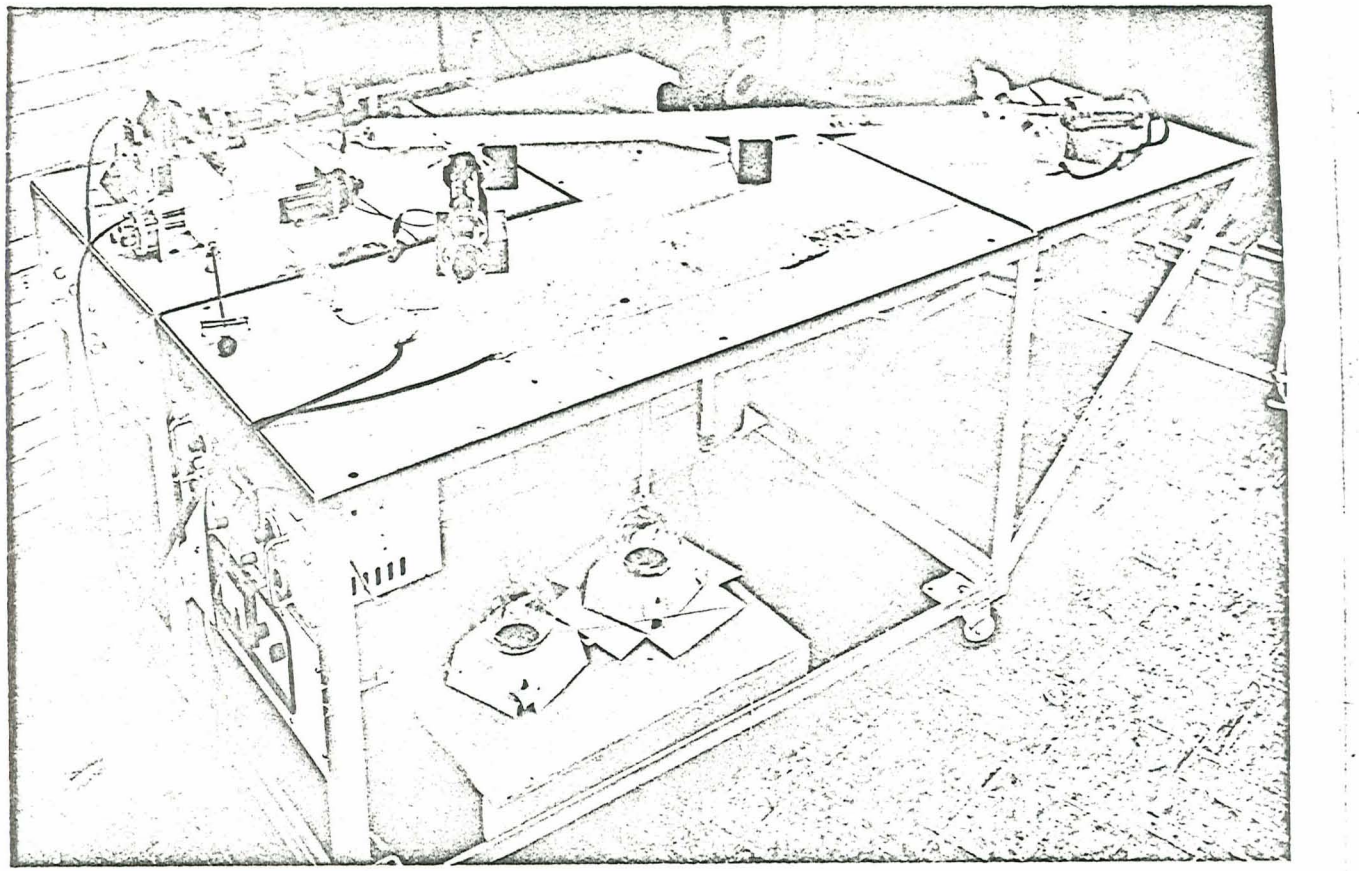

Figure 3.5-2 The Discharge Tube with a Discharge Fired

4. CONCLUSIONS AND RECOMMENDATIONS

Apparently some sources of contamination remain in the new discharge tube. However, it does seem to work properly with the exception of the cathode movement apparatus.

The threads of the cathode motion assembly seem to gall at some value of pressure as the discharge tube is pumped out. This is apparently due to the removal of adsorbed gases from the threads. It appears that these gases, when present, act as a lubricant. The cathode can be moved, but this involves a lengthy job of opening the system to atmosphere, or dry nitrogen, then moving the cathode and pumping the system down, baking it, etc., until the interior of the discharge tube is clean again.

Redesign of the cathode movement apparatus is in order, with the replacement of the threaded mechanism the primary concern. Another improvement in this region would be the installation of springs for cathode lead retraction, if the same or similar glasswork design is used. The glasswork design would be improved by straightening the right angle in the 12 mm glass tubing used for electrical insulation, to help prevent the cathode supply leads from binding in the tubing.

The best answer to the cathode motion problem may be a linear motion feedthrough arrangement with a long metal bellows. This would make the tube longer than its present length, but should help to make cathode motion more reliable.

During the localized baking of the glow discharge tube, the probe ML insulation changed color, indicating that it may be oxidizing, or more likely, decomposing at higher bakeout temperatures. One step toward a cleaner system would be the elimination of the ML insulation,

replacing it with some sort of stacked ceramic insulation such as found with some vacuum tubes, for instance type NL-740P.

It also might be desirable to move the electrical feedthrough arrangement for the Langmuir probe to a position between the rotary motion feedthrough and the linear motion feedthrough, using ceramic-to-metal seals. This would allow the complete removal of the probe from the discharge tube without disconnecting the stainless steel sleeves which attach the probe leads to the electrical feedthroughs.

The linear motion feedthrough designed for the Langmuir probe works quite well. In future designs it would be desirable to use thicker walled pipe for the outer turnbuckle, to allow a coarser thread to be used. With the device now used, it takes 12 complete revolutions of the center sleeve of the turnbuckle to move the Langmuir probe a distance of 1 inch. Special Conflat flanges are made with internally threaded bolt holes, which would make it possible to use any diameter pipe, up to 2-3/4 inch for the turnbuckle. If regular Conflat flanges are used, it is necessary to leave space for nuts or bolts, limiting the pipe diameter to approximately 2 inches.

BIBLIOGRAPHY

1. Bond, R. H., Directed Electron Velocity Distributions in Rare Gas Discharges Using Guard Ring Probes, California Institute of Technology Technical Report #25, Pasedena, Calif., June 1965.

2. Diels, K., and Jaeckel, R., Leybold Vacuum Handbook, translated by H. Adam and J. Edwards, Pergammon Press, Oxford 1966.

3. Dushman, Saul (late), and Lafferty, J. M., Editor, Scientific Foundations of Vacuum Technique, John Wiley and Sons, Inc., New York, Second Edition 1962.

4. Geppert, Donovan V., Basic Electron Tubes, McGraw-Hill Book Co., Inc., New York, First Edition 1951.

5. Guthrie, Andrew, Vacuum Technology, John Wiley and Sons, Inc., New York 1963.

6. Hoag, J. Barton, Ph. D., Electron and Nuclear Physics, D. Van Nostrand Co., Inc., New York, Second Edition 1938.

7. Holkeboer, David H., Jones, Donald W., Pagano, Frank, Sauteler, Donald J., Vacuum Engineering, Boston Technical Publishers, Inc., Cambridge, Mass., 1967.

8. Kohl, Walter H., Materials Technology for Electron Tubes, Reinhold Publishing Corporation, New York, 1951.

9. Koller, Lewis R., Ph.D., The Physics of Electron Tubes, McGraw-Hill Book Co., Inc., New York, Second Edition 1937.

10. Lewin, Gerhard S., Ph.D., Fundamentals of Vacuum Science and Technology, McGraw-Hill Book Co., Inc., New York 1965.

11. Pirani, M., and Yarwood, J., Principles of Vacuum Engineering, Reinhold Publishing Co., New York 1961.

12. Rosebury, Fred, Handbook of Electron Tube and Vacuum Techniques, Addison-Wesley Publishing Co., Inc., Reading, Mass. 1965.

13. Strong, John, Ph.D., Procedures in Experimental Physics, Prentice-Hall, Inc., New York 1938.

14. Van Atta, C. M., Vacuum Science and Engineering, McGraw-Hill Book Co., Inc., New York 1965.

15. Yarwood, John, M.Sc., F. Inst. P., High Vacuum Technique, Chapman and Hall, Ltd., London, England, Fourth Edition 1967.

Young, David Mathieson and Crowell, A. D., Physical Adsorption of Gases, Butterworth Scientific Publications 1962.

* Numbers refer to cited references.

Semi-Annual Progress Report No. 9

to the

NATIONAL AERONAUTICS AND SPACE ADMINISTRATION

in connection with

NASA Grant NGR 47-004-006

Part 6 of 8 Parts

Final Report

Part C

V.P.I. Project 313138

A Comparison of Theoretical and Experimental Directed Electron Velocity Distributions in Rare Gas Discharges

by

M. G. Funk, Jr.

R. H. Bond

Virginia Polytechnic Institute
Blacksburg, Virginia

September, 1969

TABLE OF CONTENTS

		Page
	List of Symbols	iv
	List of Tables and Figures	v
I.	Introduction	1
II.	Theory	3
III.	Solution Procedure	8
IV.	Results	20
V.	Conclusions	27
VI.	Recommendations	29
VII.	References	30
	Appendix A	31
	Appendix B	47
	Appendix C	51

LIST OF SYMBOLS

ϵ	exponential (2.718.....)
e	electronic charge
E	electric field strength
m	electronic mass
v	velocity
f	velocity distribution function
t	time
k	Boltzmann constant
T	temperature
M	neutral atom mass
N	neutral atom number density
n	electron number density
$g(v_z)$	z-directed electron velocity distribution function
erf	error function
Γ	Gamma function
θ_1	angle between the velocity and the electric field
ν_1	collision frequency
σ	collision cross section
λ	mean free path
μ	micron (10^{-6})

LIST OF TABLES AND FIGURES

Table	Title	Page
I	Neon Experimental Conditions	21
II	Helium Experimental Conditions	22
III	Druyvesteyn $G(v_z)$ Values	49

Figure

1	Collision Geometry Describing θ_1	5
2	Neon Collision Cross Section versus Energy	10
3	Helium Collision Cross Section versus Energy	11
4	$h\sigma^2 v^3$ versus Velocity	12
5	$\frac{f_0}{A}$ versus Velocity	13
6	$-\frac{f_1}{A}$ versus Velocity	15
7	$\frac{4\pi f_0 v^2}{A}$ versus Velocity	16
8	Velocity Distribution Function versus Velocity	18
9	$2\pi fr$ versus r	19
10	Neon $G(v_z)$ versus Velocity	23
11	Helium $G(v_z)$ versus Velocity	24
12	Neon Theoretical and Experimental $G(v_z)$ versus Velocity	25
13	Helium Theoretical and Experimental $G(v_z)$ versus Velocity	26

Figure	Title	Page
14	Operational Flow Chart	33
15	Distribution Curves for various Collision Cross Sections	49

I. INTRODUCTION

Conducting probes are known to have been used to explore ionized gases since the eighteen nineties when Crookes made available his work in this area. However, until the work of Irving Langmuir was presented in 1923 the use of probes was not fully understood and lay as a dormant art. Shortly after Langmuir published his probe theory in the form of a series of articles in the General Electric Review of 1924 there commenced a steadily increasing amount of study and research into the field of probes and their use for the measurement of electron velocity distribution functions.

There are, however, two basic areas of concern common to all the probe theories that were developed through the years. The first of these is that in order to apply the probe theories it is necessary to obtain the second derivative of the probe current with respect to probe voltage. Secondly, it is necessary to make the assumption of an isotropic distribution function. Many methods were devised to find the second derivative of the probe curve, but all are prone to a significant error. And quite obviously, the assumption of isotropic distribution functions places a limit on the applicability of the probe theories.

In 1962, R.H. Bond published a paper (Reference 1) in which he demonstrated that for a planar probe the first derivative of probe current with respect to probe voltage is proportional to the function $g(v_z)$, where $g(v_z)$ represents the directed electron velocity distri-

bution yielding the density of those electrons with z-directed velocities in the range v_z to v_z+dv_z. In this analysis it was shown that it is not necessary to assume that the distribution function is isotropic.

In 1965, Bond extended the aforementioned work in a report (Reference 2) to show that if the distribution function is isotropic the first derivative of the probe curve is proportional to $g(v_z)$ for cylindrical and small spherical probes as well as planar probes. Thus, it is seen that by using planar probes one is able to measure any anisotropy which the electron distribution might possess.

A series of experiments described in Reference 2 made use of a guard-ring probe to measure for the first time the directional properties of electron distributions. The plasmas probed were the positive columns of neon and helium hot cathode discharges. The experimental results and distributions obtained were then presented and discussed.

In concluding his report, Bond recommended that it would be of interest to pursue a solution of the theory which was developed for the experiments, under conditions applicable to the experiments. In this manner, by comparison of the theoretical and experimental distributions, it would be possible to determine the validity of the theory. This then is the object of this thesis. The theory is discussed in the next section.

II. THEORY

This section deals with the theory presented in Reference 2. Since a very detailed developement of the theory is given in that source, only those points of particular concern will be discussed in depth.

As stated, our interest lies in the measurement of directed velocity distributions in a plasma. The plasmas of concern are assumed to be weakly ionized so the interactions that dominate are those between electrons and neutrals. In the positive column there exists a high electric field directed along the tube axis, and since there is no applied magnetic field, the electric field is assumed to produce the only external force on the electrons. Also, the distribution function is assumed to have reached a steady state condition and to be spatially homogeneous. With the z-axis along the axis of the tube, the Boltzmann equation becomes

$$\frac{-eE}{m}\frac{\partial f}{\partial v_z} = \left.\frac{\partial f}{\partial t}\right|_{\text{collisions}} \qquad (2.1)$$

where $f(v)\underline{dv}$ gives the density of electrons with velocities within $\underline{dv} = dv_x dv_y dv_z$. The term $\left.\frac{\partial f}{\partial t}\right|_{\text{collision}}$ is the time rate of change of the distribution function due to collisions.

Through the use of:

1. the Chapman and Cowling form for the collision term (Reference 3), which is valid under the assumption of binary, elastic, short-term collisions

2. the approximation that

$$f(v,\theta_1) = f_0(v) + \cos\theta_1 f_1(v) \qquad (2.2)$$

which is obtained from an expansion of the collision term in Legendre polynomials, where higher order terms such as f_2, f_3, etc. are considered negligible and θ_1 is defined by $v\cos\theta_1 = v_z$ and Figure 1

3. and a variety of other approximations and methods of which there is no relevent need to expound

it is shown that

$$\frac{-eE}{\nu_1 m}\frac{\partial f_0}{\partial v} = -f_1 \qquad (2.3)$$

and

$$f_0 = A\varepsilon^{-\int^{v} \frac{mvdv}{kT + \frac{e^2E^2M}{3m^2\nu_1^2}}} \qquad (2.4)$$

where A is a constant. At this point, it is worth noting what the terms f_0 and f_1 represent physically. The f_0 term represents an isotropic distribution whereas f_1 represents an anisotropy which can be interpreted as a drift velocity in the direction of the applied force on the electrons.

Paying particular attention to equation (2.4), it is seen that for $kT >> \frac{e^2E^2M}{3m^2\nu_1^2}$ one obtains a Maxwellian distribution

$$f_0 = A\varepsilon^{-\frac{mv^2}{2kT}} \qquad (2.5)$$

However, for the opposite case of a strong electric field $\left(\frac{e^2E^2M}{3m^2\nu_1^2} >> kT\right)$, the distribution is not in general Maxwellian. It is not possible to evaluate an exact form of this latter distribution function unless

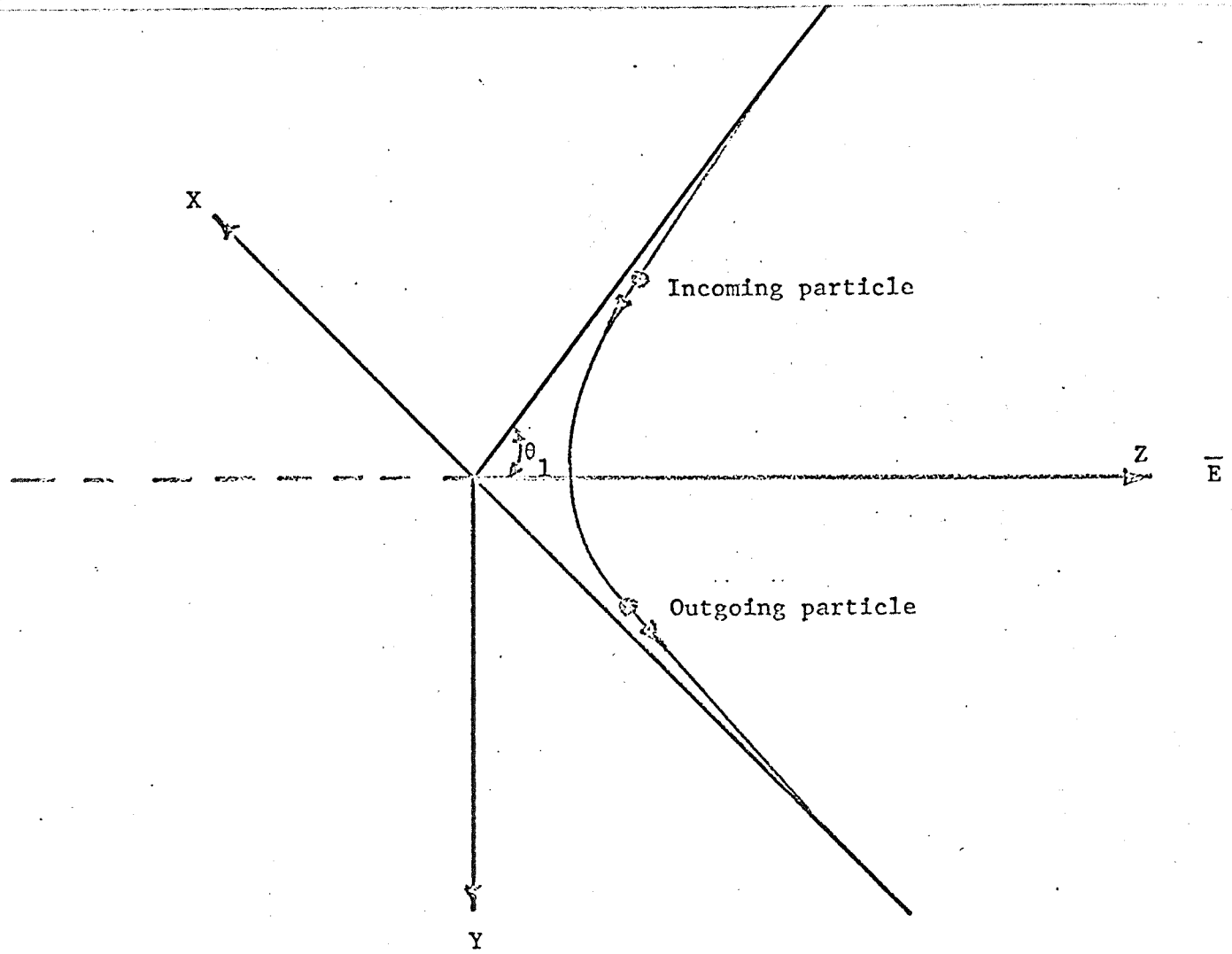

Collision Geometry Defining θ_1

Figure 1

ν_1 is known as a function of v. If the mean free path (λ) is assumed independent of v $\left(\nu_1 = \frac{v}{\lambda}\right)$, the Druyvesteyn distribution

$$f_0 = A\varepsilon^{-\frac{3m^3v^4}{4\lambda^2e^2E^2M}} = A\varepsilon^{-h^4v^4} \qquad (2.6)$$

is obtained. It is important to mention at this time that the purpose of this thesis (as will be seen in the next section) is to consider the case of non-constant mean free path and the constant case is presented only for clarification.

The constant term A in the preceding equations can be evaluated by noting that the integral of f over all velocity space yields the electron density n, i.e.,

$$n = \int_{-\infty}^{\infty} f\underline{dv} = \int_0^{\infty}\int_0^{2\pi}\int_0^{\pi} fv^2\sin\theta_1\, d\theta_1 d\phi dv \qquad (2.7)$$

where it is recalled that a relationship for f is given by equation (2.2). For the case of a Druyvesteyn distribution

$$A = \frac{nh^3}{\pi\Gamma\left(\frac{3}{4}\right)} . \qquad (2.8)$$

Now, the desired function $g(v_z)$ can easily be calculated. Remembering that this function gives the density of electrons with z-directed velocities in the range v_z to $v_z + dv_z$ without regard to their x- or y-velocities, it is seen that $g(v_z)$ is found by integration of f over all possible v_x and v_y yielding

$$g(v_z) = \int_{-\infty}^{\infty}\int fdv_x dv_y \qquad (2.9)$$

or in terms of polar coordinates

$$g(v_z) = 2\pi \int_0^\infty frdr \quad . \qquad (2.10)$$

For the Druyvesteyn distribution, equation (2.10) becomes

$$g(v_z) \simeq \frac{\sqrt{\pi} nh}{2\Gamma\left(\frac{3}{4}\right)} \{1 - \mathrm{erf}(h^2 v_z^2)\} \qquad (2.11)$$

where the f_1 term has been ignored as it is shown in the Appendix of Reference 2 that it is insignificant except for large v_z.

Thus, it is seen that the theory developed leads to a series of equations allowing calculation of the z-directed electron velocity distribution function. And this theory hinges, again, on the following major conditions:

1. The degree of ionization is low so that only electron-neutral collisions need be given attention.

2. Only elastic, short-term, binary collisions are considered.

3. The velocity distribution function f can be represented by equation (2.2).

Using this theory then, and provided the conditions and assumptions are valid, one should be able to calculate the theoretical velocity distribution functions in order to compare them with the measured experimental distributions.

III. SOLUTION PROCEDURE

The solution of the theoretical equations to obtain the distribution functions is accomplished through the use of an IBM System/360 digital computer. This section discusses the techniques and procedure followed in obtaining the computer solution.

Consider the following equations given in the previous section:

$$f_0 = A\,\epsilon^{-\int_0^v \frac{mvdv}{kT + \frac{e^2E^2M}{3m^2\nu_1^2}}} \tag{3.1}$$

$$-f_1 = \frac{eE}{-\nu_1 m}\frac{\partial f}{\partial v}0 \tag{3.2}$$

$$f = f_0 + \cos\theta_1 f_1 \tag{3.3}$$

$$n = \int_0^\infty \int_0^{2\pi} \int_0^{\pi} fv^2 \sin\theta_1 d\theta_1 d\phi dv \tag{3.4}$$

$$v\cos\theta_1 = v_z \tag{3.5}$$

$$g(v_z) = 2\pi \int_0^\infty frdr \tag{3.6}$$

Now, it is seen that equation (3.1) cannot be solved directly unless all of the terms are independent of v. And ν_1 in not independent of v, unless the collision cross section σ is constant, since

$$\nu_1 = N\sigma v \quad . \tag{3.7}$$

For the special case where σ is constant (Druyvesteyn distribution) equation (3.1) can be directly integrated and yields $g(v_z)$ as given by equation (2.11). However, since the solutions of interest are those of neon and helium it is necessary to determine the relation-

ship between σ and v for these two gases. According to Rose and Clark (Reference 4) this relationship is given by Figures 2 and 3, in which it is seen that σ and v are not independent. With the assumption of a strong electric field $\left(\frac{e^2E^2M}{3m^2\nu_1^2} >> kT\right)$ equation (3.1) becomes

$$f_0 = A\varepsilon^{-\int^v \frac{3m^3\nu_1^2 v dv}{e^2E^2M}} = A\varepsilon^{-\int^v \frac{3m^3N^2\sigma^2v^3dv}{e^2E^2M}}$$

$$= A\varepsilon^{-\int^v h_1\sigma^2v^3dv} \qquad (3.8)$$

where A and h_1 are constants for each gas. The solution of equation (3.8) is then obtained by numerical integration over the desired range of v. This is accomplished most easily on the computer by plotting $h\sigma^2v^3$ versus v to obtain a relationship similar to Figure 4. The area under this curve from zero to v yields the value of the integral term $\int^v h_1\sigma^2v^3dv$ for the desired v. Thus, the value of f_0/A can be found for each desired v and is given by a curve similar to Figure 5. Since f_0/A goes to zero so quickly, it is only necessary to integrate to values of v beyond the point where f_0/A becomes relatively small. This point is noted to be at values of v in the range 5.5-6.3 x 10^6 meters per second for neon and 2.5-3.0 x 10^6 meters per second for helium for those conditions considered. However, for both gases the integration is carried to values of 6.5 x 10^6 meters per second.

Now that f_0/A is known, it is relatively easy to determine f_1,

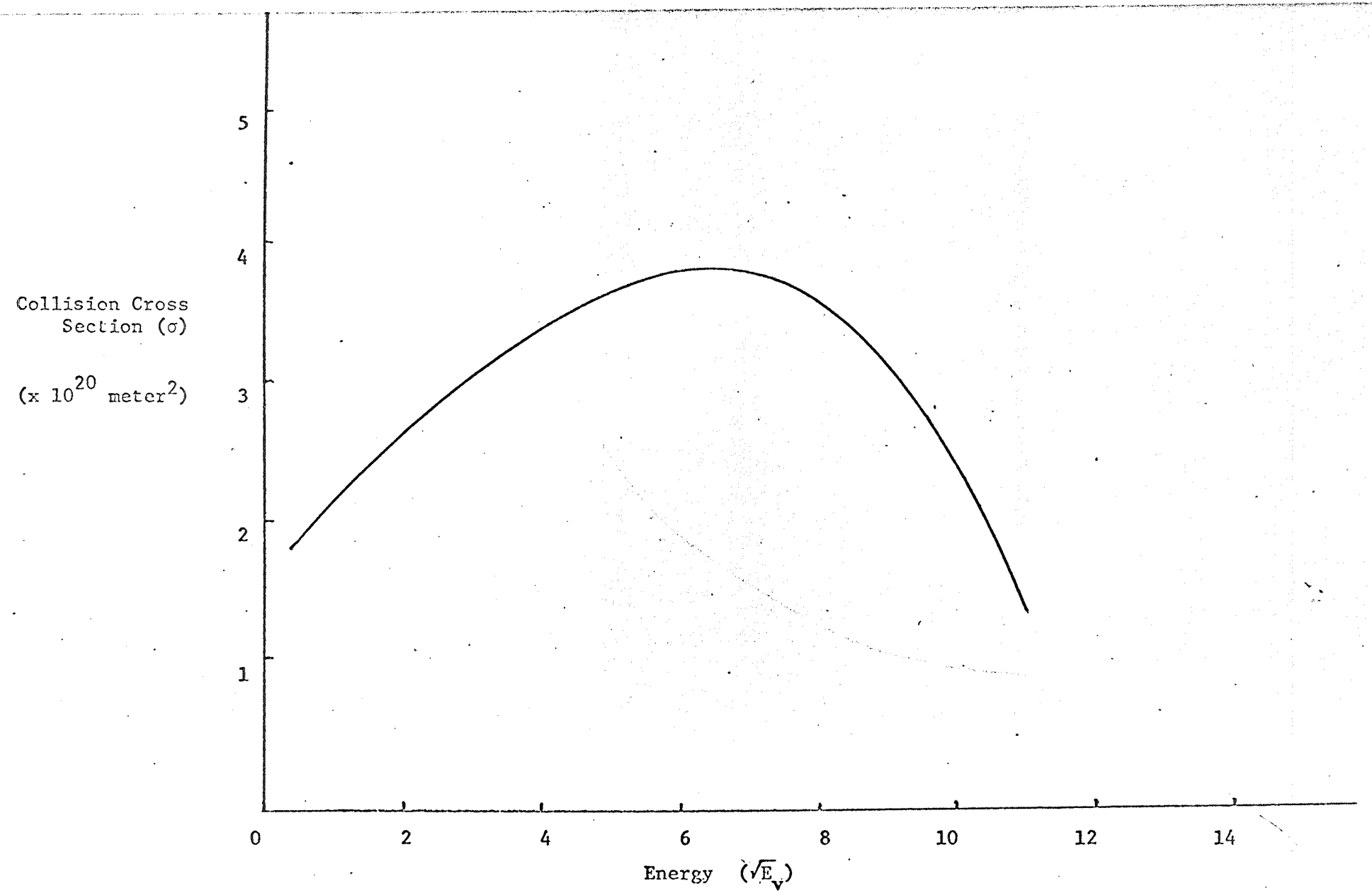

Neon Collision Cross Section versus Energy

Figure 2

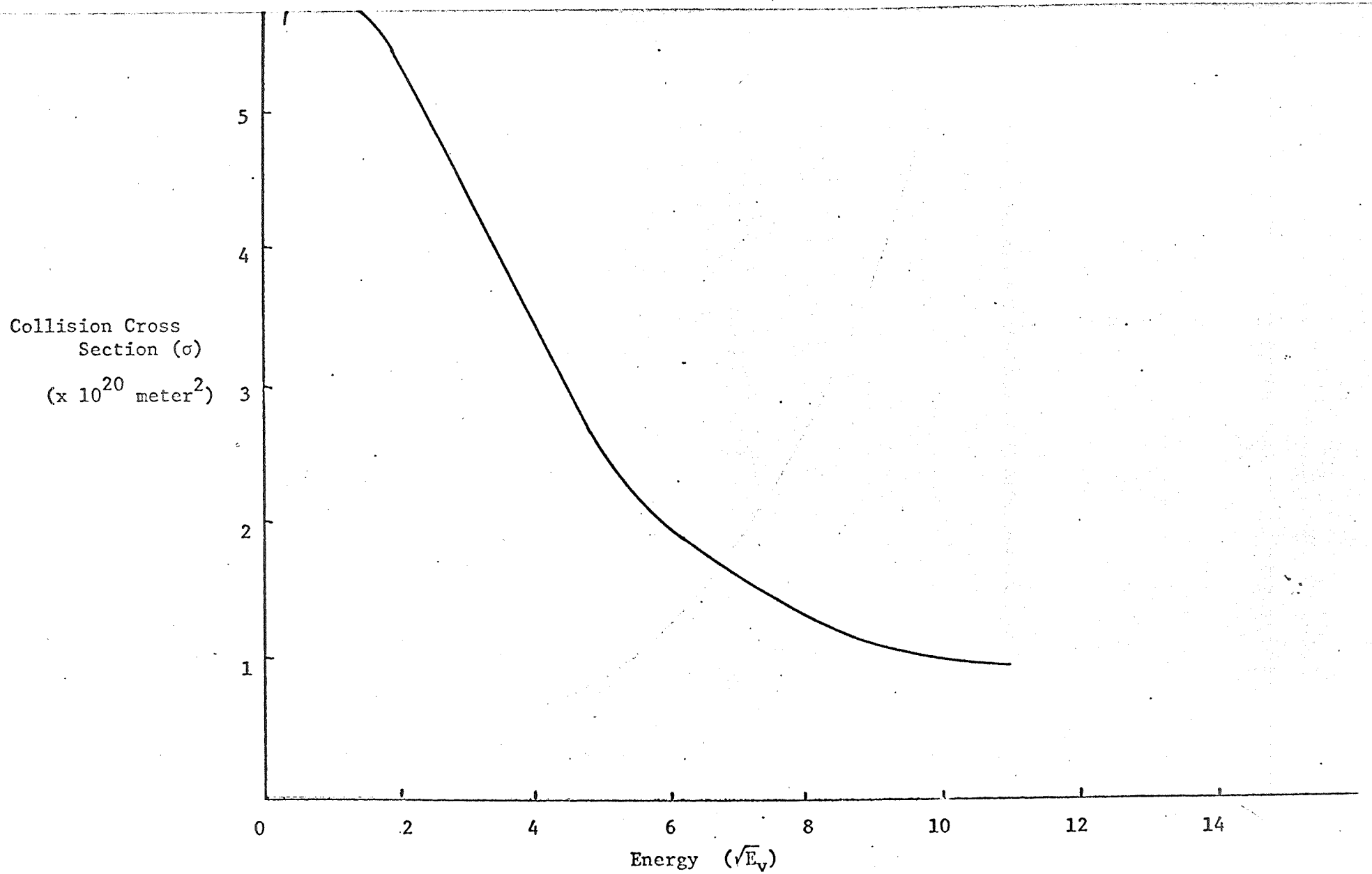

Helium Collision Cross Section versus Energy

Figure 3

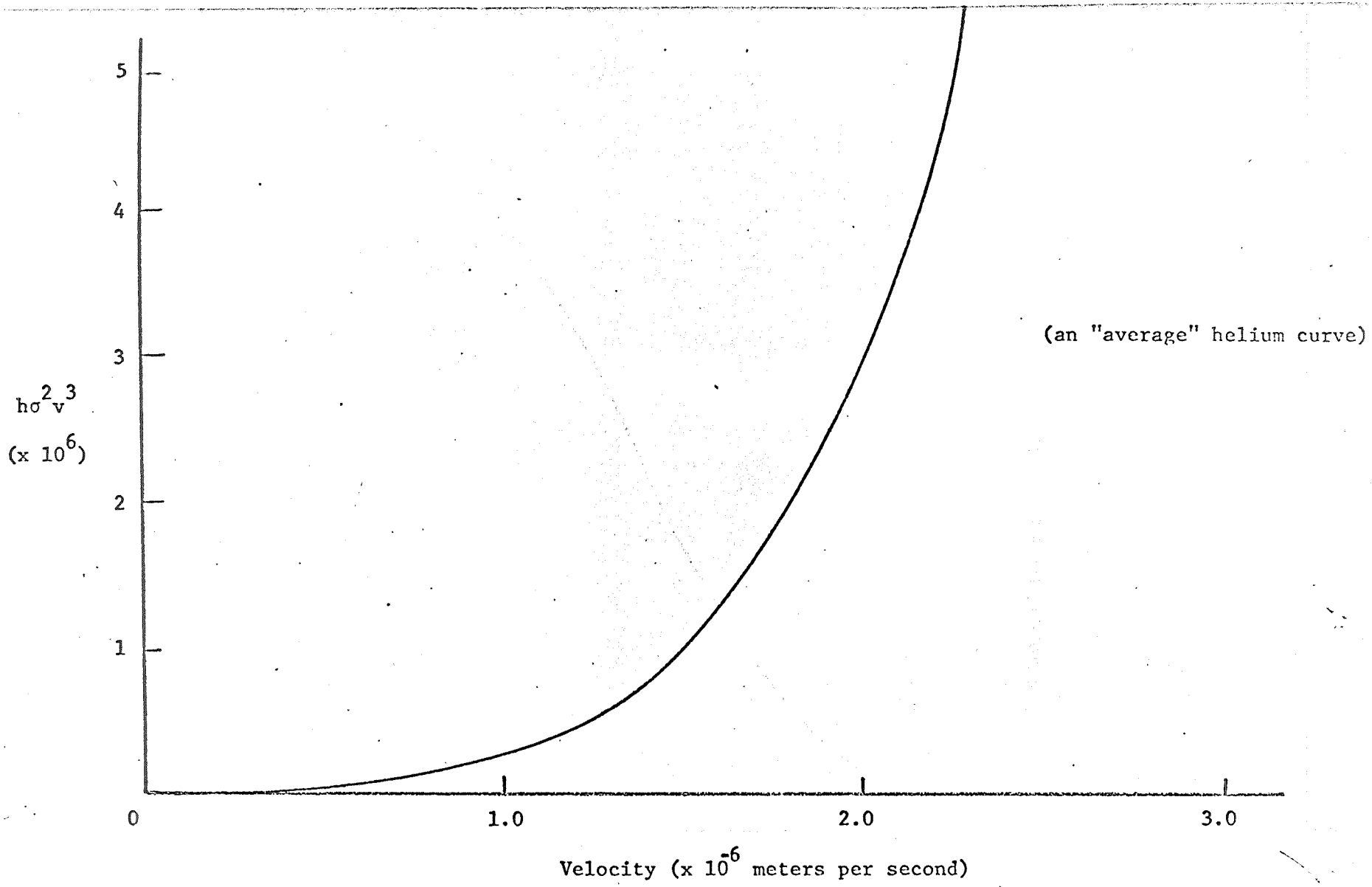

$h\sigma^2v^3$ versus Velocity

Figure 4

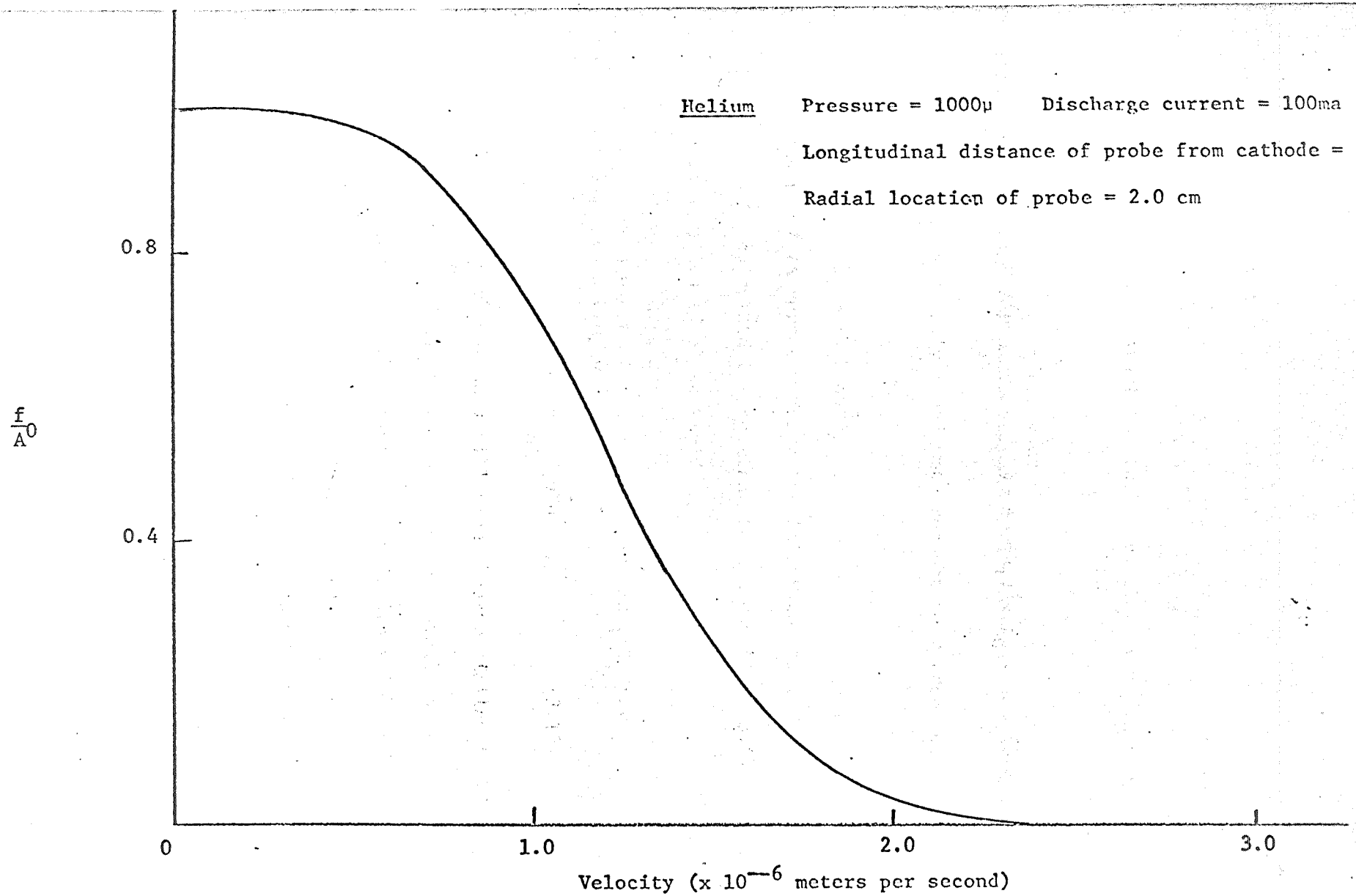

$\frac{f}{A}0$ versus Velocity

Figure 5

which is given by equation (3.2) as

$$f_1 = \frac{eE}{\nu_1 m}\frac{\partial f}{\partial v}_0 = \frac{eE}{Nm\sigma v}\frac{\partial f_0}{\partial v} = \frac{h_2}{\sigma v}\frac{\partial f_0}{\partial v} \qquad (3.9)$$

where h_2 is a constant for each gas. The term $\frac{\partial f_0}{\partial v}$ can be replaced by

$$\frac{\partial f}{\partial v}_0 = \frac{\partial (A\varepsilon^{-\int^{v} h_1\sigma^2 v^3 dv})}{\partial v} = -h_1\sigma^2 v^3 f_0 \; . \qquad (3.10)$$

Thus, f_1 is readily found with respect to v from corresponding values of f_0 as

$$f_1 = -h_2 h_1 \sigma v^2 f_0 \qquad (3.11)$$

and the f_1/A versus v curve is similar to Figure 6.

To calculate the constant term A equation (3.4) is combined with equation (3.3) to yield

$$n = \int_0^\infty \int_0^{2\pi} \int_0^{\pi} (f_0 + \cos\theta_1 f_1) v^2 \sin\theta_1 d\theta_1 d\phi dv$$

$$= 4\pi \int_0^\infty f_0 v^2 dv \; . \qquad (3.12)$$

Plotting $\frac{4\pi f_0 v^2}{A}$ versus v will give a curve similar to Figure 7. Now this curve is found to go to relatively small values for the gases considered before the point where v is 6.5×10^6 meters per second. Since n/A is given by the area under the curve of Figure 7, and it was found that the value of n/A for each gas remains the same whether numerically integrating to v values of 6.5×10^6 meters per second or larger, it is concluded that stopping integration at 6.5×10^6 meters per second is sufficient and valid, as was stated earlier. The value of the electron density is known from the experimental data in Reference 2, so A is determined from the relationship

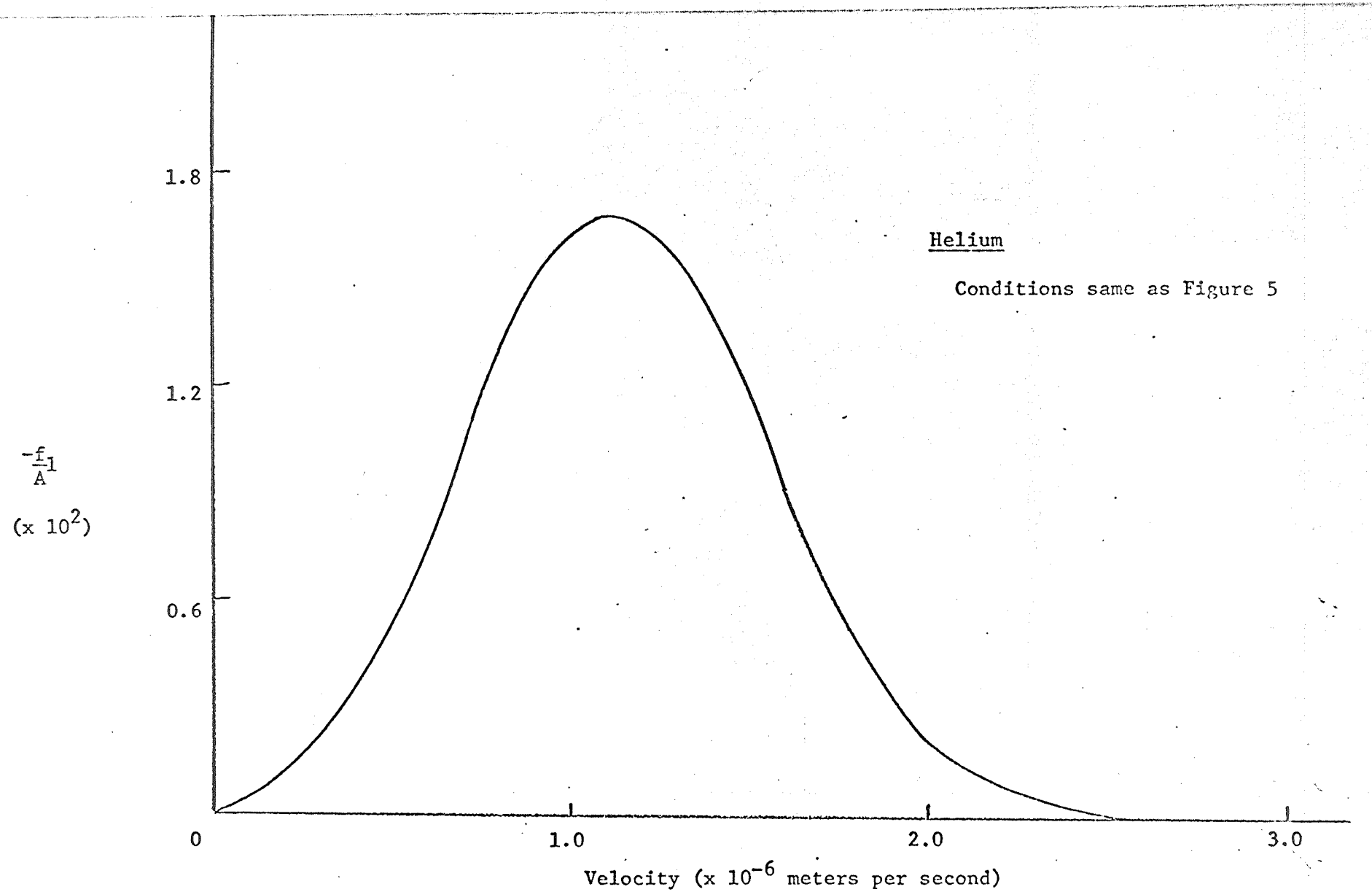

$-\frac{f}{A}1$ versus Velocity

Figure 6

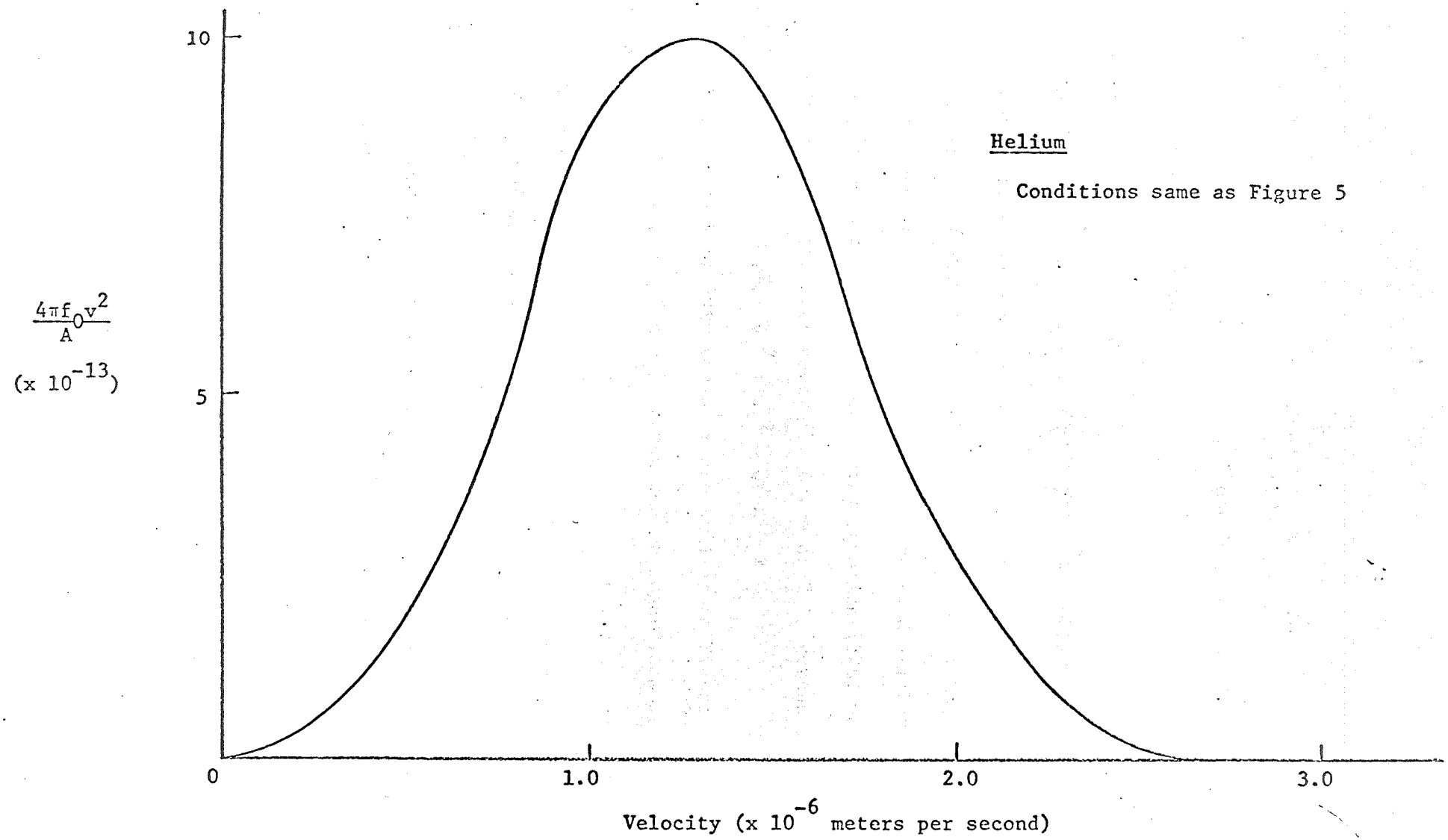

$\frac{4\pi f_0 v^2}{A}$ versus Velocity

Figure 7

$$A = \frac{n}{\text{area under curve of Figure 7}} = \frac{n}{n/A} \qquad (3.13)$$

With A thus determined, f can be determined from equations (3.2) and (3.5) to be

$$f = f_0 + f_1\cos\theta_1 = [\frac{f_0}{A} + \frac{f_1}{A}\cos\theta_1]A \qquad (3.14)$$

and it plots with v similar to Figure 8.

With f versus v now obtained the point of major interest --- the calculation of the z-directed velocity distribution function $g(v_z)$ --- has been reached. Using equation (3.6) we see that $g(v_z)$ is given by the area under the curve of $2\pi fr$ versus r, where

$$r^2 = v_x^2 + v_y^2 = v^2 - v_z^2 \qquad (3.15)$$

These curves of $2\pi fr$ versus r are similar to Figure 9. It was noted that the values of $g(v_z)$ do not change regardless of the value of v numerically integrated to, provided the value is equal to or greater than 6.5×10^6 meters per second. Thus, once again the validity of 6.5×10^6 meters per second as an integration end-point is established.

Now that the preceding method of determining the z-directed velocity distributions has been presented, it is appropriate that a comparison of those distributions obtained theoretically in the aforementioned manner be made with those measured experimentally in Reference 2.

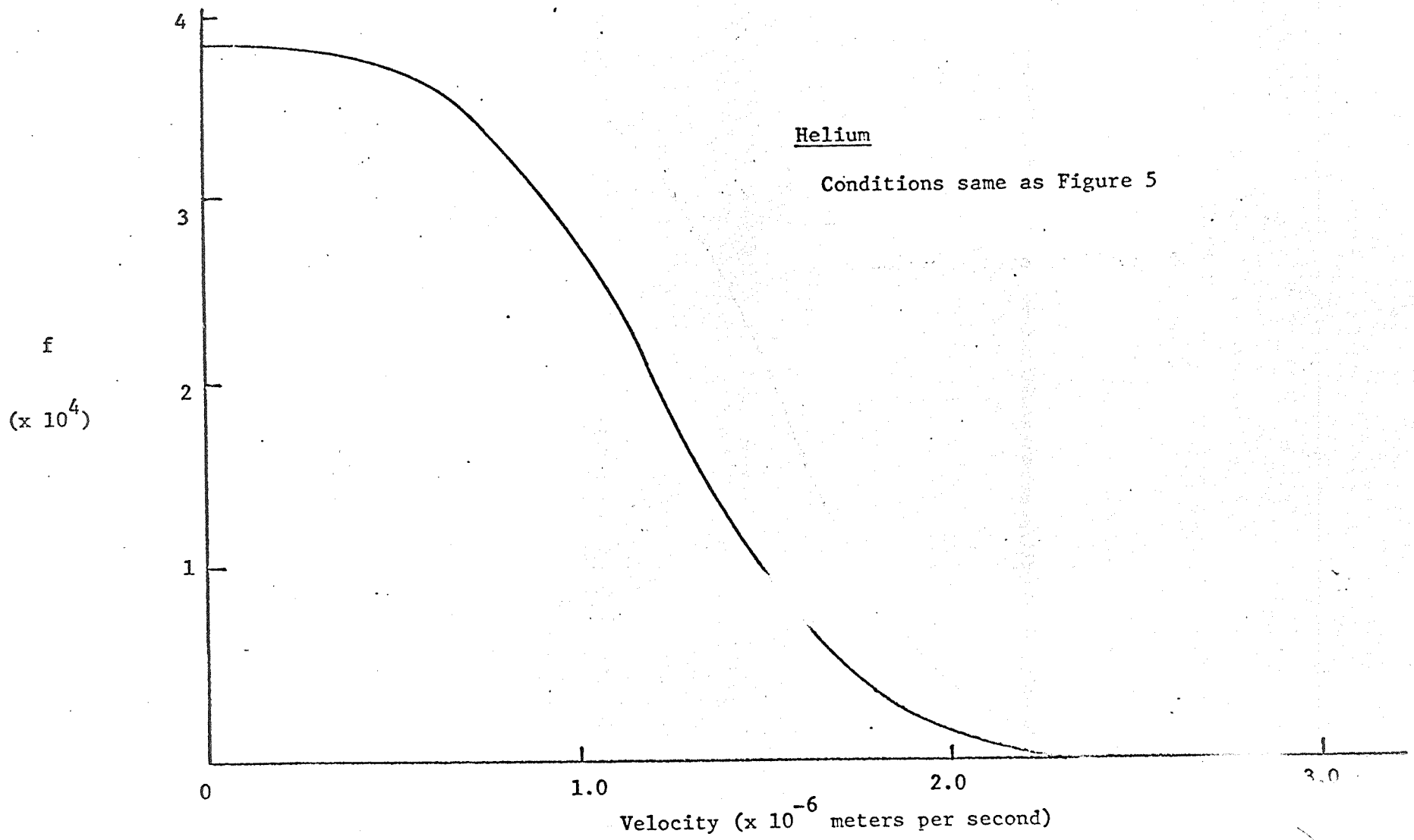

Velocity Distribution Function versus Velocity

Figure 8

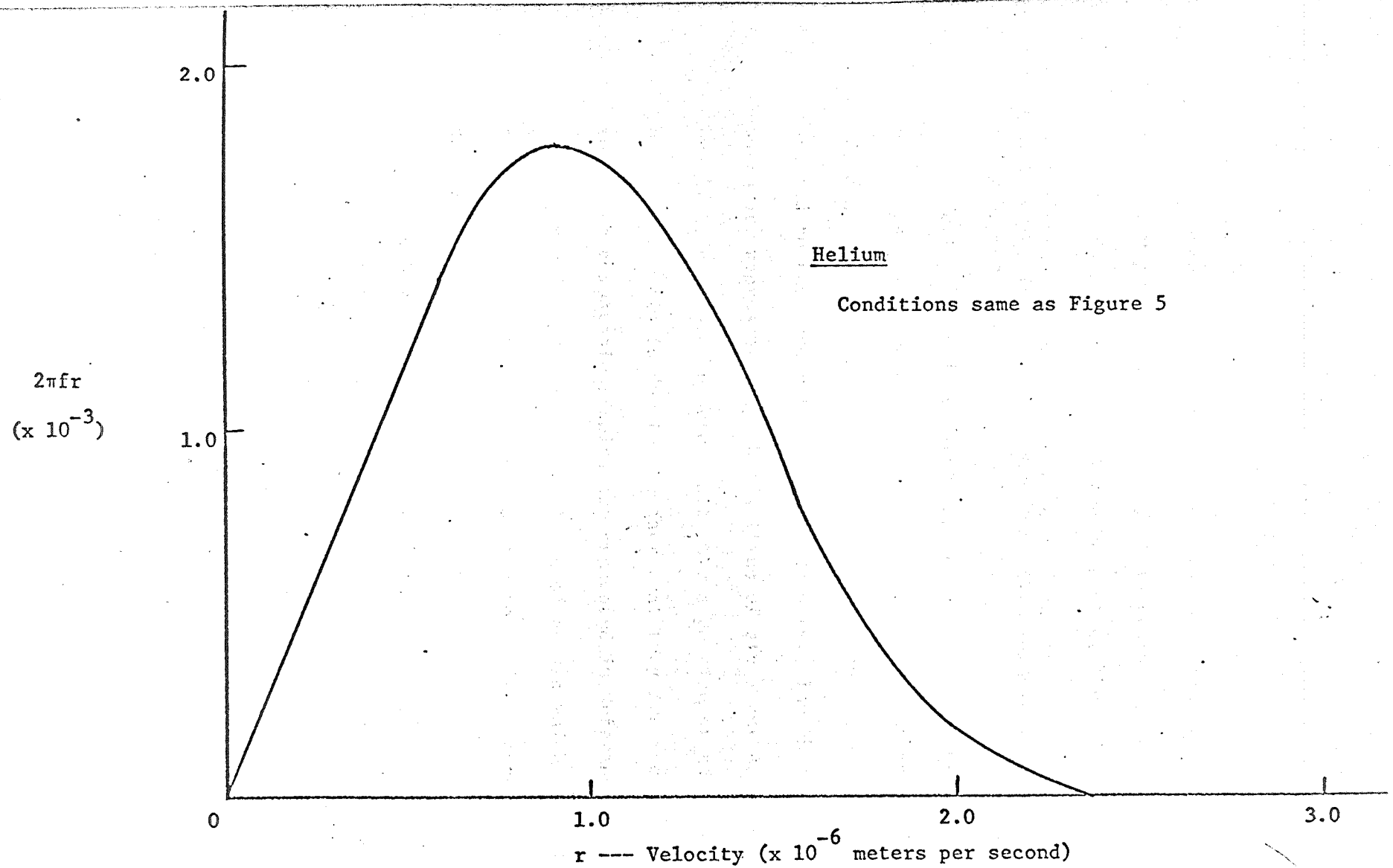

$2\pi fr$ versus r

Figure 9

IV. RESULTS

In order to arrive at conclusions concerning the validity of the theory presented previously, it is necessary to consider two separate sets of results. These consist of those measured experimentally and presented in Reference 2 and those obtained theoretically by the methods of this thesis.

Tables I and II present the conditions under which the experiments were conducted as well as the values obtained for the various electron number densities. It is these conditions that are applied to the theory to yield its results. The theoretical results are represented by the families of $g(v_z)$ curves in Figures 10 and 11. It should be noted that only a portion of the results are presented. This is due to the fact that they are the only portion for which comparable results are presented in Reference 2. The remaining results are similar families of curves which are not necessary in order to allow conclusions to be drawn concerning the theory.

If one of the curves from each set of the families of Figures 10 and 11 is compared with its counterpart measured experimentally, as is done in Figures 12 and 13, a dissimilarity is noted. The fact that the dissimilarity of the curves is large indicates a definite error. The next section deals with this problem.

Discharge description		Radial location of probe	Electron number density ($x10^{-15}$)
Pressure =	400μ		
Discharge current =	100ma	2.0cm 1.5cm 1.0cm 0.5cm	4.53 3.71 2.99 2.02
Longitudinal distance of probe from cathode =	69cm		
Pressure =	400μ		
Discharge current =	100ma	2.0cm 1.5cm 1.0cm 0.5cm	2.90 2.48 2.08 1.47
Longitudinal distance of probe from cathode =	61.5cm		
Pressure =	400μ		
Discharge current =	75ma	2.0cm 1.5cm 1.0cm 0.5cm	2.74 2.31 1.88 1.24
Longitudinal distance of probe from cathode =	69cm		
Pressure =	400μ		
Discharge current =	75ma	2.0cm 1.5cm 1.0cm 0.5cm	2.55 1.77 1.40 0.88
Longitudinal distance of probe from cathode =	61.5cm		

Neon Experimental Conditions

Table I

Discharge description	Radial location of probe	Electron number density ($\times 10^{-15}$)
Pressure = 1000μ Discharge current = 75ma Longitudinal distance of probe from cathode = 69cm	2.0cm 1.5cm 1.0cm 0.5cm	4.11 3.60 2.72 1.79
Pressure = 1000μ Discharge current = 75ma Longitudinal distance of probe from cathode = 61.5cm	2.0cm 1.5cm 1.0cm 0.5cm	3.08 2.68 2.06 1.37
Pressure = 500μ Discharge current = 100ma Longitudinal distance of probe from cathode = 69cm	2.0cm 1.5cm 1.0cm 0.5cm	4.05 3.48 2.72 1.83
Pressure = 500μ Discharge current = 100ma Longitudinal distance of probe from cathode = 61.5cm	2,0cm 1.5cm 1.0cm 0.5cm	3.10 2.82 2.16 1.47

Helium Experimental Conditions

Table II

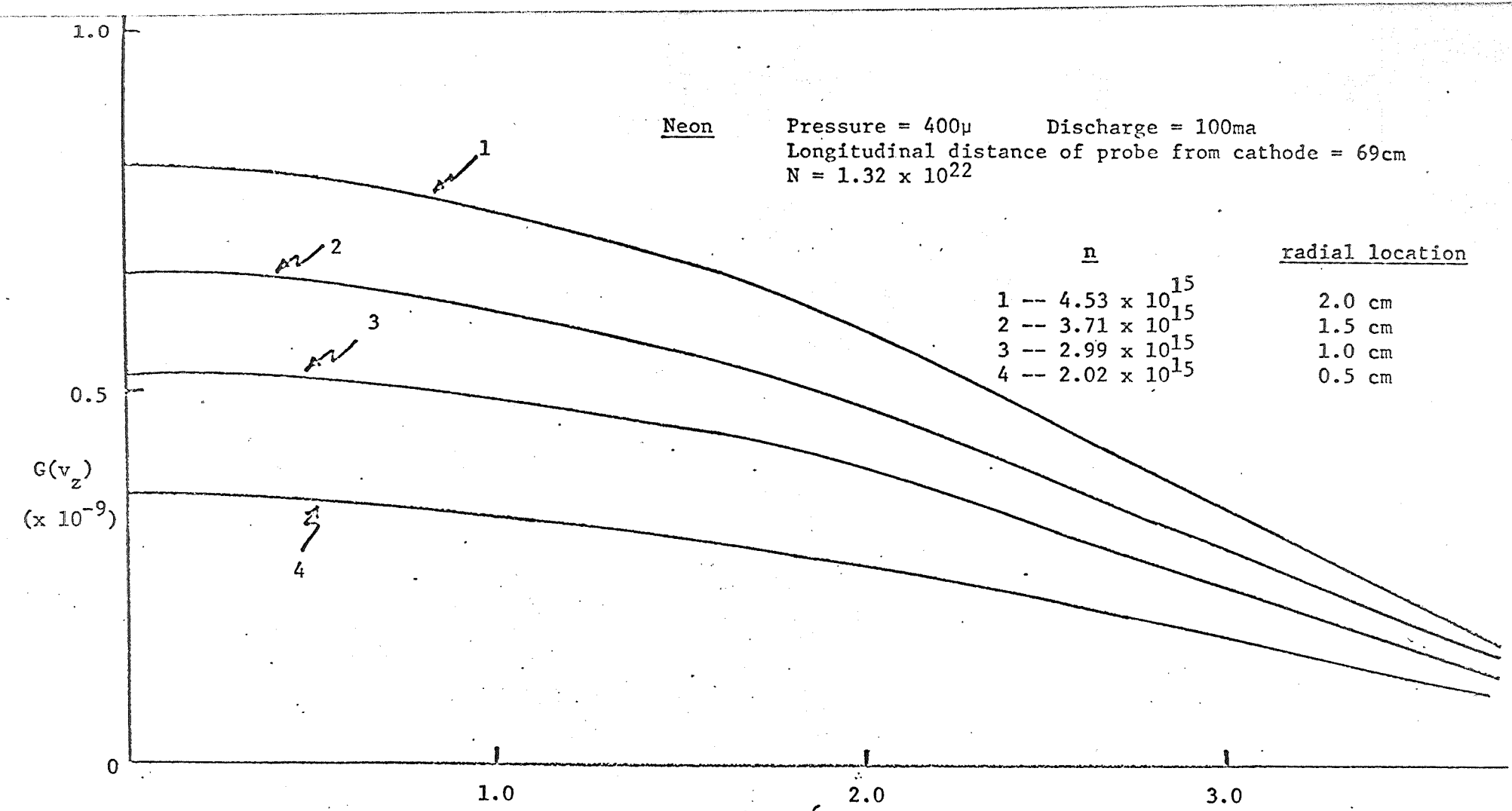

Neon

$G(v_z)$ versus Velocity

Figure 10

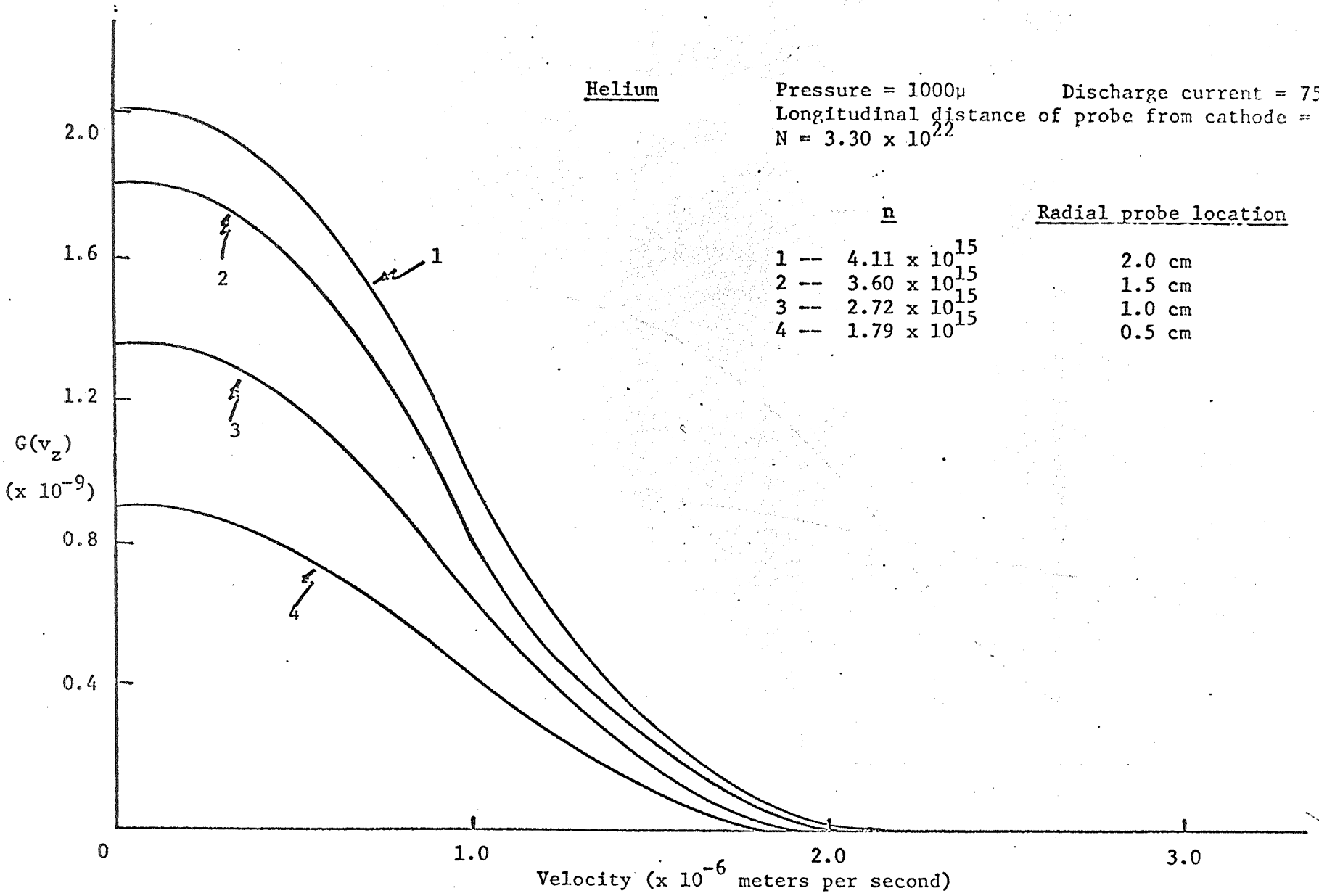

Helium
$G(v_z)$ versus Velocity
Figure 11

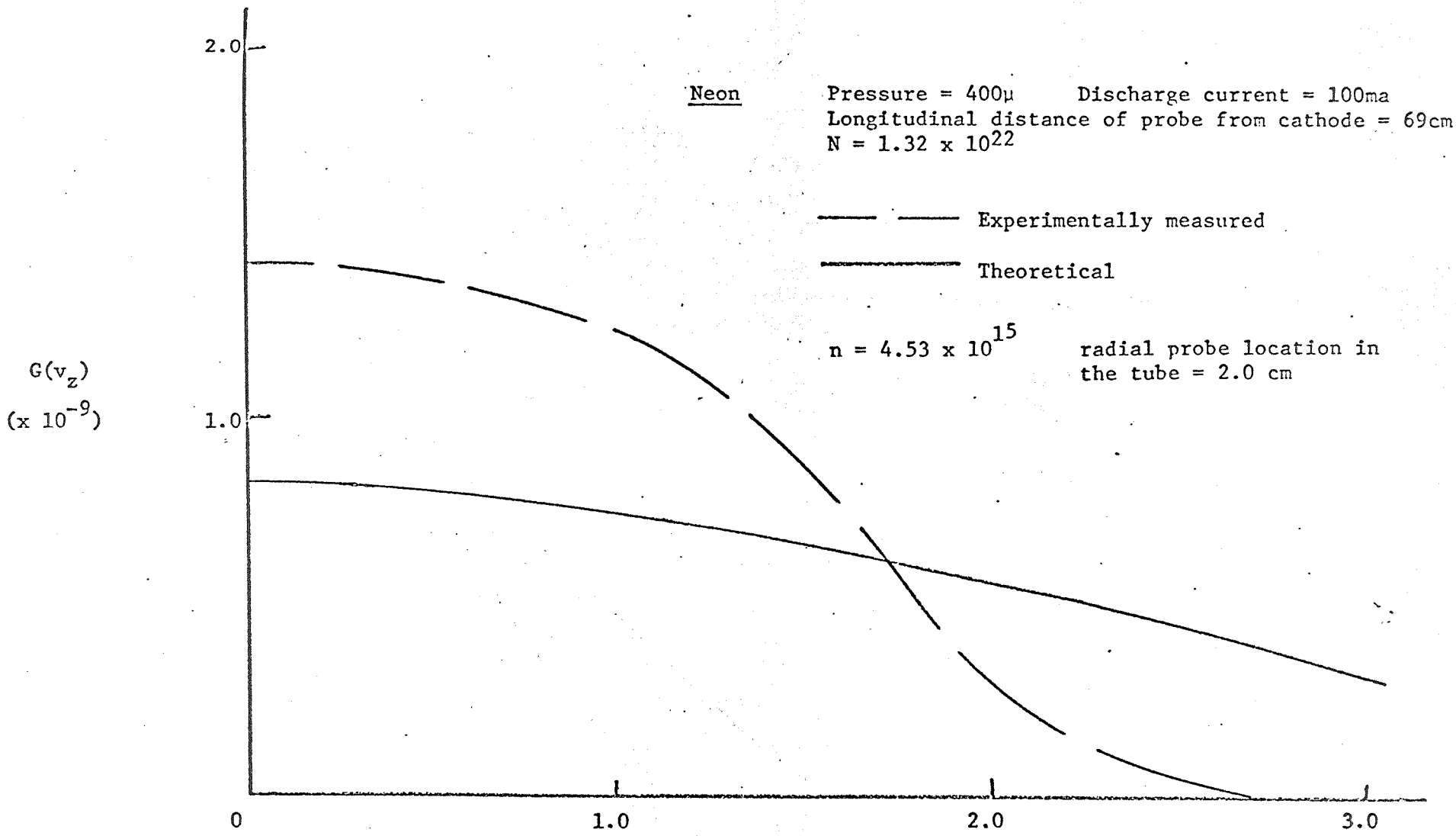

Neon
Theoretical and Experimental
$G(v_z)$ versus Velocity

Figure 12

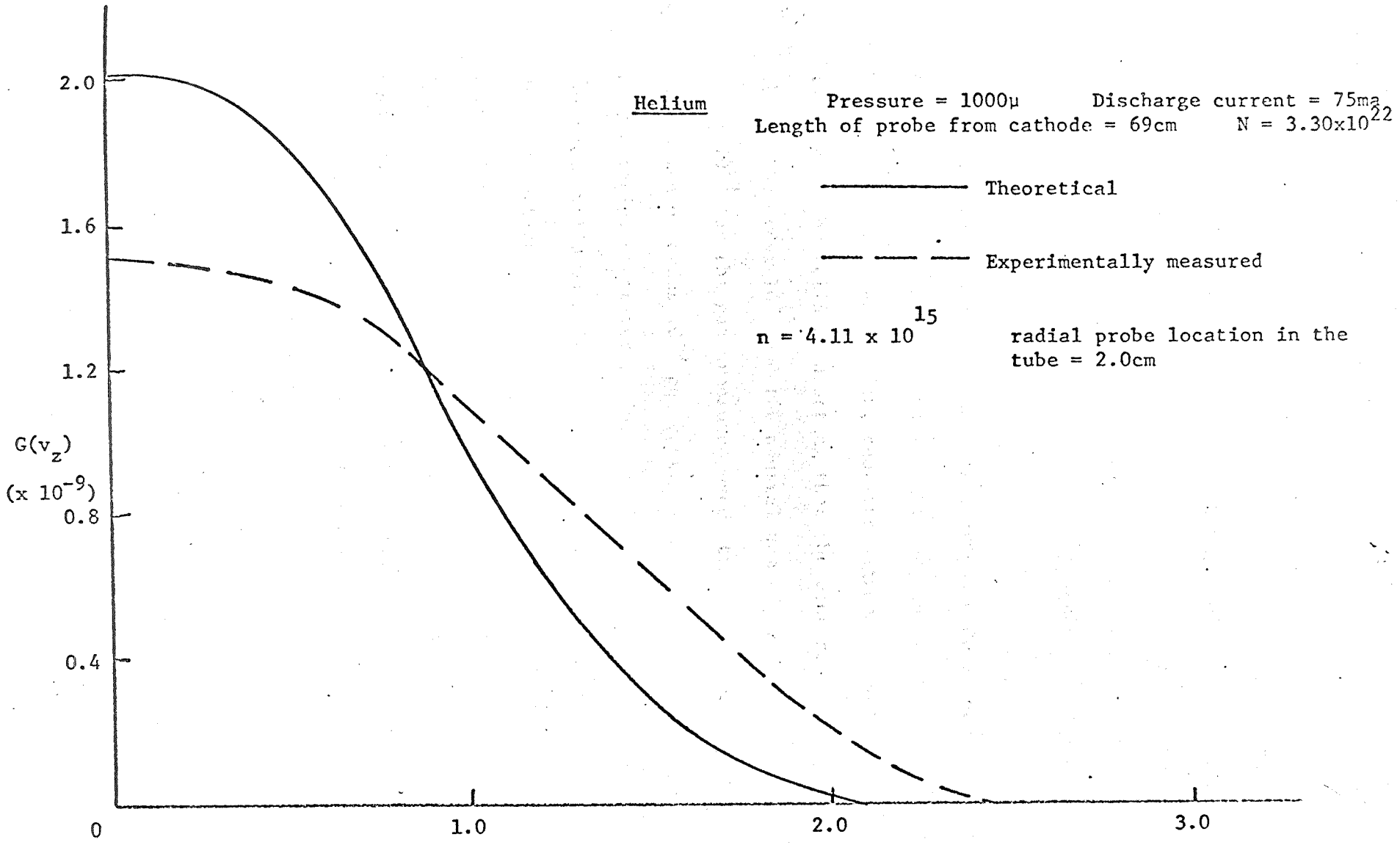

Helium
Theoretical and Experimental
$G(v_z)$ versus Velocity

Figure 13

V. CONCLUSIONS

The obvious deduction that can be made concerning the dissimilarity of the theoretical and experimental results is that the theory is not truly representative of the physical occurrences. The methodology and program used in the calculation of the theoretical distributions is shown to be correct in Appendix B, thus giving support to this deduction.

Recollection of the basic assumptions made in developing the theory will perhaps give some insight into the reasons for its collapse. The first assumption, that the degree of ionization is low, is shown to be valid when noting that the electron number densities are of the order 10^{15} and the neutral number densities are of the order 10^{22} for the gas pressures used, thus yielding a degree of ionization of order 10^{-5} per cent. The second assumption, that only elastic, short-term, binary collisions need be considered does not prove valid when it is seen that the $g(v_z)$ distributions, for neon in particular, have significant values at energies of 20 electron volts (3×10^6 meters per second). This is in the region of the first resonance potential of both helium and neon. It is evident from this that electrons with energies above the first resonance potential are undergoing inelastic collisions. This will modify the distribution functions not only in the high energy range but also where collisions are purely elastic. The third assumption, that f can be approximated by the two terms f_0 and f_1, is one which Ginzberg

(Reference 5) holds to be valid but which could concievably cause error. This could come about as the result of a higher order approximation such as f_2, f_3, etc. which is not negligible as supposed. An additional assumption, that of a strong field, was made in the solution procedure. This assumption is shown to be valid in Appendix C.

It was noticed that by adjusting the parameter h_1 in equation (3.8) one is able to "fit" the theoretical curves very closely to the measured experimental ones. A detailed analysis of this was not carried out, but preliminary investigations indicate a mathematically determinate relationship might exist between h_1 and the proper "fitting" of each set of related curves. This mathematical relationship would seem to be dependent on the physical parameters of the discharge.

With the aforementioned in mind it can be deduced that the theory could be misrepresentative of the physical occurrences due to any one, or combination of, the following factors:

1. Failure to take into account inelastic collisions.

2. Invalid series representation of the velocity distribution function f.

Naturally, there are possibly other areas where the physical situation is erroneously represented. The aforementioned are the most obvious noted by the author.

VI. RECOMMENDATIONS

The work done in this thesis was undertaken in order to determine whether the theory developed for the experiments of Reference 2 was truly representative of the physical occurrences. It was shown that this was not the case. It would be therefore logical that the theory be reworked taking into account those areas of concern. Additionally, it would be interesting and of value to study more thoroughly and to determine, if indeed possible, the mathematical relationship for h_1 for the proper "fit" of theoretical to experimental distributions in terms of various physical parameters of the discharge.

VII. REFERENCES

1. Bond, Robert H., Bulletin of the American Physics Society, Vol. 7 (1962).

2. Bond, Robert H., Directed Electron Velocity Distributions in Rare Gas Discharges Using Guard Ring Probes, California Institute of Technology, Pasadena, California (1965).

3. Chapman, S. and Cowling, T.G., The Mathematical Theory of Non-Uniform Gases, Cambridge University Press (1953).

4. Rose, David J. and Clark, Melville, Plasmas and Controlled Fusion, Massachusetts Institute of Technology and John Wiley and Sons, Inc., New York, N.Y. (1961).

5. Ginzberg, V.L. and Gurevich, A.V., Usp. Fiz. Nauk., Vol. 70 (1960).

6. Lanczos, Cornelius, Applied Analysis, Prentice Hall, Inc., Englewood Cliffs, New Jersey.

APPENDIX A

The program listed on the following pages was run on the IBM System/360 computer to calculate the electron distributions for neon and helium. It is titled DIREDIST, is in Fortran IV language, and consists of the following sections:

A. Main Program - used to control inputs and outputs, call the subroutine to calculate equations to fit data curves and pick the best "fit", print and check the data equations, calculate variables, call other sections when appropriate, and print the main headings and final $g(v_z)$ values.

B. Subroutine FOSAV - used to calculate points of an $h_1\sigma^2v^3$ versus v curve and print these points, call a subroutine to numerically integrate these points 11 at a time, and print the points of the f_0/A versus v curve thus calculated.

C. Subroutine F1SAV - used to calculate and print points of an f_1/A versus v curve corresponding to those in section B.

D. Subroutine FSACON - used to calculate and print points of a $\frac{4\pi f_0 v^2}{A}$ versus v curve, corresponding to those of sections A and B, to call the subroutine to numerically integrate these points 19 at a time, and add these integrations together.

E. Subroutine FSAV - used to calculate and print points of an f versus v curve and to print the value of the constant A obtained in section D.

F. Subroutine FR - used to change the system of refer-

ence from rectangular to polar coordinates.

G. Subroutine DIST - used to calculate and print points on a $2\pi fr$ versus r curve corresponding to those of section F, and to call the subroutine to numerically integrate these points, thus yielding a value of $g(v_z)$.

H. Subroutine ORTHO - used to "fit", by the method of least squares (Reference 6), a polynomial equation of from first to eighth order to a series of points, to calculate the sum of the squares of deviation and the maximum single deviation at a point.

I. Function SIMPUN - used to numerically integrate a series of points on a curve using the Modified Simpson's Rule.

The flow chart shown in Figure 14 is intended to describe as simply as possible the operation of the program. It is a simplified operational flow chart and as such is not intended to give a literal description of the program --- the listing following is for that purpose.

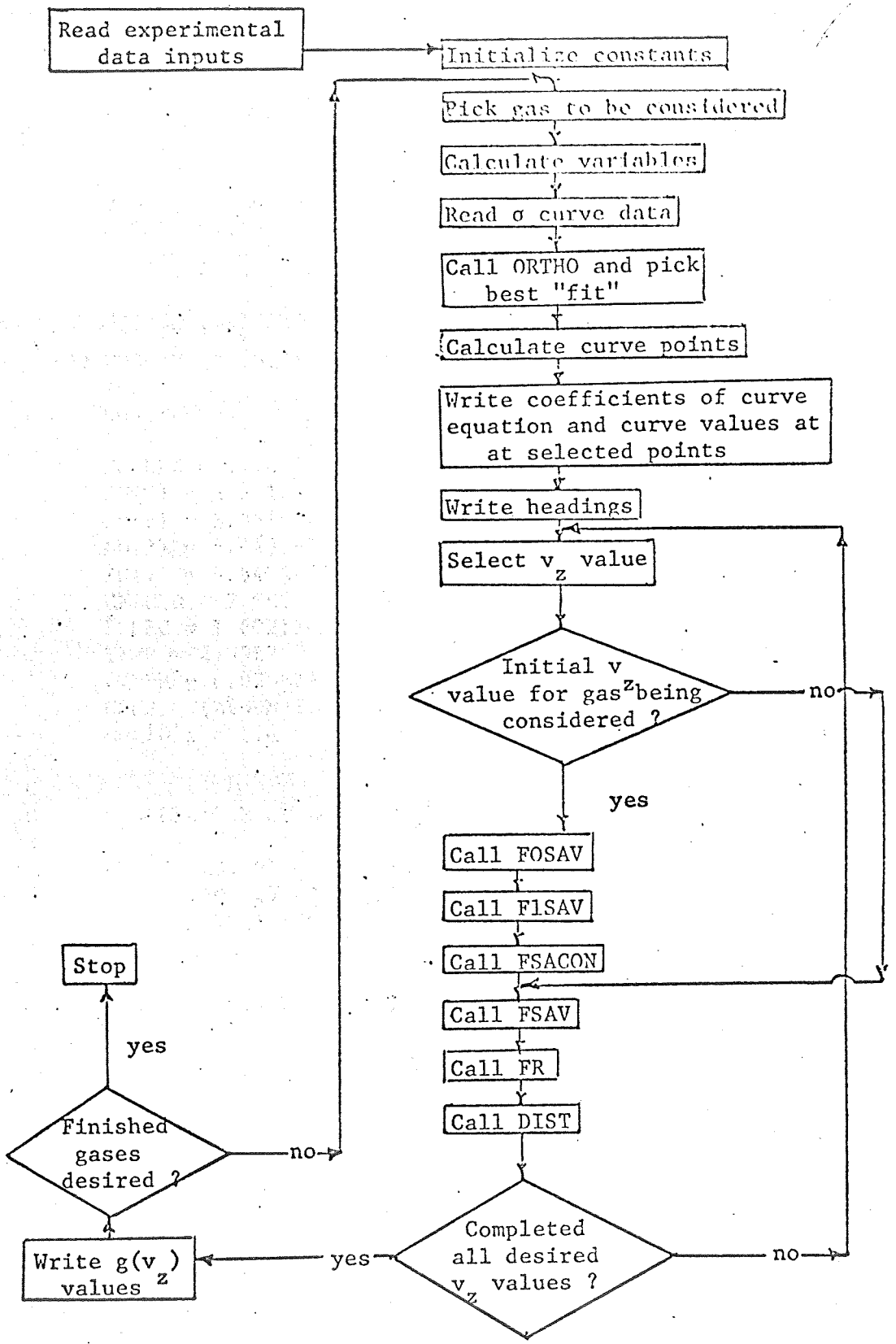

-Operational Flow Chart-
Figure 14

A. MAIN PROGRAM

```
C
C     CALCULATION OF DIRECTED ELECTRON VELOCITY DISTRIBUTIONS IN
C                        HELIUM AND NEON
C
      0DIMENSION RA(16),PHE(16),EN(19),XM(4),VZ(19),XN(16),X(40),
      1XNDNE(16),XNDHE(16),XNDN1(16),Y(40),XNDH1(16),FOSA(740),VEL(740),
      2COE(10),E(40),F1SA(740),YSIG(40),SIG(42),V(147),FSA2(147),
      3VELO(147),F(147),R(147),GVZ(19),PNE(16),CURNE(16),CURHE(16),
      4XL(16),SUMSQ(10),FSA1(147),GVZ1(19)
       READ(5,100) EN,RA,XL,XNDN1,XNDH1,PNE,PHE,CURNE,CURHE,
  100 FORMAT (5F10.5)
C
C     CONSTANTS
C
      XMELEC = 9.1086E-31
      XM(1) = 3.351E-26
      XM(2) = 3.351E-26
      XM(3) = 6.643E-27
      XM(4) = 6.643E-27
      EFIELD = 2.0E2
      ECHRG = 1.6021E-19
      TEMP = 2.93E2
      AVNUM = 6.023E26
      CONS = (AVNUM*2.73E2)/(2.24E1*760E-3*TEMP)
→→→   DO 10 I = 1,4
C
C
C     CALCULATION OF EQUATION TO FIT DATA CURVES
C
      IF (I .EQ. 2) GO TO 110
      IF( I .EQ. 4) GO TO 110
      READ (5,105) NPOINT
  105 FORMAT (I5)
      DO 210 J = 1,NPOINT
      READ (5,101) X(J),Y(J)
  101 FORMAT (2F10.0)
      YSIG(J) = Y(J)
  210 E(J) = X(J)**2
      DO 120 IDG = 1,8
      CALL ORTHO (E,YSIG,NPOINT,IDG,COE,SUMSQ,DMAX)
  120 CONTINUE
      SUMMIN = SUMSQ(1)
      DO 111 IO = 2,8
      IF (SUMMIN .LT. SUMSQ(IO)) GO TO 169
      N = IO
      GO TO 177
  169 N =1
```

```
      177 SUMMIN = SUMSQ(N)
      111 CONTINUE
          IDG = N
          CALL ORTHO (E,YSIG,NPOINT,IDG,COE,SUMSQ,DMAX)
      C
      C     PRINT AND CHECK THE RESULTS OF THE EQUATION
      C
          WRITE (6,102)
      1020FORMAT (1H1,3X,3HIDG,6X,4HX**8,6X,4HX**7,6X,4HX**6,6X,4HX**5,
         16X,4HX**4,6X,4HX**3,6X,4HX**2,6X,4HX**1,6X,4HCONS,5X,5HSUMSQ,
         26X,4HDMAX)
          WRITE(6,103) IDG,(COE(K),K=1,9),SUMSQ(IDG),DMAX
       45 FORMAT (//19X,6HENERGY,25X,5HSIGMA,25X,5HSIGIN,/)
          WRITE (6,45)
      103 FORMAT (/5X,I1,4X,11(1X,E9.3))
          DO 150 N = 1,NPOINT
          SIG(N) = COE(1)
          DO 160 M = 2,9
      160 SIG(N) = SIG(N)*E(N)+COE(M)
      150 WRITE (6,69) E(N),SIG(N),YSIG(N)
       69 FORMAT (15X,E15.8,15X,E15.8,15X,E15.8)
      C
      C     CALCULATED VARIABLES
      C
      →→→ 110 DO 10 KK = 1,16
          NFLAG = 0
      →→→     DO 15 J = 1,19
          NFLAG = NFLAG + 1
          IF (I .EQ. 2) GO TO 71
          IF (I .EQ. 4) GO TO 71
          IF (KK .GT. 1) GO TO 71
          IF (J .GT. 1) GO TO 71
          IF (I-2) 60,60,70
       60 WRITE (6,65) PNE(KK),CURNE(KK),XL(KK),RA(KK)
       650FORMAT (1H1,5X,4HNEON,5X,4HP = ,F5.0,3H MU,5X,4HI = ,F5.1,3H MA,
         15X,4HL = ,F4.1,3H CM,5X,4HR = ,F3.1,3H CM)
          GO TO 71
       70 WRITE(6,75) PHE(KK),CURHE(KK),XL(KK),RA(KK)
       750FORMAT (1H1,5X,6HHELIUM,5X,4HP = ,F5.0,3H MU,5X,4HI = ,F5.1,3H MA,
         15X,4HL = ,F4.1,3H CM,5X,4HR = ,F3.1,3H CM)
       71 IF (I .EQ.1) GO TO 76
          IF (I .EQ. 2) GO TO 77
          IF (I .EQ. 3) GO TO 76
          IF (I .EQ. 4) GO TO 77
       76 VZ(J) = (SQRT(2.0*ECHRG/XMELEC))*EN(J)
          GO TO 29
       77 VZ(J) = -(SQRT(2.0*ECHRG/XMELEC))*EN(J)
       29 IF (NFLAG .GT.1) GO TO 51
          IF (I - 2) 30,30,40
       30 XN(KK) = CONS*PNE(KK)*1.0E6
```

```
      XNDNE(KK) = XNDN1(KK)*1.0E15
      GO TO 50
   40 XN(KK) = CONS*PHE(KK)*1.0E-6
      XNDHE(KK) = XNDH1(KK)*1.0E15
   50 CALL FOSAV (XM,H,XN,KK,XMELEC,ECHRG,EFIELD,I,FOSA,VEL,COE)
      CALL F1SAV (FOSAV,VEL,XMELEC,ECHRG,XN,KK,I,EFIELD,F1SA,H,COE)
     0CALL FSACON (FOSA,VEL,I,VELO,XNDNE,KK,XNDHE,ACONT,FSA1,F1SA,
     1FSA2)
   51 CALL FSAV (VZ,J,VELO,V,MIN,FSA1,FSA2,ACONT,F,KK,I)
      CALL FR (V,R,VZ,J,MIN,KK)
      CALL DIST (F,R,GVZ,J,MIN,KK,I,GVZ1)
   15 CONTINUE
C
C     PRINTED RESULTS
C
      IF (I-2) 81,81,82
   81 WRITE (6,66) PNE(KK),CURNE(KK),XL(KK),RA(KK),XNDNE(KK),XN(KK)
   660FORMAT (1H1,5X,4HNEON,5X,4HP = ,F5.0,3H MU,5X,4HI = ,F5.1,3H MA,
     15X,4HL = ,F4.1,3H CM,5X,4HR = ,F3.1,3H CM,/5X,19HELECTRON DENSITY
     2=,E15.8,5X,15HNEON DENSITY = ,E15.8)
      GO TO 80
   82 WRITE (6,78) PHE(KK),CURHE(KK),XL(KK),RA(KK),XNDHE(KK),XN(KK)
   780FORMAT(1H1,5X,6HHELIUM,5X,4HP = ,F5.0,3H MU,5X,4HI = ,F5.1,3H MA,
     15X,4HL =,F4.1,3H CM,5X,4HR = ,F3.1,3H CM,/5X,19HELECTRON DENSITY
     2= ,E15.8,5X,17HHELIUM DENSITY = ,E15.8)
   80 WRITE (6,85)
   85 FORMAT (/14X,8HVELOCITY,23X,5HG(VZ),22X,10HNOEMALIZED,/)
→→→   DO 10 NIN = 1,19
   10 WRITE (6,95) VZ(NIN),GVZ(NIN),GVZ1(NIN)
   95 FORMAT (10X,E15.8,15X,E15.8,15X,E15.8)
      STOP
      END
```

B. SUBROUTINE FOSAV

```
C
C     CALCULATION OF THE SYMMETRICAL DISTRIBUTION FUNCTION
C
      SUBROUTINE FOSAV (XM,H,XN,KK,XMELEC,ECHRG,EFIELD,I,FOSA,VEL,COE)
     0DIMENSION V1(7392),YY(7392),XN(16),XM(4),EV(7392),SIGMA(7392),
     1X(15),Y(15),XINTEG(740),SUMINT(740),FOSA(740),VEL(740),COE(10)
      V1(1) = 0
      DO 3 K = 2,7392
      Q = K
      IF (I .EQ. 1) GO TO 71
      IF (I .EQ. 2) GO TO 72
      IF (I .EQ. 3) GO TO 71
```

```
      IF (I .EQ. 4) GO TO 72
   71 V1(K) = (Q-1)*6.55E6/7391.0
      GO TO 73
   72 V1(K) = -(Q-1)*6.55E6/7391.0
   73 H=(XMELEC**2/ECHRG**2)*(3.0*XN(KK)**2/EFIELD**2)*(XMELEC/XM(I))
      EV(K) = ((XMELEC*V1(K)**2)/(2.0*ECHRG)
      SIGMA(K) = COE(1)
      DO 25 MX = 2,9
   25 SIGMA(K) = SIGMA(K)*EV(K)+COE(MX)
      SIGMA(K) = SIGMA(K)*1.0E-20
    3 YY(K) = H*SIGMA(K)**2*V1(K)**3
      SUM = 0.0
      VEL(1) = 0.0
      FOSA(1) = 1.0
      DO 10 M = 2,740
      MM = (M-2)*10+1
      MN = (M-1)*10+1
      MK = 0
      DO 9 N = MM,MN
      MK = MK+1
      Y(MK) =YY(N)
      X(MK) = V1(N)
    9 CONTINUE
      VEL(M) = X(11)
      XINTEG(M) = SIMPUN(X,Y,11)
      SUMINT(M) = XINTEG(M)+SUM
      FOSA(M) = EXP(-SUMINT(M))
      SUM = SUMINT(M)
      IF (FOSA(M) .LT. 1.0E-50) GO TO 11
   10 CONTINUE
      GO TO 12
   11 DO 27 NO=M,740
      MO=11*NO-NO+1
      VEL(NO) = V1(MO)
   27 FOSA(NO)=0.0
   12 IF(I .EQ. 2) GO TO 13
      IF(I .EQ. 4) GO TO 13
      IF(KK .GT. 1) GO TO 13
      WRITE (6,81)
   81 FORMAT (//15X,4HFOSA,27X,3HVEL,/)
      DO 14 NL=1,740,6
   14 WRITE (6,82) FOSA(NL),VEL(NL)
   82 FORMAT (10X,E15.8,15X,E15.8)
   13 RETURN
      END
```

C. SUBROUTINE F1SAV

```
C
C     DETERMINATION OF THE DISTRIBUTION FUNCTION DUE TO DRIFT
C
     0SUBROUTINE F1SAV (F0SA,VEL,XMELEC,ECHRG,XN,KK,I,EFIELD,F1SA,H,
     1COE)
     0DIMENSION DERF0(740),F0SA(740),VEL(740),SIGMA(740),EV(740),
     1F1SA(740),XN(16),COE(10)
      SIGMA(1) = 0.0
      EV(1) = 0.0
      F1SA(1) = 0.0
      DO 10 K = 2,740
      EV(K) = (XMELEC*VEL(K)**2)/(2.0*ECHRG)
      SIGMA(K) = COE(1)
      DO 25 MX = 2,9
   25 SIGMA(K) = SIGMA(K)*EV(K)+COE(MX)
      SIGMA(K) = SIGMA(K)*1.0E-20
    9 DERF0(K) = -H*SIGMA(K)**2*VEL(K)**3*F0SA(K)
   100F1SA(K) = (ECHRG*EFIELD/XMELEC)*(1.0/(XN(KK)*SIGMA(K)*VEL(K)))*
     1DERF0(K)
      IF (I .EQ. 2) GO TO 13
      IF (I .EQ. 4) GO TO 13
      IF (KK .GT. 1) GO TO 13
      WRITE (6,31)
   31 FORMAT(//16X,3HVEL,26X,4HF1SA,27X,2HEV,27X,5HSIGMA,/)
      DO 14 N = 1,740,6
   14 WRITE (6,32) VEL(N),F1SA(N),EV(N),SIGMA(N)
   32 FORMAT (10X,E15.8,15X,E15.8,15X,E15.8,15X,E15.8)
   13 RETURN
      END
```

D. SUBROUTINE FSACON

```
C
C     DETERMINATION OF THE CONSTANT A
C
     0SUBROUTINE FSACON (F0SA,VEL,I,VELO,XNDNE,KK,XNDHE,ACONT,
     1FSA1,F1SA,FSA2)
     0DIMENSION FSASIN(740),F0SA(740),VEL(740),YYY(19),XX(19),
     1VELO(147),XINTE(147),DSA(147),C(19),FSA1(147),XNDNE(16),
     2XNDHE(16),FSA2(147),F1SA(147),D(19)
      PI = 3.141592
      IF (I .EQ. 2) GO TO 7
      IF (I .EQ. 4) GO TO 7
      IF (KK .GT. 1) GO TO 7
      WRITE (6,1)
    1 FORMAT (//15X,4HVELO,27X,3HYYY,/)
    7 DO 10 K = 1,740
   10 FSASIN(K) = 4.0*PI*F0SA(K)*VEL(K)**2
      SUMS = 0.0
```

```
      DO 15 M=1,41
      MI = (M-1)*18+1
      MJ = M*18+1
      NJ = 0
      DO 20 L=MI,MJ
      NJ = NJ+1
      D(NJ) = F1SA(L)
      C(NJ) = F0SA(L)
      YYY(NJ) = FSASIN(L)
      XX(NJ) = VEL(L)
   20 CONTINUE
      VELO(M) = XX(19)
      FSA1(M) = C(19)
      FSA2(M) = D(19)
      IF (I .EQ.2) GO TO 8
      IF (I .EQ.4) GO TO 8
      IF (KK .GT. 1) GO TO 8
      WRITE (6,9) VELO(M),YYY(6)
    9 FORMAT (10X,E15.8,15X,E15.8)
    8 XINTE(M) = SIMPUN(XX,YYY,19)
      IF (VELO(M) .LT. 0.0) XINTE(M) = -XINTE(M)
      DSA(M) = XINTE(M) + SUMS
      SUMS = DSA(M)
   15 CONTINUE
      IF (I-2) 2,2,3
    2 ACONT = XNDNE(KK)/SUMS
      GO TO 16
    3 ACONT = XNDHE(KK)/SUMS
   16 RETURN
      END
```

E. SUBROUTINE FSAV

```
C
C     DETERMINATION OF THE TOTAL DISTRIBUTION FUNCTION
C
      SUBROUTINE FSAV (VZ,J,VELO,V,MIN,FSA1,FSA2,ACONT,F,KK,I)
     0DIMENSION VELO(147),VZ(19),F1S2(740),F0S2(740),V(147),
     1FSA1(147),FSA2(147),F(147)
      MIN = 1
      DO 10 K=1,41
      XA=VELO(K)**2
      XB=VZ(J)**2
      IF (XA .LT. XB) GO TO 10
      MIN = MIN+1
      V(MIN) = VELO(K)
      F0S2(MIN) = FSA2(K)
```

```
      F1S2(MIN) = FSA2(K)
      F(MIN) = (FOS2(MIN)+F1S2(MIN)*VZ(J)/V(MIN))*ACONT
   10 CONTINUE
      IF (I .EQ. 2) GO TO 13
      IF (I .EQ.4) GO TO 13
      IF (KK .GT. 1) GO TO 13
      IF (J .GT. 1) GO TO 13
      WRITE (6,31)
   31 FORMAT (//17X,1HV,26X,4HACON,27X,1HF,/)
      DO 14 N=2,MIN
   14 WRITE (6,32) V(N),ACONT,F(N)
   32 FORMAT (10X,E15.8,15X,E15.8,15X,E15.8)
   13 RETURN
      END
```

F. SUBROUTINE FR

```
C
C     CHANGING TO POLAR COORDINATES
C
      SUBROUTINE FR (V,R,VZ,J,MIN)
      DIMENSION V(147),VZ(19),R(147)
      DO 10 K=2,MIN
   10 R(K) = SQRT(V(K)**2-VZ(J)**2)
      RETURN
      END
```

G. SUBROUTINE DIST

```
      SUBROUTINE DIST (F,R,GVZ,J,MIN,KK,I,GVZ1)
     0DIMENSION FVZ(147),F(147),R(147),XINT(29),GV(29),GVZ(19),
     1GVZ1(19)
      PI = 3.141592
      FVZ(1) = 0
      R(1) = 0
      IF (I .EQ. 2) GO TO 3
      IF(I .EQ. 4) GO TO 3
      IF (KK .GT. 1) GO TO 3
      IF (J .GT. 1) GO TO 3
    3 DO 10 K=2,MIN
   10 FVZ(K) = 2.0*PI*F(K)*R(K)
      IF (I .EQ. 2) GO TO 20
      IF (I .EQ. 4) GO TO 20
      IF (KK .GT. 1) GO TO 20
      IF (J .GT. 1) GO TO 20
      WRITE (6,1)
    1 FORMAT (//22X,2HR ,28X,2HFV,/)
```

```
      DO 15 M=1,MIN
   15 WRITE(6,21) R(M),FVZ(M)
   21 FORMAT (15X,E15.8,15X,E15.8)
   20 GVZ(J) = SIMPUN(R,FVZ,MIN)
      GVZ1(J) = GVZ(J)/GVZ(1)
      RETURN
      END
```

H. SUBROUTINE ORTHO

```
C
C     CURVE FITTING BY THE METHOD OF LEAST SQUARES
C
      SUBROUTINE ORTHO (X,Y,N,IDG,COE,SUMSQ,DMAX)
      DIMENSION X(40),Y(40),Q(40),P(40)
      DIMENSION A(10),B(10),C(10),G(10),COE(10),SUMSQ(10)
      NC = IDG + 1
      DO 5 I=1,N
      P(I) = 0.0
    5 Q(I) = 1.0
      DO 7 J=1,NC
      A(J) = 0.0
      B(J) = 0.0
    7 C(J) = 0.0
      F = 0.0
      WN = N
      DO 18 I=1,N
      W = 0.0
      DO 12 L=1,N
   12 W = W+Y(L)*Q(L)
      C(I) = W/WN
      IF (I-NC) 14,20,20
   14 E = 0.0
      DO 16 L=1,N
   16 E = E+X(L)*Q(L)*Q(L)
      E = E/WN
      A(I+1) = E
      W = 0.0
      DO 17 L=1,N
      V = (X(L)-E)*Q(L)-F*P(L)
      P(L) = Q(L)
      Q(L) = V
   17 W = W+V*V
      F = W/WN
      B(I+2) = F
   18 WN = W
   20 DO 121 L=2,10
      COE(L-1) = 0.0
```

```
121 G(L) = 0.0
    G(1) = 1.0
    DO 30 J=1,NC
    S = 0.0
    DO 23 L=1,NC
    IF (L-2) 23,21,22
 21 G(L) = G(L) - A(L)*G(L-1)
    GO TO 23
 22 G(L) = G(L) - A(L)*G(L-1)-B(L)*G(L-2)
 23 S = S+C(L)*G(L)
    COE(10-J) = S
    L = NC
    DO 25 IJ = 2,NC
    G(L) = G(L-1)
 25 L=L-1
 30 G(1) = 0.0
    SUMO = 0.0
    DMAX = 0.0
    DO 35 I=1,N
    YC = COE(1)
    DO 34 J=2,9
 34 YC = YC*X(I)+COE(J)
    R = ABS(Y(I)-YC)
    DMAX = AMAX1(DMAX,R)
 35 SUMQ = SUMQ+R*R
    SUMSQ(IDG) = SUMQ
    RETURN
    END
```

I. FUNCTION SIMPUN

```
C
C     INTEGRATION BY MODIFIED SIMPSONS RULE
C
      FUNCTION SIMPUN (X,Y,L)
      DIMENSION X(52),Y(52)
    4 M = L-1
    0 S = (X(2)-X(1))/6.*(Y(1)*((X(2)-X(3))/(X(1)-X(3))+2.)+Y(2)*
    1((X(1)-X(3))/X(2)-X(3))+2.)-Y(3)*(X(2)-X(1))**2/((X(1)-X(3))*
    2(X(2)-X(3))))
      DO 1 K=2,M
      IF (ABS(X(K+1)-X(1))-ABS(X(K)-X(1))) 3,1,1
    3 WRITE (6,2) K,X(K)
    2 FORMAT (23HONON MONOTONE X SIMPUN   I4,1PE12.4)
   10S=S+(X(K+1)-X(K))/6.*(Y(K)*((X(K+1)-X(K-1))/(X(K)-X(K-1))+2.)
    1+Y(K+1)*((X(K)-X(K-1))/(X(K+1)-X(K-1))+2.)-Y(K-1)*(X(K+1)-X(K))
    2**2/((X(K)-X(K-1))*(X(K+1)-X(K-1))))
```

```
    6 SIMPUN = S
      RETURN
      END
```

At this point, it is necessary that an explanation be given for the manner in which one should enter data and alter the "control" statements in the program so that it might be used to obtain distribution functions for cases other than those considered by the author. As it stands, the program is quite flexible and can be easily revised to suit such a need.

If you will note, there are certain statements in the program listing which are marked by arrows in the margin. These statements are the ones which control the basic operation of the program. The first is a loop in terms of I. The program is set up such that for I=1 all output will be in terms of the positive (cathode to anode) v_z axis and headings will be labeled as neon. For I=2 all output will be in terms of the negative (anode to cathode) v_z axis. Likewise for I=3 and I=4 with the exception that headings will be labeled as helium. The loop can be run independently for I values that are odd, but even I values must be run with their odd mate. And no value of I greater than 4 is acceptable. Thus, it is seen that two separate gas cases constitute the design limits of the program. Of course, any gas can be used in the program, but it should be kept in mind that all headings are in terms of neon and helium (this can be easily remedied). The second loop is in terms of KK. This parameter is nothing else than the number of separate conditions under which each gas is to be subjected. The program will not handle more than 16 such conditions. The final loops are in terms of J and NIN. These parameters are to control

the number of v_z values to be considered in the calculations. The program will handle no more than 19 values for J and NIN.

With regard to the input data there are a few points of importance to consider. For each gas to be programmed there are two separate sets of data required. The first set consists of experimental conditions for heading purposes and variable calculations. It should be entered in 5F10.5 format. That is, 5 data points per data card in F10.5 fields. The data to be entered is the selected v_z values in terms of energy (square root of electron volts), the radial location of the probe in the tube, the longitudinal distance of the probe from the cathode, the electron number density of the first gas, the electron number density of the second gas, the pressure of gases one and two respectively, and the discharge current for both gases. These inputs should be in the order above and all values of one should be input before another is begun. There can be no more than 19 values for v_z nor more than 16 values for the other conditions. These conditions, however, must have a corresponding number of values. As can be seen, the number of v_z values determines the parameters J and NIN while the experimental conditions determine the parameter KK. It should be noted that the input values used in the program as it is listed come directly from the experimental conditions of Reference 2. The second set of data required are the coordinates from the σ versus velocity curves for each gas. These are input in 2F10.8 format. That is, two values per card in F10.8 fields. The values on each card are

a corresponding abcissa and ordinate value.

For "run" time purposes, the program requires approximately two minutes to compile and 0.03 minutes per J value on the IBM System/360 computer.

With the aforementioned information, one who has a basic knowledge of computer programming should be able to use this program effectively.

APPENDIX B

It is of major importance that the DIREDIST program and methodology not be erroneous in any manner. Thus, a check on its credibilty was made.

In the theory of Reference 2 the relationship

$$g(v_z) \simeq \frac{\sqrt{\pi} n h}{2\Gamma(\frac{3}{4})} \{ 1 - \mathrm{erf}(h^2 v_z^2) \} \qquad (B.1)$$

was derived for the case of a Druyvesteyn (σ constant) distribution, where f_0 is considered the only term of f significant. Using this equation, the DIREDIST program reliabilty can be checked. By zeroing the f_1 values of the program and inputing an arbitrary constant σ, $g(v_z)$ values should be obtained similar to those predicted by equation (B.1). This was done and the results are compared in Table III. It is seen that DIREDIST calculates accurately $g(v_z)$ values. In fact, the accuracy is quite astonishing considering the iterative and numerical processes incorporated in DIREIDST.

In addition, in order to demonstrate that variation of the σ parameter is accounted for correctly by DIREDIST, the $g(v_z)$ curves for a Druyvesteyn case, a neon-like σ, and a helium-like σ were calculated for an arbitrary gas. All these cases were "run" for the same electron density and mean velocity. The results are given by Figure 15. As expected, for the case of σ (or mean free path) increasing with energy (neon) the number of high energy electrons is above that found for constant σ and for the case of

z-directed velocity ($\times 10^{-6}$)	$g(v_z) \times 10^{-9}$ as determined by DIREDIST	$g(v_z) \times 10^{-9}$ as determined by eqn. (B.1)
0.000	1.749	1.749
0.297	1.699	1.699
0.445	1.637	1.637
0.593	1.551	1.551
0.741	1.442	1.442
1.038	1.162	1.161
1.186	0.999	0.998
1.334	0.830	0.827
1.483	0.661	0.657
1.631	0.502	0.496
1.779	0.359	0.353
1.975	0.205	0.203
2.177	0.099	0.098
2.372	0.040	0.040
2.610	0.010	0.010
2.847	0.002	0.002
3.084	0.000	0.000
3.410	0.000	0.000
3.855	0.000	0.000

Druyvesteyn $g(v_z)$ Values

Table III

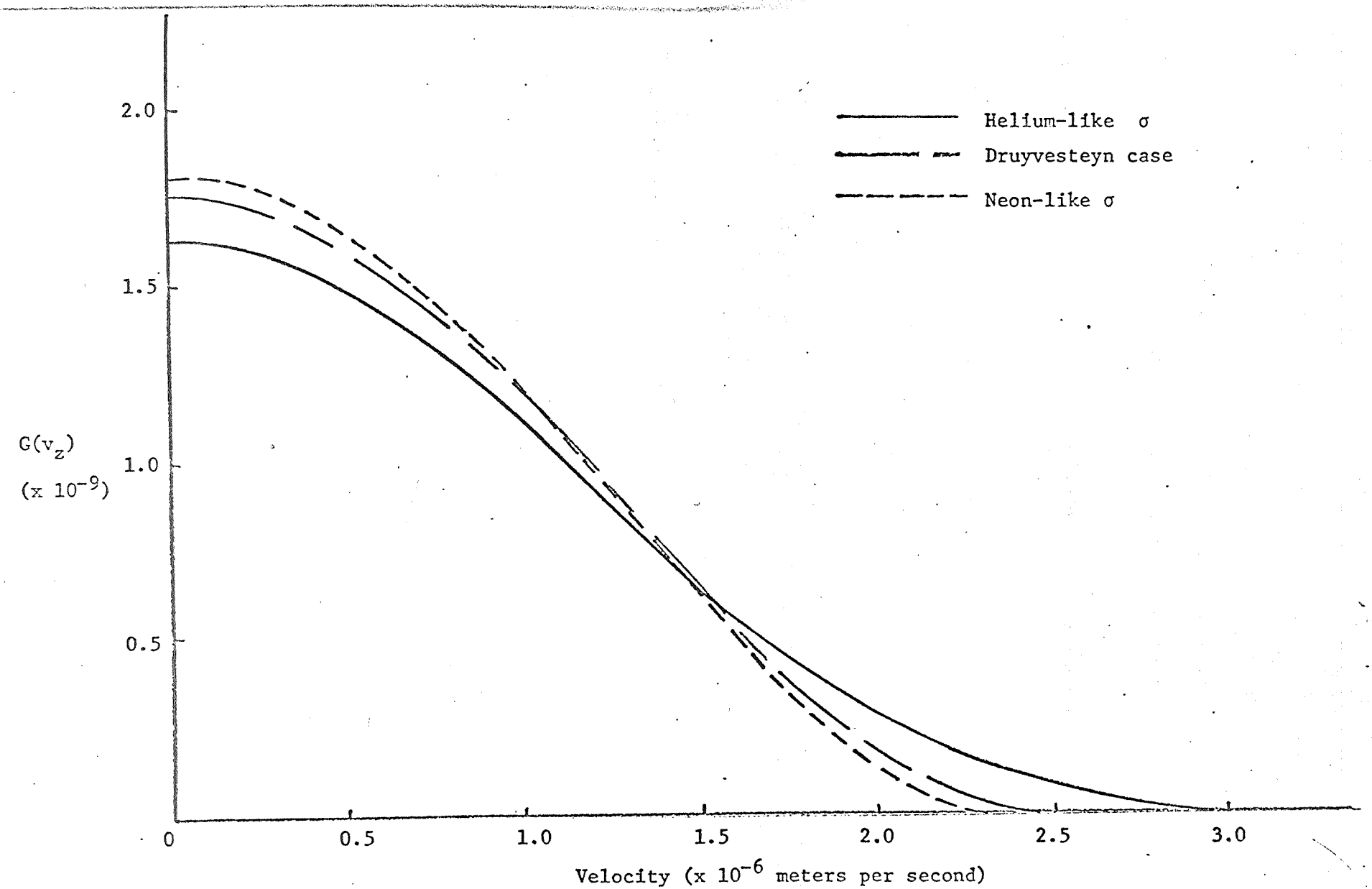

Distribution Curves for various Collision Cross Sections

Figure 15

σ decreasing with energy (helium) the opposite is true.

These two checks made on DIREDIST are a substantial proof of its credibility. And since the accuracy of the program is as excellent as Table III indicates, the methodology incorporated in the program must be valid.

APPENDIX C

For the purpose of calculating the distribution functions, it is assumed that there exists a strong electric field such that

$$\frac{e^2E^2M}{3m^2\nu_1^2} >> kT \quad .$$

In the case of helium, upon substitution of values for the vairables, the inequality becomes

$$725 >> 1 \quad .$$

For neon, again upon substitution for the variables, the inequality becomes

$$3620 >> 1 \quad .$$

Thus, the condition of a strong field is seen to be valid for either gas and the kT term can be considered neglgible with respect to the $\frac{e^2E^2M}{3m^2\nu_1^2}$ term.

Semi-Annual Progress Report No. 9

to the

NATIONAL AERONAUTICS AND SPACE ADMINISTRATION

in connection with

NASA Grant NGR 47-004-006

Part 7 of 8 Parts

Notice of Research Project

Science Information Exchange

for

New Projects

Virginia Polytechnic Institute
Blacksburg, Virginia

September, 1969

SI-SIE-78A1 REV. 6-64

NOT FOR PUBLICATION OR PUBLICATION REFERENCE

NOTICE OF RESEARCH PROJECT
SCIENCE INFORMATION EXCHANGE
SMITHSONIAN INSTITUTION

SIE NO.

AGENCY NO.

SUPPORTING AGENCY: NATIONAL AERONAUTICS AND SPACE ADMINISTRATION
Office of University Affairs
Sustaining University Program

TITLE OF PROJECT: Method for Calculating the Flow Field Over Aerodynamic Decelerators

Give names, departments, and official titles of PRINCIPAL INVESTIGATORS and ALL OTHER PROFESSIONAL PERSONNEL engaged on the project.

Dr. Fred R. DeJarnette, Principal Investigator
Department of Aerospace Engineering
College of Engineering

NAME AND ADDRESS OF INSTITUTION:

Virginia Polytechnic Institute, Blacksburg, Virginia 24061

SUMMARY OF PROPOSED WORK – (200 words or less.) – In the Science Information Exchange summaries of work in progress are exchanged with government and private agencies supporting research, and are forwarded to investigators who request such information. Your summary is to be used for these purposes. (Please indicate the number of students supported by this project.)

The purpose of this research is to develop a method for calculating the flow field over aerodynamic decelerators which are deployed in the wake of a vehicle traveling at supersonic speeds. For the decelerator, the wake produces a nonuniform free stream which has been found to cause the decelerator flow-field to deviate significantly from that of a uniform free stream. Previous research at VPI has also shown that boundary layer separation can occur, even on such simple shapes as pointed cones. The net result is a large change in the aerodynamic performance of decelerators, e.g. drag and stability coefficients, when compared with the performance for a uniform free stream.

The current approach is to formulate a method to calculate the inviscid flow field and then use the surface solution from this method to calculate the boundary layer properties up to the separation point. Beyond the point of boundary layer separation, the inviscid solution will be continued using a free streamline instead of the body surface as the inner boundary.

This project will support one graduate student.

SIGNATURE OF PRINCIPAL INVESTIGATOR _____

PROFESSIONAL SCHOOL (medical, graduate, etc.) Engineering

Semi-Annual Progress Report No. 9

to the

NATIONAL AERONAUTICS AND SPACE ADMINISTRATION

in connection with

NASA Grant NGR 47-004-006

Part 8 of 8 Parts

Selected Extended Progress Reports

V.P.I. Project 313246
Interaction of ^{50}Ti with Protons and Neutrons
by
R. J. Onega

V.P.I. Project 313241
Preparation of Glass-Ceramic Composites by Controlled Crystallization Techniques
by
J. J. Brown, Jr.

V.P.I. Project 313240
A Theoretical Investigation of Low Mass Meteoroid Cut-off
by
R. J. Adler

V.P.I. Project 313142
Harmonic Vibrations of Viscoelastic Layered Media
by
D. Frederick

Virginia Polytechnic Institute
Blacksburg, Virginia

September, 1969

Interaction of ^{50}Ti with Protons and Neutrons

Extended Progress Report

V.P.I. Project 313246

Principal Investigator: R. J. Onega
Physics Department

INTRODUCTION

The interaction of protons and neutrons with ^{50}Ti produces gamma rays. In the case of proton interactions with ^{50}Ti, both the proton capture process

$$P + {}^{50}Ti \rightarrow {}^{51}V + \gamma$$

as well as the inelastic scattering process

$$P + {}^{50}Ti \rightarrow {}^{50}Ti + P' + \gamma$$

occurs. The type of proton interaction with titanium depends upon the incoming proton energy. At some particular proton energies, resonances may be observed. These resonances arise due to energy level structures of the compound nucleus formed $(^{51}V)^*$. This nucleus subsequently decays and protons and/or gamma rays are emitted, leaving ^{51}V in the ground state.

When neutrons interact with ^{50}Ti, the $(^{51}Ti)^*$ compound nucleus is formed.

$$n + {}^{50}Ti \rightarrow (^{51}Ti)^* \rightarrow {}^{51}Ti + \gamma$$

$$\searrow \beta \searrow$$

$$^{51}V + \gamma \ .$$

The compound nucleus immediately de-excites by releasing prompt gamma rays. The ^{51}Ti, now in the ground state, beta decays into ^{51}V with a half life of 5.80 minutes. In this beta decay process gamma rays are also emitted.

The gamma ray environment in a space vehicle with some components containing ^{50}Ti will primarily be determined by the proton interaction with the titanium since the primary cosmic rays are mainly protons[1].

Secondary neutrons are produced by the interaction of the protons with matter. These neutrons undergo elastic and inelastic collisions and are then captured.

This report contains information on the neutron activation of ^{50}Ti as well as the proton interaction with titanium. The neutron activation has most recently been studied by Robinson et al.[2] in 1963. There were three gamma rays which followed the beta decay of ^{51}Ti into ^{51}V. The ^{51}Ti was formed by the neutron activation of ^{50}Ti. Three gamma rays were found with energies of 0.319, 0.613 and 0.934 MeV. The relative intensities of these gamma rays are 100, 1.6 and 5.8 respectively. Prompt gammas are associated with this neutron capture process but were not investigated.

The $^{50}Ti(P,P'\gamma)$ reaction was studied by Gray et al.[3]. They studied this reaction at incoming proton energies of 18.2 MeV and 11.5 MeV. Most of their work was concerned with the outgoing elastically scattered protons, however, rather than the gamma rays. Most of the gamma rays emitted are in the low MeV region ($\leq$ 3 MeV). The $^{50}Ti(P,P'\gamma)$ reaction was studied at an energy of 7 MeV by Belote[4] et al.

Proton fluxes ranging from 10^3 eV to 200 MeV have been investigated[5] in the magnetic field of the earth. These particles are also trapped in the magnetic field of Jupiter as well as the earth. Secondary particles originate when the protons interact with the nitrogen and oxygen in the earth's atmosphere or with other material.

The Capture of Neutrons by ^{50}Ti.

Since neutrons may be a constant environment in space due to various types of reactions of protons with material producing neutrons, a study of the capture of the neutrons by ^{50}Ti was undertaken.

The ^{50}Ti sample was inserted into the VPI reactor by means of a pneumatic transfer system. The transit time from the reactor to the counting facilities was about 5 seconds. The gamma ray spectrum due to the beta decay of ^{51}Ti was then investigated by means of a 4 cm^3 Ge(Li) detector as well as a NaI(Tl) crystal. Figure 1 is the gamma ray spectrum from the Ge(Li) detector. Only three gamma rays are observable, the 0.320, 0.613 and 0.933 MeV. The decay is such that the 0.320 and the 0.613 were in coincidence adding to give 0.933 MeV. There was, in addition, the cross over transition of 0.933 MeV.

Relative intensity measurements were performed and our results as well as those obtained by Robinson et al.[2] are compared in Table I. The detector used in the investigation of the relative intensities was a 3" x 3" NaI detector in a lead shield to reduce background to a minimum.

Table I

Relative Intensities of ^{51}Ti Gamma Rays

Energy (MeV)	Relative Intensity (Robinson)[2]	Relative Intensity (This Work)
0.320	100	100
0.613	1.6 $\pm$ 0.2	3.75 $\pm$ 0.4
0.933	5.8 $\pm$ 0.6	8.8 $\pm$ 0.8

The absorption cross section of ^{50}Ti for neutrons of 0.025 eV was 0.14b[6]. The secondary neutrons impinging on ^{50}Ti could thus be a significant source of radiation due to the gamma rays following their capture.

Proton ^{50}Ti Interactions

The V.P.I. Van de Graaff accelerator has an energy range of 4 MeV. A titanium-50 target on a bismuth backing was placed in the beam tube of the accelerator. The proton beam was allowed to impinge on the target and the gamma rays were detected as function of energy. Since the γ rays could be attenuated by going through the bismuth backing, the NaI(Tl) detector was placed at a forward angle of about 45^{o} with respect to the beam.

The gamma ray energy spectrum was taken with the proton beam at 1.5 MeV, 2.25 MeV and 3.0 MeV. The bismuth backing was then rotated 180^{o} in the scattering chamber of the Van de Graaff accelerator and the background gamma ray spectrum was taken at these same three proton energies. Figure 2 shows the difference gamma ray spectrum for the 1.5 MeV incoming proton beam case. The gamma ray energy spectrum reached about 8.5 MeV for the 1.5 MeV incoming proton beam energy and about 10 MeV γ ray energy for the 3 MeV incoming proton energy.

Figure 2 indicates there was some structure in the gamma ray spectrum. This structure was due to the fact that as the $(^{51}Ti)^{*}$ nucleus de-excited, gamma rays were emitted which were characterized by the difference of two nuclear energy levels.

CONCLUSIONS

The prompt gamma rays that were emitted following proton capture would present a very real hazard to people in capsules composed of titanium if the proton flux were significant. The same energy gamma rays would also be expected from the capture of neutrons. The energies of the gamma rays following the beta decay of the radioactive nuclei were always

much less in energy than the prompt gamma rays.

The dose rate was proportional to the energy of the gamma rays. This means that high energy gamma rays which were absorbed by a person are more damaging than low energy gamma rays. There were, however, other factors to be considered. The higher energy gamma ray had less probability of being absorbed. Foster and Wright[7] show that the absorption coefficient for gamma rays in tissue reached a peak at about 0.6 MeV and then decreased on up to beyond 10 MeV. So low energy (~ 1 MeV) gamma rays do not cause as much biological damage but there absorption probability was greater than higher energy gamma rays.

The experiment indicates that it would be the prompt gamma rays which would be troublesome for space travel. They arise from both the (P,γ) and (n,γ) reactions on titanium.

BIBLIOGRAPHY

1. R. B. Leighton, "Principles of Modern Physics", McGraw-Hill Book Company, Inc. pages 680-708, (1959).

2. R. L. Robinson, N. R. Johnson and G. D. O'Kelley, Nuclear Physics, 47, pages 506-510, (1963).

3. W. S. Gray et al., Nuclear Physics, 67, 323 (1965).

4. T. A. Belote et al., Physics Letters, 14, 323 (1965).

5. K. A. Anderson, "Energetic Particles in the Earths Magnetic Field", from Annual Review of Nuclear Science, edited by E. Segre, Vol. 16, 1966, pages 291-344.

6. D. T. Goldman, J. R. Roesser, "The Chart of the Nuclides", distributed by the General Electric Company, Schenectady, N. Y., (1966).

7. A. R. Foster and R. L. Wright, Jr., "Basic Nuclear Engineering", Allyn and Bacon, Inc., Boston, Mass., 1968, page 119.

Preparation of Glass-Ceramic Composites by Controlled Crystallization Techniques

Extended Progress Report

V.P.I. Project 313241

Principal Investigator: J. J. Brown, Jr.
Department of Metals and
Ceramic Engineering

ABSTRACT

Strengthening of glass by introducing a second immiscible phase was investigated using a portion of the ternary system SiO_2, Li_2O, and TiO_2. The major portion of the work was confined to compositions taken along the 70 weight percent SiO_2 isopleth. Modulus of rupture (bending) and elasticity data indicate that strengthening increases as the TiO_2 content is increased beginning with composition "C" (a miscible glass), which yielded an average modulus of rupture strength of 20,900 psi. A marked increase was recorded as compositions were formed inside the immiscibility region and continued until a maximum of 34,600 psi was attained with a TiO_2 content of approximately 15 weight percent. At this point, nucleation could no longer be controlled and crystallization became predominant when 20 weight percent TiO_2 was used. The modulus of rupture (bending) of this crystallized composition decreased rapidly, yielding an average strength of 26,800 psi.

TABLE OF CONTENTS

		Page
I.	Introduction	1
II.	Related Literature	4
III.	Materials and Apparatus	
	A. Chemicals and Composition Preparation	7
	B. Processing Apparatus	7
	C. Testing Apparatus	8
	D. Data Processing	8
IV.	Results and Discussion	
	A. Composition "C", 70 SiO_2 · 25 Li_2O · TiO_2	10
	B. Composition "G", 70 SiO_2 · 20 Li_2O · 10 TiO_2	10
	C. Composition "E", 70 SiO_2 · 15 Li_2O · 15 TiO_2	11
	D. Composition "F", 70 SiO_2 · 13 Li_2O · 17 TiO_2	11
	E. Composition "F-2", 70 SiO_2 · 20 Li_2O · 10 TiO_2	11
V.	Summary	15
VI.	Acknowledgments	15
VII.	Anticipated Future Work	16
VIII.	References	17

I. INTRODUCTION

Ternary silica-rich glasses are extremely attractive for structural applications in the industrial community and particularly the aerospace industry. The silica-rich compositions have very low thermal expansion (approximately 6.7×10^{-7} per °C) and outstanding thermal shock resistance compared with other glass compositions. Other attributes are their potential high strength-to-weight ratio, high softening temperature, and excellent resistance to chemical attack.

The major shortcoming of silica-rich glasses is their brittleness. In contrast to most metals, the surface condition of glass is very critical. Any type of rupture (scratch) on the surface of a glass will act as a stress riser and potential site for fracture initiation.

Numerous investigations have been conducted and others are now in progress to find ways to increase the strength of glass by designing an abrasive resistant surface. Another approach to this problem is to prevent propagation of fracture throughout a bulk glass body by incorporating a second phase such as that of imbedding fibers in a glass matrix. This approach has met with limited success, because of the difficulty of producing strong bonds between the phases and moreover, it only changes the propagation direction to that of the direction of the long dimension of the fibers.

Methods of strengthening glass-crystal composites have been a controversial subject since the discovery of finely dispersed microcrystalline bodies in a glass matrix. The technique of embedding particles of higher expansion into a matrix of lower expansion, which puts the glass in compression, has been used for most of the previous investigations. In contrast to this, is that of immiscibility strengthening which consists of dispersing a liquid phase within a liquid phase. The dispersed phase is in the form of spherical liquid droplets that are expected to effectively act as a void in the matrix to supress crack front propagation. A model was proposed by Ohlberg, Golob and Hollabaugh[3] which relates very closely to this type of experimental approach. Therefore, the following two approaches were considered for this study.

One consisted of mixing two glass compositions together in the molten state which, in most cases, would eventually form a homogeneous glass. However, if the two were not well mixed, they would retain regions of different compositions upon cooling. If the kinetics of crystallization are considerably different, or if a classical nucleating agent such as TiO_2 is incorporated into one of the glasses, it then becomes possible to selectively form a fine microcrystalline phase dispersed in that of the other phase, which then becomes a glass-ceramic composite. Thus, strengthening results when crystalline grains of high strength and modulus of elasticity are introduced into a glass of similar or slightly lower thermal expansion.

The other approach which was used in this study was to take advantage of the liquid immiscibility region of the SiO_2-rich system containing Li_2O and TiO_2. A series of compositions were selected for investigation at points inside, outside and on the boundary line itself of the immiscible region. The silica content was held constant while the ratio of Li_2O to TiO_2 was varied. This silica-rich region was selected because the system would not yield a clear glass when more than approximately 5 to 10 percent TiO_2 was dissolved in the melt. The solubility of TiO_2 decreased rapidly as the Li_2O was decreased and the SiO_2 increased. Nucleation could not be controlled in compositions containing less than 70 percent SiO_2 and larger percents of TiO_2, since crystallization resulted immediately upon cooling the melt. Although both approaches were pursued originally, it becomes increasingly evident that the immisibility approach held the most promise, because it eliminated such variables as determining the degree of mixing of the separate glass phases and more important, the complexity of processing test samples was considerably reduced.

II. RELATED LITERATURE

Some of the earliest work related to microcrystalline bodies dispersed in a glassy phase was reported by Stookey[1] in 1957. His pioneer work in the field has since stimulated many investigations on nucleation in glass, such as that of Maurer, Vogel, Gerth, and Ohlberg. Kim and Hummel[2] compiled considerable data on new ternary compounds, liquid immiscibility, and compatibility triangles as a result of their work on the phase equilibrium relations of the system Li_2O-TiO_2-SiO_2. They reported that the liquid immiscibility originating in the binary system SiO_2-TiO_2 extends over a substantial portion of the ternary system. This led to the construction of a diagram outlining the two-liquid immiscibility region of the system. It was further reported that all compositions selected in the two-liquid region were observed to be translucient, milky or optically dense and opaque, due to phase separation which in most cases could only be identified with the aid of an electron microscope.

Some of the first studies of fracture surfaces of glass related to supression of crack front propagation by liquid-in-liquid colloidal immiscibility was reported by Ohlberg, Golob, and Hollabaugh.[3] With the use of an electron microscope, they observed tail-like structures emanating from the dispersed phase to be related to the crack front propagation. From this, they designed a model illustrating propagation of the front in an immiscible system. When the front reaches one of the dispersed droplets, that droplet acts as a void and splits the original crack front into two new crack fronts. As the two fronts approach each other after going around the droplets, they are in different planes and

must curve toward each other in order to recombine. The tail effect, previously described, is a result of the nonplanarity of the two fronts when they recombine. The tail effect should not be interpreted as a continuation and neither as a crack in the immiscible phase; however, it is a measure of a difference in level on the fracture surface.

MacDowell and Beall[4] studied metastable glass-in-glass separation in the Al_2O_3-SiO_2 system, using electron microscope and x-ray diffraction techniques. They reported the following:

1. Phase separation is the essential cause of nucleation of the dispersed phase.
2. The tendency toward crystallization of the dispersed liquid phase increased with (a) increasing Al_2O_3 concentrations in the melts, and (b) decreasing cooling rate.
3. Crystallization on cooling and emulsion formation were both reduced or inhibited in intermediate and high-alumina compositions by the addition of modifying oxides (alkaline earth's).

Some of the latest work on strengthening of glass-crystal composites was reported by Tummala[5] and Friedberg taken from their investigation on glass-ZrO_2 composites. They discussed the two schools of thought as to the effect of crystals on the strength of these composites. One method was that of embedding crystalline particles of higher expansion in a continuous glass matrix of lower expansion which would put the glass in compression and increase its strength. This has come to be known as the prestress

theory. The other theory states that when crystalline grains of high strength and elasticity are introduced into a glass of similar expansion, the strength and modulus of elasticity are increased. The objective of their investigation was to determine how the shape of dispersed particles influenced strength. Their findings supported the prestress theory when rounded particles were used in the composites which indicated that there is a substantial effect of grain shape on strength.

III. MATERIALS AND APPARATUS

A. Chemicals and composition preparation:

All compositions in the $Li_2O \cdot TiO_2 \cdot SiO_2$ system were prepared from carbonates and oxides of the various components.

Basic composition materials -

1. Lithium carbonate, Li_2CO_3, manufacturing grade, Foote Chemical Company, M.W. 73.89.
2. Titanium oxide, TiO_2, high grade, Tam Mineral Company, M.W. 79.90.
3. Potter's Flint, SiO_2, commercial grade, Pennsylvania Glass Sand Company, M.W. 60.06.

Batch materials were weighed to an accuracy of 0.5 grams in batch sizes of 500 grams. Mixing of the materials was accomplished by a "V"-shell blender with a standard mixing time set at two hours for each batch. After mixing was completed, each composition was placed in a fire clay crucible and prepared for melting.

B. Processing Apparatus:

1. Melting of the batch compositions was accomplished by the use of a large Glo-bar furnace (Box-type) which was capable of operating at temperatures up to 1425°C. Melting temperatures were standardized at 1315°C for all compositions.
2. A small annealing furnace was used to heat the graphite mold for casting the glass rods. The mold temperature for casting was standardized at 400°C for all compositions.

3. A graphite mold was constructed to facilitate casting of rod type specimens. Six casting cavities were incorporated in the mold with the following approximate dimensions: cavity diameter, 0.5 inches, length 5.0 inches.

C. Testing Apparatus:

Modulus of rupture (bending) and elasticity data was accumulated by testing the glass rods horizontally using the three point loading technique. The apparatus used was a Tinius Olsen tension testing machine adapted with a three-point loading fixture. A dial gauge was attached to the loading fixture to measure the deflection of the rod.

D. Data Processing:

1. Modulus of rupture (bending)

All modulus of rupture data were acquired using the following procedure:

a) Ten diameter measurements were taken on each rod in a systematic manner and averaged to get a representative diameter.

b) Distance between knife edges on test fixture was 3 inches.

c) The modulus of rupture was then calculated for each specimen using the formula:

$$MR = \frac{MC}{I} = \frac{8\ PL}{\pi d^3}$$

d) Finally, the data of the 10 specimens were averaged to give the representative modulus of rupture data recorded in Table II.

2. Modulus of Elasticity

All modulus of elasticity data were acquired using the following procedure:

a) Flexure readings were taken at each 100 pound interval as the load was applied during testing.

b) Data of approximately four rods were selected to represent each composition, and the modulus of elasticity was calculated at each 100 pound interval for that rod. The elasticity intervals were averaged and finally a grand average was calculated for the total composition using the average elasticity of each of the individual rods.

c) It should be noted that an average rod diameter was used to compute the modulus of elasticity that represents each composition.

d) The modulus of elasticity was calculated using the following formula:

$$E = \frac{4}{3} \frac{PL^3}{\pi d^4 \cdot V_{max}}$$

where V_{max} represents maximum deflection of the rod.

e) The grand average that represents each composition is reported in Table II.

IV. RESULTS AND DISCUSSION

A. Composition "C", 70 SiO_2 · 25 Li_2O · 5 TiO_2 (Table I)

This composition was selected first, because it existed well outside of the immiscibility boundary. It was expected to yield a clear miscible glass which could be used to establish a control standard. Its position on the ternary diagram is illustrated in Graph I.

The raw batch was melted at a temperature of 1315°C, and held there for one hour to insure fining of the melt after which 10 rods were cast in order to obtain a representative sample. Modulus of rupture (bending) and elasticity data based on the average of the sample is reported in Table II. It should be noted that this composition yielded a clear glass as expected, and the modulus of rupture strength averaged 20,900 psi which was within the parameters of that of a typical silica-rich miscible glass.

B. Composition "G", 70 SiO_2 · 20 Li_2O · 10 TiO_2 (Table I)

This composition was second in the SiO_2 isopleth sequence series. Upon observing the 10 rods cast from this melt, it was obvious that there was some deviation from a transparent medium. Although it was still very transparent, a faint amber cloudiness was observed. This composition appeared to be very close to the immiscibility boundary line, if not directly on it, which is illustrated in Graph I. Modulus of rupture data reported in Table II showed a 50 percent increase over that of composition "C", indicating that some immiscibility was present. This is also reinforced by the observed amber color which indicated that some nuclei were present in one of the immiscible phases.

C. Composition "E", 70 SiO_2 · 15 Li_2O · 15 TiO_2 (Table I)

This composition is positioned well within the immiscibility region and has shown more promise than any of the other compositions in the series. It exhibited the highest modulus of rupture strength (ave. 34,600 psi) with one individual rod as high 69,000 psi) and elasticity data of all the compositions investigated, even those with large TiO_2 concentrations. Most of the samples revealed a deep amber appearance which indicated that a considerable amount of nuclei had formed in one of the immiscible phases. This appearance correlates well with the theory that nucleiation present in one of the phases promotes strengthening of the composite.

D. Composition "F", 70 SiO_2 · 13 Li_2O · 17 TiO_2 (Table I)

In contrast to all the others, this composition was the first to show a high degree of crystallization and separation of the two phases causing it to be opalescent and opaque in appearance. Strength data decreased significantly for this composition which indicates that too much crystallization of one of the phases is detrimental to the prestress mechanism of strengthening glass-ceramic composites.

E. Composition "F-2", 70 SiO_2 · 10 Li_2O · 20 TiO_2

Another variation of composition "F" containing 3 percent more TiO_2 was investigated. It was very difficult to cast rods from this composition because the reaction of SiO_2 in dissolving the TiO_2 into the melt was very sluggish. Furthermore, when a few rods were finally cast, crystallization was extremely difficult to control.

TABLE I. TERNARY COMPOSITIONS

Composition	SiO_2 Wt. %	Li_2O Wt. %	TiO_2 Wt. %
C	70	25	5
E	70	15	15
F	70	13	17
G	70	20	10

TABLE II. PROPERTIES VS COMPOSITIONS

Composition	Casting Temp. °C	Mold Temp. °C	Mod. of Rup. psi	Mod. of Elas. psi	Appear
C	1315	400	20964	3.01×10^6	Clear
E	1315	400	34665	4×10^6	Amber
F	1315	400	29771	3.07×10^6	Opalescent
G	1315	400	26056	2.89×10^6	Lt. Amber

FIGURE I

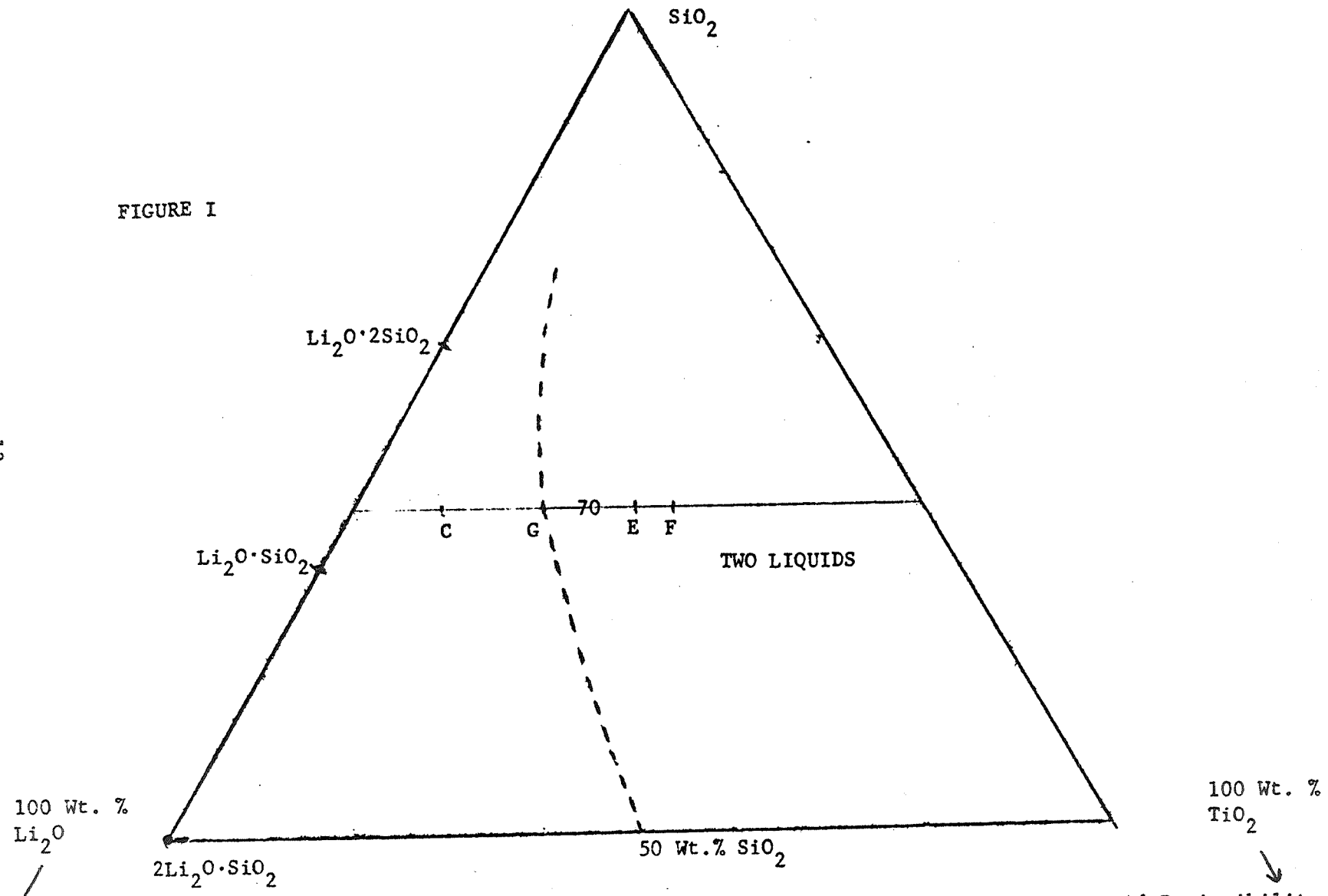

Figure I. 50-100% SiO_2 Region of $SiO_2 \cdot TiO_2 \cdot LiO_2$ Ternary Diagram Showing Liquid Immiscibility Boundary (-- -) and Sample Compositions.

Figure II. Modulus of Rupture vs. TiO_2; Li_2O Ratio on 70% SiO_2 Isopleth

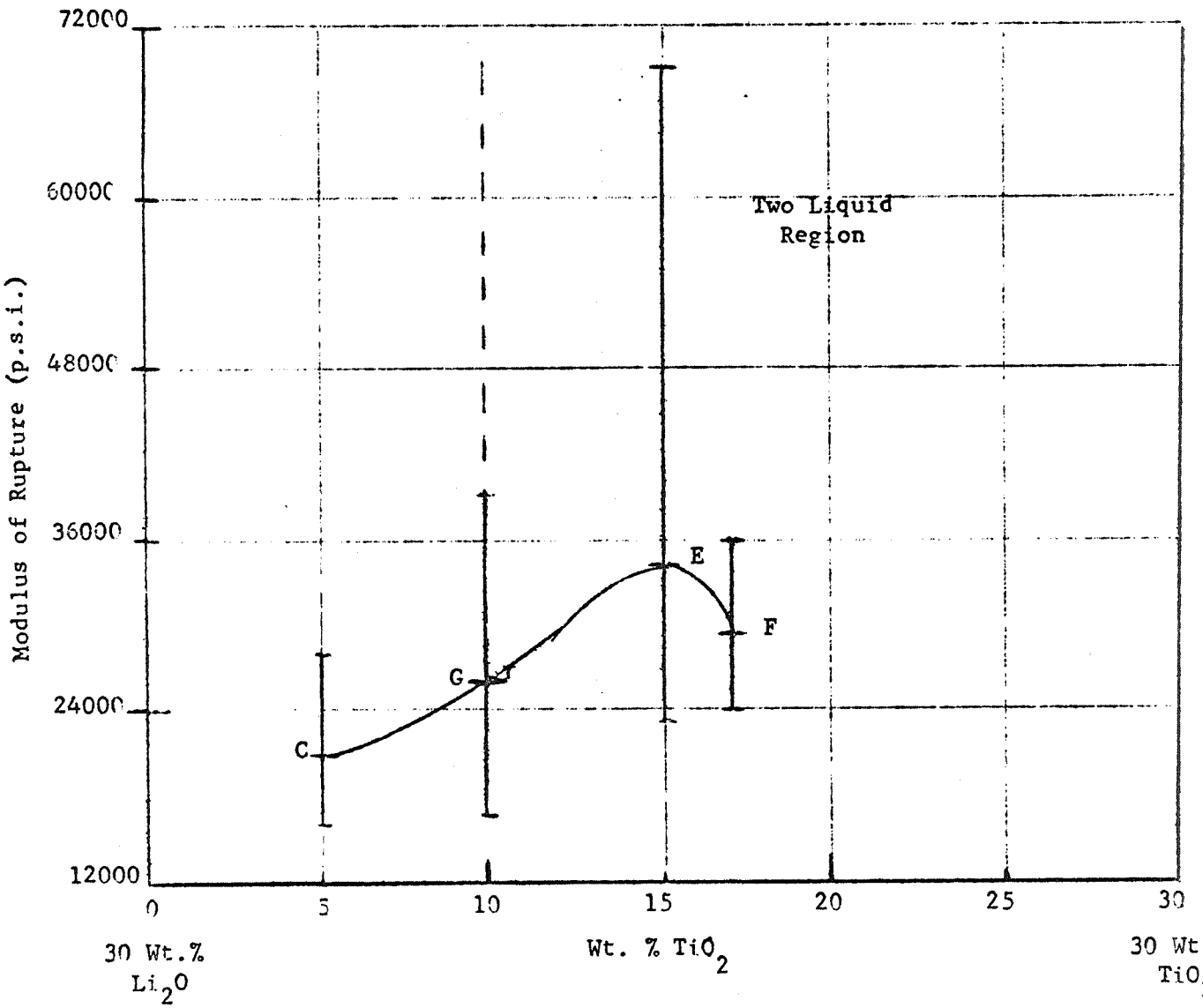

V. SUMMARY

Glass formation and crystallization correlated with modulus of rupture (bending) data were determined for several compositions along the 70 percent SiO_2 isopleth. The following conclusions were made:

1. The immiscibility boundary line was confirmed at a point on the ternary diagram near composition "G" which is reported in Table I.
2. The observed amber color is probably an indication that nuclei are being formed as a result of phase separation.
3. The classical mechanism of nucleation and growth appears to be operative during two phase separation in the 70 percent SiO_2 isopleth along the region of 10 to 20 percent TiO_2 concentrations. Any further increase in TiO_2 concentration promotes uncontrolled crystallization.
4. Strengthening of the glass-ceramic composite reaches a maximum at a point on or near composition "E" as compositions are investigated, starting at composition "C" from the left and moving through "E" to that of "F".

VI. ACKNOWLEDGMENT

The authors wish to express their appreciation to Robert Frankson for some exploratory work which led to the selection of the compositions examined in this investigation.

VII. ANTICIPATED FUTURE WORK

Further study on these immiscible systems is necessary in order to characterize certain behavior of their properties. Some of the areas to be investigated are as follows:

1. Other compositions along the 70 percent SiO_2 isopleth should be investigated, especially those near composition "E" to determine the exact one that produces optimum strength.
2. Heat treating studies should be conducted to determine the effect of temperature on the strength of the various compositions.
3. Electron micrographs should be prepared to study fracture characteristics supported by electron probe analysis to give the distribution of Ti and Si.

VIII. REFERENCES

1. S. D. Stookey, "Corning Develops New Ceramic Materials," Am. Ceram. Soc. Bull., 36 [7] 279-80 (1957).

2. K. H. Kim and F. A. Hummel, "Studies in Lithium Oxide Systems, VI, Progress Report on the System Li_2O-SiO_2-TiO_2," J. Am. Ceram. Soc., 42 [6] 286-291 (1959).

3. S. M. Ohlberg, H. R. Golob, and C. M. Hollabaugh, "Fractography of Glasses Evidencing Liquid-in-Liquid Colloidal Immiscibility," J. Am. Ceram. Soc., 45 [1] 1-4 (1962).

4. J. F. MacDowell and G. H. Beall, "Immiscibility and Crystallization in Al_2O_3-SiO_2 Glasses," J. Am. Ceram. Soc., 52 [1] 17-25 (1969).

5. R. R. Tummala and A. L. Friedberg, "Strength of Glass-Crystal Composites," J. Am. Ceram. Soc., 52 [4] 228-229 (1969).

A Theoretical Investigation of Low Mass Meteoroid Cut-off

Extended Progress Report

V.P.I. Project 313240

Principal Investigator: R. J. Adler
Physics Department

Introduction

Work on the meteoroid cut-off is nearly complete. The main processes which affect cut-off have been investigated and only a couple of other processes remain to be looked into, primarily to present a complete picture.

Figure 1 presents the Explorer and Pegasus penetration data along with a best-fit parabola[1] to this data. The parabola was required because the slopes defined by the Explorer and Pegasus data on log-log scales are different and there is no way to fit the data with a straight line. The parabola indicates that the maximum penetration flux is about 7×10^{-6} m^{-2} sec^{-1}. Some supporting data for the existence of a maximum flux is also shown in the Figure. The data came from the Ariel II satellite[2] which has exposed the thinnest thicknesses thus far to the meteoroid environment. It is evident that the supposition of a maximum flux (and a minimum sized particle) has been somewhat strengthened by the Ariel II penetration data.

The following section presents descriptions of the processes considered thus far and also the two processes which still remain to be examined. The last section presents tentative conclusions reached thus far and the relationship of the present study with the hazard which meteoroids pose to manned spacecraft.

A. Physical Processes Responsible for Cut-Off

Poynting-Robertson Effect:

One of the most striking effects from the viewpoint of cosmology predicted by the special theory of relativity is the Poynting-Robertson Effect. A particle in motion around the sun will experience pressure from the sun's radiation not only in the radial direction but also tangentially against the particle's motion. This "tangential drag" will cause the particle to lose angular momentum and to eventually spiral into the sun. Using the development given by Robertson[3], we can sketch the derivation of this effect, with the expressed interest of getting a typical particle's lifetime in the solar system.

Consider a small, spherical particle of radius a, density ρ, moving with a unit four-velocity u^μ in the system S, in which the sun is instantaneously at rest. In S, the sun's radiation falling on the particle can be considered to be a plane-parallel wave with the incident direction defined by the null four-vector ℓ^μ. The energy-momentum-stress tensor can be written as

$$S^{\mu\nu} = d(\ell^\mu \ell^\nu) \tag{A.1}$$

where d is the energy density of the radiation.

Upon going to the proper frame of the particle, P, the four-velocity of the particle and the direction of the incident radiation are given by

$$v^\mu = \delta^\mu_o \ , \quad \lambda^a = c\lambda^o{}_\nu{}^a \quad (a = 1, 2, 3) \tag{A.2}$$

respectively. We assume that the particle is in thermodynamic equilibrium;

that is, the rate at which the radiation is absorbed is equal to the rate at which the particle isotropically re-emits radiation. This means that mass is invariant in P, or

$$\frac{dmv^{o}}{d\tau} = 0 \tag{A.3}$$

where τ is the proper time. Let us denote the radiation pressure by

$$\Phi = \sigma\delta \tag{A.4}$$

where σ is a purposely ambiguous cross-section and δ is the energy density of the radiation in the system P. This force acts in the direction ν^{a}. Therefore,

$$\frac{dmv^{a}}{d\tau} = \Phi\nu^{a} = \frac{\Phi}{c\lambda^{o}}\lambda^{a} \tag{A.5}$$

Putting (3) and (5) together, we have

$$\frac{dmv^{\mu}}{d\tau} = \frac{\Phi}{\lambda^{o}c}(\lambda^{\mu} - \lambda^{o}v^{\mu}) \tag{A.6}$$

Going back to the sun's rest frame, we find

$$\frac{dmu^{\mu}}{dt} = \frac{fw}{c}(\ell^{\mu} - wu^{\mu}) \tag{A.7}$$

where $w = \ell_{\alpha}u^{\alpha} = \lambda^{o}$, $\delta = w^{2}d$, and $f = \sigma d$ which is the force which the particle would experience if it were at rest in the sun's system. The proper time is t.

We now take the low velocity approximation,

$$(A.8) \qquad v^a = \frac{dx^2}{dt}, \quad n^a = \frac{\ell^a}{c}$$

This implies,

$$(A.9) \qquad m\frac{dv^a}{dt} = f(1 - \frac{v_n}{c})n^a - f\frac{v^a}{c}$$

where $v_n = \underline{v} \cdot \underline{n}$. The first term is now the force due to radiation weakened by a Doppler factor. The second term is the so-called "tangential drag" although a drag arises from both the first and second terms of equation (9).

Let S be the solar constant (radiation falling on a square centimeter normal to the sun's rays at the mean distance b of the earth). This implies that

$$(A.10) \qquad d = \frac{Sb^2}{cr^2}; \quad f = \frac{m\alpha c}{r^2}; \quad \alpha = \frac{ASb^2}{mc^2} = \frac{2.5 \times 10^{11}}{a\rho}$$

Now let us write equation (9) in polar coordinates (r,θ) for a particle in the plane of the eclptic.

$$(A.11) \qquad \ddot{r} - r\dot{\theta}^2 = \frac{-\mu}{r^2} - \frac{2\alpha\dot{r}}{r^2}; \quad \frac{1}{r}\frac{d}{dt}(r^2\dot{\theta}) = -\frac{\alpha\dot{\theta}}{r}$$

where $\mu = \mu_o - \alpha c$, $\mu_o = GM$. From the second equation of (11) we find that the angular momentum per unit mass decreases according to

$$(A.12) \qquad r^2\dot{\theta} = h - \alpha\theta$$

The first equation of (11) can be put into the form of an inhomogeneous Bessel's equation via the transformations

$$\theta = \frac{h}{\alpha} - \phi \quad ; \quad \frac{1}{r} = u = \mu\phi \frac{z}{\alpha^2} \tag{A.13}$$

Equation (A.11) then becomes

$$\frac{d^2z}{d\phi^2} + \frac{1}{\phi}\frac{dz}{d\phi} + (1 - \frac{1}{\phi^2})z = \frac{1}{\phi^3} \tag{A.14}$$

and Equation (A.12) is now

$$\dot{\phi} + u^2\alpha\phi = 0 \tag{A.15}$$

The asymptotic expansion of the solution of (A.14) for $\phi >> 1$ is

$$\phi z \sim \frac{1}{\phi^2}\left\{1 - \frac{8}{\phi^2} + \ldots + \frac{(-1)^n 2^{2n} n!(n+1)!}{\phi^{2n}} + \ldots\right\} \tag{A.16}$$

Upon expressing ϕz in terms of r, we find

$$r = \alpha^2\mu^{-1}(\phi^2 + 8 + \ldots) \tag{A.17}$$

which in turn implies that (A.15) becomes

$$2\alpha dt + r(1 + \frac{8\alpha^2}{\mu r} + \ldots)dr = 0 \tag{A.18}$$

Integrating this we find that

$$t = \frac{(r^2 - r_1^2)}{4\alpha} + \frac{4\alpha}{\mu}(r - r_1) + \ldots \tag{A.19}$$

$$= 7.0 \times 10^6(R^2 - R_1^2)(a\rho)$$

$$+ 5.0 \times 10^{-4}(R - R_1)(1.31 \times 10^5 a\rho - 7.53)^{-1}$$

where t is in years, R and R_1 in AU, and $\mu > 0$, $R > R_1$. Equation (A.19) holds as long as $\frac{\alpha c}{\mu_o} < .99$. For values of ap small enough for this inequality to be violated, the radius is of the order of 10^{-5} cm., which is comparable to the wavelength of radiation which the sun emits. Thus the cross section, σ, of the particle is subject to quantum mechanical effects. When the radiation pressure overcomes the gravitational pull of the sun the radius of the particle must be $< 10^{-5}$ cm. in order for the particle to be blown out of the solar system.

As a simple numerical example, consider an asteroidal particle of radius 5.0×10^{-2} cm., density 3.5 gm/cc, lying in a circular orbit in the midst of the asteroid belt, $\sim$ 3.0 AU. The time it takes for this particle to fall into the sun, assuming that it doesn't boil completely away, is $\sim 10^7$ years, which is comparatively short relative to the lifetime of the solar system.

B. Comminution Process.

The comminution or grinding process examined was originally investigated by Piotrowsky[4] and more recently by Dohnanyi[5,6,7]. The main ideas and equations of the comminution process are described below. The formulation described is the one presented by Dohnanyi in the three references quoted above.

Consider the collision of two objects of mass M_1 and M_2 where $M_1 < M_2$. The velocity of collision is assumed to be several kilometers per second. Only two situations will occur:

1) M_1 will create a crater in M_2 and destroy itself

2) M_1 will completely destroy M_2 and itself. This will be referred to as a catastrophic collision.

For the first case it was assumed that the total mass, M_e, of the debris is given by

$$M_e = \Gamma M_1 \qquad \Gamma = 5v^2 \tag{B.1}$$

where v is the velocity of impact and is measured in km/sec. The expression for Γ is a rough fit to experimental data[8] for basalt targets. The mass range of M_2 which can be catastrophically disrupted by M_1 is given by

$$M_2 \leq \Gamma' M_1 \tag{B.2}$$

where

$$\Gamma' \leq 50\Gamma \tag{B.3}$$

according to Dohnanyi[7].

The ejecta produced during collision and catastrophic events will have a certain mass distribution, and on the average, it is taken as

$$g(m;M_1,M_2)dm = C(M_1,M_2)m^{-n}dm \tag{B.4}$$

where $g(m;M_1,M_2)dm$ is the number of fragments of mass between m and m + dm produced by the collision of M_1 with M_2. The mass of the biggest fragment, M_b, is assumed to be

$$M_b = \Lambda M_1 \tag{B.5}$$

where Λ is approximately given by

$$\Lambda = \Gamma/10 \tag{B.6}$$

from experimental evidence.[8] For collisions which M_2 survives, it must be that

$$M_e = \int_{\mu}^{M_b} g(m;M_1,M_2)dm \tag{B.7}$$

where μ is the mass of the smallest fragment produced by the collision. Evaluating (B.7) given

$$C(M_1,M_2) = (2 - \eta)\Lambda^{\eta-2}M_1^{\eta-1} \qquad M_2 > \Gamma' M_1 \tag{B.8}$$

and for catastrophic collisions, the integration yields

$$C(M_1,M_2) = (2 - \eta)\Lambda^{\eta-2}(M_1 + M_2)M_1^{\eta-2} \qquad M_2 \leq \Gamma' M_1 \tag{B.9}$$

The differential equation of the collision process is next set up. It is given by

$$\frac{\partial f(m,t)}{\partial t}\,dm = \frac{\partial f(m,t)}{\partial t}\,dm\Big|_{\text{Erosion}} + \frac{\partial f(m,t)}{\partial t}\,dm\Big|_{\text{Catastrophic + collisions}}$$

$$+ \frac{\partial f(m,t)}{\partial t}\,dm\Big|_{\text{Creation by Fragmentation}}$$

where $f(m,t)dm$ is the number of particles per volume in the mass range dm. The various terms were evaluated by Dohnanyi[6] who attempted to find a "steady state" equation for the process. In a later paper[7] he shows that if the number density function $f(m,t)$ is given by the equation

$$f(m,t)dm = Am^{-\alpha}dm \qquad \text{(B.11)}$$

where A is a function of time and α is a constant at time t, then the distribution is unstable for $\alpha > 11/6$ and will decay to a lower value of α over a sufficiently long time. He considers the problem of comet fragments colliding with asteroids and asteroid fragments and concludes that such a process would produce a meteoroid environment characterized by different values of α (see Eq. B.11).

Also in his latest paper, Dohnanyi[7] states that collision processes are more efficient than radiation damping in producing very small particles. Small particles are produced by radiation damping since the Poynting-Robertson effect drives small particles close enough to the sun to cause them to

evaporate to the point where they're small enough to be blown out of the solar system by radiation pressure. Thus what he envisions are particles colliding with one another frequently enough so that the particles blown out of the solar system are small as a result of collision and not because they evaporated near the sun.

C. Solar Interaction and Dynamical Effects.

The solar interactions which will be considered are charged meteoroid interactions with the sun's time-varying magnetic field and also with the solar wind. There is a possibility that electromagnetic effects such as this are important in determining the existence of a minimum sized meteoroid. The reason of course is the very high strength of the Lorentz force.

Dynamical effects must be considered since they will hopefully serve as an upper limit on times which are important in the solar system. If a particle cannot survive a certain time in the solar system due to dynamical perturbations of its orbit, then there is little use in considering effects which take a longer time to destroy the particle.

Conclusions

The tentative conclusions arrived at thus far are the following:

1) Particle collision predominate as a means of producing very small particles. The Poynting-Robertson tangential drag has profound physical implications but is insignificant for creating small particles according to Dohnanyi[7]. He, however, did not concern himself with attempting to calculate a lower mass limit for meteoroids.

2) Erosion processes tend to produce a great deal of very small particles. About the only convincing process found to date which tends to impose a small particle limit seems to be radiation pressure.

The importance of cut-off to manned spacecraft is especially critical in interplanetary space. The problem is that very few measurements involving meteoroids in interplanetary space are possible from the earth. Knowledge of the interplanetary meteoroid environment is presently obtained from only two sources; observations of zodiacal light and observations of the asteroids. The existence of a lower limit on meteoroid size in the solar system would make the zodiacal light observations yield more information about the meteoroid population far from earth. Since it is expected that future spacecraft will go through the asteroid belts, such knowledge is needed about the belt. An improved estimate of the danger in the asteroid belt could be obtained from corrected zodiacal light estimates, crushing theory, and asteroid belt observations.

Knowledge of the near-earth meteoroid environment would also be obtained since definite knowledge of the meteoroid cut-off would help greatly in interpreting penetration data.

References

1. Alvarez, Jose M., "Satellite Measurements of Particles Causing Zodiacal Light," Proceedings of the Zodiacal Light and the Interplanetary Medium Symposium. Held January 30 to February 2, 1967 at Honolulu, Hawaii.
2. Jennison, R. C.; McDonnell, J. A. M.; Rogers, I.; "The Ariel II Micrometeorite Penetration Measurements." Proc. of the Royal Soc., 300, 251-269 (1967).
3. Robertson, H. P., "Dynamical Effects of Radiation in the Solar System." Royal Astronomical Soc., Monthly Notices, 97, 423-438 (1937).
4. Piotrowsky, S., Acta Astronomica, Ser. A, 5, 115 (1953).
5. Dohnanyi, J. S., "Collisional Model of Meteoroids." Bellcomm. Rept. TR-67-340-3, 1967.
6. Dohnanyi, J. S., "Collisional Model of Asteroids and Their Debris." Bellcomm. Rept., TR-68-710-4, 1968.
7. Dohnanyi, J. S., "On the Origin and Distribution of Meteoroids." Bellcomm. Rept., TR-69-105-3-2, 1969.
8. Gault, D. E.; Heitowit, E. D.; "The Partition of Energy for Hypervelocity Impact Craters Formed in Rock." Sixth Symp. Hypervelocity Impact, 2, 419-457 (1963).

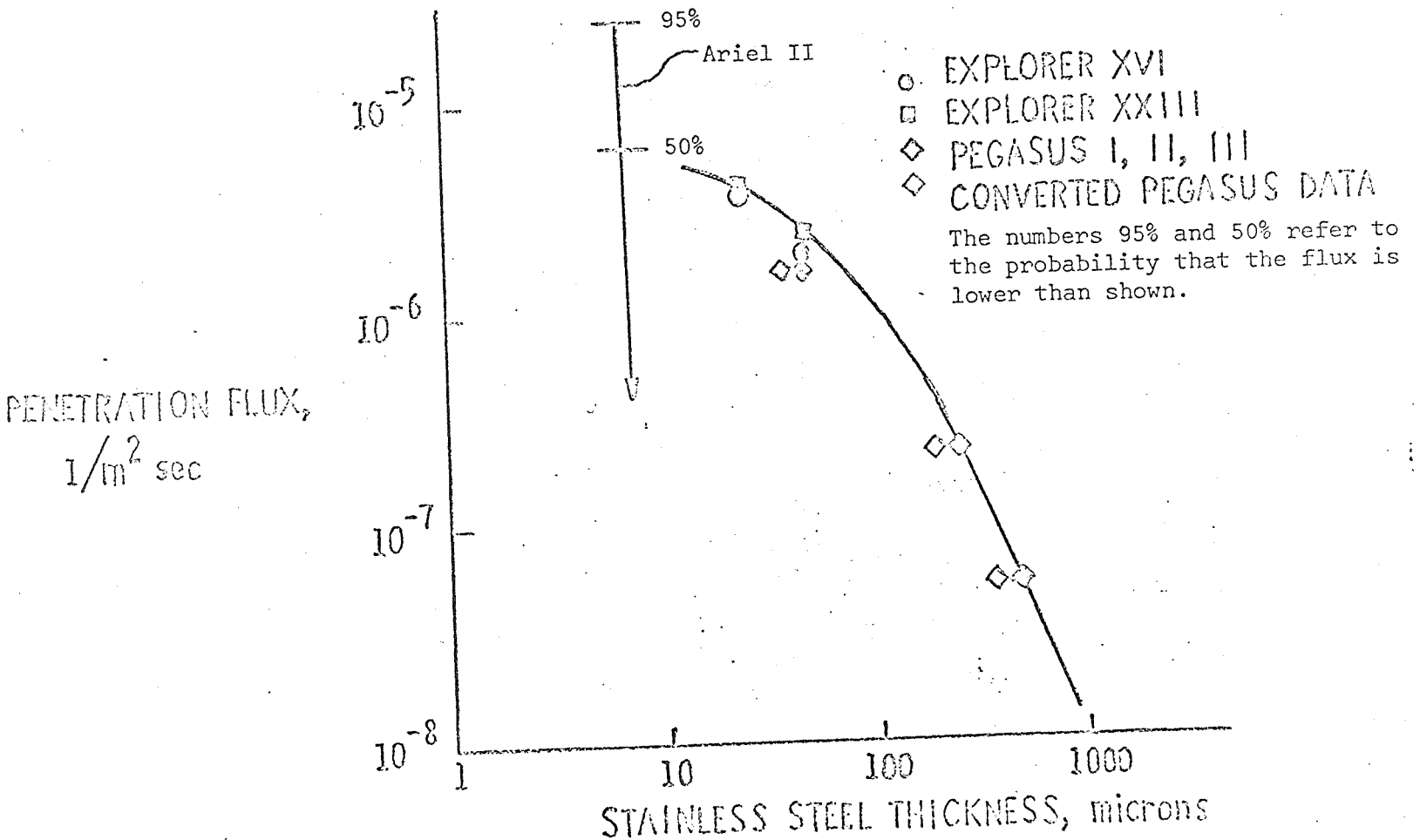

Figure I. Penetration Satellite Results

Harmonic Vibrations of Viscoelastic Layered Media

Extended Progress Report

V.P.I. Project 313142

Principal Investigator: D. Frederick
Department of Engineering Mechanics

TABLE OF CONTENTS

		Page
I.	LIST OF SYMBOLS	1
II.	SUMMARY	3
III.	VIBRATIONS OF VISCOELASTIC MEDIA	4
	A. Introduction	4
	B. Governing Equations	5
	C. Forced Harmonic Vibrations	7
	D. Free Vibrations	11
	E. Circular Cylinder in Torsional Oscillation	13
IV.	SHEAR DEFORMATION OF A BEAM	18
	A. Basic Analysis	18
	B. Segmented Normals	21
V.	REFERENCES	27

I. LIST OF SYMBOLS

σ_{jk}	stress tensor
ε_{jk}	strain tensor
s_{jk}	stress deviator tensor
e_{jk}	strain deviator tensor
u_j	displacement vector
f_j	forcing function
δ_{jk}	Kronecker delta
ρ	density
ω	frequency
t	time
G	complex shear modulus
K	complex bulk modulus
E	complex tensile modulus
ν	complex Poisson's ratio
G',...	real part of G,...
G'',...	imaginary part of G,...
G_R	stress relaxation modulus in shear
K_R	stress relaxation modulus in bulk
g	intensity of the relaxation spectrum for shear
b	intensity of the relaxation spectrum for bulk
P, Q, P', Q'	linear time operators
δ	damping factor
i	$\sqrt{-1}$
Re	means take real part of
Im	means take imaginary part of
r, θ, z	radial, angular, and axial coordinates of cylinder, resp.

T	torque
x, y, z	coordinates of beam
u_x, u_y, u_z	deformations of beam
κ	Timoshenko shear coeeficient
W	average deflection of cross section of beam
Q	transverse shear force
M	moment
U	displacement of cross section in axial direction
Φ	total angle of rotation of cross section
ϕ	angle of rotation of cross section due to transverse shear
A	area of cross section of beam
I	moment of inertia
$\bar{\ }$	a bar over a function indicates a complex function of coordinates

Subscripts:

$j, k, m, \ldots$	indices for rectangular Cartesian coordinates
r, θ, z	indices for cylindrical coordinates
δ	means quantity is for free vibration case
x, y, z	indices for coordinates of beam

II. SUMMARY

The purpose of the investigation was to study vibrations of structures made of alternate layers of elastic and viscoelastic materials. Many approaches have been taken by numerous researchers to solve vibrations of the viscoelastic materials, and the various approaches are discussed later in this report. Most authors seem to prefer handling free vibration rather than forced vibration of lossy materials but their methods have been found here to be approximately correct for small damping only. The theory of forced vibration is verified here and the torsional pendulum is solved using damped traveling waves which gives a physical picture of what is occurring in the bar. In addition a study of shear deformation is made using the recent and very lucid paper on the Timoshenko beam written by Cowper [31].

III. VIBRATIONS OF VISCOELASTIC MATERIAL

A. Introduction

A viscoelastic material converts mechanical energy of loading into heat. Because of this property, viscoelastic layers may be applied to elastic layers to damp out free vibrations and to decrease the amplitude of forced vibrations. Such multilayered media have been analyzed in the forms of beams, plates, and shells. The viscoelastic material has been treated by many investigators by assuming that it obeys the stress-strain laws of a spring-dashpot model [6], [7], [8], [9], [10], [11]. But a fairly simple model describing the behavior of a real material gives good results over only a narrow frequency range, and taking a larger number of springs and dashpots becomes mathematically unwieldy. In solving forced harmonic vibrations, some authors such as Henry and Freudenthal [12] and Biot and Pohle[13] under certain conditions correctly substitute complex moduli for the elastic moduli in the elastic solution and consequently solve the viscoelastic problem of the same shape and loading as the elastic problem. However, most authors seem to prefer treating free vibration [14], [15], [16], [17], [18], [19], rather than forced vibration. The usual procedure for free vibration is to select the time dependence for all stresses and displacements as $\exp(i\omega t - \delta t)$. This amounts to changing the frequency ω in the elastic solution to a complex frequency in addition to changing the elastic moduli to complex values. This procedure seems to be approximately correct for small damping only.

In attempts to simplify solutions, authors have made the assumption that the material is viscoelastic in shear but elastic in bulk [13], [24], or, alternately, the shear and bulk moduli have the same phase angle [13], [25].

Experiments have shown that neither of these assumptions is accurate. Kolsky [26] and Lifshitz and Kolsky [29] have shown experimentally for three familiar polymers that the tangent of the phase angle of the bulk modulus should be taken as two-tenths of the phase angle of the shear modulus. Another common assumption is that the material is incompressible [25], [27], [28].

Investigators such as Lee [20], Hunter [21], and Ward and Pinnock [22] who are interested primarily in the presentation of the theory of deformation of a three-dimensional linear viscoelastic body give only a one-dimensional theory for harmonic vibration. In reality, it appears that the three-dimensional vibration theory can be formulated by extending the one-dimensional case. The three-dimensional case appears in Bland's book [2], and is also presented here.

B. Governing Equations

The material considered is assumed to be isotropic, homogeneous, and to obey the linear viscoelastic laws. The stress-strain laws in integral form are [5], [21]

$$\sigma_{jk} = 2\int_{-\infty}^{t} G_R(t-u)\frac{d\varepsilon_{jk}}{du}\,du + \delta_{jk}\int_{-\infty}^{t}\left[K_R(t-u)-\frac{2}{3}G_R(t-u)\right]\frac{d\varepsilon_{mm}}{du}\,du \tag{1}$$

where

$$G_R(t) = \int_0^\infty g(\tau)\,e^{-t/\tau}\,d\tau \tag{2a}$$

$$K_R(t) = \int_0^\infty b(\tau)\,e^{-t/\tau}\,d\tau \tag{2b}$$

$G_R(t)$ and $K_R(t)$ are the stress relaxation moduli in shear and bulk, respectively, $g(\tau)$ and $b(\tau)$ are the intensities of the relaxation spectrums for shear and bulk, respectively, t is the time, and (t - u) is the elapsed time.

The differential forms of the stress-strain laws are [20]

$$P s_{jk} = Q e_{jk} \tag{3a}$$

$$P' \sigma_{mm} = Q' \varepsilon_{mm} \tag{3b}$$

where

$$P = \sum_{n=0}^{\infty} p_n D^n \quad , \quad Q = \sum_{n=0}^{\infty} q_n D^n$$

$$P' = \sum_{n=0}^{\infty} p'_n D^n \quad , \quad Q' = \sum_{n=0}^{\infty} q'_n D^n \tag{3c}$$

and

$$D^n = \frac{\partial^n}{\partial t^n}$$

Also, s_{jk} and e_{jk} are the deviator tensors for stress and strain, respectively. They are related to the stress and strain tensors by the following equations.

$$s_{jk} = \sigma_{jk} - \frac{1}{3} \sigma_{mm} \delta_{jk} \tag{4a}$$

$$e_{jk} = \varepsilon_{jk} - \frac{1}{3} \varepsilon_{mm} \delta_{jk} \tag{4b}$$

The strain-displacement relations for infinitesimal strains are

$$\varepsilon_{jk} = \frac{1}{2} (u_{j,k} + u_{k,j}) \tag{5}$$

where the comma means partial differentiation with respect to the coordinates.

The equations of motion are

$$\sigma_{jk,k} + f_j = \rho \frac{\partial^2 u_j}{\partial t^2} \tag{6}$$

where f_j is the forcing function or, alternately, a function describing a source of traveling waves. In simplifying the governing equations, the following lemma from Harrington [1] is needed. If $\mathrm{Re}(Ae^{i\omega t}) = \mathrm{Re}(Be^{i\omega t})$ where Re means to take the real part, and A and B are independent of time, then A = B. This is easily verified by letting t = 0 for which Re(A) = Re(B), and then letting $\omega t = \frac{1}{2}\pi$ for which Im(A) = Im(B) where Im means to select the imaginary part.

C. Forced Harmonic Vibration

If a linear viscoelastic material experiences forced harmonic vibration for a long enough time, a steady state will exist in which transient effects have died out and the stresses, strains and displacements vary harmonically in time. This statement has been used by Bland [2] in formulating the general three-dimensional equations of wave propagation in a linear viscoelastic media. To show the validity of the statement and therefore of Bland's work, the type of transient term involved is derived in the following analysis taken from Albrecht and Freudenthal [3]. It is assumed that the body is at rest for all negative time, and that a shearing strain

$$\varepsilon_{12} = \frac{\gamma_0}{2} \sin \omega t \tag{7a}$$

is imposed at zero time at some point in the material. The resulting shear stress from equations (1) and (2a) is

$$\begin{aligned} \tau_{12} &= 2\int_0^t G_R(t-u)\frac{\partial \varepsilon_{12}}{\partial u}\,du \\ &= \int_{u=0}^{t}\left[\int_{\tau=0}^{\infty} g(\tau)\, e^{(-t+u)/\tau}\,d\tau\right]\gamma_0 \omega \cos \omega u\, du \\ &= \gamma_0\left[G' \sin \omega t + G'' \cos \omega t\right] \\ &\quad - \gamma_0 \int_0^{\infty} g(\tau)\, e^{-t/\tau}\,\frac{\tau\omega}{1+\tau^2\omega^2}\,d\tau \end{aligned} \tag{7b}$$

where

$$G'(\omega) = \int_0^{\infty} g(\tau)\,\frac{\tau^2\omega^2}{1+\tau^2\omega^2}\,d\tau \tag{8a}$$

$$G''(\omega) = \int_0^{\infty} g(\tau)\,\frac{\tau\omega}{1+\tau^2\omega^2}\,d\tau \tag{8b}$$

The quantities G' and G" are the storage and loss moduli in shear, respectively. The third term of (7b) is nonharmonic and exponentially damped in time. Denoting this transient term as f(t) where

$$f(t) = \int_0^\infty g(\tau)\, e^{-t/\tau} \frac{\tau\omega}{1+\tau^2\omega^2}\, d\tau ,$$

it is noted that f(0) = G" and f(t) approaches zero as t approaches infinity. Therefore, after a sufficient length of time has passed, (7b) may be written as

$$\sigma_{12} = \gamma_0 \left(G' \sin \omega t + G'' \cos \omega t \right) \tag{9}$$

Thus ε_{12} and σ_{12} may be taken in the following more convenient form after steady state conditions are attained.

$$\varepsilon_{12} = \mathrm{Re}\left(\bar{\varepsilon}_{12}\, e^{i\omega t} \right) \tag{10a}$$

$$\sigma_{12} = \mathrm{Re}\left(\bar{\sigma}_{12}\, e^{i\omega t} \right) \tag{10b}$$

where the value of $\varepsilon_{12} = -\frac{1}{2} i \gamma_0$ gives the previously defined strain. Equations (10) are the type of definitions used in the equations of wave propagation and they are valid for time large enough.

The forcing function for the case of steady state forced vibration may be considered as a source of traveling waves of a single frequency equal to the frequency of the forcing function. In the following, the governing equations for motion in a linear viscoelastic medium are simplified for wave propagation and, in a later section, it is shown how traveling waves may be added together to construct solutions to forced vibration problems. Following Bland [2], the forcing function (or source), displacements, strains, and stresses for linear viscoelastic media are taken in the forms

$$f_j = \mathrm{Re}\left(\bar{f}_j\, e^{i\omega t} \right) \tag{12a}$$

$$u_j = \mathrm{Re}\left(\bar{u}_j\, e^{i\omega t} \right) \tag{12b}$$

$$\varepsilon_{jk} = \mathrm{Re}\left(\bar{\varepsilon}_{jk}\, e^{i\omega t}\right) \tag{12c}$$

$$\tau_{jk} = \mathrm{Re}\left(\bar{\tau}_{jk}\, e^{i\omega t}\right) \tag{12d}$$

$$e_{jk} = \mathrm{Re}\left(\bar{e}_{jk}\, e^{i\omega t}\right) \tag{12e}$$

$$s_{jk} = \mathrm{Re}\left(\bar{s}_{jk}\, e^{i\omega t}\right) \tag{12f}$$

where the functions having a bar are complex functions of the coordinates and are independent of time. Substituting (12e) and (12f) into (3a),

$$P\,\mathrm{Re}\left(\bar{s}_{jk}\, e^{i\omega t}\right) = Q\,\mathrm{Re}\left(\bar{\varepsilon}_{jk}\, e^{i\omega t}\right)$$

$$\mathrm{Re}\left[\bar{s}_{jk}\, e^{i\omega t} \sum_{n=0}^{\infty} p_n (i\omega)^n\right] = \mathrm{Re}\left[\bar{e}_{jk}\, e^{i\omega t} \sum_{m=0}^{\infty} q_m (i\omega)^m\right]$$

The differential forms of the stress-strain laws have been used here because they are much simpler when used with (12) than the integral forms. Applying the lemma and then dividing by the series in p_n,

$$\bar{s}_{jk} = \left[\frac{\sum_{m=0}^{\infty} q_m (i\omega)^m}{\sum_{n=0}^{\infty} p_n (i\omega)^n}\right] \bar{e}_{jk} \tag{13a}$$

or,

$$\bar{s}_{jk} = 2G\,\bar{e}_{jk} \tag{13b}$$

where 2G is defined as the quantity in brackets in (13a). Also,

$$G(\omega) = G'(\omega) + i\,G''(\omega)$$

The quantity G is the complex shear modulus; its components G' and G" are the same as those defined by (8). Substituting (12c) and (12d) into (3b) and proceeding as before, the complex equation governing the dilatation is obtained.

$$\bar{\tau}_{mm} = 3K\,\bar{\varepsilon}_{mm} \tag{15}$$

where

$$3K = \frac{\sum_{m=0}^{\infty} q'_m (i\omega)^m}{\sum_{n=0}^{\infty} p'_n (i\omega)^n}$$

and

$$K(\omega) = K'(\omega) + iK''(\omega) \tag{16}$$

K' and K'' are the storage and loss moduli in bulk, respectively, for forced vibration. Applying the lemma and the definitions (12) to equations (4), (5), and (6), the corresponding complex equations are obtained.

$$\bar{s}_{jk} = \bar{\sigma}_{jk} - \tfrac{1}{3}\bar{\sigma}_{mm}\delta_{jk} \tag{17a}$$

$$\bar{e}_{jk} = \bar{\varepsilon}_{jk} - \tfrac{1}{3}\bar{\varepsilon}_{mm}\delta_{jk} \tag{17b}$$

$$\bar{\varepsilon}_{jk} = \tfrac{1}{2}(\bar{u}_{j,k} + \bar{u}_{k,j}) \tag{18}$$

$$\bar{\sigma}_{jk,k} + \bar{f}_j + \rho\omega^2\bar{u}_j = 0 \tag{19}$$

Define

$$\nu = \frac{3K - 2G}{2(G+3K)} \tag{20}$$

and

$$E = 2G(1+\nu) \tag{21}$$

where ν is the complex Poisson's ratio and E is the complex tensile modulus for forced vibration. Equations (13) and (17) can be solved to give

$$\bar{\sigma}_{jk} = 2G\bar{\varepsilon}_{jk} + (K - \tfrac{2}{3}G)\bar{\varepsilon}_{mm}\delta_{jk} \tag{22}$$

Substituting (20) and (21) into (22),

$$\bar{\sigma}_{jk} = \frac{E}{1+\nu}\left[\bar{\varepsilon}_{jk} + \frac{\nu}{1-2\nu}\bar{\varepsilon}_{mm}\delta_{jk}\right] \tag{23}$$

Equation (23) may be solved for the complex strain. The result is

$$\bar{\varepsilon}_{jk} = \frac{1+\nu}{E}\bar{\sigma}_{jk} - \frac{\nu}{E}\bar{\sigma}_{mm}\delta_{jk} \tag{24}$$

Equations (18), (19), and (23) may be solved together to get the governing equation for the complex displacements.

$$\bar{u}_{j,kk} + \frac{1}{1-2\nu}\bar{u}_{m,mj} + \frac{1}{G}\bar{F}_j + \frac{\rho\omega^2}{G}u_j = 0 \qquad (25)$$

The forcing function may be dropped from the governing equation and applied instead through the boundary conditions. If this is done, (25) becomes

$$\bar{u}_{j,kk} + \frac{1}{1-2\nu}\bar{u}_{m,mj} + \frac{\rho\omega^2}{G}\bar{u}_j = 0$$

or, in vector notation,

$$\left(\nabla^2 + \frac{\rho\omega^2}{G}\right)\bar{u}_j\vec{e}_j + \frac{1}{1-2\nu}\vec{\nabla}\left(\vec{\nabla}\cdot\bar{u}_j\vec{e}_j\right) = 0 \qquad (26)$$

where $\vec{e}_j$ is a unit vector in the direction of the coordinate x_j.

D. Free Vibration

An exact solution to the equations of viscoelasticity for free vibration appears to be much more difficult to obtain than for forced vibration. The standard procedure in solving free vibration problems in viscoelasticity is to assume the time dependence to be of the form $\exp(i\omega t - \delta t)$ which may also be written as $\exp(i[\omega + i\delta]t)$. This assumed time dependence can be imposed on the equations for forced harmonic vibration by substituting $\omega + i\delta$ for ω in the governing equations. However, this procedure results in a shear modulus for free vibration, G_δ, which is different from the one for forced vibration. This is demonstrated in the following example. It is assumed first that a specimen is forced to vibrate at a natural frequency until all transient effects have become negligibly small. Then zero time is taken as the time when the load is removed after which the specimen is allowed to vibrate freely. The deflection for this motion is

$$u_j = \begin{cases} \mathrm{Re}\left(\bar{u}_j e^{i\omega t}\right), & -\infty < t < 0 \\ \mathrm{Re}\left(\bar{u}_j e^{i\omega t - \delta t}\right), & t > 0 \end{cases} \qquad (27)$$

Hence the shearing strain ε_{12} is

$$\varepsilon_{12} = \begin{cases} \mathrm{Re}(\bar{\varepsilon}_{12} e^{i\omega t}) & , -\infty < t < 0 \\ \mathrm{Re}(\bar{\varepsilon}_{12} e^{i\omega t - \delta t}) & , t > 0 \end{cases} \tag{28}$$

The corresponding stress may be found by substituting (2a) and (28) into (1).

$$\sigma_{12} = \mathrm{Re}\left\{ \int_{-\infty}^{0} 2G_R(t-u) \frac{d}{du}(\bar{\varepsilon}_{12} e^{i\omega u})\, du + \int_{0}^{t} 2G_R(t-u) \frac{d}{du}(\bar{\varepsilon}_{12} e^{i\omega u - \delta u})\, du \right\} \tag{29}$$

or,

$$\sigma_{12} = \mathrm{Re}\left\{ 2G_\delta \bar{\varepsilon}_{12} e^{i\omega t - \delta t} \right\} + \mathrm{Re}\left\{ 2\int_0^\infty g(\tau) e^{-t/\tau} \bar{\varepsilon}_{12} \left[\frac{\tau\omega(\tau\omega + i)}{1+\tau^2\omega^2} - \frac{\tau^2\omega^2 - \delta\tau(1-\delta\tau) + i\tau\omega}{(1-\delta\tau)^2 + \tau^2\omega^2} \right] d\tau \right\} \tag{30}$$

where

$$G_\delta = G_\delta' + i G_\delta'' \tag{31}$$

$$G_\delta' = \int_0^\infty g(\tau) \left[\frac{\tau^2\omega^2 - \delta\tau(1-\delta\tau)}{(1-\delta\tau)^2 + \tau^2\omega^2} \right] d\tau \tag{32a}$$

$$G_\delta'' = \int_0^\infty g(\tau) \left[\frac{\tau\omega}{(1-\delta\tau)^2 + \tau^2\omega^2} \right] d\tau \tag{32b}$$

A comparison of equations (8) with (32) reveals that G may be obtained from G_δ in theory by setting δ equal to zero in (32). But the shear modulus is a material property and is independent of the nature of the loading applied. Thus the assumed time dependence for free vibration leads to the erroneous conclusion that the shear modulus for free vibration is different from the one for forced vibration. However, when δ is small, G_δ is nearly equal to G, and $\exp(i\omega t - \delta t)$ may then be valid approximately for damping small enough.

No exact solutions for free vibration of a viscoelastic specimen have been found in a search of the literature, and all efforts to find such a solution under this project have so far been fruitless.

E. Circular Cylinder in Torsional Oscillation

For forced torsional oscillations of a circular cylinder, all normal strains are zero in the usual circular cylindrical coordinates (r, θ, z). Thus the dilatation vanishes, and (26) becomes

$$\left(\nabla^2 + \frac{\rho\omega^2}{G}\right)\bar{u}_j\,\vec{e}_j = 0 \tag{33}$$

Furthermore, only the angular displacement u_θ has a value in this case. Therefore, (33) reduces to

$$\left(\nabla^2 + \frac{\rho\omega^2}{G}\right)\bar{u}_\theta\,\vec{e}_\theta = 0 \tag{34}$$

Equation (34) is known as a vector wave equation. Complex equations of this form occur in the study of electromagnetic wave propagation in lossy media[1]. Thus the well-developed electromagnetic wave theory may be used as a guide in constructing solutions to (34).

Torsional waves in a circular cylinder travel in the axial, or z, direction. A plane torsional wave traveling in the positive z direction is given by

$$\bar{u}_\theta = V(r)\,e^{-ikz} \tag{35}$$

where

$$k = k' - ik'' \tag{36}$$

In electromagnetic wave theory, k' is called the propagation constant, and k'' is known as the attenuation constant. These quantities have the same names in linear viscoelasticity even though they are in reality not constants, but

functions of frequency. The same wave as (35) traveling in the negative z direction is expressed as

$$\bar{u}_\theta = V(r)\, e^{ikz} \tag{37}$$

Consider an infinitely long cylindrical bar with a source of plus z traveling waves of torsion located at a large negative value of z and an identical source of negative z traveling waves located at a large positive value of z. The waves will interact to produce a displacement-free surface at the origin when the displacement is the difference of (35) and (37).

$$\bar{u}_\theta = V(r)\left(e^{ikz} - e^{-ikz}\right) \tag{38}$$

For k" not equal to zero, there are no other displacement-free surfaces. The complex stress $\sigma_{z\theta}$ from (22) and (18) is

$$\bar{\sigma}_{z\theta} = G\frac{\partial \bar{u}_\theta}{\partial z} \tag{39}$$

Substituting (38) into (39)

$$\bar{\sigma}_{z\theta} = G V(r) ik\left(e^{ikz} - e^{-ikz}\right) \tag{40}$$

It can be shown with this equation that for k" not equal to zero, there are no surfaces free of this stress. Substituting (38) into (34) and simplifying, the relationship for V(r) is obtained.

$$\frac{\partial}{\partial r}\left[\frac{1}{r}\frac{\partial}{\partial r}(rV)\right] + (ik)^2 V + \frac{\rho\omega^2}{G}V = 0 \tag{41}$$

Let

$$\alpha^2 = \frac{\rho\omega^2}{G} - k^2 \tag{42}$$

Then

$$\frac{\partial}{\partial r}\left[\frac{1}{r}\frac{\partial}{\partial r}(rV)\right] + \alpha^2 V = 0 \tag{43}$$

The solution for $\alpha = 0$ is

$$V = Ar + \frac{B}{r} \tag{44}$$

For a solid bar, B = 0, and

$$V = Ar \tag{45}$$

Substituting (45) into (38)

$$\bar{u}_\theta = Ar\left(e^{ikz} - e^{-ikz}\right) \tag{46}$$

For $\alpha = 0$, (42) gives

$$k^2 = \frac{\rho\omega^2}{G} \tag{47}$$

The shear modulus may be expressed in terms of its magnitude, $|G|$, and phase angle, γ, by

$$G = |G|\, e^{i\gamma}$$

This can be used to solve for k' and k" from (47). The result is

$$k' = \omega\sqrt{\frac{\rho}{|G|}}\,\cos\frac{\gamma}{2} \tag{48a}$$

$$k'' = \omega\sqrt{\frac{\rho}{|G|}}\,\sin\frac{\gamma}{2} \tag{48b}$$

The shear stress $\bar{\sigma}_{r\theta}$ must vanish on the surface of the bar. Equations (18) and (22) expressed in cylindrical coordinates and solved with (46) yield

$$\begin{aligned}\bar{\sigma}_{r\theta} &= 2G\bar{\varepsilon}_{r\theta} \\ &= G\left[\frac{\partial\bar{u}_\theta}{\partial r} - \frac{\bar{u}_\theta}{r}\right] \\ &= 0\end{aligned}$$

It can be shown that all stresses vanish except $\sigma_{z\theta}$.

Since (46) gives no displacement at z = 0, it is also the solution for a semi-infinite circular bar built in at z = 0 if the portion of the bar along the negative z axis is discarded. The solution may then be interpreted physically as a train of waves emanating from a source at a large value of positive z and reflecting from the fixed end at the origin. The solution for forced oscillation

of a torsional pendulum in terms of the torque applied at one end may also be obtained from (46). A plane perpendicular to the z-axis is passed through the semi-infinite bar at z = L, and the portion of the bar beyond z = L is discarded. A forcing function placed at z = L exactly duplicates the stress distribution occurring before the cut was made. From (40) and (45), this stress distribution is

$$\bar{\tau}_{z\theta}\Big|_{z=L} = GAr\,ik\left(e^{ikz} - e^{-ikz}\right) \tag{49}$$

The applied torque is

$$T = Re\left(\bar{T}\, e^{i\omega t}\right) \tag{50}$$

$$\bar{T} = \int_{\theta=0}^{2\pi}\int_{r=0}^{a} r\,\bar{\tau}_{z\theta}\Big|_{z=L}\, r\,dr\,d\theta \tag{51}$$

where a is the radius of the cylinder. Substituting (49) into (51) and solving for the constant A,

$$A = \frac{2\bar{T}}{\pi a^4}\left[Gik\left(e^{ikz} - e^{-ikz}\right)\right]^{-1} \tag{52}$$

The deflection from (46) and (52) is

$$\bar{u}_\theta = \frac{2\bar{T}r\left(e^{ikz} - e^{-ikz}\right)}{\pi a^4 ikG\left(e^{ikL} + e^{-ikL}\right)} \tag{53}$$

Since the deflection varies linearly with r, it may be duplicated experimentally by attaching a rigid disk to the end at z = L and forcing the disk to oscillate. For an elastic material, (53) becomes

$$\bar{u}_\theta = \frac{2\bar{T}r\sin kz}{\pi a^4 kG\cos kL} \tag{54}$$

The viscoelastic deflection could have been obtained from the elastic solution (54) by making k and G complex. A third technique is used by Berry [4] who

seems to be the first to have solved torsional oscillation of a viscoelastic pendulum. He used a separation of variables technique and applied the forcing function through the boundary conditions. The advantage of using traveling waves to construct a solution is that it gives a physical picture of what is occurring in the bar.

IV. SHEAR DEFORMATION OF A BEAM

A. Basic Analysis

In the following, a study is made of the Timoshenko beam which includes the effects of rotary inertia and shear deformation in the governing equations. Shear deformation and rotary inertia also occur in a shell, but a study of these effects in a beam gives all the information necessary to understand the same effects in a shell and has the advantage of involving only one coordinate in the governing equations. The ultimate application of the derived theory presented here will be to vibration of multilayered shells.

The initial analysis is taken from Cowper's [31] derivation of the beam equations by integrating the equations of elasticity over the cross section of the beam. The beam coordinates x, y, z have directions as shown in figure 1.

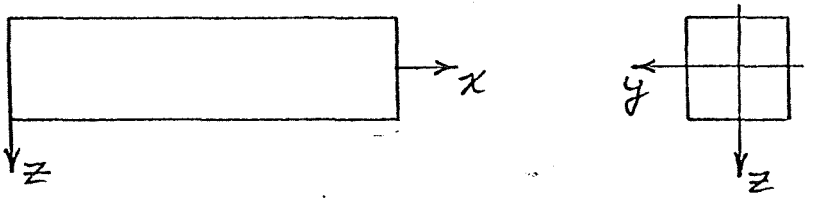

Figure 1

The deflections u_z and u_x in the z and x directions, respectively, are written as

$$u_z = W + v_z \tag{55a}$$

$$u_x = U + z\Phi + v_x \tag{55b}$$

where

$$W = \frac{1}{A}\iint u_z \, dy \, dz \tag{56a}$$

$$U = \frac{1}{A}\iint u_x \, dy \, dz \tag{56b}$$

$$\Phi = \frac{1}{I}\iint z u_x \, dy \, dz \tag{56c}$$

W is the average deflection of the cross section in the z direction, U is the average displacement of the cross section in the x direction, Φ is the average angle of rotation of the cross section about the neutral axis, A is the area of the cross section, and v_x and v_z are residuals. Integrating equations (55) over the cross section and applying equations (56) yields

$$\iint v_z \, dy \, dz = \iint v_x \, dy \, dz = \iint z v_x \, dy \, dz = 0 \tag{57}$$

The equations (55) are substituted into the following stress-strain relation from elasticity.

$$\frac{\partial u_z}{\partial x} + \frac{\partial u_x}{\partial z} = \frac{\tau_{xz}}{G} \tag{58}$$

The result is

$$\frac{\partial W}{\partial x} + \Phi = \frac{\tau_{xz}}{G} - \frac{\partial v_x}{\partial z} - \frac{\partial v_z}{\partial x} \tag{59}$$

This is integrated over the cross section to obtain

$$\frac{\partial W}{\partial x} + \Phi = \frac{Q}{AG} - \frac{1}{A} \iint \frac{\partial v_x}{\partial z} \, dy \, dz \tag{60}$$

Cowper assumes that the distribution of the residual, v_x, for a vibrating beam is the same as the distribution for a static load on the beam. This allows him to evaluate the last term in (60) as a constant times the factor $\frac{Q}{AG}$. After performing the integration, (60) becomes

$$\frac{\partial W}{\partial x} + \Phi = \frac{Q}{\kappa AG} \tag{61}$$

where κ is called the Timoshenko shear coefficient. It is easily seen that if v_x is neglected in (60), the result is

$$\frac{\partial W}{\partial x} + \Phi = \frac{Q}{AG} \tag{62}$$

which is the same as setting κ equal to unity in (61). For elementary beam theory, the shear deformation is neglected and (60) becomes

$$\frac{\partial W}{\partial x} + \Phi = 0 \tag{63}$$

Three other equations derived by Cowper are

$$\frac{\partial Q}{\partial x} + p = \rho A \frac{\partial^2 W}{\partial t^2} \tag{64a}$$

$$\frac{\partial M}{\partial x} - Q = \rho I \frac{\partial^2 \Phi}{\partial t^2} \tag{64b}$$

$$EI \frac{\partial \Phi}{\partial x} = M \tag{64c}$$

where

$M = \iint z \, \sigma_{xx} \, dy \, dz$ is the bending moment acting at a section, I is the moment of inertia of the cross section, p is the total force acting in the z direction on the beam, E is the tensile modulus, and ρ is the density. The governing equation on W can be obtained by eliminating the unknowns Q, M, and Φ in (61) and (64). The deflection W may further be written as

$$W = W_H + W_P$$

where W_H is the homogeneous solution to the governing equation on W, and W_p is the particular solution. Assuming a harmonic time dependence, the equation governing W_H is

$$\frac{d^4 W_H}{dx^4} + \left[\frac{\rho\omega^2}{\kappa G} + \frac{\rho\omega^2}{E}\right] \frac{d^2 W_H}{dx^2}$$

$$+ \frac{\rho\omega^2}{E}\left[\frac{\rho\omega^2}{\kappa G} - \frac{A}{I}\right] W_H = 0 \tag{65}$$

A quantity which is needed later is ϕ which is the rotation of the cross section due to transverse shear. Its relationship to previously defined quantities is

$$\frac{\partial W}{\partial x} + \Phi = \phi \tag{66a}$$

Φ and ϕ are positive when measured counterclockwise, but $\frac{\partial W}{\partial x}$ is positive when measured clockwise in the coordinate system used here. Equations (66a) and (62) lead to

$$\phi = \frac{Q}{AG} \tag{66b}$$

B. Segmented Normals

The warped surfaces of certain statically loaded beams are known functions of the beam coordinates, and Cowper assumed that these surfaces were the same as the warped surfaces when a vibratory load was applied. This led to an equation for the shear coefficient as a function of Poisson's ratio. For an elastic shell, the shear coefficients have been found by means of a free vibration solution, but this is not practical at this time for viscoelastic materials since free vibration of these materials has not been satisfactorily described mathematically as yet. Another procedure which in effect gives a better approximation than unity for the shear coefficient is to divide the normal into segments each of which can rotate independently of the other segments but each of which remains straight after deformation. This procedure is applied here to the Timoshenko beam in order to show the kind of accuracy that may be expected from this method.

The solid beam is first divided into three layers of equal thicknesses as shown in figure 2 for the purpose of assigning a number to each of the segments

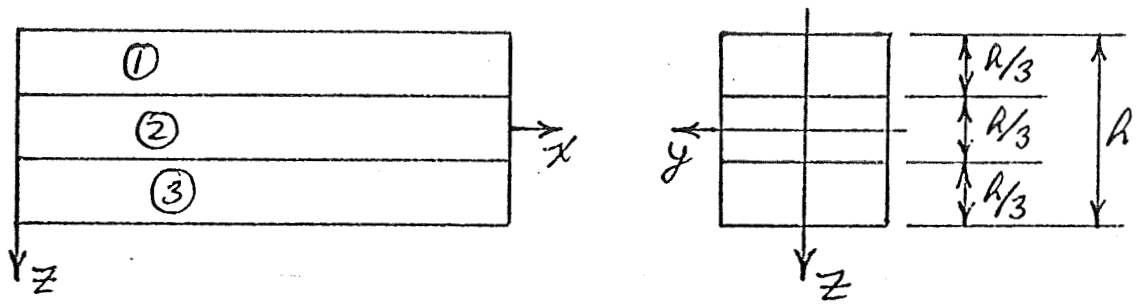

Figure 2

of the normal. A subscript on a variable will refer to the corresponding layer, and the same variable without a subscript indicates a quantity which describes the beam as a single unit. The deflections will be taken as follows:

$$u_{z_1} = u_{z_2} = u_{z_3} = W \tag{67a}$$

$$u_{x_1} = U_1 + \left(z + \frac{h}{3}\right)\Phi_1 \tag{67b}$$

$$u_{x_2} = U_2 + z\Phi_2 \tag{67c}$$

$$u_{x_3} = U_3 + \left(z - \frac{h}{3}\right)\Phi_3 \tag{67d}$$

U_1, U_2, and U_3 are shown in figure 3.

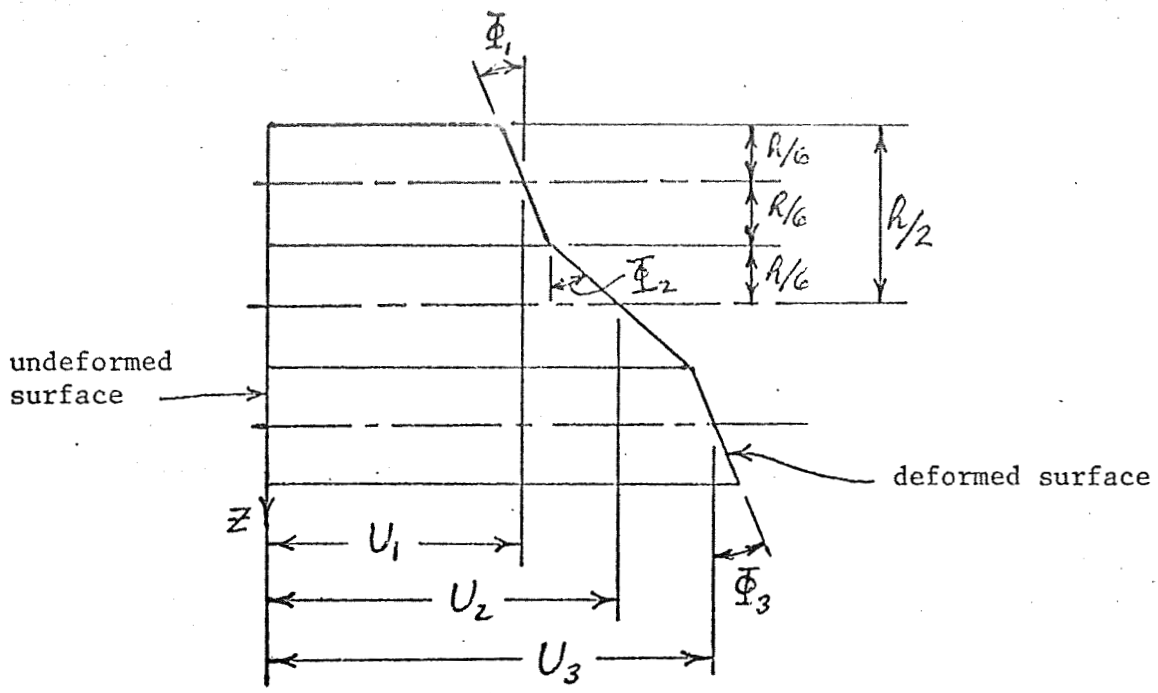

Figure 3

Equation (58) integrated over each layer yields the following three equations.

$$\Phi_1 + \frac{\partial W}{\partial x} = \frac{Q_1}{A_1 G} \tag{68a}$$

$$\Phi_2 + \frac{\partial W}{\partial x} = \frac{Q_2}{A_2 G} \tag{68b}$$

$$\Phi_3 + \frac{\partial W}{\partial x} = \frac{Q_3}{A_3 G} \tag{68c}$$

where

$$Q_1 + Q_2 + Q_3 = Q \tag{69a}$$

$$A_1 = A_2 = A_3 = \frac{1}{3} A \tag{69b}$$

Also, the following assumption is made.

$$\Phi_1 = \Phi_3 \tag{70a}$$

which leads to

$$Q_1 = Q_3 \tag{70b}$$

The result of adding the equations (68) and applying (69) and (70) is

$$\frac{1}{3}(2\Phi_1 + \Phi_2) + \frac{\partial W}{\partial x} = \frac{Q}{AG} \tag{71a}$$

The three following equations are derived similarly.

$$\frac{\partial Q}{\partial x} + p = \rho A \frac{\partial^2 W}{\partial t^2} \tag{71b}$$

$$\frac{\partial M}{\partial x} - Q = \frac{\rho A \ell^2}{324}\left[38\frac{\partial^2 \Phi_1}{\partial t^2} + 13\frac{\partial^2 \Phi_2}{\partial t^2}\right] \tag{71c}$$

$$M = \frac{EA\ell^2}{324}\left[38\frac{\partial \Phi_1}{\partial x} + 13\frac{\partial \Phi_2}{\partial x}\right] \tag{71d}$$

The four equations (71) involve the five unknowns Φ_1, Φ_2, W, Q, and M. Thus another relationship between these variables must be found.

From (66), (68), and (69b),

$$\phi_1 = \Phi_1 + \frac{\partial W}{\partial x} \tag{72a}$$

$$\phi_2 = \Phi_2 + \frac{\partial W}{\partial x} \tag{72b}$$

and

$$\phi_1 = \frac{3Q_1}{AG} \tag{73a}$$

$$\phi_2 = \frac{3Q_2}{AG} \tag{73b}$$

Also, (70) and (68) yield $\phi_3 = \phi_1$. The angles ϕ_1 and ϕ_2 are the rotations of the segments of normal due to transverse shear. A relationship between ϕ_1 and ϕ_2 can be chosen to make the shearing stresses have the best fit to a parabolic distribution in the z-direction. This is accomplished by first writing a parabolic distribution for σ_{xz}. The correct result is

$$\tau_{xz} = \frac{3Q}{2R^2A}\left(R^2 - z^2\right) \tag{74}$$

Next, the average of σ_{xz} is taken over each layer.

$$\iint_{\text{LAYER \#1}} \tau_{xz}\, dy\, dz = Q_1 \tag{75a}$$

$$\iint_{\text{LAYER \#2}} \tau_{xz}\, dy\, dz = Q_2 \tag{75b}$$

The final result of evaluating equations (75) and using (73) is

$$\phi_1 = \frac{7}{13}\,\phi_2 \tag{76}$$

The functions ϕ_1, ϕ_2, Φ_1, Φ_2, M, and Q may be eliminated from equations (71), (72), and (76) resulting in the governing equation on W. The result for W_H assuming a harmonic time dependence is

$$\frac{d^4 W_H}{dx^4} + \left[\frac{81}{89}\frac{\rho\omega^2}{G} + \frac{\rho\omega^2}{E}\right]\frac{d^2 W_H}{dx^2} + \frac{\rho\omega^2}{E}\left[\frac{81}{89}\frac{\rho\omega^2}{G} - \frac{A}{I}\right] W_H = 0 \tag{77}$$

This is the same equation as (65) with κ taking the value

$$\kappa = \frac{81}{89} = 0.912 \tag{78}$$

for three segments of normal. Cowper's value for κ which allows the normal to warp is (for a rectangular beam)

$$\kappa = \frac{10(1+\nu)}{12+11\nu} \tag{79a}$$

where ν is Poisson's ratio. (79a) gives

$$\kappa = 0.833 \quad \text{for} \quad \nu = 0 \tag{79b}$$

$$\kappa = 0.857 \quad \text{for} \quad \nu = 0.5 \tag{79c}$$

For a single straight normal with warping neglected,

$$\kappa = 1.00 \tag{80}$$

A comparison of (78), (79) and (80) reveals that dividing the normal into three segments decreases by more than 50% the difference between the shear coefficient for a single straight normal with no warpage and the best known value of the shear coefficient as determined by Cowper. Dividing the normal into more than three segments should improve the accuracy further. As mentioned previously, the purpose of applying this analysis to a beam was to evaluate the accuracy of the method before applying it to a shell.

REFERENCES

1. Harrington, R. F., Time-Harmonic Electromagnetic Fields, McGraw-Hill, New York, 1961

2. Bland, D. R., The Theory of Linear Viscoelasticity, Pergamon Press, London, 1960

3. Albrecht, B., and Freudenthal, A. M., "Second-Order Visco-Elasticity in a Filled Elastomer," International Journal of Solids and Structures, Vol. 2, No. 4, Oct. 1966, pp. 555-571

4. Berry, D. S., "Stress Propagation in Visco-Elastic Bodies," Journal of the Mechanics and Physics of Solids, Vol. 6, 1958, pp. 177-185

5. Staverman, A. J., and Schwarzl, F., "Linear Deformation Behaviour of High Polymers," chapter one of Die Physik der Hochpolymeren, edited by H. A. Stuart, Springer, Berlin, 1956

6. Achenbach, J. D., and Chao, C. C., "A Three-Parameter Viscoelastic Model Particularly Suited for Dynamic Problems," Journal of the Mechanics and Physics of Solids, Vol. 10, 1962, pp. 245-252

7. Maybee, J. S., "Normal and Quasi-Normal Modes in Damped Linear Dynamic Systems," Journal of Applied Mechanics, Vol. 33, No. 2, June 1966, pp. 413-416

8. Newman, J. K., "Viscous Damping in Flexural Vibrations of Bars," Journal of Applied Mechanics, Vol. 26, No. 3, Sept. 1959, pp. 367-376

9. Williams, M. L., "Structural Analysis of Viscoelastic Materials," AIAA Journal, Vol. 2, No. 5, May 1964, pp. 785-808

10. Eller, S. A., and Cohen, L., "Investigation of the Vibration Damping Properties of Viscoelastic Materials Using a Delay Angle Technique," Shock and Vibration Bulletin, No. 35, Part 5, Feb. 1966, The Shock and Vibration Information Center, U. S. Naval Research Lab, Washington, D. C., pp. 159-168

11. Pan, H. H., "Vibration of Viscoelastic Plates," Journal de Mecanique, Vol. 5, No. 3, Sept. 1966, pp. 355-374

12. Henry, L. A., and Freudenthal, A. M., "Standing Waves in a Viscoelastic Cylinder Case Bonded to a Thin Shell," AIAA Journal, Vol. 4, No. 2, Feb. 1966, pp. 313-319

13. Biot, M. A., and Pohle, F. V., "Validity of Thin-Plate Theory in Dynamic Viscoelasticity," Journal of the Acoustical Society of America, Vol. 36, No. 6, June 1964, pp. 1110-1117

14. Parke, S., "Logarithmic Decrements at High Damping," British Journal of Applied Physics, Vol. 17, No. 2, pp. 271-273

15. Jones, I. W., Salerno, V. L., and Savacchio, A., "An Analytical and Experimental Evaluation of the Damping Capacity of Sandwich Beams with Viscoelastic Cores," Trans. ASME, Series B, Vol. 89, No. 3, Aug. 1967, pp. 438-444, Journal of Engineering for Industry

16. Yu, Y.-Y., "Damping of Flexural Vibrations of Sandwich Plates," Journal of Aerospace Sciences, Vol. 29, No. 7, July 1962, pp. 790-803

17. DiTaranto, R. A., "Theory of Vibratory Bending for Elastic and Viscoelastic Layered Finite-Length Beams," Journal of Applied Mechanics, Vol. 32, No. 4, Dec. 1965, pp. 881-886

18. DiTaranto, R. A., and Blasingame, W., "Composite Damping of Vibrating Sandwich Beams," Journal of Engineering for Industry, Trans. ASME, Series B, Vol. 89, No. 4, Nov. 1967, pp. 633-638

19. Nicholas, T., and Heller, R. A., "Determination of the Complex Shear Modulus of a Filled Elastomer from a Vibrating Sandwich Beam," Experimental Mechanics, J. Soc. Exp. Stress Analysis, Vol. 7, No. 3, March 1967, pp. 110-116

20. Lee, E. H., "Viscoelastic Stress Analysis," Structural Mechanics, Proc. First Symposium Naval Structural Mechanics, Stanford U., Calif., 1958, edited by J. N. Goodier and N. J. Hoff, Pergamon Press, New York, 1960, pp. 456-482

21. Hunter, S. C., "The Solution of Boundary Value Problems in Linear Viscoelasticity," Mechanics and Chemistry of Solid Propellants, Proc. Fourth Symposium Naval Structural Mechanics, April 1965, edited by A. C. Eringen, et al., Pergamon Press, New York, 1967, pp. 257-295

22. Ward, I. M., and Pinnock, P. R., "The Mechanical Properties of Solid Polymers," British Journal of Applied Physics, Vol. 17, No. 1, Jan. 1966, pp. 3-32

23. Love, A. E. H., A Treatise on the Mathematical Theory of Elasticity, Dover, New York, 1944

24. Lockett, F. J., "Interpretation of Mathematical Solutions in Viscoelasticity Theory Illustrated by a Dynamic Spherical Cavity Problem," Journal of the Mechanics and Physics of Solids, Vol. 9, 1961, pp. 215-229

25. Pan, H. H., "Vibration of a Viscoelastic Timoshenko Beam," Journal of the Engineering Mechanics Division, Proc. ASCE, Vol. 92, No. EM 2, April 1966, pp. 213-234

26. Kolsky, H., "Experimental Studies in Stress Wave Propagation," Proc. of the Fifth U. S. Nat. Congress of Applied Mechanics, 1966, pp. 21-36

27. Achenbach, J. D., "Dynamic Response of a Long Viscoelastic Cylinder," AIAA Journal, Vol. 3, April 1965, pp. 673-677

28. Pilkey, W. D., "Vibrations of a Viscoelastic Timoshenko Beam," Journal of the Engineering Mechanics Division, Proc. ASCE, Vol. 92, EM 6, Dec. 1966, pp. 254-257

29. Lifshitz, J. M., and Kolsky, H., "The Propagation of Spherically Divergent Stress Pulses in Linear Viscoelastic Solids, Journal of the Mechanics and Physics of Solids, Vol. 13, No. 6, Dec. 1965, pp. 361-376

30. Sokolnikoff, I. S., Mathematical Theory of Elasticity, McGraw-Hill, New York, 1956

31. Cowper, G. R., "The Shear Coefficient in Timoshenko's Beam Theory," Journal of Applied Mechanics, Vol. 33, June 1966, pp. 335-340